Epigenetic DNA modification monitored by a new fluorescence based tool

Vasyl Kilin

UNIVERSITÉ DE STRASBOURG

ÉCOLE DOCTORALE DES SCIENCE DE LA VIE ET DE LA SANTE
UMR 7213

THÈSE présentée par :

Vasyl KILIN

soutenue le : **26 Février 2016**

pour obtenir le grade de : **Docteur de l'université de Strasbourg**

Discipline/ Spécialité : Biophysique

Analyse par de nouveaux outils de fluorescence du mécanisme de la protéine UHRF1 dans la méthylation de l'ADN

THÈSE dirigée par :
M. MELY Yves Professeur, Université de Strasbourg

RAPPORTEURS :
M. MERGNY Jean Louis Directeur de Recherches, INSERM
M. MAUFFRET Oliver Directeur de Recherches, Université PARIS-SACLAY

AUTRES MEMBRES DU JURY :
Mm. DANTZER Françoise Directeur de Recherches, IREBS
M. BURGER Alain Professeur, Université de Nice

LIST OF ABBREVIATIONS

DNA	deoxyribonucleic acid
RNA	ribonucleic acid
TET	ten-eleven translocation
UHRF	Ubiquitin-like, containing PHD and RING finger protein
PHD	Plant Homeo Domain
RING	Really Interesting New Gene domain
SRA	SET and RING Associated domain
DNMT	DNA methyltransferase
AdoMet	S-adenosylmethionine
HDAC	Histone deacetylase
MBP	methyl binding protein
MBD	methyl binding domain
αHL	Alpha hemolysin
MspA	Mycobacterium smegmatis porin
M.HhaI	Haemophilus haemolyticus methyltransferase
mC	methylcytosine
SMRT	single-molecule real-time
AFM	Atomic Force Microscopy
PET	photoinduced electron transfer
ESIPT	excited state intramolecular proton transfer
BPT	back proton transfer
3HF	3 hydroxyflavone
3HC	3 hydroxychromone
3HCnt	3hydroxychromone nucleotide

Contents

RESUME

Toutes les cellules de mammifères possèdent le même code génétique et le même nombre de gènes. Pourtant, lorsqu'elles se différencient, les cellules vont acquérir des profils d'expression caractéristiques d'un tissu et exprimer les seuls gènes nécessaires à leurs fonctions. L'existence d'épigénomes distincts explique pourquoi le même génotype peut générer différents phénotypes. Ce sont les modifications épigénétiques, héritables lors des divisions cellulaires, qui régissent ainsi le destin d'une cellule, en régulant l'expression de ses gènes sans affecter la séquence de l'ADN (Berger et al. 2009). Parmi ces modifications, la méthylation de l'ADN, les modifications post-traductionnelles des histones, les changements de variants d'histones, et les ARNs non-codant vont entraîner des modifications de l'architecture de la chromatine, support de l'information épigénétique. Ces mécanismes sont régulés par un grand nombre d'acteurs capables d'écrire, de lire ou d'effacer ces modifications et qui vont travailler en coopération pour inhiber ou activer l'expression de gènes spécifiques. L'épigénétique joue un rôle essentiel dans un grand nombre de mécanismes tels que le développement embryonnaire, la différenciation cellulaire et l'identité cellulaire (Smallwood & Kelsey 2012). Par ailleurs, les altérations épigénétiques sont aussi impliquées dans un grand nombre de pathologies telles que le cancer, les maladies neurologiques ou auto-immunes (Portela & Esteller 2010). Les modifications épigénétiques étant réversibles, la compréhension des mécanismes régissant leur régulation ouvre la porte à de nouvelles stratégies thérapeutiques.

La principale modification épigénétique est la méthylation des cytosines, qui correspond à l'ajout d'un groupement méthyl sur le carbone 5 des résidus cytosines de l'ADN (Figure 1A). Elle concerne principalement les cytosines associées à une guanine dans un doublet CpG et joue un rôle central dans l'épigénétique. Généralement la méthylation de l'ADN et la condensation de la chromatine sont connectées et résultent en l'extinction de gènes (Figure 1B).

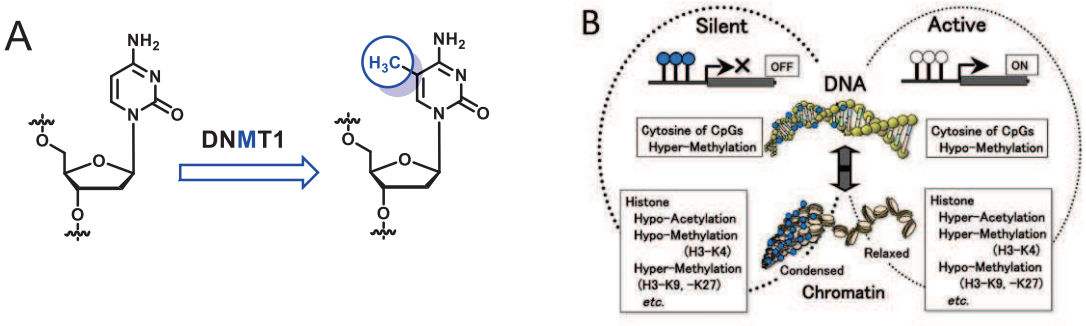

Figure 1. Méthylation de la cytosine par DNMT1 (A) et mécanismes de régulation épigénétique de l'ADN et de la structure de la chromatine (B) (Ohgane et al. 2008).

La méthylation de l'ADN est assurée par le couple de protéines formé par UHRF1 et la méthyl transférase DNMT1, qui jouent un rôle clé dans la réplication de l'ADN en transférant le patron de méthylation du brin d'ADN parent au brin d'ADN néo-synthétisé. La protéine UHRF1 possède un domaine SRA (Set and Ring Associated) capable de reconnaître l'ADN hémi-méthylé (Arita et al. 2008; Avvakumov et al. 2008). Par son domaine SRA, la protéine UHRF1 participerait au maintien des profils de méthylation de l'ADN en recrutant la DNMT1 au niveau des sites CpG hémi-méthylés générés après réplication. La liaison de la DNMT1 au domaine SRA déstabiliserait le complexe SRA/ADN, permettant le transfert du site CpG hémi-méthylé vers la DNMT1 qui induirait le basculement de la cytosine non-méthylée du brin nouvellement synthétisé dans le site actif de l'enzyme, permettant ainsi sa méthylation (Figure 2). Le domaine SRA de UHRF1 et l'enzyme DNMT1 travailleraient donc de concert afin de transmettre les profils de méthylation lors de la réplication de l'ADN.

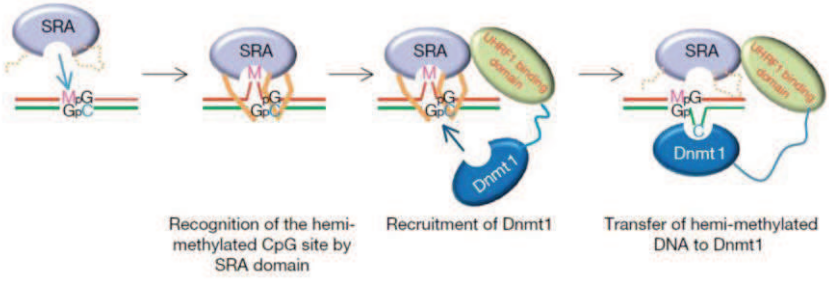

Figure 2: Mécanisme de maintenance des profils de méthylation de l'ADN après réplication (Arita et al. 2008). Le domaine SRA de UHRF1 et son partenaire DNMT1 coopèrent pour maintenir la méthylation des dinucléotides CpG. M représente la cytosine méthylée. Le brin d'ADN nouvellement synthétisé après réplication de l'ADN est représenté en vert et le brin rouge représente le brin parental.

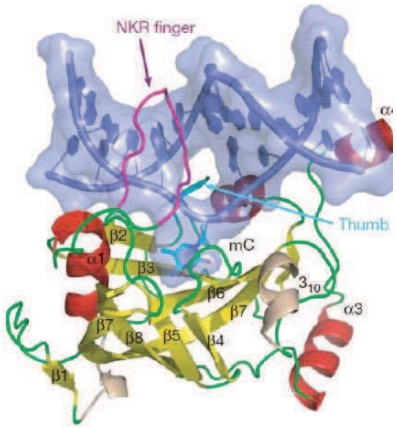

Figure 3 : Structure du domaine SRA de UHRF1 en complexe avec l'ADN hémi-méthylé (Avvakumov et al. 2008). Le domaine SRA est représenté avec ses boucles flexibles, ses feuillets β et ses hélices α en vert, jaune et rouge, respectivement. Le duplex d'ADN est montré dans une représentation de surface avec les atomes et les bases de l'hélice colorés en bleu. La cytosine méthylée basculée est annotée "mC". Le doigt NKR (violet) et le pouce (cyan) de la protéine prennent la place de la cytosine basculée dans l'espace libéré dans l'ADN.

La résolution de la structure tridimensionnelle du domaine SRA (Delagoutte et al. 2008; Qian et al. 2008) et du complexe SRA/ADN (Arita et al. 2008; Avvakumov et al. 2008; Hashimoto et al. 2008) a permis de proposer un modèle moléculaire de reconnaissance de l'ADN hémi-méthylé (Figure 3). Le domaine SRA de la protéine UHRF1 se comporte comme une main dont le doigt NKR (Asp 489, Lys 490, Arg 491) et le pouce permettent le basculement de la cytosine méthylée dans le grand sillon de l'ADN. Ce mécanisme de basculement de base est un processus largement utilisé par les enzymes de modification des nucléotides telles que les méthyltransférases de l'ADN, les enzymes de réparation de l'ADN et les enzymes de modification des ARNs. Cependant, le domaine SRA est le seul domaine connu capable de se lier spécifiquement à l'ADN et de basculer une base sans activité enzymatique. Dans ce contexte, notre projet vise à mieux comprendre la dynamique et les mécanismes intimes de l'interaction du domaine SRA de UHRF1 avec l'ADN hémi-méthylé et du basculement de la cytosine méthylée.

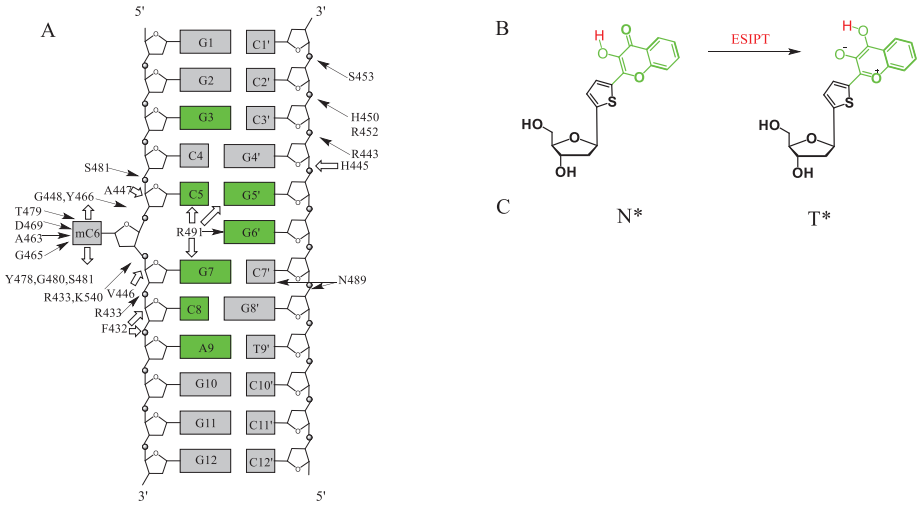

Figure 4. Structure du duplex et de la 3HCnt utilisés. (A) Structure du duplex. Les interactions du duplex avec SRA, tel que déterminées par cristallographie sont indiquées par des flèches. Les liaisons hydrogène et van der Waals sont indiquées par des flèches en noir et en blanc, respectivement. Les positions substituées par 3HCnt sont surlignées en vert. (B) Structure de 3HCnt et réaction ESIPT. (C) Spectres de fluorescence de la 3HCnt libre (courbe bleue) ou incorporée à la position G5' dans le duplex (courbe noire). Les expériences ont été effectuées en tampon phosphate 20 mM, NaCl 50 mM, TCEP 2,5 mM, 0,05% de PEG, à pH 7,5, à T = 20°C. Les spectres ont été normalisés au maximum de la bande T*.

Afin de suivre le basculement de la cytosine méthylée par le domaine SRA, nous avons utilisé un analogue de nucléoside fluorescent, la 2-thiényl-3-hydroxychromone (3HCnt). En raison d'un transfert intramoléculaire de proton à l'état excité (ESIPT) (Figure 4 B), cette base fluorescente présente deux formes à l'état excité, à savoir la forme normale (N*) et la forme tautomère (T*), toutes deux sensibles aux changements de leur environnement (Figure 4C). Ces deux formes répondent cependant différemment à certains paramètres physico-chimiques tels la polarité et l'hydratation. En outre, 3HCnt se comporte comme une base universelle capable de remplacer toute base avec un effet minimal sur la stabilité des duplex.

Nous avons marqué le duplex de 12 paires de bases utilisé pour résoudre la structure 3D du complexe SRA/ADN, avec la base fluorescente 3HCnt à plusieurs positions, à proximité du site central de reconnaissance CpG (Figure 4A). Ce site de reconnaissance contient soit une cytosine non-modifiée (NM duplex), soit une cytosine méthylée (HM duplex).

Figure 5. Spectres de fluorescence de l'ADN marqué avec 3HCnt aux positions 8 (A) et 5' (B). Spectres de l'ADN libre (courbes noires, les spectres de HM et NM sont superposables), de NM lié avec SRA (courbes bleues) et de HM lié avec SRA (courbes rouges). Les expériences ont été réalisées comme décrit dans la Figure 4C. Concentration de duplex : 1 µM. La concentration de SRA a été ajustée pour obtenir au moins 80% de complexes.

En utilisant la spectroscopie de fluorescence à l'état stationnaire, la spectroscopie de fluorescence résolue en temps et la spectroscopie *"stopped flow"*, nous avons pu approfondir notre compréhension au niveau moléculaire des mécanismes d'interaction du domaine SRA de UHRF1 avec l'ADN. Après une étude détaillée des propriétés photophysiques de 3HCnt dans l'ADN, nous avons caractérisé la réponse de 3HCnt à la liaison de SRA à toutes les positions de marquage. Bien que la liaison de SRA puisse être détectée pour chacune d'elles, seules certaines positions peuvent signaler le basculement de la base (Figure 6 A et B). En effet, la comparaison des réponses obtenues pour les séquences HM et NM a révélé que la sonde est particulièrement sensible au basculement de la cytosine méthylée par SRA sur les positions 8 et 5' (Figure 5 et Figure 6). Cette conclusion a été renforcée par l'utilisation de mutants SRA incapables de faire basculer les cytosines méthylées. La corrélation de ces données avec la structure cristallographique du complexe SRA-ADN suggère que la réponse observée à ces positions résulte de la sensibilité de 3HCnt aux modifications de son microenvironnement induit par le basculement de la méthylcytosine (Figure 6 A et B). Ainsi, à notre connaissance, nous avons obtenu pour la première fois un test capable de suivre le basculement de la base induit par UHRF1.

Figure 6. Modification induite par le domaine SRA du rendement quantique (A) et du rapport N*/T* (B) des duplexes NM (barres bleues) et HM (barres jaunes) marqués par le 3HCnt. Les expériences ont été réalisées comme décrit dans la Figure 4C. L'augmentation de rendement quantique (QY) dans (A) correspond au rapport du rendement de 3HCnt dans le complexe SRA/ADN à celui dans l'ADN libre. La diminution du rapport N*/T* (B) correspond aux variations du rapport N*/T* de 3HCnt dans le complexe ADN / SRA par rapport à l'ADN libre. Les données correspondent à des moyennes sur 5 expériences indépendantes.

Nous avons également suivi par « stopped-flow » la cinétique d'interaction de l'ADN marqué par 3HCnt avec SRA. Nous avons ainsi pu pour la première fois caractériser la cinétique de l'interaction de SRA avec sa cible ainsi que la cinétique de basculement de la base (Figure 7). Notre étude a montré que l'interaction de SRA avec l'ADN est initiée par une liaison non spécifique du domaine SRA au duplex, puis par son glissement vers le site de reconnaissance CpG. De manière remarquable, les sites de reconnaissance avec des cytosines méthylées présentent une cinétique lente additionnelle, qui a pu être associée au basculement de base. En conséquence, la durée de vie du complexe formé par UHRF1 lié à un site CpG dans les duplex HM est beaucoup plus longue que dans les duplex NM, ce qui augmente évidemment le temps et la probabilité de recruter DNMT1, afin de dupliquer le profil de méthylation de l'ADN. Un article portant sur ces résultats est en cours de soumission.

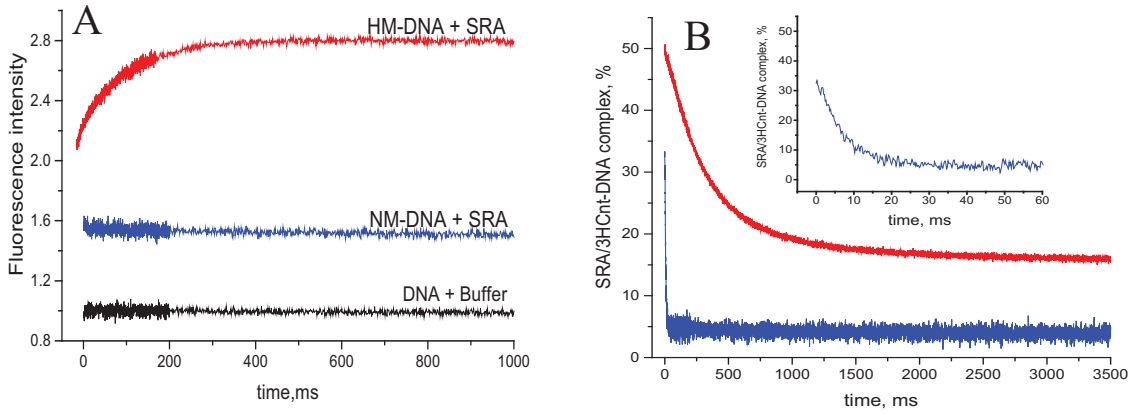

Figure 7. Cinétiques d'interaction de SRA avec des duplex HM et NM marqués par 3HCnt en position 5 ', suivies par stopped-flow. (A) Cinétique d'association. La courbe noire correspond aux duplex HM ou NM mélangés avec le tampon. Les courbes bleues et rouges correspondent aux cinétiques obtenues pour l'interaction de SRA avec les duplex NM et HM, respectivement. (B) Cinétique de dissociation des complexes de SRA avec les duplex HM (rouge) et NM (bleu). Ces cinétiques ont été enregistrées après addition d'un excès d'ADN de thymus de veau aux complexes. La concentration de SRA a été ajustée pour obtenir au moins 50% de complexes. L'intensité de fluorescence a été convertie en pourcentage de duplex lié à SRA. En insert: cinétique enregistrée pendant les 60 premières ms avec le duplex de NM marqué par 3HCnt.

En conclusion, le 3HCnt est un analogue nucléosidique fluorescent sensible à l'environnement, qui apparaît comme un outil unique pour suivre avec une grande sensibilité le basculement de la méthylcytosine par SRA et caractériser sa dynamique. Cet outil devrait permettre d'étudier le rôle des autres domaines de UHRF1 dans le basculement de la cytosine méthylée ainsi que la coopération de UHRF1 avec d'autres protéines impliquées dans la maintenance du profil de méthylation de l'ADN. En outre, nos études cinétiques ont apporté de nouveaux éclairages sur le mécanisme par lequel UHRF1 peut recruter l'enzyme DNMT1. D'autres expériences utilisant des techniques de molécule unique devraient nous permettre d'en apprendre davantage sur ces mécanismes.

I Introduction

1.1 Epigenetics

The term epigenetics refers to heritable changes in gene expression that do not involve changes in the underlying DNA sequence; a change in phenotype without a change in genotype. Epigenetic modifications act as a genomic response to the environment and serve as genomic memory of these exposures at different time scales. They stably alter gene expression and thus modulate the physical and behavioral phenotypes in response to these environment changes. One of the most striking examples of environmentally controlled phenotypic polymorphism is illustrated with the metamorphosis of a caterpillar into a butterfly. The caterpillar closes itself in a cocoon, before forming a butterfly (**Figure** 1.1). The caterpillar has the same genes as the butterfly but the genes are expressed differently depending on its life stage.

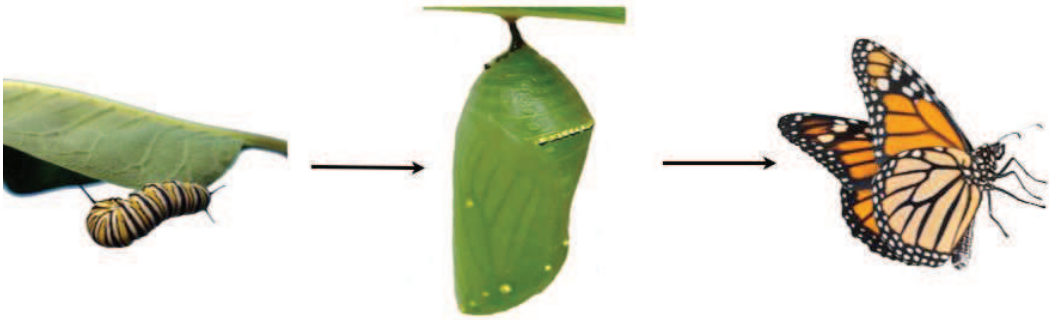

Figure 1.1 Butterfly life cycle

Another example of epigenetic controlled phenotypic polymorphism is the development of honey bee queens and workers. The only difference between the queen bee and the worker bee is their food source. Although the queen bee is genetically identical to all of the other bees, it lives up to 28 times longer and grows 3 times larger. The queen bee is the only bee that is allowed to consume the protein-rich royal jelly, which triggers a cascade of molecular events resulting in the development of a queen (Maleszka 2008). It has been shown that this phenomenon is mediated by DNA methylation (Kucharski et al. 2008). Silencing the expression of an enzyme that methylate DNA in newly hatched larvae led to a royal jelly-like effect on the larval developmental trajectory; the majority of individuals with reduced DNA methylation levels emerged as queens with fully developed ovaries (Kamakura 2012). Another example of differentially altered expression of epigenetic information by nutritional input was demonstrated on twin mice. One of the two mice was deprived of important nutrients called methylators (vitamin B12 and folic acid) and became obese. The other mouse was given all of

the essential nutrients and remained lean and healthy (Waterland & Jirtle 2003). Direct comparisons of identical twins constitute an optimal model for interrogating environmental epigenetics. In the case of humans with different environmental exposures, monozygotic (identical) twins are epigenetically indistinguishable during their early years, while older twins had remarkable differences in the overall content and genomic distribution of 5-methylcytosine DNA and histone acetylation (Moore 2015).

1.2 Genome and Epigenome

DNA carries most of the genetic information used in the development, functioning and reproduction of living organisms.

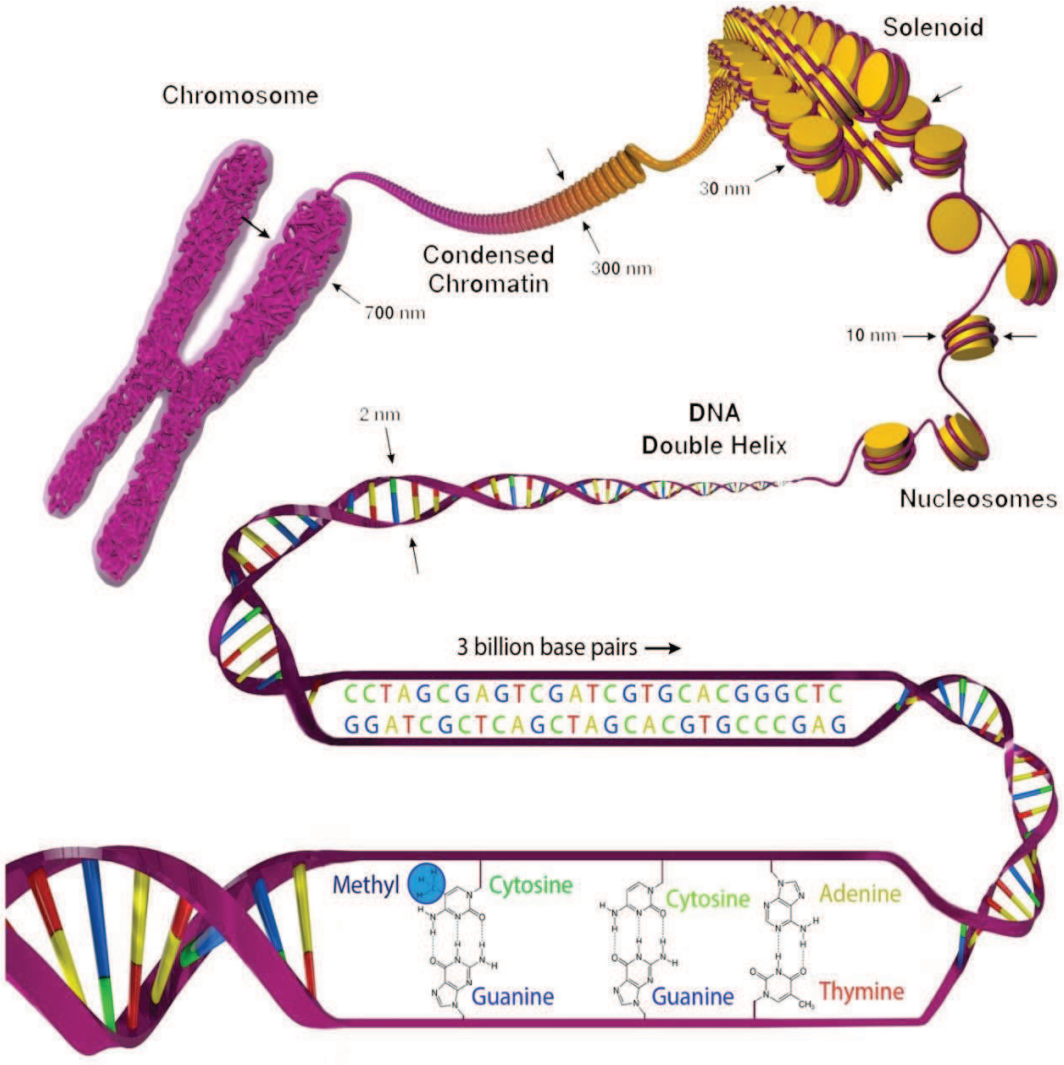

Figure 1.2 Genome and Epigenome structure.

DNA is a long double-stranded biopolymer with strands coiled around each other and made from repeating organic molecules that serve as units of nucleic acids (nucleotides). Each

nucleotide contains a nucleoside composed of a nitrogen-containing base, either purine - adenine (A) or guanine (G) or pyrimidine - cytosine (C) or thymine (T), attached to a sugar (deoxyribose). Nucleotides result from the addition of a phosphate group to nucleosides. Through covalent bonding between the sugar of one nucleotide and the phosphate of the next, nucleotides are joined together to form one DNA strand.

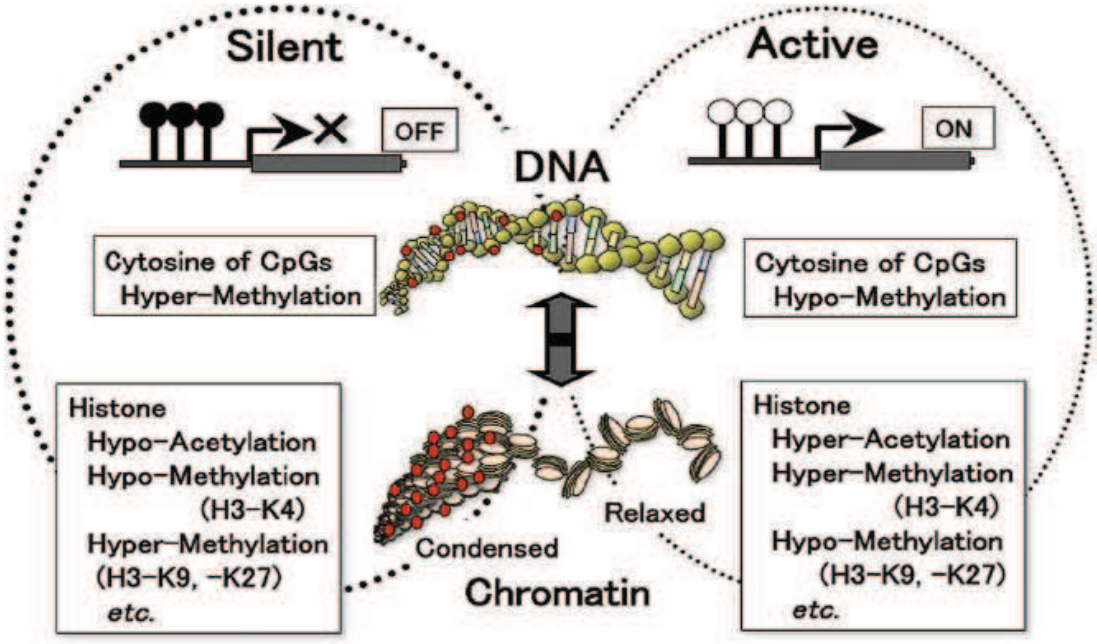

Figure 1.3. Epigenetic regulatory mechanisms: DNA methylation and chromatin structure. Methylation of DNA and chromatin structure are coordinated through modification of histones, including by acetylation and methylation. In general, DNA methylation and chromatin condensation are associated with gene silencing. The epigenetic state consisting of DNA methylation and chromatin configuration plays an important role in the differentiation of cells. Once established, the epigenetic state is maintained during the proliferation of cells (**Figure** taken from (Ohgane et al. 2008)).

The double-stranded DNA helix is formed through hydrogen bonding between the bases of two complementary polynucleotide strands. Stable base pairing are possible for G-C and A-T base pairs due to the appropriate structural fit between their hydrogen bond donor and acceptor groups. DNA molecules are segmented into regions – genes - encoding for a functional RNA or a protein. All genes together form the genome which contains all the information needed to build and maintain a given organism. In humans, the entire genome is composed of more than

3 billion of DNA base pairs. A single DNA molecule is about 2 m long (Bloomfield 2001) and is tightly packed inside the nucleus of cells. In eukaryotic cells, the DNA molecule is wrapped around histone proteins, forming the nucleosome core (**Figure** 1.2). These nucleosomes are further coiled around each other to form the chromatin fiber. Histones wrap into fibers constructed from compactly packed nucleosome arrays.

The organization of chromatin has several functions: to pack DNA into small compartments which fit to the cell nucleus, condense the DNA during mitosis, to prevent DNA damage, and most importantly to control gene expression and DNA replication. The loosely packed regions of chromatin (euchromatin) are associated with genes that actively transcribe ("active" state of the gene), while more tightly packed chromatin regions (heterochromatin) correspond to inactive genes ("silent" state) (Corces 1995). The local structure of chromatin is determined by chemical modifications of histone proteins and DNAs. These modifications are generally resulting from a covalent binding to histone aminoacids or DNA nucleotides that does not change their structure. Such modifications, called epigenetic modifications, correspond either to histone methylation/acetylation or DNA methylation/hydroxymethylation. Gene specific epigenetic marks patterns on histones and on DNA form the epigenome. In contrast to the static genome, the epigenome can be dynamically altered by environmental conditions, which is essential for the regulation of gene expression, development, tissue specific differentiation and silencing of transposable elements. The link between epigenetic modifications of histones and DNA as well the processes which determine the biological role of epigenetic marks are an active area of research (Suzuki & Bird 2008). DNA methylation is generally associated with chromatin condensation (Ikegami et al. 2009) and plays an important role in gene activity regulation (Bird & Wolffe 1999; Shiota 2004) (**Figure** 1.3). Low DNA methylation and high accessibility in promoter regions correlate with relaxed states of chromatin, and high DNA methylation correlates with promoter regions of repressed genes and with condensed states of chromatin (Lister et al. 2009; Bernstein et al. 2012; Kundaje et al. 2015).

1.3 Naturally occurring modified bases and DNA methylation

Modified bases occur in many nucleic acids, but the largest amount of modified bases is observed in transfer RNAs (tRNA). Some of them correspond only to slight modifications of normal bases; others are hypermodified. All modifications are resulting from the action of specific enzymes after tRNA synthesis. The different derivatives found in tRNA include:

1. Adenine derivatives: 1-methyladenosine, N^6-methyladenosine, inosine (deaminated adenosine), q-methylinoine.
2. Cytosine derivatives: 3-methylcytidine, 5-methylcytidine, 2-thiocytidine, N^4-acetylcytidine.
3. Guanine derivatives: 1-methylguanosine, N^2-methylguanosine, N^2, N^2-dimethylguanosine, 7-methylguanosine.
4. Uracil derivatives: ribosylthymine (5-methyluridine), 5-methoxyuridine, 5,6-dihydrouridine, 4-thiouridine, 5-methyl-2thiouridine, pseudo-uridine (uracil is attached to ribose at the C5).

The role of modified bases in tRNA functions is currently started to be studied and few of them were associated with particular functions (Agris 1996; Ashraf et al. 2000).

1.4 DNA methylation

Natural DNAs contain 5-methylcytosine, N^6-methyladenine, N^4-methylcytosine and 5-hydroxymethyluracil. The determination of their exact roles in DNA functions is an extremely hot research area because of growing evidence that these modified bases are directly involved in the regulation of numerous essential biological process. 5-methylcytosine is largely present in DNA and is the most studied modified base. This modification generally referred as DNA methylation is maintained by the DNA methyltransferase enzymes (DNMT). DNA methylation is a stable epigenetic modification realized by covalent addition of a methyl group to the 5' carbon atom of the cytosine base (C) (**Figure** 1.4).

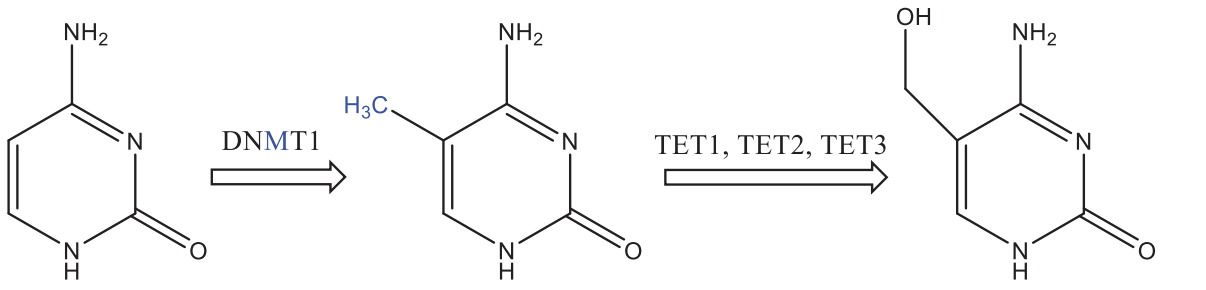

cytosine 5-methylcytosine 5-hydroxymethylcytosine

Figure 1.4. Chemical structure of cytosine and its epigenetic modifications.

The addition of a methyl group does not modify the structure of the cytosine nucleotide and does not have any effect on hybridization with guanine (G) (**Figure** 1.4). Recently, it was found that the TET enzyme family converts 5-methylcytosine to 5-hydroxymethylcytosine (Tahiliani et al. 2009). Currently, the occurrence and role of hydroxymethylation are not well understood. In contrast, methylation of DNA is the most studied epigenetic modification and is found in most eukaryotic organisms, with a few exceptions (Yeast and C.elegans) (Colot & Rossignol 1999). In mammals, methylation is mainly observed in CpG dinucleotides. DNA regions with high content of CpG dinucleotides are called CpG islands (CGIs). These DNA regions are about 500bp length, with a GC content around 55%. Asymmetrically methylated CpGs are generally located within repetitive elements and coding regions of genes. About half of the genes contain CGIs in promoter regions and their methylation is associated with silencing of gene. DNA methylation was reported to be essential in embryonic development (Okano et al. 1999), genomic imprinting (Li et al. 1993) and X-inactivation in mammals (Goto & Monk 1998). Also, alteration of DNA methylation was associated with abnormal developmental processes and cancer (Plass & Soloway 2002). Patterns of DNA methylation is a major mechanism of heritable cell memory (Holliday & Pugh 1975; Riggs 1975; Riggs 1989) which allows mammalian cells to keep with high fidelity their proper state of differentiation during the organism life cycle. DNA methylation has a strong influence in different biological process through transcriptional repression. Silencing of genes could be achieved by direct blockage of binding of transcriptional factors when present at their target sites (Rottach et al. 2009; Bird 2002). Alternatively, specific recognition of methylated CpG dinucleotides by methylcytosine binding proteins can recruit repressive chromatin modifiers and remodeling complexes (Rottach et al. 2009). The fundamental role of the DNA methylation in mammals was demonstrated by the early lethality observed when enzymes maintaining DNA methylation and DNA methyltransferases (DNMTs) are altered (Li et al. 1992; Okano et al. 1999).

1.5 DNA methylation patterns

The differentially methylated regions in the mammalian genome are important for tissue differentiation, development and cancer mechanisms. DNA methylation patterns in mammals are tissue-specific (Maunakea et al. 2010).

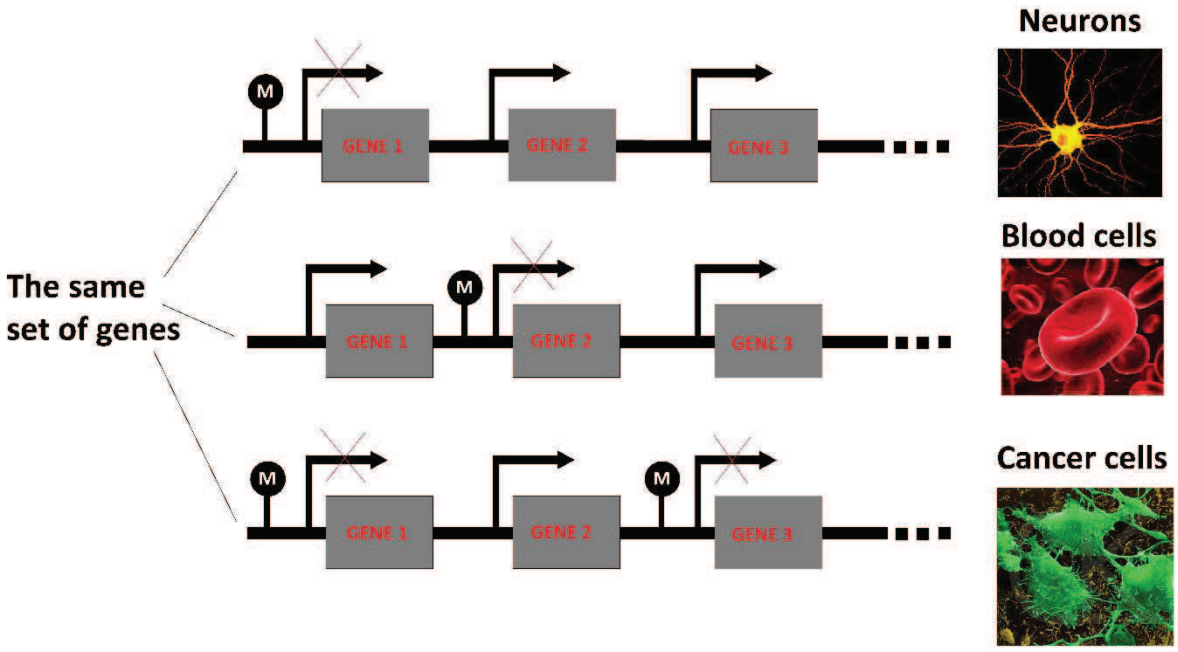

Figure 1.5 Schematic representation of tissue specific DNA methylation patterns.

These DNA methylation patterns are largely formed during early development (Monk et al. 1987) through the activity of the DNMT3a and DNMT3b DNA methyltransferases. The patterns could be dynamically changed by age-related factors (Madrigano et al. 2012), environmental factors (Bind et al. 2013), nutritional factors, and pathogenic factors, such as viruses (Liu et al. 2003; Leonard et al. 2012). The dynamic nature of epigenetic marks was demonstrated on monozygotic (identical) twins. They share a very similar epigenetic profile at birth, but variations in their epigenome accumulate over their lifetime.

They are also specific for individual genes present in small proportions in CGIs promoters and across gene bodies. Up to now, only methylation of promoters was related to regulation of gene expression, the role of methylation of gene bodies being still a matter of debate (Ball et al. 2009). Methylation in promoter regions of genes is thought to silence this particular gene. Thus, tissue specific expression from the same genome is achieved through differences in methylation patterns (**Figure** 1.5). Such a tissue specific regulation in human body is sufficient to build up about 200 types of cells with various functions from the same DNA molecule. At the same time, any cell hypothetically can become cancerous due to abnormal methylation.

1.6 DNA methylation pattern replication

During DNA replication, two identical replicas are produced from one original DNA molecule. This process is mediated by several proteins and notably by the DNA polymerase which synthesizes a new DNA by adding complementary nucleotides to the template strand. DNA polymerase has no specific properties that allow recognizing CpG sites or distinguishing methylcytosine from cytosine in the original DNA. Thus, a newly synthetized DNA strand is not methylated. The result of genome replication is a DNA duplex which contains methyl groups only on the parental strand (hemimethylated DNA).

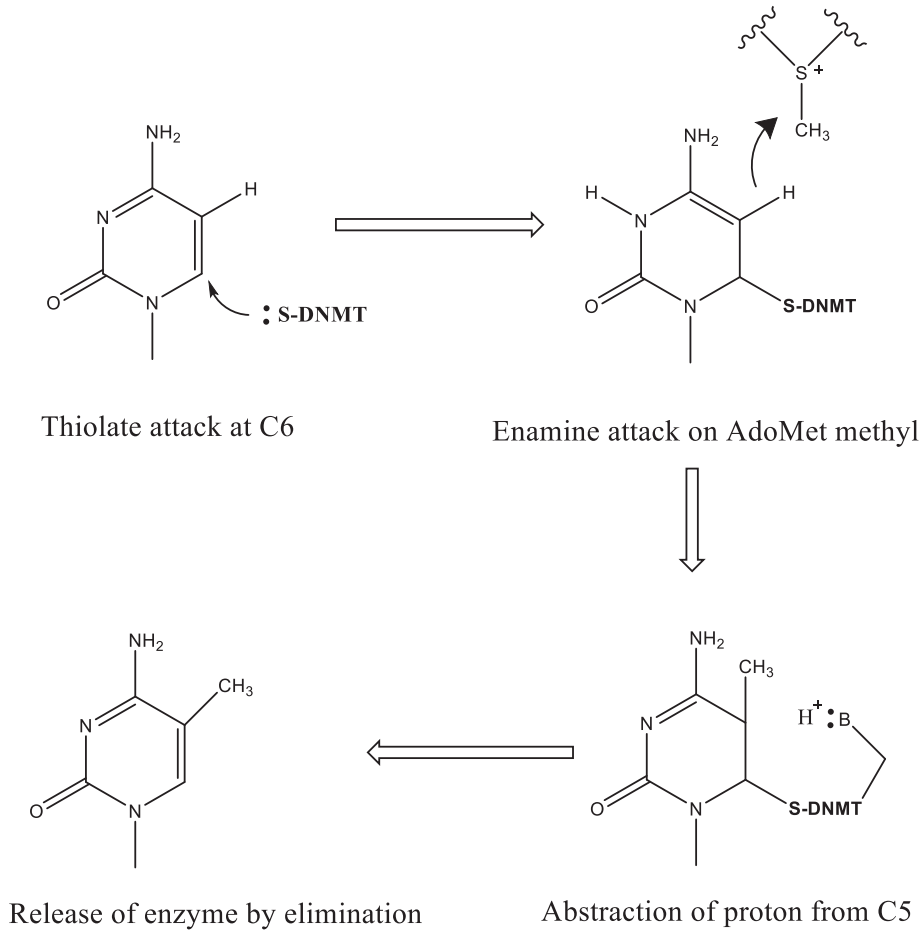

Figure 1.6. **Catalytic mechanism of cytosine methylation by DNMT1**. Enzyme mechanism originally proposed by (Santi et al. 1983) and modified by (Chen et al. 1991) and (Erlanson et al. 1993). Protonation of the N3 position is mediated by the highly conserved ENV tripeptide in motif VI.

Replication and establishment of methylation patterns and therefore of the epigenome is

mediated by a family of enzymes called DNA methyltransferases (DNMTs). In eukaryotes, there are three different families of DNMTs: DNMT1, DNMT3a and DNMT3b (Bestor 2000; Colot & Rossignol 1999). DNMT1 is a maintenance methyltransferase, while DNMT3a and 3b are de novo DNMTs**.**

Although the biological roles are different, the mechanism of transfer is similar between the different family members. It was proposed that DNA methyltransferases could act in the same way as other enzymes catalyzing electrophilic substitutions at carbon-5 of pyrimidines (Santi et al. 1983). The contact between DNA and the enzyme is established through a distortion of the DNA helix. The reaction starts when a cytosine is flipped out of the DNA and inserted into the binding pocket of a methyltransferase enzyme. In the active site, the catalytic cysteine thiolate forms a transition state intermediate with the carbon-6 of the cysteine ring (**Figure** 1.6). This creates a reactive negatively charged 4-5 enamine which attacks the methyl group provided by the AdoMet cofactor (S-adenosyl methionine, SAM) acting as a methyl donor (Villar-Garea & Esteller 2003). After transfer of the methyl group to the C-5 position within the cytosine ring, the proton is removed from this position leading to the reconstitution of the 5,6 double bond and the release of the enzyme by ß-elimination (Erlanson et al. 1993). The tissue specific methylation reaction of particular CpG sites is essential for proper replication of epigenome. However, none of DNMTs enzymes has significant inherent sequence specificity beyond the CpG dinucleotide, suggesting that their targeting to DNA should be achieved by other mechanisms.

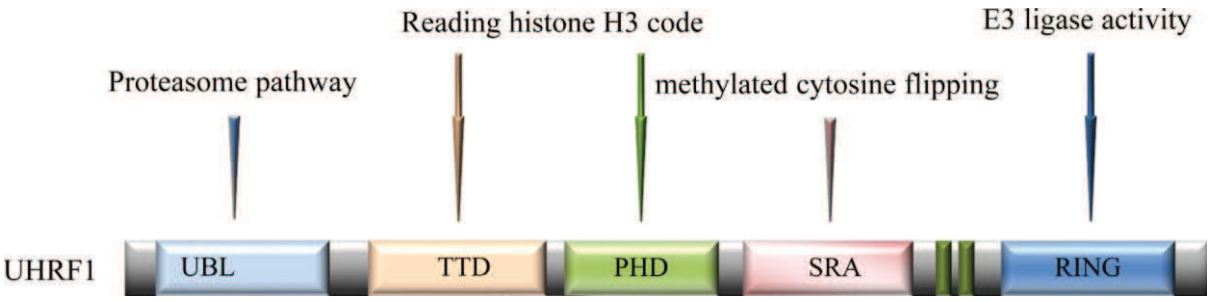

Figure 1.7. Functional role of UHRF1 domains. The role of ubiquitin-like domain (UBL) is still not elucidated but is likely involved in the proteasome degradation pathway. The PHD (Plant Homeo Domain) finger domain acts in concert with the TTD (Tandem Tudor Domain) to read the N-terminal H3 histone code. The SRA (Set and Ring associated) domain flips the methylated cytosine out of the DNA helix. The RING (Really Interesting New Gene) finger is characterized by an E3 ubiquitin ligase activity. **Figure** taken from (Bronner et al. 2013).

Major breakthroughs have been achieved by identifying the UHRF1 (Ubiquitin-like PHD RING) protein as a fidelity factor of DNMT1 (Kim et al. 2009). UHRF1 contains multiple domains (**Figure** 1.7) and exhibits preferential affinity for hemi-methylated DNA through its SRA domain (Bostick et al. 2007; Arita et al. 2008; Avvakumov et al. 2008; Hashimoto et al. 2008) which is required for proper localization of DNMT1 (Bostick et al. 2007). The suggested mechanism of the collective action of UHRF1/DNMT1 tandem is described in **Figure** 1.8 (Arita et al. 2008). First, UHRF1 binds selectively to hemimethylated CpG and such a complex will be recognized by DNMT1. Due to the preferential binding of UHRF1 to hemimethylated DNA over nonmethylated DNA, this protein directs DNMT1 to methylated cytosine in unsymmetrically methylated CpG. Interaction of UHRF1 with DNMT1 remains unclear, but likely involves several domains of both proteins (Achour et al. 2008; Bostick et al. 2007; Hashimoto et al. 2009). However, a simultaneous binding to the same CpG site by UHRF1/DNMT1 is unlikely from a structural point of view. Therefore, DNMT1 is thought to interact with UHRF1, which in turn results in the dissociation of the UHRF1/DNA complex.

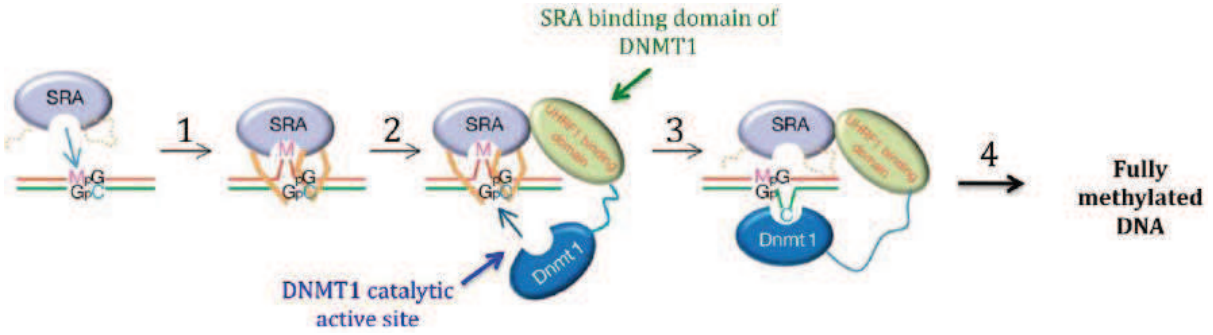

Figure 1.8. DNA transfer model for maintenance of DNA methylation by UHRF1 and DNMT1: schematic model showing cooperative action of UHRF1 and DNMT1 for maintenance of DNA methylation. Pre-existing and newly synthesized DNA strands are indicated by red and green lines, respectively (Arita et al. 2008). **Step 1**: The SRA domain of UHRF1 behaves as a "hand", which recognizes the methylated cytosine (M) of the hemimethylated CpG island and then flips this residue out from the DNA helix into the major DNA groove. **Step 2**: The SRA/DNA complex allows the recruitment of DNMT1 through a second motif of recognition leading to a ternary and transitory complex. **Step 3**: DNMT1 binding to SRA destabilizes the SRA/DNA complex permitting the transfer of the hemi-methylated CpG to DNMT1 resulting in the flip out of the daughter strand cytosine into the major DNA groove to bind to DNMT1 active site. **Step 4**: Cytosine methylation of the daughter strand. **Figure** taken from (Arita et al. 2008).

Moreover, UHRF1 was found to interact with a histone methyltransferase that catalyzes histone methylation (G9a) suggesting a possible link between histone and DNA methylation. The combined effect of DNA and histone epigenetic modifications was shown in gene silencing associated with H3 hypo-acetylation, H3K9 methylation and DNA methylation. In all these processes, UHRF1 was found to be involved (Bronner, Chataigneau, et al. 2007; Bronner, Achour, et al. 2007; Bostick et al. 2007; Arima et al. 2004; Unoki et al. 2004a; Hopfner et al. 2000; Jeanblanc et al. 2005).

The link induced by UHRF1 between histone H3 methylation and cytosine methylation is considered to be a possible fundamental basis in epigenome replication processes. It remains to be determined by which mechanism UHRF1 maintains a relationship between histone methylation and DNA methylation. The central role of UHRF1 in this process becomes the dominant hypothesis (Bronner et al. 2009; Arita et al. 2008). Another mechanism was proposed to explain how UHRF1/DNMT1 maintains the epigenetic modifications of DNA and histones (Bronner et al. 2009) . UHRF1, localized at the interface between DNA and histones, determines the presence of hemimethylated DNA and H3K9 methylation via its SRA and TTD domains, respectively, and signals its enzymatic partners such as DNMT1, HDAC1, and G9a to exert their catalytic activities on the newly synthesized DNA strand and on newly assembled histones (Bronner et al. 2009). In this model, the ability of UHRF1 to recognize specifically hemimethylated DNA is critical. It was shown that this unique feature of UHRF1 is a consequence of the ability of SRA to recognize specifically methylcytosine over cytosine and other nucleobases in CpG dinucleotides (Avvakumov et al. 2008; Arita et al. 2008; Hashimoto et al. 2008). The specificity of the SRA domain could serve as a messenger through a not yet determined interaction of UHRF1 with enzymatic partners. Thus, the reading role of the SRA domain is a key mechanism in the epigenome replication machinery. This domain has several features which distinguish this protein from other methyl binding proteins.

II Methyl CpG binding proteins

2.1 MBD proteins

Currently, three family of proteins were identified to bind preferentially to methylated CpG named by their binding domains: the MBD family, the zinc finger family and the SRA family. The methyl binding domain (MBD) family contains proteins which are believed to convert the information represented by methylation patterns into the appropriate functional state (Jaenisch & Bird 2003; Wade 2001). The MBD is a common motif of about 75 amino-acids for currently identified MBD proteins (Nan et al. 1993). The first initially identified MBD domain was in MeCP2 (methyl CpG binding protein 2 (Rett syndrome)). This domain, necessary and sufficient to bind mCpG DNA, was found in six other proteins named MBD1-6. Three of these proteins (MBD1, MBD2 and MeCP2) are involved in methylation-dependent repression of transcription (Bird & Wolffe 1999). Each of the four MBD1-4 proteins was shown to be associated with a different repressor complex (Jones et al. 1998; Nan et al. 1998; Sarraf & Stancheva 2004). The MBD5 and MBD6 currently are poorly studied, however it was shown that their binding to methylated DNA is very weak (Laget et al. 2010). MBD2 is the DNA binding component of the MeCP1 complex, which was observed to be specific for methylated DNA in a variety of mammalian cell types (Meehan et al. 1992). The structure studies of the MBD1, MBD2 and MeCP2 proteins bound to the methylated DNA showed that the methyl groups of methylcytosines are deeply immersed in the DNA-MBD interface (Ohki et al. 2001; Scarsdale et al. 2011; Ho et al. 2008). The three proteins adopt a similar overall fold comprised of an α/β sandwich and a comparable mode of binding. The core of the β-sheet interacts with the major groove of the DNA making base specific contacts at the methyl-CpG site through conserved arginine and tyrosine residues. The binding interaction is further stabilized through extensive sugar and phosphate backbone interactions mediated by residues in the α-helix as well as a conserved loop within the β-sheet that forms a stabilized hairpin structure upon DNA recognition **Figure** 2.1A. Despite similarities in interaction of MBD proteins with methylated DNA, they exhibit varying sequence preferences outside the core methylated CpG site (Scarsdale et al. 2011; Klose et al. 2005; Clouaire et al. 2010).

2.2 Zinc finger proteins

Another family of methyl binding proteins (MBP) is the recently identified zinc finger family. This family contains the Kaiso protein and its two close paralogs Zbtb4 and Zbtb38, as well as the ZFP57 protein. ZFP57 was shown to be involved in DNA methylation-dependent maintenance of imprinted genes (Quenneville et al. 2011). As a protein from the MBD family, the Kaiso protein is also able to discriminate between symmetrically methylated and unmethylated DNA (Prokhortchouk et al. 2001).

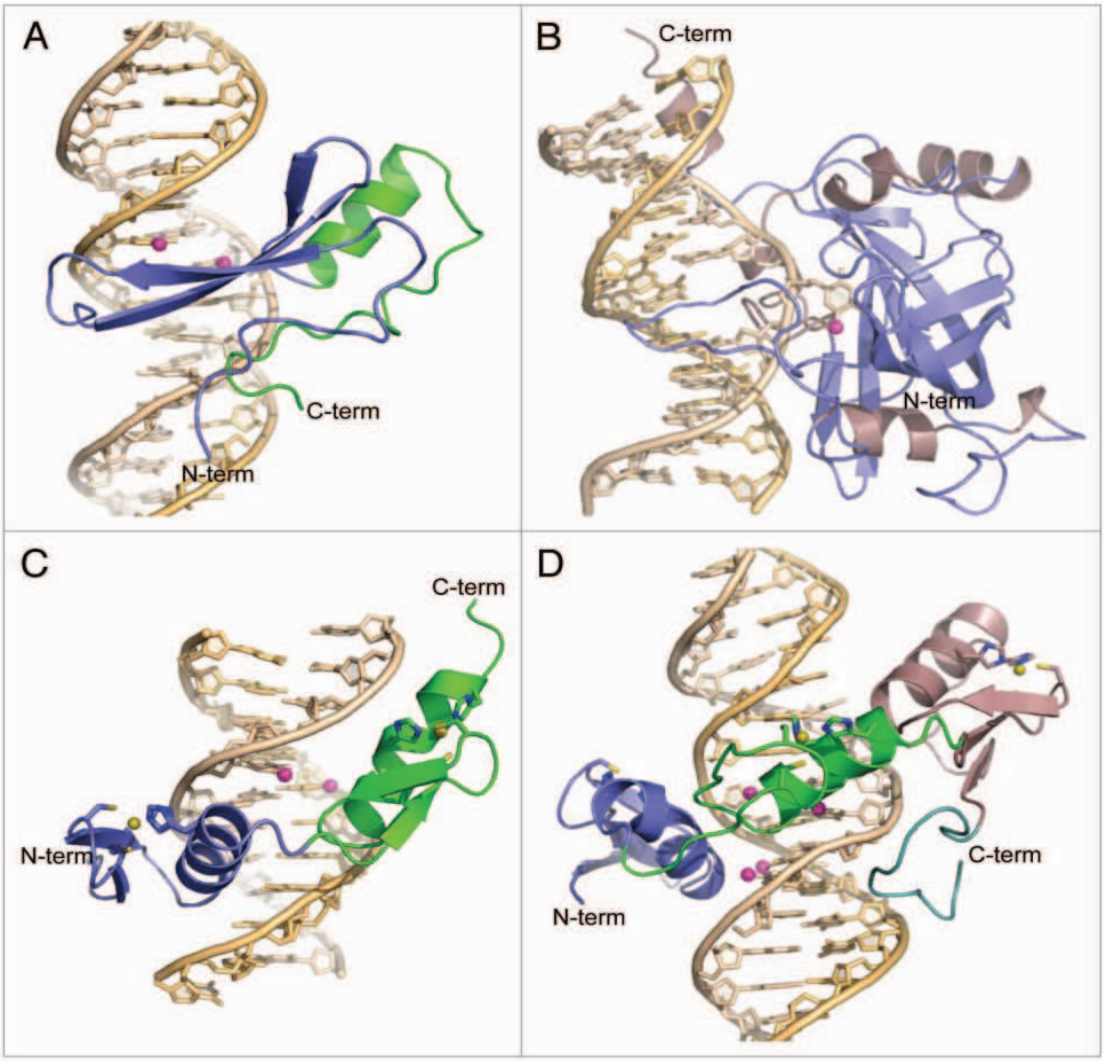

Figure 2.1. Representative structures for each MBP family. (A) Crystal structure of the MBD of human MeCP2 in complex with a methylated DNA consensus site derived from the brain-derived neurotrophic factor (BDNF) promoter (PDB 3C2I) (Ho et al. 2008). (B) Crystal structure of the SRA domain of human UHRF1 in complex with hemimethylated DNA (PDB 3CLZ) (Avvakumov et al. 2008). (C) Crystal structure of the mouse Cys2 His2 zinc finger

protein ZFP57 in complex with a methylated DNA target known to be localized in imprinting control regions (PDB 4GZN) (Liu et al. 2012). (D) Crystal structure of the human Cys2 His2 zinc finger protein Kaiso in complex with a methylated DNA. **Figure** taken from (Buck-Koehntop & Defossez 2013).

The structure of Kaiso and ZFP57 showed that these two proteins interact with methylated DNAs in different manner (**Figure** 2.1 C and D). In case of ZFP57, the two Cys_2His_2 zinc fingers, responsible for methylated DNA recognition adopt a ββα- folding, positioning the α-helices for making canonical major groove interactions with three base pairs per zinc finger. The methylated cytosines in the core mCpG site are recognized by hydrogen bonding and van der Waals interactions between protein residues, methylated cytosine and neighboring nucleotides. In contrast, Kaiso utilizes three Cys_2His_2 zinc fingers (ZF) and additional N- and C-terminal extensions to provide structural stability and enhance the overall binding affinity. ZF2 adopts the standard ββα fold, while ZF1 and ZF3 each contain three-stranded β-sheets with ββββα and ββαβ motifs, respectively. Kaiso is the only MBP that was identified to have preference for recognizing two consecutive methylated CpG sites (Prokhortchouk et al. 2001).

2.3 SRA containing MBPs

One more methylcytosine specific family of proteins currently contains two members, UHRF1 and UHRF2 proteins, which could bind methylated DNA via their SRA domains (Unoki et al. 2004). The crystal structure of the SRA domain of UHRF1 complexed with hemi-methylated DNA indicates that the protein–DNA interaction involves the flipping of the recognized methyl-cytosine out of the DNA helix (Avvakumov et al. 2008; Arita et al. 2008; Hashimoto et al. 2008). In addition to DNA methylation, the base flipping is used by many different enzymes in varying biological processes such as multiple DNA repair mechanisms, RNA transcription and DNA replication (Roberts & Cheng 1998). The specificity of the SRA domain for methylcytosine is unique and critical for DNA methylation replication. Moreover, base specific interactions for UHRF1 are limited to the unsymmetrically methylated CpG, in contrast to the MBD and Zinc finger families. Thus, the sequence context of the mCpG site is not critical for recognition. The SRA domain is a 210 residues protein (**Figure** 2.1 B and 2.2). The sides of its β- barrel are covered with α-helical elements: α2 at one side connects strands β5 and β6, and a helix–loop pair at the other side connects strands β6 and β7. The extensive twist of the barrel partially separates strands β2 and β4 and forms the center of the interaction surface with the hemi-methylated DNA, which runs parallel to the β-barrel along the β2 strand. The SRA

binding domain induces base flipping and replaces lost Watson–Crick hydrogen bonds between the methylcytosine and its paired guanine by hydrogen bonds and π-stacking interactions between the methyl-cytosine and the protein.

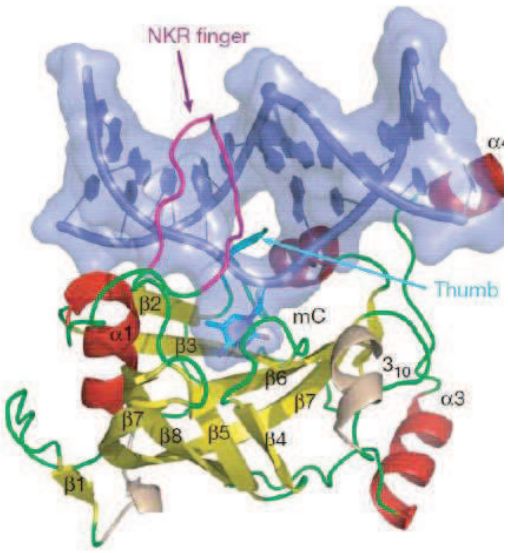

Figure 2.2. Structure of the SRA domain of UHRF1 in complex with DNA**.** The SRA domain is shown with flexible loops, β-strands and α-helices colored in green, yellow and red, respectively. The DNA duplex is shown with backbone atoms and bases colored in blue. The flipped, methylated deoxycytidine (C6) is labelled as 'mC'; the resulting hole in the DNA is partially filled by the NKR finger (magenta) and the thumb (α1–β2 loop, cyan) (Avvakumov et al. 2008).

Structural studies also show how the NKR finger is sensitive to the presence of a methyl group on the cytosine residue of the complementary CpG. Indeed, this methyl group is thought to perturb the network of interactions at the NKR finger-DNA interface and destabilize the conformational state of Arg 491. Noticeably, Arg 491 in the finger substitutes for the methylcytosine nucleotide, and forms hydrogen bonds to the orphaned guanosine (Avvakumov et al. 2008). The specificity for methylcytosine over cytosine is explained by a hemisphere of approximately 2Å radius, which exactly fits the methyl group at position 5 of methyl-cytosine (Avvakumov et al. 2008). This methyl-group-binding site is deep within the methylcytosine pocket and would be occupied by solvent and therefore unfavorably hydrated if non-methylated cytosine were the ligand. This methyl specificity role of the hemisphere is debated because about half of the atoms surrounding this cavity are hydrophilic with the potential of forming

hydrogen bonds with a water molecule (**Figure** 2.3). In addition, the stability of this sphere is doubtful because adjustments on the order of 1Å in the positions of few residues of the protein could modify this sphere significantly (Bianchi & Zangi 2012). In another study, van der Waals interactions and weak CH···O hydrogen bonds of the methyl group with surrounding atoms were proposed to explain the selectivity for hemimethylated over nonmethylated strands (Arita et al. 2008). However, similar interactions also exist in the unbound state of the DNA. In this case, water molecules are in contact with the methyl group at position 5 (in both, the flipped-in and flipped-out conformations) and can form the same type of interactions as do the surrounding residues of the protein.

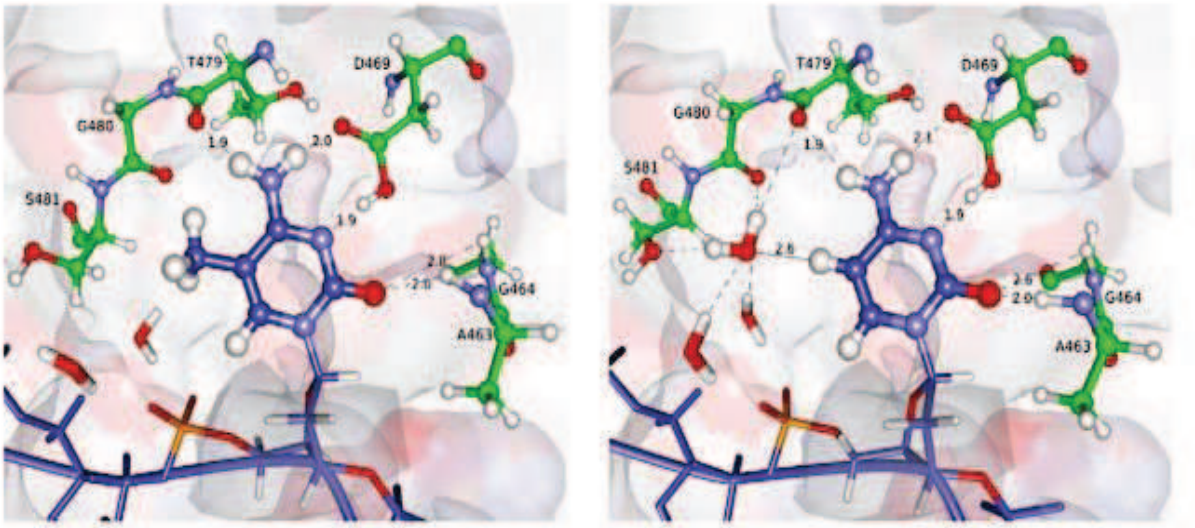

Figure 2.3. Modeled structure of UHRF1 with hemi-methylated DNA (left panel) and with nonmethylated DNA (right panel) including all water molecules found within a radius of 6Å from C(5-Me)/H5. The flipped methyl-cytosine, as well as the (intruding) water molecule that occupies the space of the methyl group in the unmethylated complex, is emphasized by thick ball-and-stick representation. The protein–DNA hydrogen bonds are indicated by broken lines, and the numbers shown correspond to the H–acceptor hydrogen bond distances (Å) averaged over all trajectories. Note that the intruding water molecule can form hydrogen bonds with two other water molecules, Ser481, Gly480, and Thr479. The distance corresponding to the first peak of the radial distribution function between H5 and oxygen of waters is also indicated and represented by a continuous line. **Figure** taken from (Bianchi & Zangi 2012).

Computer simulations indicated that cytosine and methylcytosine differ in the charge distribution of their aromatic ring because of the methylation reaction. This difference is proposed to reduce the magnitude of the dipole moment which strengthens the interaction

energy in the bound complex between UHRF1 and hemi-methylated DNA. Thus, structure and modeling studies of the bound complex between hemi-methylated DNA and UHRF1 reveal mechanistic aspects of specificity of SRA to hemimethylated DNA. However, the exact molecular mechanism responsible for distinguishing between hemi-methylated and nonmethylated duplexes is not evident. Moreover, these studies do not give any understanding on how flipping of methyl cytosine by UHRF1 allows directing DNMT1 to its target site.

III Methods to study DNA methylation patterns

As described above, DNA methylation has fundamental regulatory roles and functions in different biological processes. The investigation of DNA methylation and its heritability is being recognized as an increasingly important area of research that looks for an understanding of the molecular mechanisms of epigenetic machinery. However, the direct examination of DNA methylation is complicated by the fact that standard methods are unable to distinguish 5-methylcytosine from unmodified cytosine. To fill this gap, a number of methodologies has been developed for detecting DNA methylation, each with its own advantages and disadvantages.

3.1 Bisulfite sequencing

One of the most common technic is based on the treatment of single stranded DNA with sodium bisulfite (NaHSO3). This results in the conversion of unmethylated cytosines to uracil, whereas 5-methylcytosines are unreactive (Hayatsu et al. 1970).

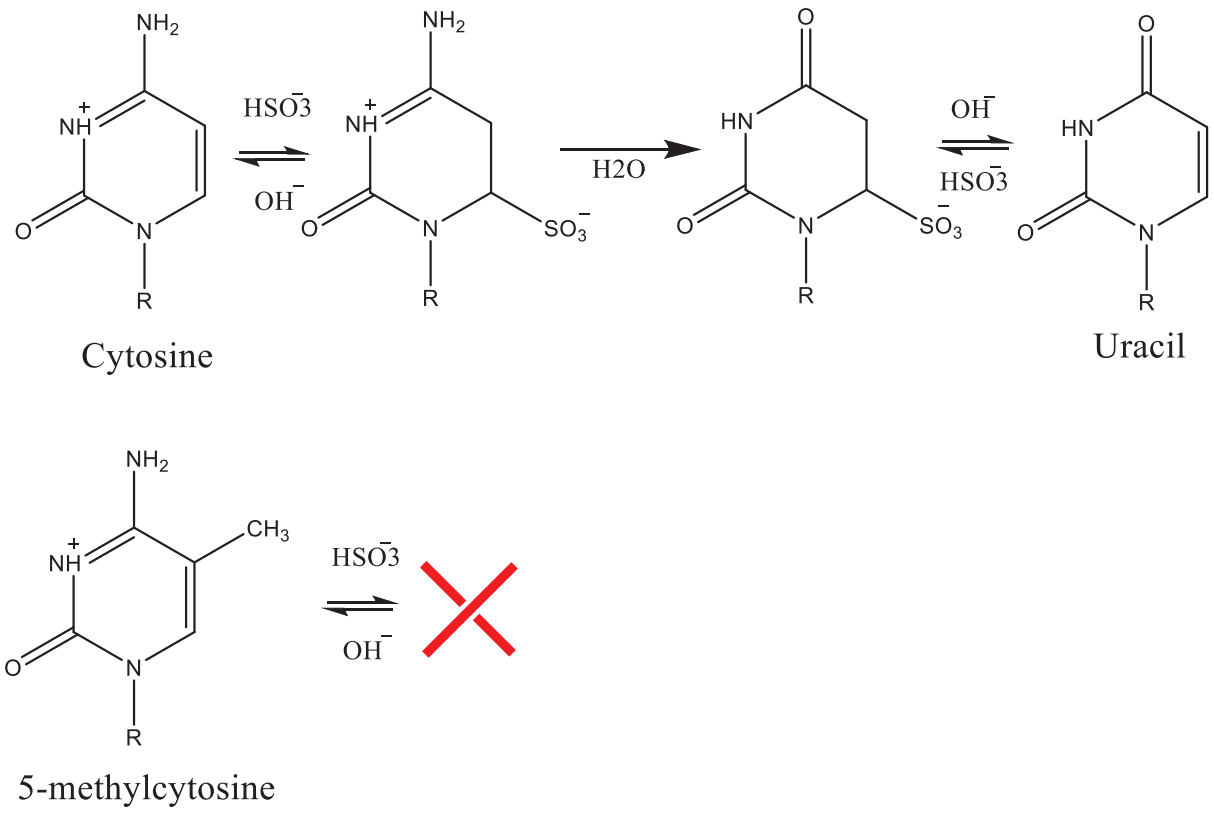

Figure 3.1. Chemical reaction during bisulfite treatment. Cytosine derivatives undergo reversible reactions with bisulphite yielding a 5,6-Dihydro-6-sulfonate, which deaminates

spontaneously. After that the sulphate is eliminated under alkaline conditions, leaving Uracil.

The reaction occurs as shown on **Figure** 3.1. The methylated cytosine is not affected by this reaction, due to the steric hindrance of the methyl-group in 5'-position. After bisulfite treatment, the product is amplified by PCR using two specific primers. The PCR-product can then be sequenced, directly or after subcloning of the amplified fragment. Direct sequencing gives information about the average methylation of a CpG site in a sample, while sequencing of cloned DNA allows the analysis of individual CpG sites. However, sequencing of bisulfite-treated DNA is very laborious and time-consuming and therefore not practicable on a global scale. Despite its disadvantages, this approach became very important in the investigation of methylation of cancer-related genes (Dai et al. 2001; Yoshikawa et al. 2001).

3.2 5-methylcytosine specific osmium oxidation

Direct modification of 5-methylcytosine was used to distinguish it from cytosine. It was found that the rate of reaction of cytosine oxidation by osmium drops when a methyl group is present (Okamoto et al. 2006; Okamoto 2007). The obtained rate constants for nonmethylated and methylated duplexes were 1.1×10^{-2} and 2.5×10^{-5} s^{-1}, respectively. This large difference in rates was attributed to electron donation of the methyl group to the C5– C6 double bond and to the lower ionization potential of methylcytosine as compared to cytosine. This selective modification of methylated cytosine was used to study the methylation patterns through cleavage or reading out by sequencing of the bulge formed by osmium oxidation (**Figure** 3.2)

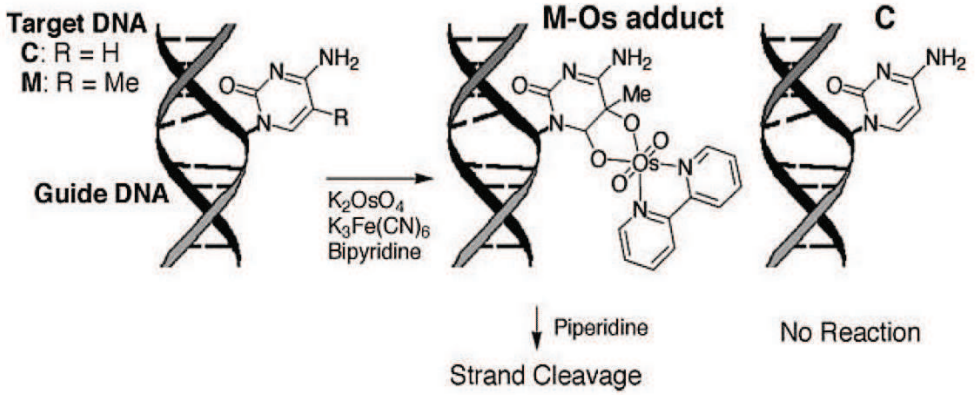

Figure 3.2. Selective oxidation of 5-methylcytosine (M) using a single base bulge formation.

This method allows detecting in a relatively easy way methylation of cytosine. However, the reaction requires the use of organic solvents and thus is performed in conditions far from physiological. Because of these limitations, this method is not widely used.

3.4 Solid-State Nanopores

An attractive alternative to bisulfite-based sequencing is sequencing by using solid-state nanopores. This method does not require any pretreatment of DNA and is considered as one of the most powerful technique to simultaneously sequence both genome and epigenome. Generally, nanopores are holes in a solid-state matrix with internal diameters of several nm. The matrix is immersed in a conducting fluid and an electric current due to conduction of ions through the nanopores can be observed when a potential is applied (**Figure** 3.3).

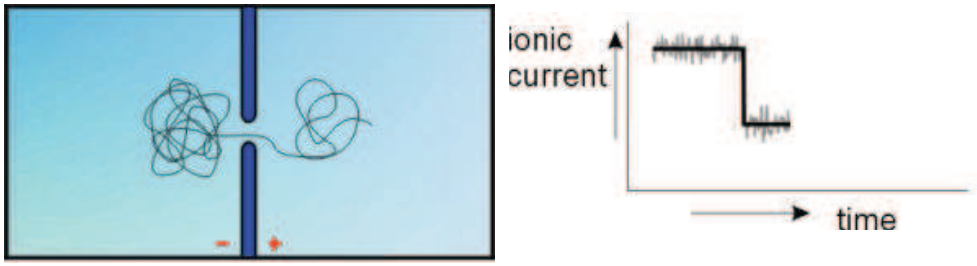

Figure 3.3. Schematic representation of DNA passing through a nanopore.

A modulation of this current occurs when DNA strand passes through a nanopore. The current which can pass through the nanopore at any given moment varies depending on whether the nanopore is blocked by an A, a C, a G or a T or a section of DNA. This change of current represents a direct reading of DNA sequence.

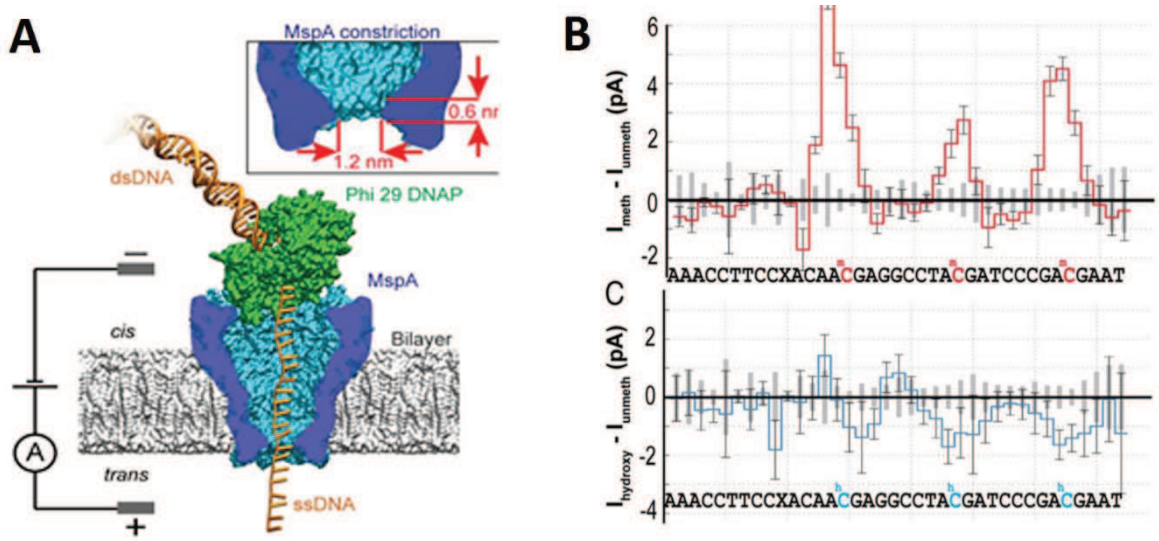

Figure 3.4. (A) Scheme of a typical MspA–phi29 DNA polymerase experiment. MspA (in blue) is a membrane protein embedded in a phospholipid bilayer. A voltage across the membrane causes an ion current to flow through the pore. (B) Ion current levels for DNA sequences containing methylation (top) or hydroxymethylation (bottom). The currents obtained with these sequences are subtracted by the currents obtained with the corresponding non modified sequences.

Most nanopores-based approaches are hampered by difficulties in sculpting suitable nano-holes to implement single nucleotide resolution. The possibility to use nano-holes in graphene, which may provide single atom thickness, is currently actively studied (Vicarelli et al. 2015).
These limitations are absent if nanopores are filled with proteins (**Figure** 3.4), such as alpha hemolysin (αHL) and Mycobacterium smegmatis porin A (MspA). The alpha hemolysin (αHL) allows identification of all four bases (Stoddart et al. 2009; Purnell et al. 2008). Due to favorable structure and diameter, the MspA allows identification of DNA nucleotides with tenfold higher base specific electrical current signals than αHL. Moreover, by using a polymerase, which directs DNA into MspA nanopores, it was possible to identify 5-methylcytosine and 5-hydroxymethylcytosine residues. Indeed, mC was found to increase the ionic current relative to C, whereas hC generally decreased it (Laszlo et al. 2013).

As an alternative, the DNA-binding MBD-1 protein was used to specifically label mC residues (Shim et al. 2013). The DNA-bound MDB-1 was observed to modulate the ionic current through solid-state pore, so that a single mC residue could be detected **Figure** 3.5. Due to the

large size of the protein, this method relaxes the requirements for the quality of nanopores and allows using 20 nm pores.

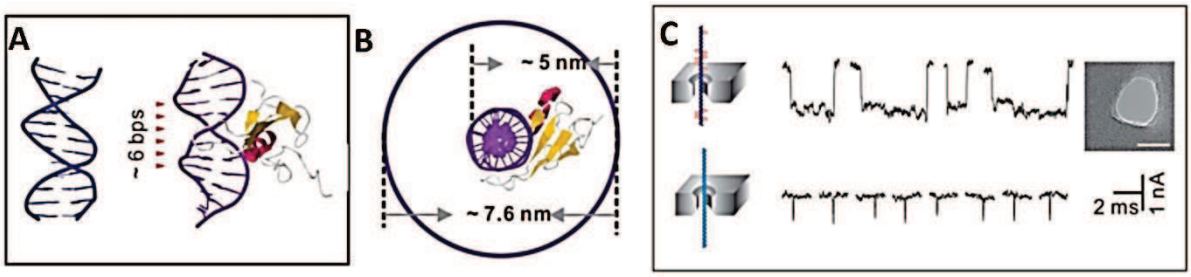

Figure 3.5. Identification of mC residues with MBD-1 protein, using the nanopore sequencing approach. (A) Structure of B-form dsDNA (left) and methylated DNA/MBD-1 complex (right). A single MBD-1 protein binds to the methylated CpG site on the major groove of dsDNA, occupying about 6 bp. (B) Top-down view: the cross-sectional diameter of the complex with a single bound MBD protein is 5 nm. Multiple bound proteins along the DNA major groove increase complex diameter to 7.6 nm. (C) Characteristic translocation signatures for free DNA (bottom) versus DNA-MBD-1 complexes (top) through 12 nm nanopores.

3.5 Single-molecule, real-time sequencing

Recently, single-molecule real-time (SMRT) sequencing was used to map DNA methylation (Flusberg et al. 2010). In SMRT sequencing, DNA polymerases catalyze the incorporation of fluorescently labeled nucleotides into complementary nucleic acid strands (**Figure 3.6**).

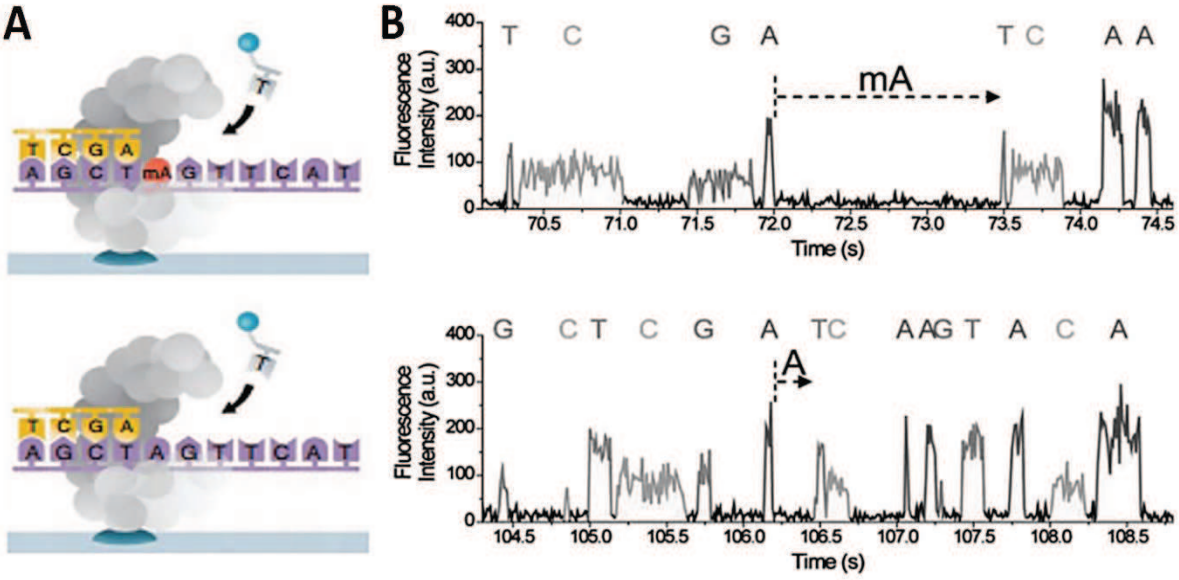

Figure 3.6. Principle and corresponding example of DNA methylation detection during SMRT sequencing. (**A**) Scheme of polymerase synthesis of DNA strands containing a methylated (top) or an unmethylated (bottom) adenosine. (**B**) Typical SMRT sequencing fluorescence traces.

Fluorescence pulses in SMRT sequencing are characterized by their emission spectra, also by their duration and by the interval between successive pulses. The polymerase kinetics was found to be modulated by the presence of a methyl group on A and C residues and by the presence of a hydroxymethyl group on C nucleotides in the template strand. This modulation of polymerase kinetics is consistent with the modulation of ion current pulses observed with the MspA-polymerase nanopore method.

3.6 Luciferase-Based Sensors of DNA Methylation

The above-described methods of studying methylation of DNA require a pretreatment of DNA or some specific systems to detect in an indirect way methyl groups on DNA. More direct and less invasive methods based on fluorescent tools were developed. One of them is based on the recovery of fluorescence upon fusion of two parts of firefly luciferase protein (Fluc) directed by two MBD-2 proteins (**Figure 3.7)**. This split-luciferase biosensor is composed of two fusion proteins: a DNA-binding domain fused to the N-terminal portion of Fluc, and a second DNA-binding domain fused to the Fluc C-terminus (Badran et al. 2011) The fusion proteins are expressed in a cell-free expression system, then incubated with the target DNA to allow DNA binding. If multiple methylated CpG sites exist in proximity, the N-terminal and C-terminal portions of Fluc will interact. The level of restored Fluc activity is measured using a firefly luciferase assay, such as the Steady-Glo ® or Dual-Glo ® Luciferase Assay System, and luminescence levels are indicative of DNA methylation levels throughout the genome.

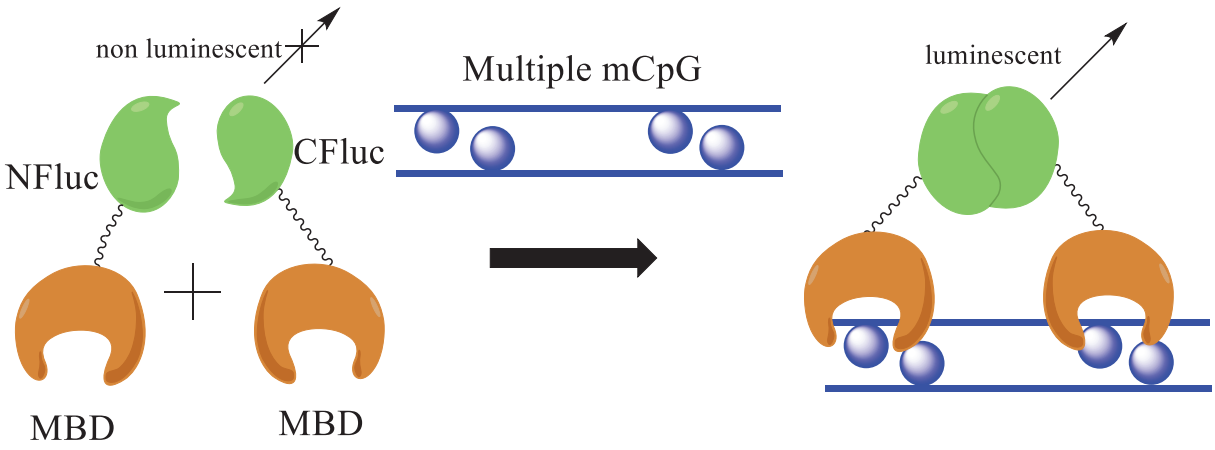

Figure 3.7. Principle of the split-luciferase biosensor to assess DNA methylation at the genome level.

To measure sequence-specific methylation levels, the N-terminus of Fluc is coupled to the MBD DNA-binding domain, while the C-terminus is coupled to a sequence-specific DNA-binding domain (Porter et al. 2008).

3.7 Atomic Force Spectroscopy

The possibility to use force spectroscopy to study DNA methylation was also explored. Force spectroscopy measures the relationship between the length of the molecule and the tension. This method is widely used to examine the nanomechanics and mechanochemistry of DNA, sugars and proteins (Zhu et al. 2010; Fisher et al. 2000). To evaluate DNA methylation patterns, methylated single stranded DNA molecules are linked to a glass substrate and an anti-5-methylcytosine antibody is attached to the tip of an AFM (**Figure 3.8A**) (Zhu et al. 2010).

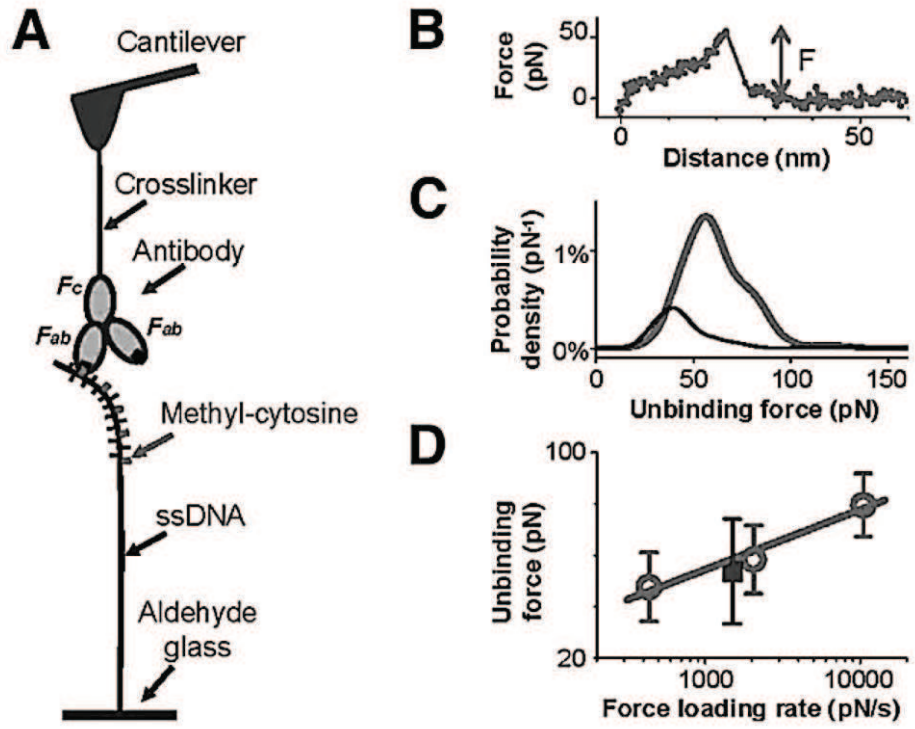

Figure 3.8. Schematic representation of force measurements using AFM. A: Single-stranded DNA (ssDNA) is conjugated to a glass surface through an amine group at its end, and the antibody is conjugated to the cantilever tip via flexible polyethylene glycol cross-linkers. The two Fab arms and the Fc arm of the antibody are indicated. B: A typical force-distance curve

measured with an AFM showing a single unbinding event. C: The distribution of the unbinding force between ssDNA and anti-5-methylcytidine antibody showed a maximum at approximately 57 pN for ssDNA containing five 5-methylcytidines (grey line). D: Unbinding forces between antibody and DNA containing one (square) or five (circles) 5-methylcytidines at different force loading rates.

When the tip contacts the DNA, a complex is formed with the two Fab arms of the antibody. Force peaks are recorded by stretching the DNA/antibody complex that is attached to the AFM tip. The methylation patterns are then analyzed through the distance distribution of the force peaks. However, the inability to detect two neighboring 5-methylcytosines is a drawback of this technique. To eliminate this limitation, an antibody fragment instead of the whole antibody could be used (**Figure 3.8 B and D**) (Zhu et al. 2010).

The above-described techniques provide the methylation maps for multiple human and mouse cell types. However, these techniques rely on indirect examination of already formed DNA methylation patterns and thus do not provide any possibility to study the dynamics of multiple proteins involved in DNA methylation maintenance.

IV Methods to study base flipping

The methods which are used to map DNA methylation patterns provide static snapshots, but are not applicable to investigate the dynamics of DNA methylation. Most studies which investigate dynamics of DNA methylation are based on DNMT-mediated base flipping. Base flipping is a fundamental mechanism in DNA modification and repair. Recently, it was also suggested that UHRF1- and UHRF2-mediated base flipping could be used to achieve specific recognition of nucleotides. Currently, there is a variety of biophysical methods to study DNA base flipping, which could be applied to study UHRF1 activity.

4.1 X-Ray Crystallography

X-ray crystallography structural studies reveal details at atomic resolution of protein-DNA complexes and are the ultimate technique which can prove base flipping. In this technique, incident X-rays are diffracted by crystalline atoms into a diffraction pattern which could be converted into a three-dimensional distribution of electrons in the crystal. From this distribution, positions of atoms are determined as well as their chemical bonds. By using this technique, many base flipping systems were disclosed, such as DNA methyltransferases, DNA glycosylases, apurinic/apyrimidinic endonucleases, glucosyltransferases, restriction endonucleases and the SRA binding domain. In these systems, the flipping could affect one target base (Larivière & Moréra 2002), a base located on the opposite DNA strand to the target base(Min & Pavletich 2007) or both nucleosides of a target base pair (Hosfield et al. 1999). Crystal structures allow studying base flipping with atomic resolution, but provide only a static snapshot at the end of the flipping process. Moreover, co-crystallization of protein with their target DNA is often difficult.

4.2 NMR Spectroscopy

NMR spectroscopy is another technique able to provide information about protein/DNA interaction with atomic resolution. In contrast to X-ray crystallography, NMR is suited for studying dynamics of base flipping. NMR is widely used to study the dynamics of base pairing in free DNA in solution, showing notably that conformations of double helical nucleic acids fluctuate in physiological conditions. These fluctuations include transient disruption of base pairing (a phenomenon called DNA breathing). The lifetimes of the closed and open state were found to be in range of 1-5 ms for A:T and 10-50 ms for G:C. Experiments on protein-DNA

complexes revealed that there are two possible modes of base flipping which are used by proteins. The first one is a passive mechanism in which an enzyme merely catches the spontaneously flipped out base (Parker et al. 2007) with rates comparable to rates of DNA breathing in free state. The second one is an active mechanism in which enzymes "push" the base out of the DNA helix, with rates faster than 1 min^{-1}, independently of spontaneous base flipping. These rates are difficult to measure with typical NMR time resolution and the analysis of large protein-DNA complexes is often complicated by slow molecular tumbling or insufficient solubility.

4.3 Chemical probing

The chemical reactivity of individual bases of DNA could be modulated by extrahelical conformations as a result of changes in accessibility, unpairing or unstacking events. Multiple chemicals have been developed to probe such increased reactivity resulting from protein-induced base flipping (Glick & Matsuda 2001). The general approach is to chemically modify bases, in order to block base pairing. This base could then be cleaved with nuclease S1 (Mclean et al. 1987). Studies of interaction of M.HhaI with DNA substrate having an cleaved base at the position of target cytosine showed that the enzyme still flips the sugar-phosphate backbone (O'Gara et al. 1998). Moreover, the affinity increased significantly suggesting that the binding energy of the enzyme to DNA is used to destabilize the target base pair and induce flipping.
Chemical probing is complicated by low base or sequence selectivity. Moreover, the main drawback of chemical probing of protein-induced base flipping is the decreased reactivity of the flipped bases due to multiple contacts with the protein. Additionally, for such study, only reactions that proceed at near physiological conditions can be used.

4.4 Long range charge transfer for base flipping detection

Base flipping events can be studied by monitoring nucleobase-mediated charge transfer along a DNA helix containing a binding site of M.HhaI (Haemophilus haemolyticus methyltransferase). To study such long-range charge effects, a DNA system was designed in which a rhodium photo-oxidant tethered (Rh) to one end of the DNA induces the oxidation of guanines (**Figure** 4.1).

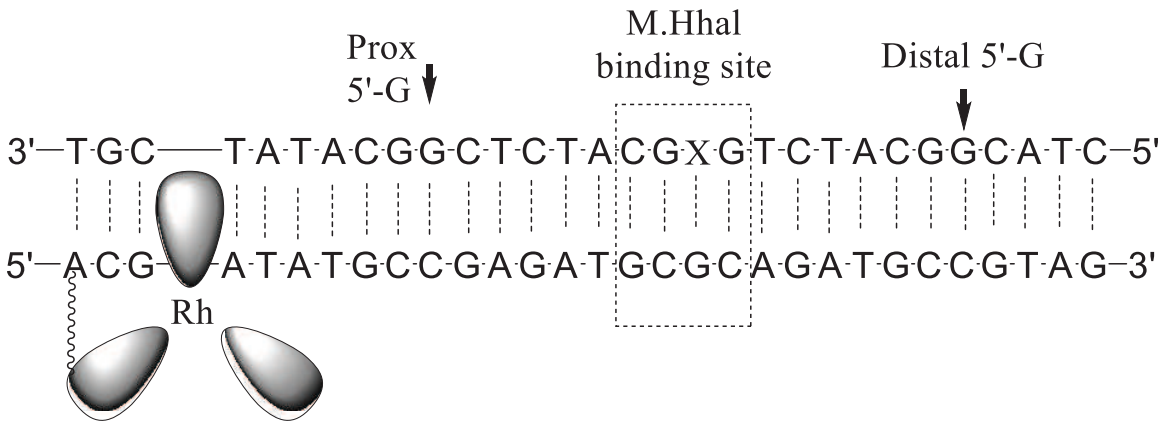

Figure 4.1. Rh-DNA substrate for study of long range charge transfer. The photo-oxidant (Rh) induces the oxidation of proximal and distal guanines separated by the target site of M.Hhal. X is the target base for flipping by M.Hhal or an abasic site.

The efficiency of charge transfer in such system is estimated by the level of oxidation of the guanines proximal and distant to photo-oxidant. It was observed that this efficiency correlates with the protein-induced changes in base stacking in the center of the duplex. Interactions that disturb the DNA π-stack inhibit DNA charge transport. The base flipping activity of M.HhaI was found to effectively prevent the charge transfer (Rajski & Barton 2001). This method allows identifying the region where the protein flips the nucleobase, but cannot report about the base flipping event. Moreover, detection of the level of guanosine oxidation requires additional techniques. This makes such method impossible to use for investigating base flipping in real time.

4.6 Fluorescence Spectroscopy

The spectral properties of molecules in UV-visible range are determined by their structure, including their intermolecular chemical bonds, as well as by the photophysical processes which occur after excitation (absorption of photon). The fluorescence process is usually described by the Jablonski diagram (**Figure 4.2)**. Photon absorption induces an electronic transition from the ground state to a higher energy state (excited state), generating the so-called Frank-Condon state within 10^{-15}s. The efficiency of this transition from ground state to excited state (**Figure 4.2**) is characterized by the absorption cross-section (σ) of the molecule. This absorption cross-section is determined by the molecular structure and by the vibrational states of the molecule. Vibrational relaxations, which occur within 10^{-12} - 10^{-10} s, lead to a fast transition to the lowest vibrational level of the first excited electronic state that corresponds to the emissive state. This

process results in a lower emission energy of the molecule compared with its excitation energy (Stokes shift). The excited state exists for a time range between 0.1ns - 20ns that characterizes the fluorescence lifetime and that depends on the balance between the radiative and non radiative deexcitation pathways that bring the molecule back to the ground state. The balance between the pathways is also characterized by the fluorescence quantum yield of the chromophores, which characterizes the fraction of excited molecules that emit a photon. These parameters are sensitive to various environmental parameters such as pH, polarity, viscosity or the presence of other molecules in close proximity. The uniqueness of the spectral properties for each molecule and its sensitivity to environment make molecular fluorescence an extremely informative tool for biophysical and biochemical research.

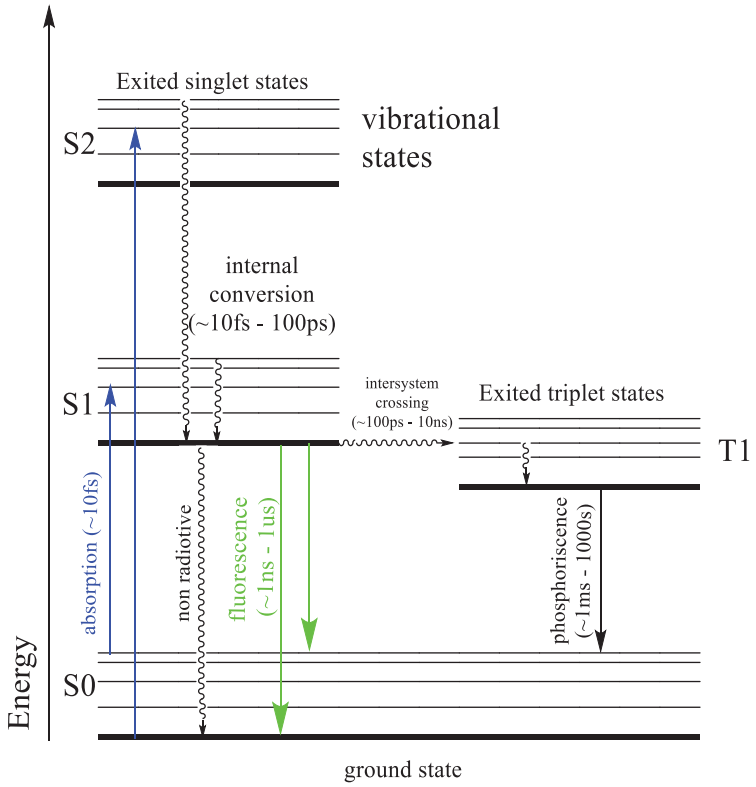

Figure 4.2. Jablonski diagram

Nucleotides exhibit exceedingly low fluorescence quantum yields on the level of $(0.5\text{-}3)\times10^{-4}$ and thus cannot be used to probe protein-DNA interactions. However, they are very efficient light absorbers at wavelengths around 260 nm and their absorbance is significantly modulated by base pairing. Indeed, in double-strand DNA, the hydrogen bonds beteween base pairs limit the resonance of the aromatic rings so that their absorbance is decreased compared to unpaired bases (hypochromicity effect). For example, UV absorbance changes were used to monitor base flipping of cytosine by M.Hal methyltransferase in real time (Gerasimait et al. 2011). These

experiments showed that M.Hal-induced flipping out of the helix occurs with a rate of 30 s^{-1} and flipping back with a rate of 0.2 s^{-1}. The great advantage of this approach consists in the real time observation of an unperturbed system. However, as most of the proteins and all DNAs are strong absorbers in the UV region, this greatly complicates studies of multi partner interactions. Because of this limitation, chemically modified analogs of natural nucleotides, which possess good fluorescent properties and which could be excited at wavelength greater than 260 nm, are widely used. This approach requires a good compromise between desired fluorescent properties and sufficient mimicking of natural nucleotides. For some base flipping methyltransferases, the target base is not recognized during initial flipping, and thus, can be substituted with fluorescent probes or structural nucleotide analogs (Wang et al. 2000). Until now, the most widely used fluorescent probe for investigating base flipping is the structural analog of adenine, 2-aminopurine (2Ap) (Ward et al. 1969). Its high quantum yield in aqueous solution is strongly quenched when 2Ap is incorporated into DNA. Its fluorescent intensity is strongly dependent on charge transfer with neighbor bases and the efficiency of this process is determined by base stacking in the DNA helix. This charge transfer process is the main decay pathway of the 2Ap excited state in DNA (Shana O. Kelley 1999; Jean & Hall 2001; Rachofsky et al. 2001). Thus, when 2Ap is introduced in the target site, base flipping leads to recovery of its intensity or its ~ 10 ns fluorescence lifetime, due to a decrease of base stacking with its neighbors (Lenz et al. 2007; Neely 2005). This was shown with EcoRI methyltransferase, a base flipping enzyme which induced several ten-fold fluorescence enhancement on binding (Allan & Reich 1996). A more limited enhancement in fluorescence is observed when the flipped out base is in close proximity with the non-polar or aromatic residues of the protein (Tamulaitis et al. 2007; Lenz et al. 2007). In this case, 2Ap cannot serve as a reliable probe for base flipping, since a complete flipping of 2AP from the DNA into a quenched environment would be indistinguishable from a partial unstacking of the 2AP base in the helix (Reddy & Rao 2000; Christine 2002).

The strategy of substituting the target mC by 2Ap works only with methyl binding proteins that do not recognize mC during initiation of flipping event. Therefore, this strategy is not be applicable for proteins which specifically recognize mC, such as the SRA family (Greiner et al. 2015). In addition, 2Ap is also unable to sense mC flipping when it replaces neighbor bases of mC. Indeed, once introduced within and outside of CpG site, 2Ap is sensitive only to SRA binding, but not to base flipping (Greiner et al. 2015).

V Fluorescent Nucleoside Analogs

DNA nucleotide modifications are widely used in order to obtain fluorescent probes within the DNA molecule. The aromatic pyridine and pyrimidine heterocycles are receptive to a variety of modifications. Minimal structural and electronic perturbations were found to dramatically modulate their photophysical characteristics. Modifications of natural nucleotides could be classified as external and internal. External modifications use covalently attached fluorophores to the backbone at the end of DNA or within sequence, but outside the actual base stack. Internal modifications of DNA generally used modified nucleobases.

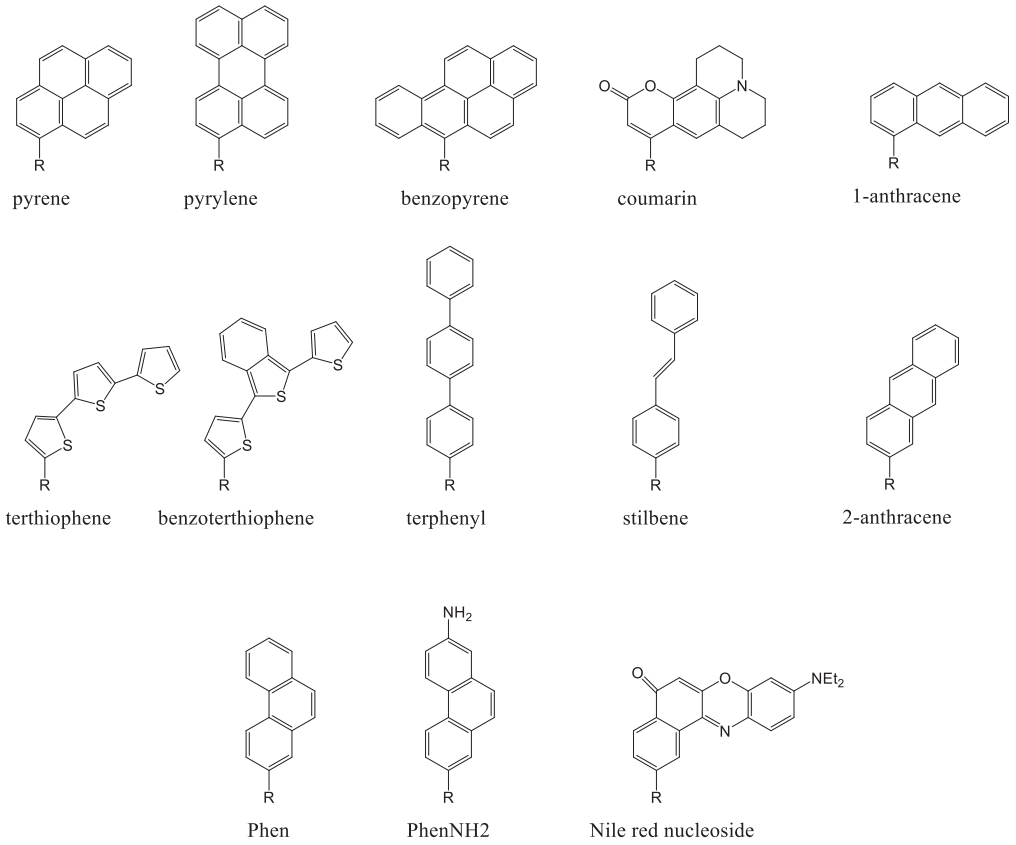

Figure 4.3. Selected examples of chromophoric base analogs, where R = 2′-deoxyribose

There are several well developed approaches for modifications of nucleobases (Sinkeldam et al. 2010). One of them consists in replacing the natural nucleobases with established fluorophores, which yields an artificial family of chromophoric base analogs that lack the Watson-Crick hydrogen bonding ability. The relative latitude of chromophore choice allows obtaining high emission quantum yields and red-shifted absorption bands that facilitate

selective excitation in the presence of natural nucleobases (**Figure** 4.3**)** (Wilson & Kool 2006). However, these chromophoric base analogs do not properly mimic naturally occurring nucleotides what greatly limits their application.

Another class of nucleobases is obtained by extending the conjugation of the natural nucleobases through fusing additional aromatic rings onto the pyrimidine and purine nuclei (**Figure** 4.4). An extended aromatic surface typically results in red-shifted absorption bands compared with their natural counterparts, emission bands near or in the visible range, and rather high emission quantum yields (Sinkeldam et al. 2010). These expanded nucleobases in general retain their Watson-Crick hydrogen bonding ability, although their large surface area could structurally perturb the resulting oligonucleotides.

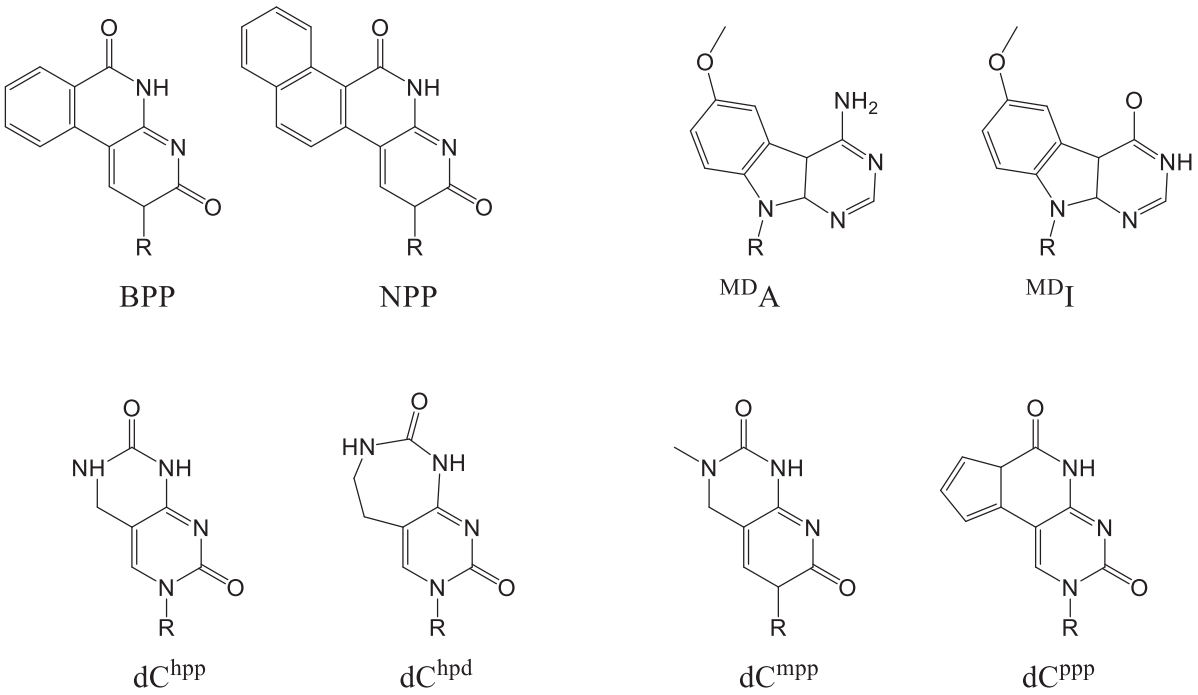

Figure 4.4. Expanded nucleobase analogs (R =2′-deoxyribose).

Alternatively, extension of natural bases with chromophores was used successfully to create fluorescent nucleotides analogues. These extended fluorescent nucleoside analogs are formed by fluorescent moieties that are linked or conjugated to the natural nucleobases, via either flexible or rigid linkers (**Figure** 4.5). This approach allows obtaining nucleotide analogs with photophysical features that are similar to that of the parent fluorophore, and remain natural bases (Sinkeldam et al. 2010). However, extended fluorescent nucleotides perturb the DNA structure, depending on the chromophore used for the extension of base.

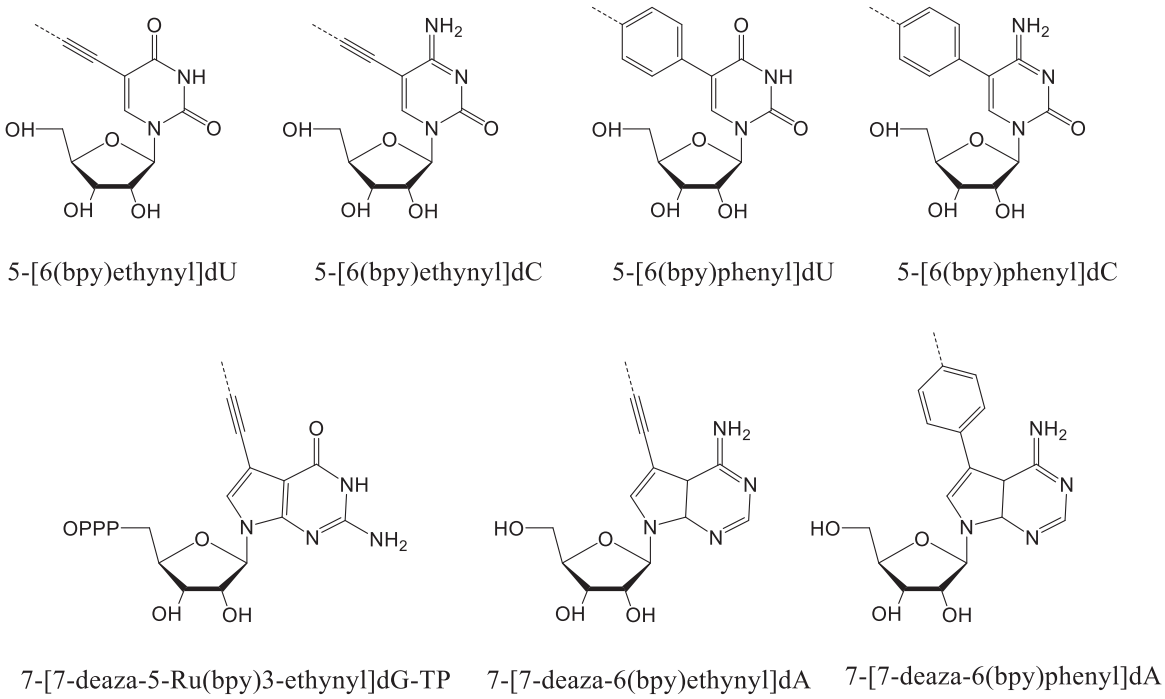

Figure 4.5. Examples of extended nucleobase analogs

Ideally, to study biophysical events, it is necessary to have fluorescent nucleotide analogs, which show good fluorescent properties and mimic natural nucleotides as close as possible. This can be achieved by using isomorphic nucleobase analogs that closely resemble the natural nucleobases with respect to their overall dimensions, hydrogen bonding patterns, and ability to form isostructural Watson Crick base pairs.

The restricted criteria of minimal modification of natural base make isomorphic fluorescent nucleosides the most challenging to design. Currently, plenty of such nucleotides were developed. The general approach is to add functional groups to bases which varies in its nature, or to shift/remove already present groups (**Figure 4.6**) (Sinkeldam et al. 2010). The most widely used is 2-Aminopurine which is a structural analog of adenine obtained by removal of amidogen group at 6 position and by addition of NH_2 group at position 2 (Ward et al. 1969). This relatively small modification transforms the non-fluorescent adenine to a highly emissive probe. As discussed above, the sensitivity of the emission of 2-AP to the microenvironment is very useful and is applied to study base flipping. Most of these fluorescent nucleotides have a quantum yield that is highly sensitive to their local environment. Factors such as hydrogen bonding, single- or double-stranded environment, and neighboring bases are important factors that modulate the fluorescence quantum yield of a base analog inside the base stack. The biggest

impact is related to charge and energy transfer inside of DNA duplex that generally resulted in very low quantum yields. This is especially the case with 2-Ap, where the large quantum yield as a free base (0.68) dropped to about 0.01, when included in oligonucleotides, close to a G.

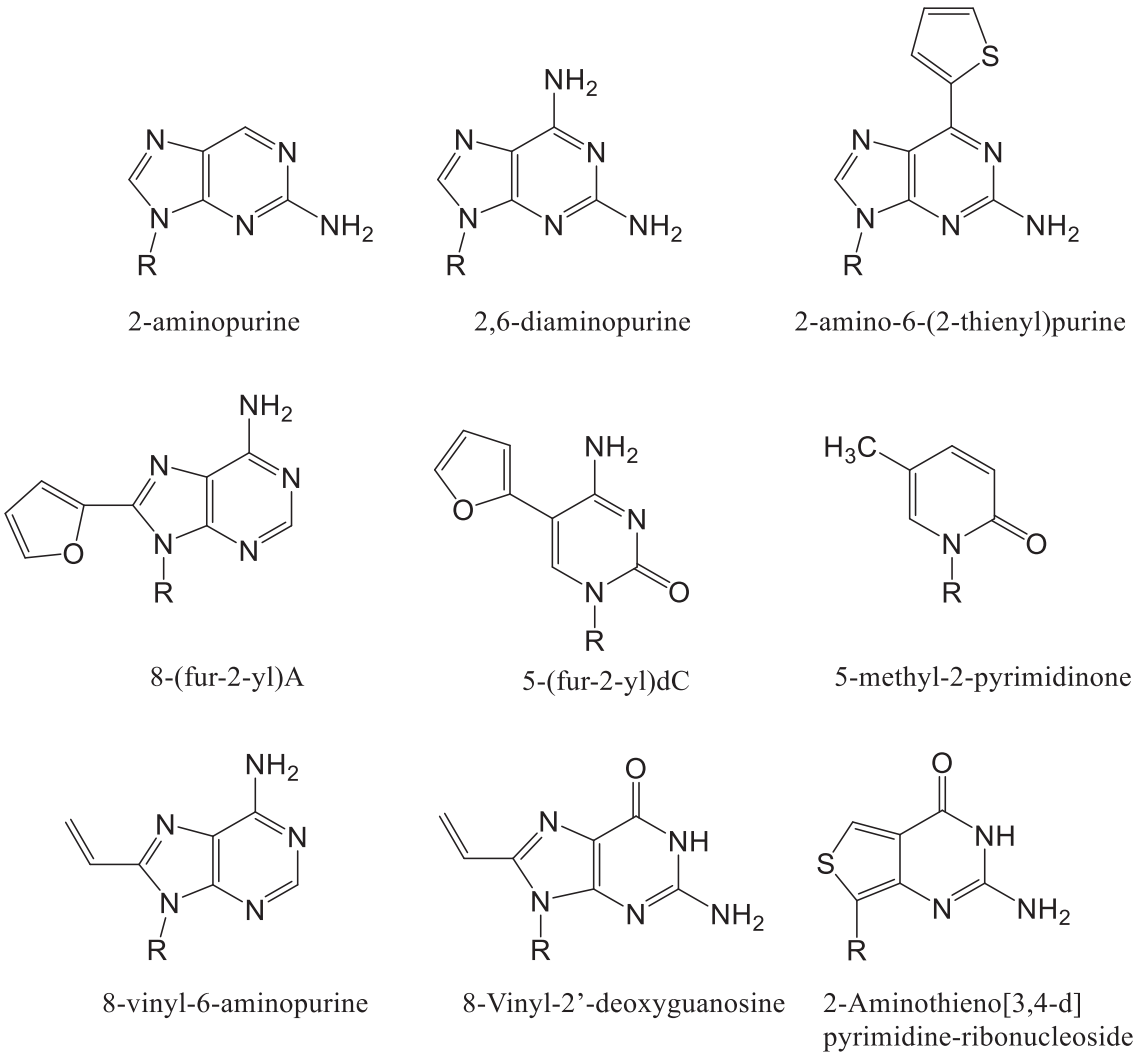

Figure 4.6. Selected examples of isomorphic nucleoside analogs

VI Photo physical processes of fluorescent nucleotides in DNA

6.1 Quenching mechanism and photoinduced electron transfer

The intensity changes of fluorescent nucleotides are used to obtain information about molecular mechanisms involved in DNA/proteins interactions. Most frequently, a quantum yield enhancement is related to the decrease of the quenching of the fluorescent base by its neighboring nucleotides. Three mechanisms of quenching can be considered: intersystem crossing or the heavy atom effect; electron exchange or Dexter interactions and photo-induced electron transfer (PET). Electron transfer in DNA occurs through π-stacked base pairs which are strongly coupled. The strong coupling is critical for charge transfer, which was demonstrated by single-base mismatches in DNA duplex that diminished the yield of the process. Electron transfer reactions are controlled by the free energy of the reaction, the reorganization energy, the electronic interaction geometry, and the distance between donor and acceptor (Lakowicz 2006). All of these mechanisms are short-range interactions that occur efficiently only upon van der Waals contact between fluorophore and quencher. In case of internal labeling of DNA, the quenching is mostly associated with PET and depends on the base and the fluorophore (Seidel et al. 1996; Torimura et al. 2001). The efficiency of PET after photoexcitation of a molecule can be estimated by the Rehm-Weller equation:

$$\Delta G_{cs} = E_{ox} - E_{red} - E_{0,0} + E_{Coul} \qquad eq.6.1$$

where E_{ox} and E_{red} are the first one-electron oxidation potential of the donor and the first one-electron reduction potential of the acceptor. $E_{0,0}$ is the transition energy from the ground state to the lowest excited singlet state, and E_{Coul} is the Coulomb energy term between donor and acceptor radicals.

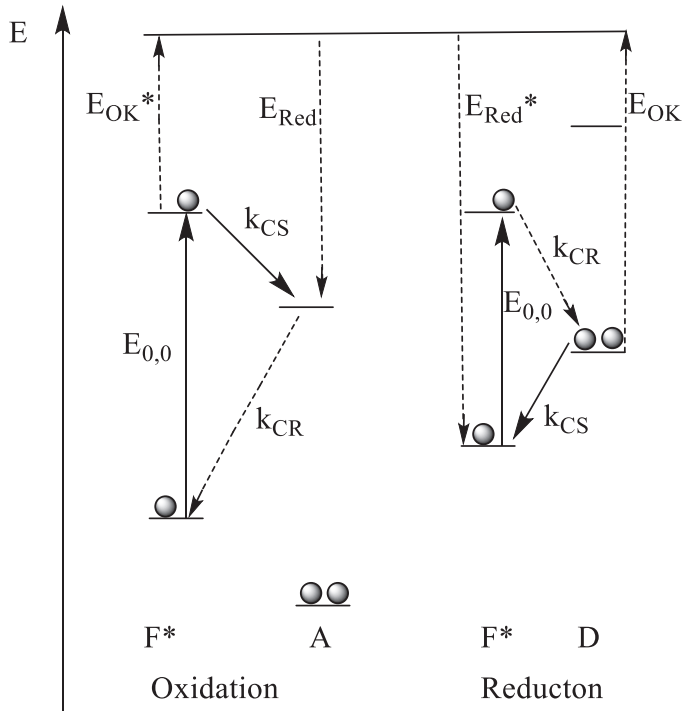

Figure 6.1. Scheme of photoinduced electron transfer (PET). An excited fluorophore is oxidized by transferring an electron to a nearby molecule. After charge recombination, the fluorophore relaxes to the ground state and its fluorescence is quenched. Alternatively, the fluorophore can be reduced before charge recombination completes the non-radiative relaxation of the fluorophore.

A chromophore in the excited state can be reduced by an electron from a donating quencher D or oxidized by an electron accepting quencher A (**Figure** 6.1). The formed radical ions relax electronically by charge recombination to complete the energetic cycle. The PET occurs with transfer rates above 10^{12} s^{-1}. Thus, the excited state will be depopulated via the non-radiative PET pathway as long as the fluorescence lifetime is on the order of 10^{-9}s. Among the DNA bases, guanine appears to be the most efficient quencher due to its tendency to donate an electron. However, the order of quenching efficiency is G<A<C<T if the nucleobase is reduced but it is the reverse, G>A>C>T, if the nucleobase is oxidized (Seidel et al. 1996).

6.2 Excited-state intramolecular proton transfer

The sensitivity of the most widely used internal fluorescent nucleotide analogs is essentially determined by the process of electron transfer because the nucleotides are well stacked in the DNA duplex and thus, only internal DNA processes might affect spectral properties. This limits the applications of such nucleotides for DNA/protein interactions which occur with significant distortion of the duplex structure. A promising alternative is to use fluorescent nucleotides with intramolecular processes highly sensitive to minute changes in the local environment such as excited-state intramolecular proton transfer (ESIPT). Generally, ESIPT involves a transfer of a hydroxyl proton to the carbonyl oxygen through a pre-existing intramolecular hydrogen bonding configuration.

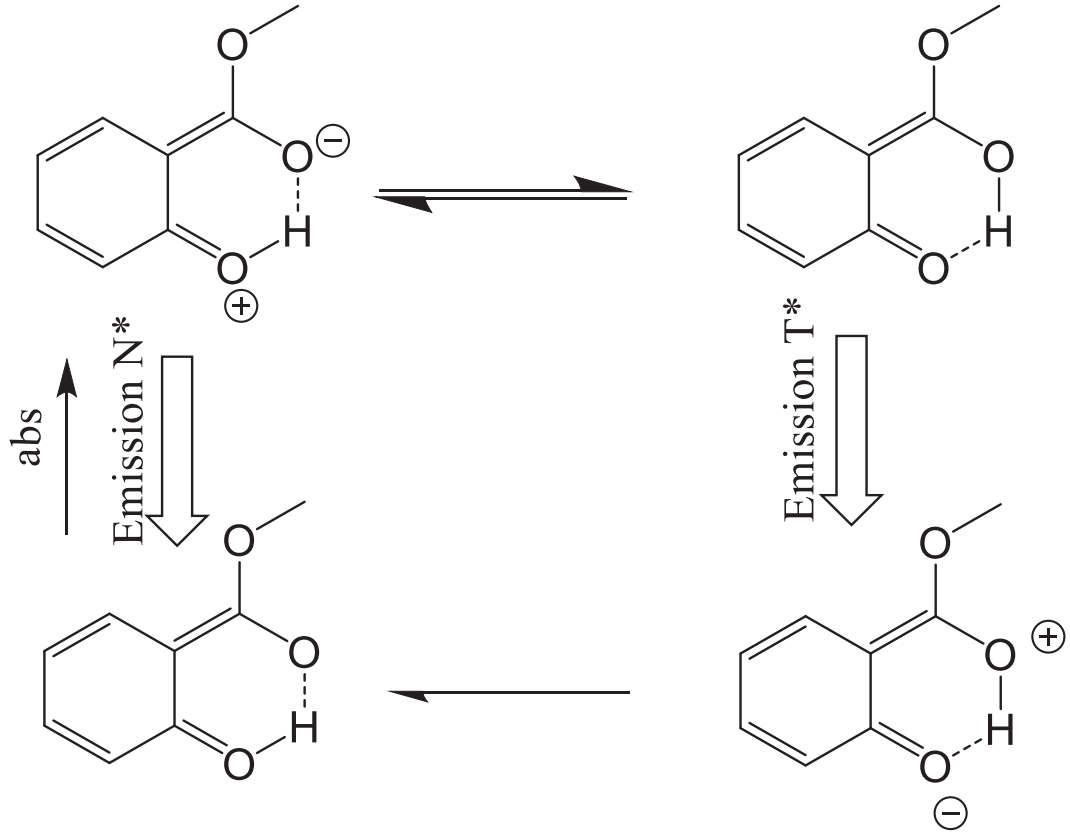

Figure 6.2. Example of ESIPT in methyl salicylate. In the ground state the normal (N*) form is strongly favored. After excitation, the tautomer (T*) form with a shifted proton has a lower energy and thus, the ESIPT reaction becomes favorable.

The ESIPT reaction was observed and characterized for the first time in salicylic acid ester (**Figure** 6.2) (Weller 1956). The methylsalicylate ion displays an unusual large Stokes shift which was attributed to an ESIPT reaction from the hydroxy- to the carbonyl-group. This

decreases the energy of the excited-state species, giving a red-shifted emission band. The main requirement of the ESIPT reaction is that the molecule must have close hydrogen bond donating and acceptor groups, with a strong intramolecular hydrogen bond. The ESIPT occurs after photo-generation of a Franck-Condon state during the lifetime of the excited state, leading to the formation of a tautomeric product T* that is more or comparably stable than the normal excited state N*. Excited states of both forms undergo relaxation to the ground state, and back proton transfer (BPT) leads to the reconversion to the normal ground state (T → N). The movement of a proton between a donor and an acceptor atom in the strong intramolecular H-bonding system could be described as the movement of electronic charge density from the donor–hydrogen covalent bond to the acceptor. The distribution of electronic density changes weaken the proton interaction with the donor and increase the attraction of the proton by the acceptor. This leads to an enhanced distribution of electronic charge and thus a large change of the dipole moment of the molecule. Both the rate and the equilibrium of ESIPT are controlled by the proton transfer energy barrier and the energy difference between the normal (N*) and tautomer (T*) forms of the excited molecule (**Figure** 6.3**)**. The reversibility of ESIPT determined by energetic barrier between two form as well as by relation of two energy states. In general, ESIPT occurs without direct involvement of the surrounding molecules but the solvent may influence the relative energy levels and the most favorable conformations of the tautomers.

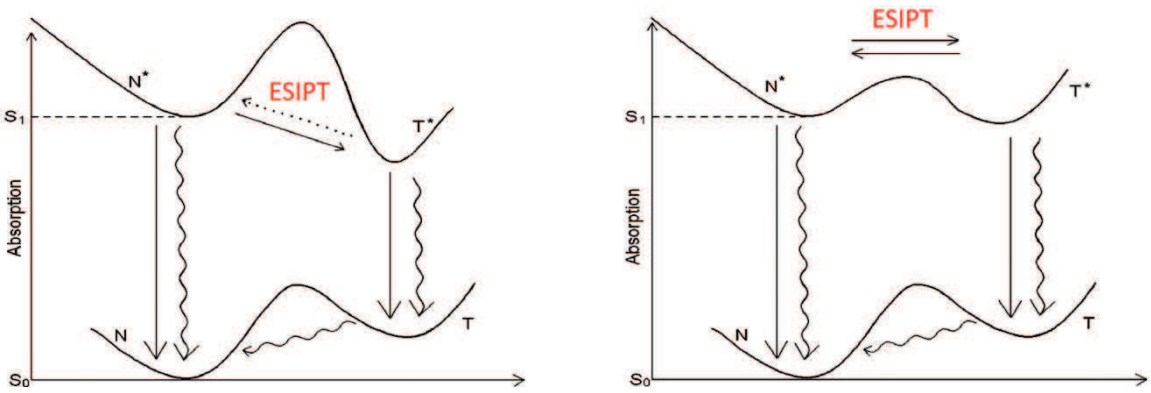

Figure 6.3. Energy diagram of the ESIPT reaction. ESIPT could be characterized by its rate which depends on the energy barrier. When the energy barrier is large, a irreversible ESIPT is observed, while a negligible or relatively small barrier results in a reversible ESIPT. It should be taken into account that relation between energy states of two form could also modify ESIPT.

Chromophores undergoing ESIPT exhibit the most significant Stokes shifts that can be obtained in any intramolecular photophysical reaction. This shift lies in range of hundreds nanometers because absorption and emission originate from two proton-transfer isomers. Well separated spectrally, the normal (N*) and tautomer (T*) forms provide a large spectral window convenient for spectroscopic measurements. Despite the strong decrease in the energy of emission, the observation of emission from both tautomers is possible in most cases. The ESIPT reaction could be effectively modulated by chemical modifications produced at distance from the site of the ESIPT reaction. These modifications change the electronic distribution within the molecule, switching the emission between N* and T* forms in broad ranges. This was shown to be extremely productive for the design of white-light emitters by properly selecting the positions and intensities of the two fluorescence bands (Tang et al. 2011).

A variety of organic fluorophores exhibiting ESIPT was described in the literature. The fluorophores based on 3-hydroxychromone (3HC) and its derivatives are of high interest since they possess unique properties. 3HCs have been shown to be powerful probes for a large range of applications in model and bio-membranes (Shynkar et al. 2007; Kilin et al. 2013; Kilin et al. 2015), and in proteins (Enander et al. 2008). Chromones are natural dyes frequently containing phenyl (aryl) substituents in position 2 of the heterocycle (**Figure** 6.4)

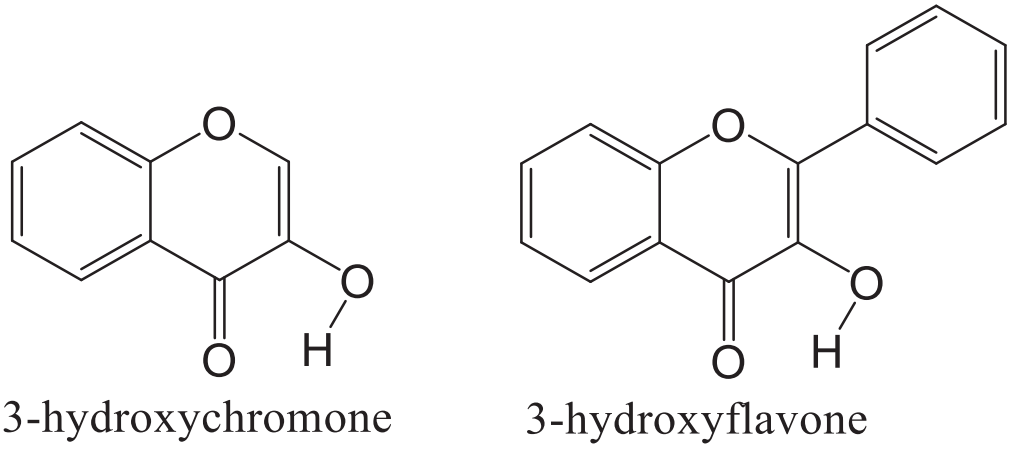

Figure 6.4. Chemical structure of 3-hydroxychromone and 3-hydroxyflavone.

The flavone derivatives bearing a hydroxyl group in position 3 of the heterocycle are called 3-hydroxyflavones (3HF). In 3HCs, the ESIPT occurs between structurally and energetically asymmetric states and therefore results in a dual emission, so that two emission bands are observed. ESIPT results from an intramolecular H-bond in this fluorophore formed through a 5-membered cycle (Sengupta & Kasha 1979).

The effect of H-bond length on the ESIPT rate was also observed for 3-hydroxyquinolones (Yushchenko et al. 2006) (**Figure** 6.5**).** Due to an increased length of the ESIPT pathway, the H-bond is relatively weak and can be easily disrupted by H-bonding interactions with the environment (McMorrow & Kasha 1984). This perturbation of ESIPT results in two emission bands: the short- wavelength band corresponding to the normal excited state (N*) and the long-wavelength band to the photo-tautomer product (T*). The different mechanisms of 3HF sensitivity to its environment through modulation of ESIPT make these dyes extremely useful for the development of environment-sensitive fluorescent probes.

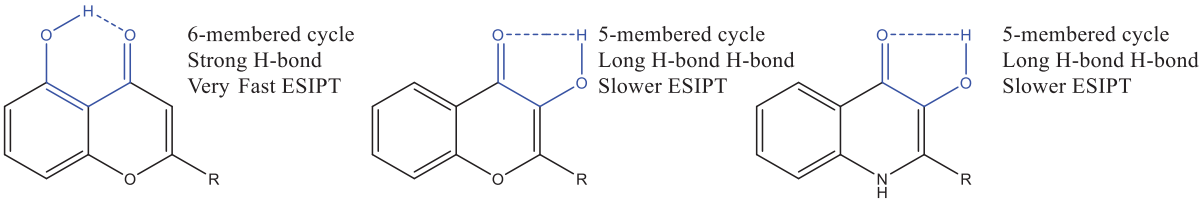

5-hydroxychromone-4 3-hydroxychromone-4 3-hydroxyquinolone-4

Figure 6.5. Structure of 5-hydroxychromone-4, 3-hydroxychromone-4 and 3-hydroxyquinolone-4.

6.3 Solvatochromic effect on ESIPT

Environment and polarity have strong effects on the spectral properties of polar chromophores. These molecules exhibit shifts in their emission maxima (solvatochromic effect) and less frequently changes in their fluorescence quantum yield as a function of polarity and hydration of their environment (Reichardt 1994). In these dyes, upon electronic excitation (S0-S1 transition), the dipole moment increases dramatically because of an intramolecular charge transfer from the electron-donor group to the electron-acceptor group, thus resulting in an asymmetric distribution of charge (**Figure** 6.6).

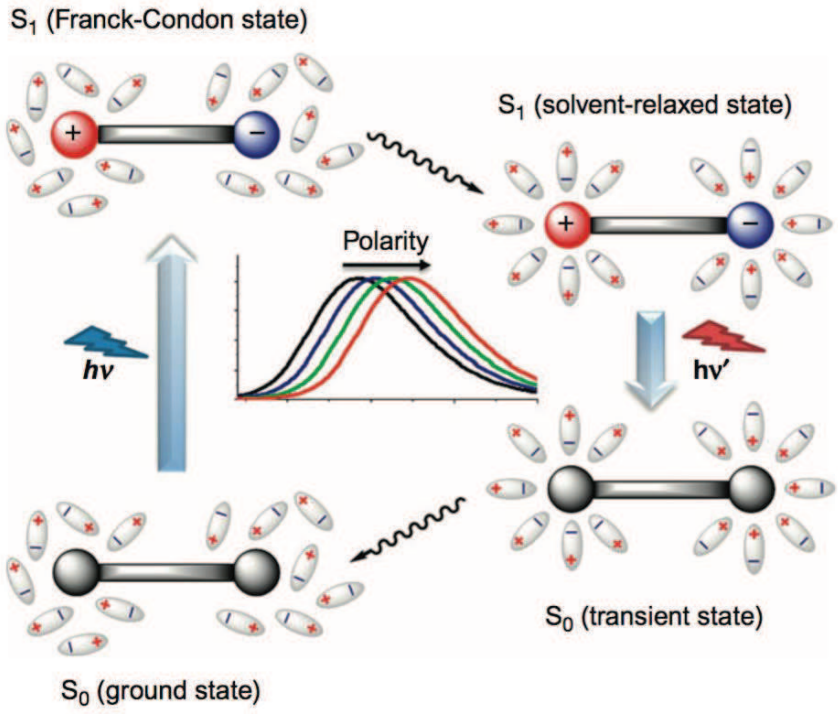

Figure 6.6. Simplified diagram explaining the phenomenon of solvatochromism. **Figure** taken from (Klymchenko & Mely 2013).

As a result, the photoinduced chromophore dipole induces through dipole-dipole interactions the rearrangement of polar solvent molecules. In turn, polarization of solvent molecules around the fluorophore dipole relaxes the excited state to S_1^{solv}. The magnitude of the corresponding energy decrease directly depends on solvent polarity. An increase in polarity results in a red shift of the chromophore emission. In addition, protic solvents which contain hydrogen atoms bound to oxygen (hydroxyl) or to nitrogen (amine, amide) interact with the fluorophore through H-bonding and thus can also decrease the energy of S_1^{solv} state.

The ESIPT dyes provide an alternative mechanism for sensitivity to polarity. In the excited state, solvent relaxation modulates the energetic barrier of the ESIPT reaction, leading to a stabilization of the excited state with the highest dipole moment. This stabilization changes the relative amounts of N* and T* states which could be observed as a change in the ratio of the fluorescence intensities of these bands. Among 3HC derivatives, the 4'-(dialkylamino)-3-hydroxyflavone (3HC-A) and 2-(2-furyl)-3- hydroxychromone (3HC-B) were developed as polarity sensors (**Figure** 6.8**)**.

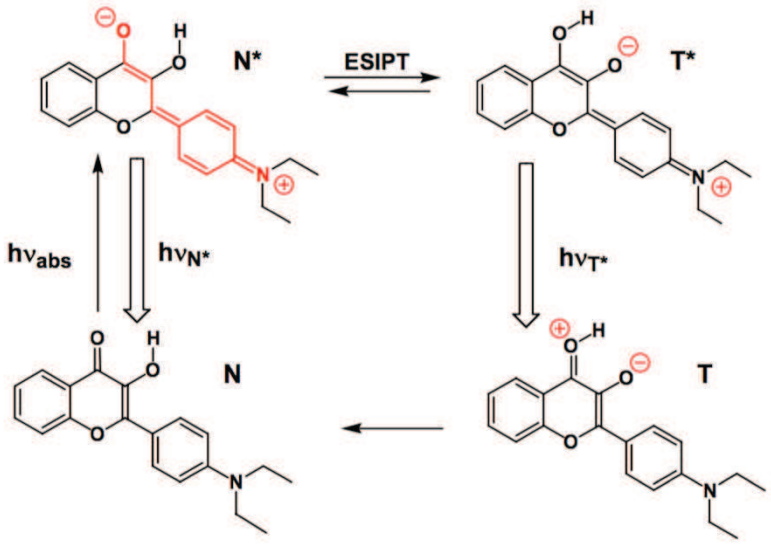

Figure 6.7. Photophysical cycle of 4'-(N,N-diethylamino)-3-hydroxyflavone. On electronic excitation (N→N*), a charge transfer from the 4'-dialkylamino group to the 4-carbonyl takes place followed by an ESIPT process (N*→T*). After T*→T transition, the proton remains at the 4-carbonyl group, producing a zwitterionic T state that rapidly converts into the stable N state. **Figure** taken from (Klymchenko & Demchenko 2003).

The dipole moment of 3HC-A in the N* state is significantly different from that in the T* state due to the 4'-dialkylamino group (**Figure** 6.7**)**. In the excited state, the electron density shifts from the dialkylamino group to the chromone moiety, creating a large dipole moment in the N* state (Klymchenko & Demchenko 2003). Therefore, only the N* state shows dipole-dipole interaction with solvent. This is observed as a red shift together with an increase in the relative intensity of the N* band, because this state becomes energetically more favorable than the T* state (Shynkar et al. 2003). The intensity ratio of the N* and T* bands (N*/T*) was observed to directly represent solvent polarity. However, 3HC-A was found to exhibit dual emission only in low-polar and polar aprotic solvents. For more polar media, the 3HC-B dye is more appropriate. In this dye, the dipole moment of the N* state is relatively low due to its much weaker electron-donor 2-aryl group. Therefore, this state cannot be stabilized even in highly polar aprotic solvents so that its emission is almost negligible. It is suitable for probing polar protic environments characterized by high hydration, which further stabilizes the N* form by H-bonding (see chapter 6.4).

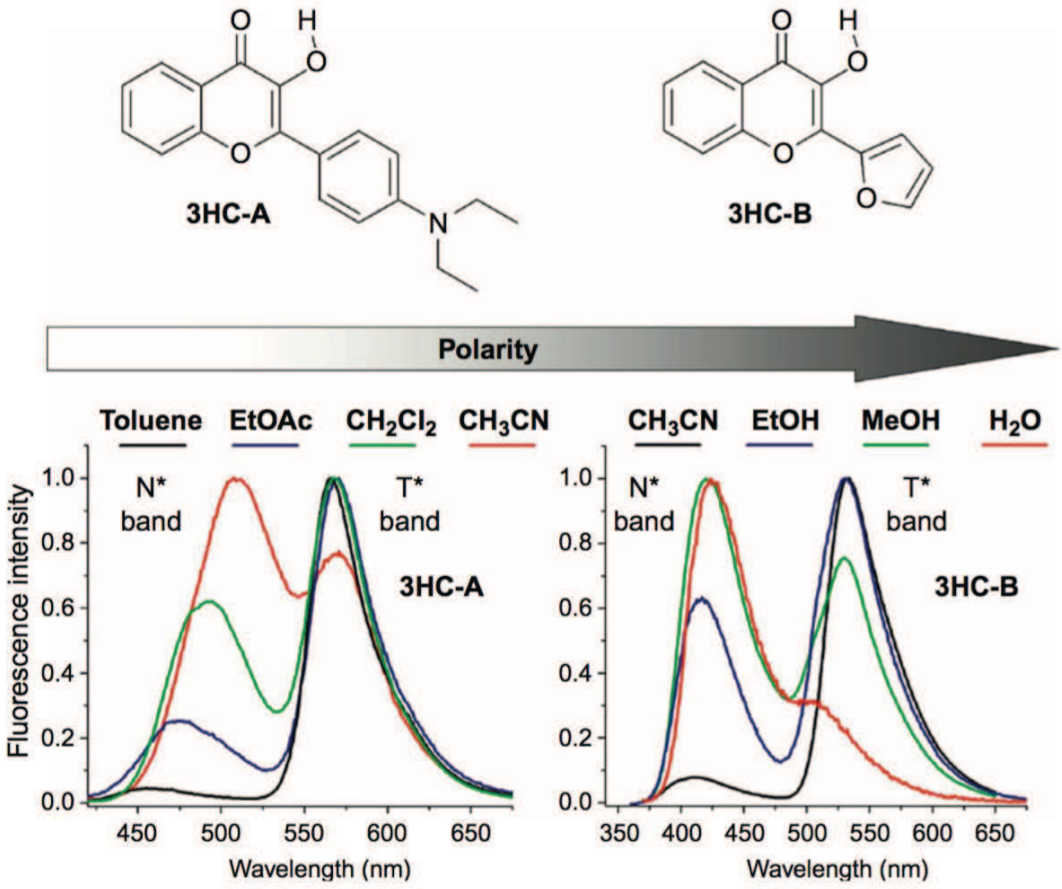

Figure 6.8. Chemical structure of 3HC dyes and their solvent-dependent dual emission. **Figure** taken from (Klymchenko & Mely 2013).

These fluorophores provide a multiparametric response to changes in their environment by changes of band positions and of their relative intensities. This feature allowed to use them as informative probes for investigating conformational changes of proteins (Boudier et al. 2009), peptide-DNA interactions (Shvadchak et al. 2009), protein-protein interactions (Enander et al. 2008) and peptide membrane interactions (Postupalenko et al. 2011).

6.4 H-bonding effect on ESIPT in 3HC

Under some conditions, in addition to the intramolecular hydrogen bond in 3HCs between the hydroxyl group at 3-position and the carbonyl group at 4-position, intermolecular hydrogen bond between carbonyl group and hydrogen atoms from surrounding molecules can occur. In this case, intermolecular hydrogen bonding will compete with intramolecular proton transfer and therefore will affect the N*/T* ratio. This effect was used to quantify the local hydration of the probe (Pivovarenko et al. 2012). Unfortunately, intermolecular H-bonding frequently

inhibits the ESIPT reaction. To prevent this, a 3HF derivative was designed in which an additional benzene ring protects the 4-carbonyl from H-bonding with protic solvent, which allows the ESIPT reaction (5.6-benzo-4'-diethylamino-3-hydroxyflavone) (**Figure** 6.9).

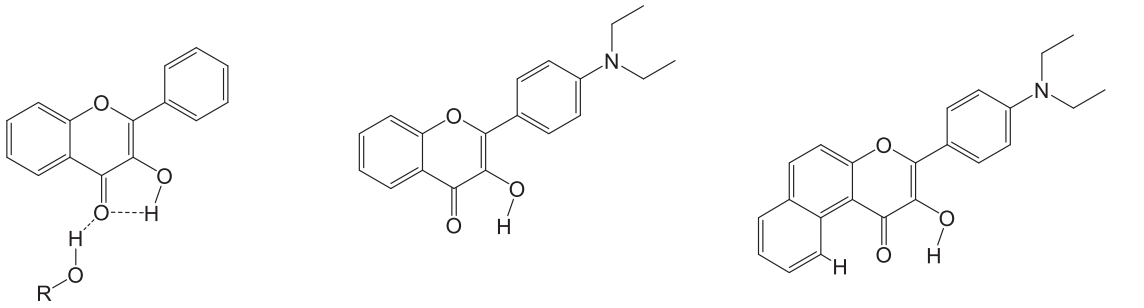

H-bonded 3-hydroxyflavone | 4'-(N,N-diethylamino)-3-hydroxyflavone | 5.6-benzo-4'-diethylamino-3-hydroxyflavone

Figure 6.9. Chemical structure of H-bonded form of 3-hydroxyflavone and of 4'-(N,N-diethylamino)-3-hydroxyflavone without and with protection of the carboxyl group from intramolecular H-bonding by addition of benzene ring**.**

Thus, intermolecular bonding is an additional efficient mechanism modulating the ESIPT reaction of 3HC-based chromophores.

6.5 Electrochromic effect

Proton transfer in ESIPT dyes can be further modulated by an external electrical field. In an external electrical field, the electronic density of the dye is reoriented according to the direction and magnitude of this field. This modified electronic density determines the energy levels of the molecule. In most cases, an applied external electrical field leads to spectral shifts of both absorption and emission spectra (Stark effect). This effect found an important application in the design of probes sensitive to biomembrane potential (Gross et al. 1994). In the dipole approximation, the direction and magnitude of this shift $\Delta\upsilon_{obs}$ depend on the relative distance and orientation between the dipole moment for electronic transition $\Delta\mu$ and the magnitude and direction of the electric field F:

$$h\Delta\upsilon_{obs} = -\frac{1}{\varepsilon} \cdot |\Delta\mu| \cdot |F| \cdot \cos\theta \qquad eq.6.2$$

where θ is the angle between $\Delta\mu$ and F vectors, ε is microscopic dielectric constant which accounts for dielectric screening. When the electric field is created by proximal charges on the probe itself, the Stark effect is considered as an intramolecular phenomenon. In dyes exhibiting an ESIPT reaction, the effect of an external field is more than just shifts in spectral bands as for

usual chromophores. The electric field may affect the energetic barrier of ESIPT (and therefore the rates of ESIPT) and thus, stabilize one of the ESIPT state. An intramolecular Stark effect on ESIPT was demonstrated on derivatives of 3-hydroxyflavone, which contain neutral and positively charged substituents in position 6 of the chromone ring. These compounds were studied in solvents of different polarities (Klymchenko & Demchenko 2002) (**Figure** 6.10**)**.

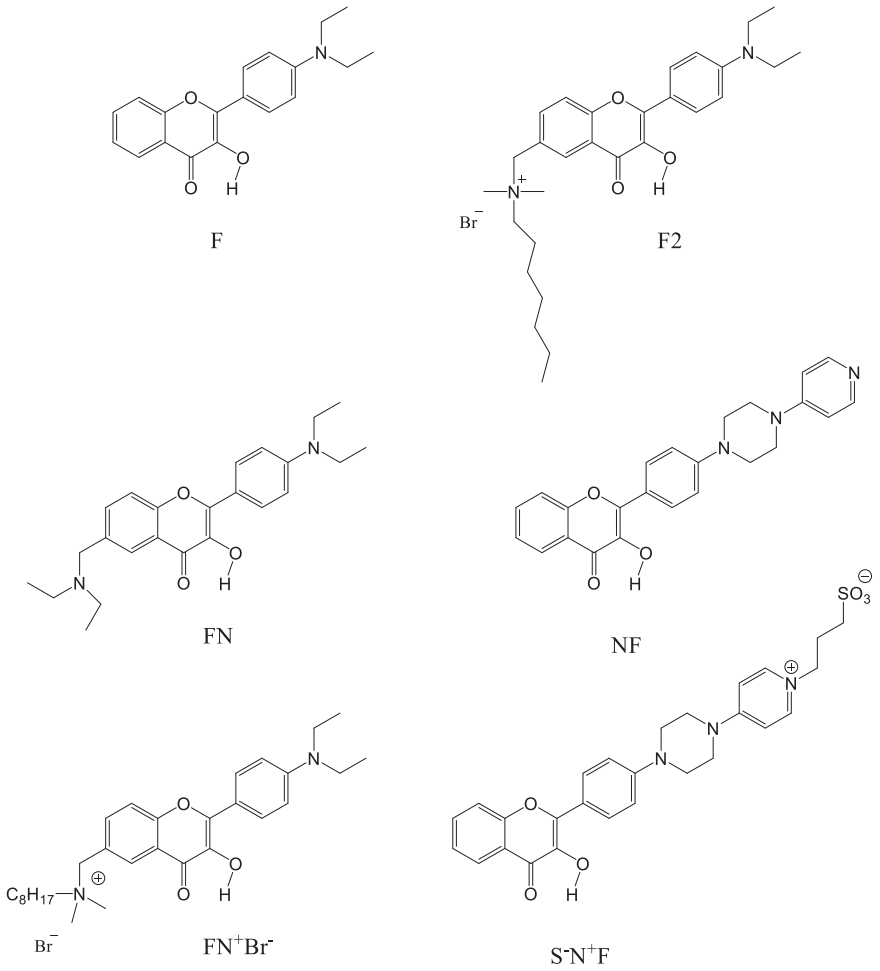

Figure 6.10. Dyes of the 3-hydroxyflavone family sensitive to electrochromic effect (Klymchenko & Demchenko 2002).

For these compounds, the shift in the absorption spectra and of both normal and tautomer emission bands was as predicted by the Stark effect theory (Fig 6.11). Moreover, a dramatic increase in the N*/T* ratio was observed by introducing a positive charge from the left side of the chromone ring, evidencing an intramolecular Stark effect.

Figure 6.11. Fluorescence spectra and chemical structure of FN and F2 dyes.

Varying the position of the added charge, in order to invert the direction of the electric field, was observed to result in opposite spectral changes (Klymchenko et al. 2003). As the ESIPT reaction in 3HF derivatives is very sensitive to electric field perturbations, these derivatives can be used as basic elements in molecular sensors that detect changes in the electric field.

6.6 Anionic form

If the 3HF environment exhibits strong proton-acceptor properties, the 3-OH group can dissociate, yielding a ground-state anionic (proton-dissociated) form. This form is easily excited at the red side of the absorption band, around 410–450 nm. **Figure** 6.12 shows a scheme of energy levels that describes the fluorescence of all three forms of dyes from 3-hydroxyflavone family. This scheme includes six energy levels: the ground N and excited N* levels of the normal form (N), the ground T and excited T^* levels of the tautomeric form (T), and the ground A and excited A^* levels of the anionic form (A). The excited-state A* does not transform into T^* form and emits at 470 nm, in between the emission of the N* and T* forms. 3HF anions can thus be detected by recording absorption/excitation and emission spectra (Arnaut & Formosinho 1993).

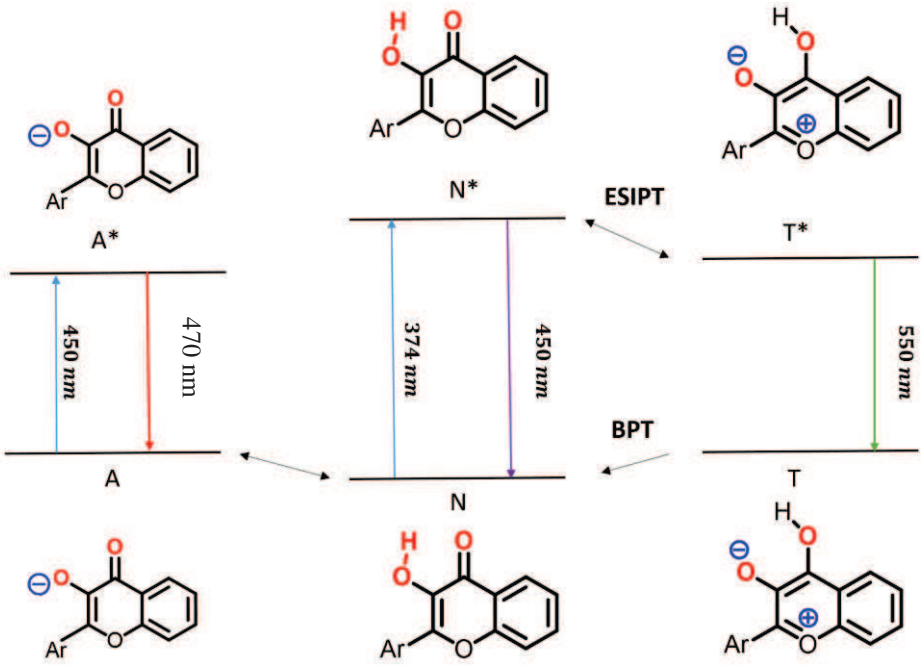

Figure 6.12. Energy diagram of dyes from 3-hydroxyflavone family, where Ar = 2′-deoxyribose.

Fluorescence emission of the A* form has been studied and analyzed in detail for 3-hydroxyflavone (Mandal & Samanta 2003) in methanol and in a mixture of methanol with acetonitrile. The anionic form was also observed in 2-propanol, 1-butanol and ethanol, but was absent in water and in the methoxy derivative of 3HF in the same alcohols (Mandal & Samanta 2003). Time-resolved studies further revealed that the lifetime of the A* form was 2 ns in methanol and 3.7 ns in acetonitrile.

The fluorescence at 470 nm progressively disappears on addition of increasing water concentration (Tomin & Jaworski 2014; Tomin & Javorski 2007). As a result, the fluorescence spectrum of solutions with a rather high concentration of water (1–10 M) shows, again, only the emission of N* and T* forms. Similarly, absorption of A band also disappears upon addition of water molecules (Tomin & Javorski 2007). These data directly point to the disappearance of the A form in the ground state in water, which is known to be an effective donor of protons. Thus, the reactions leading to the formation of the A form in pure acetonitrile and to its disappearance with the addition of water can be written as:

$$\mathbf{3HF} + \boldsymbol{S} \rightarrow \mathbf{3HF^-} + \boldsymbol{SH^+}$$

$$\mathbf{3HF^-} + \boldsymbol{H_2O} \rightarrow \mathbf{3HF} + \boldsymbol{OH^-} \qquad \text{eq.6.3}$$

In the first reaction, the solvent molecules S, which have proton-acceptor properties, form a cation by capturing a proton of the hydroxyl group of 3HF. As a result, the A form of the fluorophore can be observed. On addition of water to the acetonitrile solution, the efficient proton donor H_2O gives a proton to the $\mathbf{3HF^-}$ anion, which transforms then into a neutral molecule.

Thus, it is clear that, to describe the fluorescent properties of 3HF and related molecular compounds, it is necessary to take into account the levels of the A form. In most cases, the role of the A form and the reactions responsible for its formation in pure solvents were disregarded, and the properties of this form remained inadequately studied.

6.7 **Kinetics of ESIPT and Two-State Excited-State Reaction**

The kinetics of ESIPT in non-substituted 3HFs were intensively studied in the 1980s. The first dynamic studies of ESIPT in non-substituted 3HFs by picosecond time-resolved spectroscopy revealed that ESIPT occurs very rapidly, usually in less than 10 ps, and that the kinetic constants of the proton-transfer reaction are temperature-dependent (Sengupta & Kasha 1979; Itoh et al. 2015).

Kinetic two-state models were developed for describing excited-state processes, in particular in the case of intermolecular proton transfer (Birks 1970; Laws & Brand 1979) and intramolecular proton transfer (Woolfe & Thistlethwaite 1981; Itoh et al. 1982). This became possible due to the development of ultrafast time-resolved fluorescence spectroscopy that was suited for measuring the time constants of ESIPT processes (Marks et al. 1997). The ESIPT in 2-(2′-hydroxyphenyl)benzothiazole and in 2-(2′-hydroxy, 5′-methylphenyl)benzotriazole in methylcyclohexane and acetonitrile is extremely fast, showing an estimated time constant of 35 fs (Ameer-Beg et al. 2001). In ethanol, a slower time constant of 60 fs was observed, likely due to the greater strength of the solute-solvent interactions.

Introducing new techniques for measuring the decay curves and new methods for treating the lifetime data allowed revisiting the results of previous experiments and building new concepts.

Picosecond time-resolved fluorescence study of the ESIPT dynamics of dialkylamino-3HF derivatives helped understanding the differences in the spectroscopic properties of dialkylamino -3HFs as compared to their parent 3HF (Shynkar et al. 2003).

In parent 3HF, slow ESIPT kinetics (in the picosecond time range) occurs only in protic solvents where the solvent hydrogen bonding with the dye leads to a high activation barrier. In this case, the reaction is *irreversible* (Strandjord et al. 1983; Strandjord & Barbara 1985). Later, the fluorescence decay kinetics of both the short-wavelength normal (N*) and long-wavelength tautomer (T*) bands of dialkylamino 3HF derivatives were shown to be characterized by the same two lifetime components, which were constant over the whole wavelength range of emission (Shynkar et al. 2003). Meantime, the pre-exponential factor of the short-lifetime component changed its sign, being positive for the N* and negative for the T* emission band. Moreover, the two pre-exponential factors of the T* emission decay were of the same magnitude but opposite in sign. All together, these features pointed to a fast *reversible* two-state ESIPT reaction in dialkylamino 3HFs.

The model which could be used to describe the reversible ESIPT reaction is presented in **Figure 6.13**. In this model, the N* form is the only initially excited species, and its time-dependent evolution involves forward transition to the T* state with a kinetic rate constant k_+, together with radiative and non-radiative decay to the ground N state with kinetic constants k_R^N and k_{nR}^N respectively.

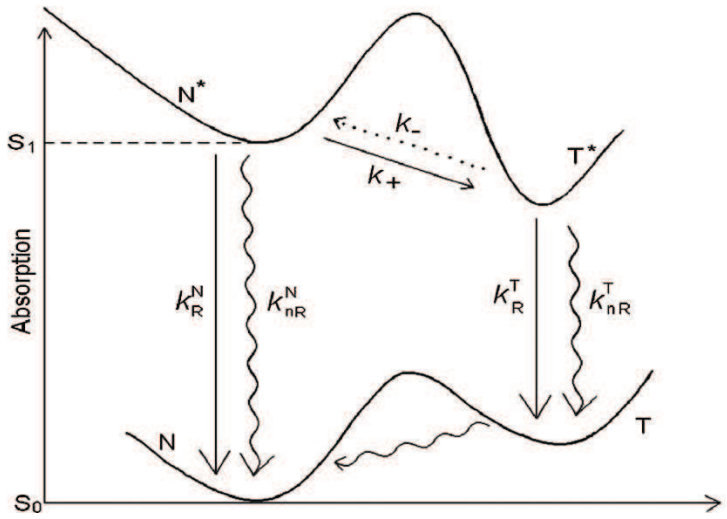

Figure 6.13. An energy diagram of the ESIPT reaction and kinetic processes.

Likewise, the decay of the T* state takes place owing to reverse transition k_- to the N* state and by radiative conversion with constant k_R^T and non-radiative conversion with constant k_{nR}^T to the ground T state. Therefore, kinetic description of the ESIPT reaction includes the determination of six kinetic constants. Interplay of these constants determines the time-dependent and steady-state characteristics of emission of both forms. For the four-level reaction scheme, the differential rate equations for the change in concentration of the N* and T* forms, after excitation by a δ-pulse at t=0, with time are given by: (Zhao & Han 2012) :

$$\frac{dN^*}{dt} = -(k_R^N + k_{nR}^N + k_+)N^* + k_-T^* \qquad eq.6.4$$

$$\frac{dT^*}{dt} = -(k_R^T + k_{nR}^T + k_-)T^* + k_+N^* \qquad eq.6.5$$

Solution of these equations, under the condition of fast establishment of excited-state equilibrium ($k_+;k_- \gg k_R^N, k_{nR}^N, k_R^T, k_{nR}^T$) shows that, in this limit, the two forms will exhibit identical rates of fluorescence decay that will be the weighted average of the decay rates of two excited-state forms (Birks 1970). If this condition is not met, the decay rates will be different.
A detailed kinetic analysis of dialkylamino 3HFs in various solvents enabled the determination of radiative and nonradiative decay rate constants of both N* and T* forms and of forward and reverse rate constants for transitions between them (Shynkar et al, 2003). The ESIPT reaction occurs on the scale of tens of picoseconds and thus is uncoupled with the dielectric relaxation of the solvent occurring at sub-picosecond times. Moreover, the radiative and nonradiative deactivation processes were found to be much slower than the ESIPT reaction, suggesting that the relative intensities of the two emission bands are mainly governed by the ESIPT equilibrium. Therefore, both electrochromic and solvatochromic effects on the relative intensities of the two emission bands in 4′-(dialkylamino)-3-hydroxyflavones resulted from shifts in the ESIPT equilibrium.

VII 3-hydroxychromone based fluorescent nucleotides

The highly sensitive multiparametric response of 3HC probes to their environment make them very promising for investigating biophysical processes, such as base flipping which occur without significant changes in the structure of the interacting partners. Recently 3-hydroxychromone was used for designing the fluorescent nucleotide 2-thienyl-3-hydroxychromone (3HCnt) (Spadafora et al. 2009) (**Figure** 7.1**)**.

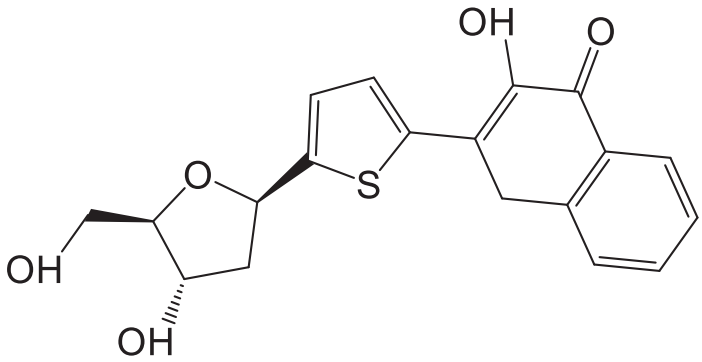

Figure 7.1. **2-thienyl-3-hydroxychromone (Spadafora et al. 2009)**

This DNA base analog was shown to exhibit appreciable quantum yield (from 5 % in buffer to 20% in aprotic solvents) and strong variations of the intensity ratio of its two emission bands in response to environment changes (Spadafora et al. 2009; Dziuba et al. 2012).

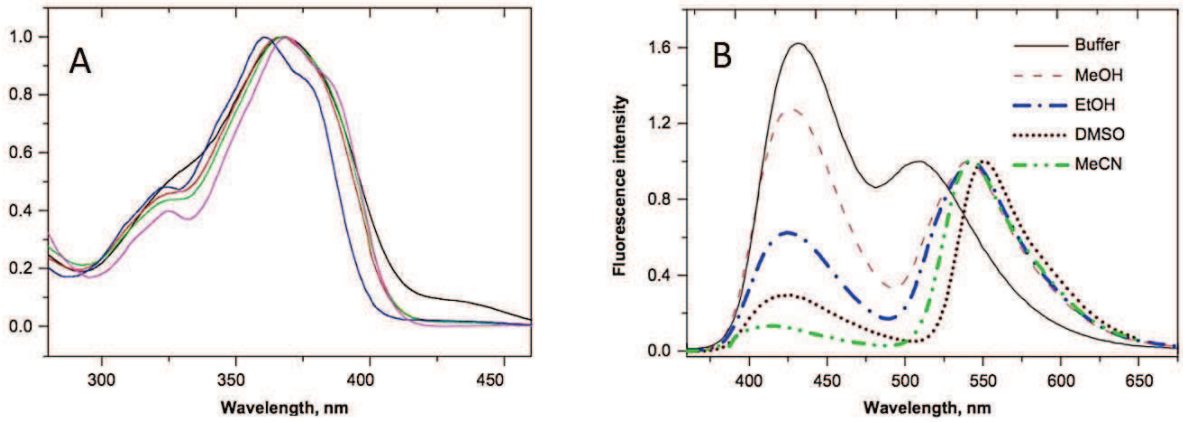

Figure 7.2. Normalized absorption (A) and fluorescence (B) spectra of 3HCnt in different solvents. (Spadafora et al. 2009).

Studies of 3HCnt in DNA duplexes showed that it can substitute any natural base without significant perturbation of the DNA structure. 3HCnt behaves thus as a universal base.

Introduction of 3HCnt in DNAs induced strong changes in its quantum yield and dual emission characteristics as compared to the free 3HCnt in buffer (**Figure** 7.2). In DNA duplexes, the chromophore resides within the DNA helix, being protected from the solvent. This resulted in a low N*/T* ratio and a changed fluorescence. In case when 3HCnt was neighbored by G or C significant quenching of fluorescence was observed. In contrast when T or A were neighbors emission of 3HCnt was comparable with or higher with emission observed for free nucleotide and the brightness of 3HCnt was up to 50-fold higher than for 2Ap (Dziuba et al. 2012).

Figure 7.3. Fluorescence spectra of a 3HCnt-labeled DNA duplex in the absence (red) and in presence of NCp7 (black dashed) peptide.

The potency of 3HCnt for DNA/Protein interaction studies was demonstrated by the interaction of a 3HCnt-labeled DNA duplex with the NCp7 protein of HIV-1 (Dziuba et al. 2012) (**Figure** 7.3). Binding of the NCp7 peptide to the labeled DNA leads to an increase in N*/T* ratio due to the insertion of its folded finger motifs between the bases, increasing the environment polarity of 3HCnt.

Moreover, in a comparative study of 3HCnt with commonly used fluorescent nucleotides (2-aminopurine, pyrrolocytosine, 1,3-diaza-2-oxophenoxazine) it was found that the multiparametric response of 3HCnt provided the most detailed information on the DNA structural transitions during interaction with endonuclease VIII (from Escherichia coli (Nei)) (Kuznetsova et al. 2014). Moreover, stopped flow kinetics studies showed that 3HCnt but not

2Ap is able to properly report on the kinetics steps of Endonuclease VIII activity. Thus, it was possible with 3HCnt to complement the mechanism of Endonuclease VIII.

3HCnt demonstrates all the advantages of wavelength-dependent ratiometric detection, including a large separation between the two emission bands and a dramatic variation of their relative contributions. Moreover, the high sensitivity of the dual emission of this nucleotide to the polarity of the environment, makes it highly sensitive to the interaction with its flanking bases and its accessibility to water molecules. Therefore, this base is a highly promising tool for DNA research.

Objectives of the thesis

The aim of this work was to use fluorescence-based tools to investigate the dynamics of UHRF1-induced base flipping in hemimethylated DNA duplexes. Despite the large variety of tools and methods used to study DNA methylation patterns, most of them are not suited to monitor dynamic aspects. In the context of the DNMT1/UHRF1 tandem, the flipping of mC is a key and distinctive process. Therefore, a careful investigation of its underlying mechanism appears crucial for a better understanding of the role of the DNMT1/UHRF1 tandem, and for providing new clues to inhibit it in various diseases. To reach this end, the most suitable technique is likely fluorescence spectroscopy, which is well suited to monitor molecular events in real time. However, this method relies on fluorescent probes that should allow to sensitively monitor the process of interest without perturbing the system. This is especially challenging for the interaction of the SRA domain of UHRF1 with hemi-methylated DNA, since base flipping induced minute changes in the DNA structure. In addition, substitution of any natural nucleobase by a fluorescent one could alter the proper recognition of the DNA, as well as the flipping process. Herein, we used three fluorescent nucleotide analogues to monitor base flipping. The first one, 5-methyl-2-pyrimidinone, m5k, a fluorescent analogue of mC was found insensitive to the interaction with SRA. A second one, 8-vinyl-2'-deoxyguanosine, a fluorescent analogue of G was used to replace G in the CpG recognition motif. Though, it showed some sensitivity on UHRF1 binding, it does not show any difference between HM and NM duplexes. The third one was the recently developed 3HCnt, which behaves as a universal nucleobase and shows exquisite sensitivity to changes in its environment. In contrast to the two first nucleotide analogues and to 2Ap, the 3HCnt was found to show much stronger spectroscopic changes in HM duplexes as compared to the corresponding NM duplexes, when included at strategic positions close to the central CpG recognition site. These stronger spectroscopic changes were unambiguously attributed to mC flipping. The kinetics of base flipping was also characterized by stopped-flow techniques, providing insights in the mechanism of DNMT1 recruitment by UHRF1. In addition to advancing the mechanistic understanding of UHRF1 in the replication of DNA methylation patterns, it also provides a platform for developing screening assays targeting UHRF1.

VIII MATERIALS AND METHODS

8.1 Fluorescent nucleotide analogues

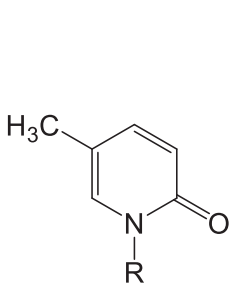

5-methylpyrimidin

M5k

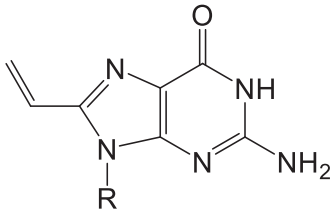

8-Vinyl-2'-deoxyguanosine

8VdG

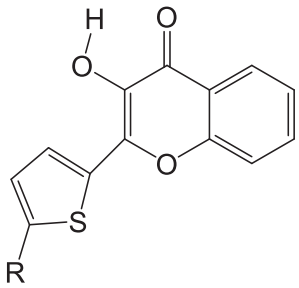

2-thyenil-3-hidroxychromone

3HCnt

Figure 8.1. Chemical structures of the fluorescent nucleotide analogues used in this study

8.2 SRA binding domain (408-643) of UHRF1 protein

Wild-type SRA (**Figure** 8.2) and three SRA mutants (**Figure** 8.3-8.5) were used in this study.

GHM ^{408}KEC TIVPS NHYGP IPGIP VGTMW RFRVQ VSESG VHRPH VAGIH GRSND GAYSL VLAGG YEDDV DHGNF FTYTG SGGRD LSGNK RTAEQ SCDQK LTNTN RALAL NCFAP INDQE GAEAK DWRSG KPVRV VRNVK GGKNS KYAPA EGNRY DGIYK VVKYW PEKGK SGFLV WRYLL RRDDD EPGPW TKEGK DRIKK LGLTM QYPEG YLEAL ANRER EKENS KREEE EQQEG GFASP RTG^{643}

Figure 8.2. Sequence of SRA domain of UHRF1

GHM ^{408}KEC TIVPS NHYGP IPGIP VGTMW RFRVQ VSESG VHRPH VADIH GRSND GAYSL VLAGG YEDDV DHGNF FTYTG SGGRD LSGNK RTAEQ SCDQK LTNTN RALAL NCFAP INDQE GAEAK DWRSG KPVRV VRNVK GGKNS KYAPA EGNRY DGIYK VVKYW PEKGK SGFLV WRYLL RRDDD EPGPW TKEGK DRIKK LGLTM QYPEG YLEAL ANRER EKENS KREEE EQQEG GFASP RTG^{643}

Figure 8.3. Sequence of the G448D SRA mutant. The glycine at position 448 was replaced with aspartic acid (highlighted with red color).

GHM [408]KEC TIVPS NHYGP IPGIP VGTMW RFRVQ VSESG VHRPH VAGIH GRSND GAYSL VLAGG YEDDV DHGNF FTYTG SGGRD LSGAK RTAEQ SCDQK LTNTN RALAL NCFAP INDQE GAEAK DWRSG KPVRV VRNVK GGKNS KYAPA EGNRY DGIYK VVKYW PEKGK SGFLV WRYLL RRDDD EPGPW TKEGK DRIKK LGLTM QYPEG YLEAL ANRER EKENS KREEE EQQEG GFASP RTG[643]

Figure 8.4. Sequence of the N489A SRA mutant. The asparagine at position 489 was substituted with alanine (highlighted with red color).

GHM [408]KEC TIVPS NHYGP IPGIP VGTMW RFRVQ VSESG VHRPH VAGIH GRSND GAYSL VLAGG YEDDV DHGNF FTYTG SGGRD LSGNK ATAEQ SCDQK LTNTN RALAL NCFAP INDQE GAEAK DWRSG KPVRV VRNVK GGKNS KYAPA EGNRY DGIYK VVKYW PEKGK SGFLV WRYLL RRDDD EPGPW TKEGK DRIKK LGLTM QYPEG YLEAL ANRER EKENS KREEE EQQEG GFASP RTG[643]

Figure 8.5 Sequence of the R491A SRA mutant. The arginine at position 491 was replaced with alanine (highlighted with red color).

8. 3 Production and purification of the SRA

The SRA domain of UHRF1 (residues 408-643) and its mutants was expressed and purified in Escherichia coli BL21-pLysS (DE3) 3839 (Delagoutte et al. 2008) by the team of Catherine Birck of the Department of Structural Biology Integrative of IGBMC.

8.4 Storage of the SRA

For long-term storage of SRA, the method of shock freezing - also called 'snap freezing' - of the protein solution was used with addition of Glycerol as cryoprotectant. The solution of SRA protein was frozen by immersing aliquots (150 µL) into liquid nitrogen. Then, the samples were stored at -20°C. The storage buffer was PBS 20 mM, pH 7.5, NaCl 50mM, 2.5 mM TCEP (Tris(2-carboxyethyl)phosphine), 5% glycerol.

8.5 Buffer exchange of the SRA

The SRA stock solution was thawed by incubation at 37 °C with gentle shaking. It was then added to 15 mL of 20mM PBS, pH 7.5, NaCl 50mM, TCEP 2.5 mM, 1 mM EDTA

(Ethylenediaminetetraacetic acid). For the buffer exchange, Amicon Ultro-15 centrifugal Filters were used. The filters were loaded in the centrifuge Sigma3k10 (Avantec) equipped with the Nr11133 rotor. The speed was set to 4500 rpm for 30 minutes with resuspension of the solution each 5 minutes. The procedure was repeated several times to achieve a 10 000- fold dilution of the initial buffer.

8.6 DNA samples

The 12-bp duplex sequence was 5'-GGGCCXGCAGGG-3'/5'-CCCTGCGGGCCC-3' with a single CpG site that was either non-methylated (X = C) or hemi-methylated (X = 5mC). Unmodified oligonucleotides (DNAs) were synthesized and HPLC-purified by IBA GmbH Nucleic Acids Product Supply (Germany). The M5k and 3HCnt nucleotides were introduced by solid-phase chemistry in the DNAs by the team of Alain Burger (Nice Institute of Chemistry) (Dziuba et al. 2012).

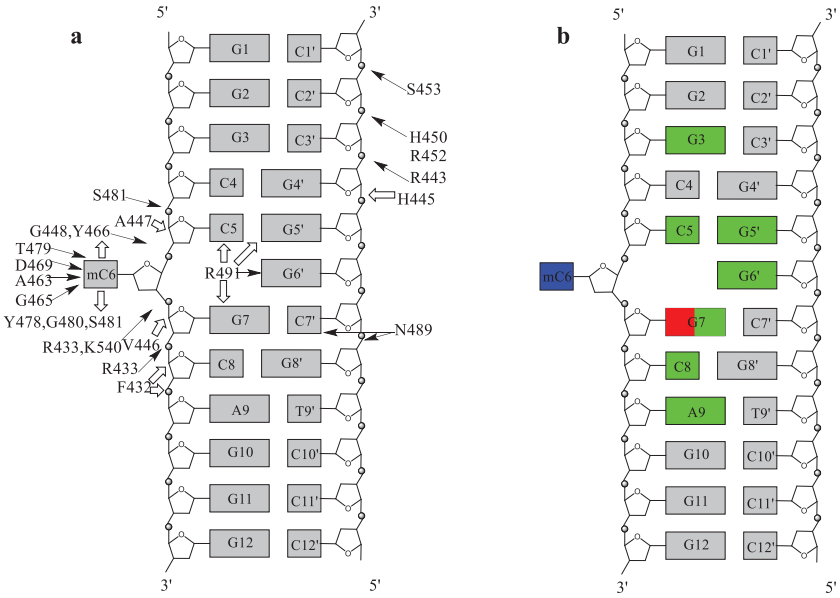

Figure 8.6. Structure of the duplex: (a) The interactions of the duplex with SRA amino acids, as determined by X-ray crystallography are indicated by arrows. Hydrogen bonding and van der Waals interactions are indicated by black and white arrows, respectively. (b) Positions substituted by M5k, 8VdG and 3HCnt are highlighted in blue, red and green respectively.

The 8VdG and DNAs labelled by 8VdG were produced by the team of Ulf Diederichsen (Institute of Organic and Biomolecular Chemistry, Göttingen University).

The oligonucleotides were labelled at the positions indicated in **Figure 8.6**. The lyophilized calf thymus DNA (ctDNA) was purchased from Sigma Aldrich.

8.7 Storage and reconstitution of the DNA samples

The lyophilized DNAs were stored at -20 ^{o}C and solubilized in distilled water. Extinction coefficients between 85,500 and 107,300 $M^{-1}cm^{-1}$ were used to determine the concentrations of the duplexes at 260 nm. The lyophilized calf thymus DNA (ctDNA) was reconstituted overnight at 10^{o}C and its molar concentration, expressed in nucleotides, was determined from its absorption at 260 nm using an extinction coefficient of 6600 M^{-1} cm^{-1} (Reichmann et al. 1954).

8.8 Hybridization of the DNA

The duplexes were prepared by mixing the complementary strands in equal molar amounts in PBS 20 mM, pH 7.5, NaCl 50 mM, EDTA 1 mM buffer and annealing them by heating to 90°C for 5 min, followed by cooling down to room temperature at a cooling speed of 0.7°C/min. Duplex samples were then kept at +4°C for a few weeks.

8.9 Experimental conditions for studies of SRA/DNA interaction

Spectroscopic measurements of the SRA/DNA interaction were performed at 20 ^{o}C in PBS 20 mM, pH 7.5, NaCl 50mM, TCEP 2.5 mM, 1 mM EDTA, PEG 0.05%.(so-called Spectroscopic Buffer). The working buffer was stored no longer than one week at +4^{o}C. TCEP was used to prevent formation of disulfide bonds between proteins. Compared to the other two most common agents used for this purpose (dithiothreitol and β-mercaptoethanol), TCEP has several advantages: being odorless, a more powerful and irreversible reducing agent, more hydrophilic and more resistant to air oxidation (Rüegg & Rudinger 1977). EDTA was used to chelate trace ions in solution to avoid their binding to DNA (Hart 2000). Polyethylene glycol 20 000 (PEG) was used to prevent adsorption of the SRA to quartz walls of cuvettes.

8.10 UV-visible absorption spectroscopy

Absorption spectra were recorded on a Cary 400 spectrophotometer (Varian) using a dual beam mode with slits set to 1nm. The measurements were performed in thermostated quartz cuvettes with 1 cm optical path. The spectra were recorded in 230 nm to 550 nm range. The Beer-Lambert equation was used to calculate molar concentrations in solution:

$$A = \varepsilon C l \qquad eq.8.1$$

where l is the optical path, C the molar concentration, ε the extinction coefficient at a given wavelength, A the absorption measured at this wavelength. For used DNAs, ε values in the range between 85,500 and 107,300 $M^{-1}cm^{-1}$ were used to determine the concentrations of the duplexes at 260 nm. Extinction coefficient of 45890 $M^{-1}cm^{-1}$ was used to determine the concentration of the proteins at 280 nm. All measurements were performed in spectroscopic buffer.

8.11 DNA stability measurements

The hydrogen bonds in DNA double helix are broken during heating, so that DNA duplexes are dissociated. This phenomenon is referred to as "melting". The absorption at 260 nm is measured as a function of increasing or decreasing temperature (**Figure** 8.7a). At the melting temperature (Tm), the ratio of double stranded to single stranded DNA is unity. Tm is an index of the thermal stability of a duplex, and is dependent on the base sequence, number of nucleotides, nucleic acid concentration, solvent conditions (salt composition, organic solvent composition, pH), presence of mismatch (non-complementary base pairs) and nucleotide analogues. Measurements were performed in the spectroscopic buffer, without PEG and TCEP.

Melting curves (2 µM concentration of each strand) were recorded by following the temperature-dependence of the absorbance changes at 260 nm on a Cary 400 spectrophotometer (Varian) equipped with a Peltier thermostated cell holder. The optical path length of the cell was 1 cm. The temperature range was 20 – 80° C, with a heating speed of 0.5°C/min. The values of melting temperatures were extracted from the fit of the first derivative of the melting curves by a Gaussian function (Breslauer 1995) (**Figure** 8.7b).

Figure 8.7. DNA melting, as monitored by absorption spectroscopy. (a) Hyperchromicity of DNA expressed as $h(\%) = 100\frac{A_{ss}-A_{ds}}{A_{ds}}$, where A_{ss} and A_{ds} are the absorbance of single- and double-stranded DNAs, respectively. (b) First derivative of melting curve (black dots) and Gaussian fit (red line).

8.12 Steady-state fluorescence spectroscopy

Fluorescence spectra were recorded at 20°C on a FluoroLog spectrofluorometer (Jobin Yvon) equipped with a thermostated cell compartment. Spectra were corrected for buffer fluorescence, lamp fluctuations, and detector spectral sensitivity. Excitation wavelength was 315 nm for M5k and 8vdG and 374 nm for 3HC. The SRA/DNA interaction was studied first by recording the fluorescence spectra of labelled DNA free in solution and then after, addition of either the SRA wild type or its mutants. Measurements were performed in the spectroscopic buffer.

Quantum yield of the labelled duplexes in the absence or presence of SRA proteins were determined by using 2Ap as a reference (QY = 0.68 in buffer) for DNAs labelled by M5k and 8vdG and quinine sulfate (QY = 0.577 in 0.5 M H2SO4) for 3HCnt-labelled duplexes. Measurements were performed using SRA concentrations ensuring that at least 80% of the 3HCnt-labeled duplexes are bound to SRA.

Quantum yield was calculated as:

$$QY = \frac{I}{I_{ref}}\frac{A_{ref}}{A}\cdot QY_{ref} \qquad eq.8.2$$

where QY is the sample quantum yield, I and A are the integrated intensity and absorbance at the excitation wavelength of the sample, I_{ref} and A_{ref} are the integrated intensity and absorbance of the reference. QY_{ref} is the quantum yield of the reference. Eq.8.2 applies if the sample and the reference are in the same solvent.

8.13 Determination of the binding parameters by fluorescence anisotropy measurements

When molecule is excited with a vertically polarized light, only those fluorophores that have their absorption dipoles oriented parallel to the electric field vector of the incident radiation are excited. This phenomenon is commonly known as photoselection (Lakowicz 2006). Fluorescence intensity is collected at right angles (**Figure** 8.8) to the incident beam through a polarizer oriented either parallel ($I_{\parallel}$) or perpendicular ($I_{\perp}$) to the electric field vector of the exciting light.

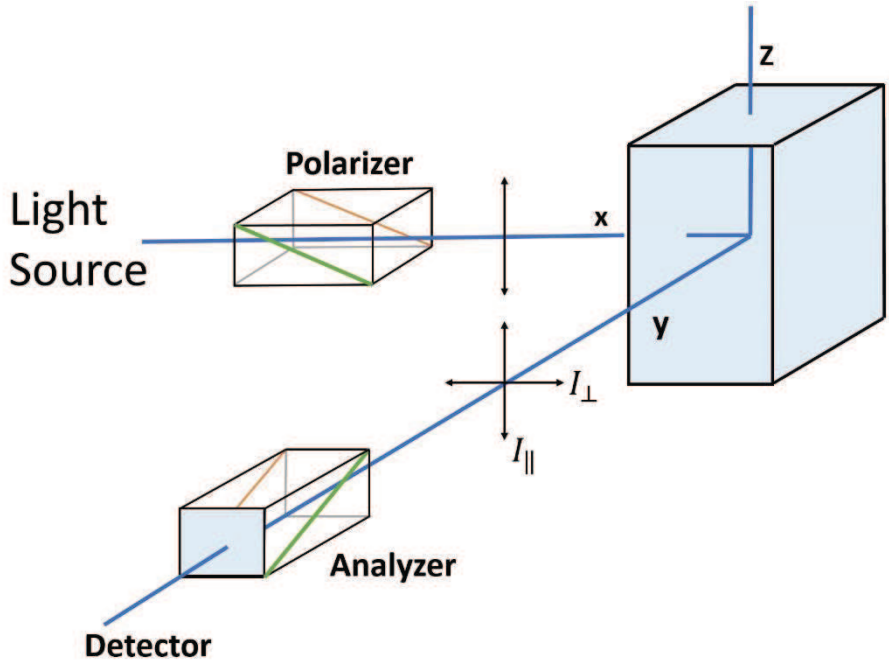

Figure 8.8. Schematic diagram for fluorescence anisotropy measurement. The sample is excited with a vertically polarized light. The electric vector of the excitation light is oriented parallel to the vertical axis. The intensity of the emission is measured through a polarizer. When the emission polarizer is oriented parallel (||) to the direction of the polarized excitation, the

observed intensity is called $I_{\parallel}$. Likewise, when the polarizer is perpendicular ($\perp$) to the excitation, the intensity is called $I_{\perp}$.

Fluorescence anisotropy (r) is defined as:

$$r = \frac{I_{\parallel} - I_{\perp}}{I_{\parallel} + 2I_{\perp}} \qquad eq.8.3$$

The anisotropy values are additive, which considerably simplifies theoretical expressions for ligand binding.

The intrinsic anisotropy (r_0) is obtained in the absence of molecular motion and depends on the probability of excitation by polarized light beam (photoselection) and on the angle between the absorption and emission dipoles:

$$r_o = \frac{2}{5}\left(\frac{3cos^2\alpha - 1}{2}\right) \qquad eq.8.5$$

The term $\frac{2}{5}$ results from the probability of photoselection and α is the angle between the excitation and emission dipoles. Hence, r_o can range from 0.4 (α =0°) to -0.2 (α = 90°) and frequently, depends on the excitation wavelength.

The observed steady-state anisotropy (r) is a function of r_o , the rotational correlation time (φ) and the fluorescence lifetime (τ) of the fluorophore according to the Perrin equation:

$$\frac{r_o}{r} = \left(1 + \frac{\tau}{\varphi}\right) \qquad eq.8.6$$

The anisotropy (r) is most sensitive to changes in rotational motion if the values of τ and φ are in the same order of magnitude. If $\varphi \gg \tau$, no substantial depolarization will be observed because the fluorescence intensity will decay before any measurable motion occurs and then r will approach r_o . If $\varphi \ll \tau$, the orientation of the fluorophore will be random before any decay of fluorescence occurs, and r approaches zero.

Rotational diffusion could be expressed as the rotational diffusion coefficient (D_{rot}), which is related to the rotational correlation time as $\varphi = 1\frac{1}{6}D_{rot}^{-1}$. From the Stokes-Einstein relation of diffusion, the rotational correlation time of a sphere may be described as:

$$\varphi = \frac{V\eta}{RT} \qquad eq.8.7$$

where V is the hydrated molecular volume of the rotating species, η the viscosity of the solution, R the gas constant, and T the absolute temperature. This dependence allows monitoring the binding of ligands by measuring the anisotropy.
The bound fraction (v) could be calculated as:

$$v = \frac{r - r_F}{(r - r_F) + R(r_B - r)} \qquad eq.\,8.8$$

where r_F and r_B are the anisotropies of the free and bound forms, respectively. R is ratio of the intensities of the bound and free forms.

Anisotropy measurements of 3HCnt labelled DNA were performed at 20°C on a FluoroLog 3 spectrofluorometer (Jobin Yvon) equipped with a thermostated cell compartment. Measurements were performed in the spectroscopic buffer. Anisotropy values were obtained by averaging 10 consecutive measurements. The affinity of the wild-type SRA and its mutants to labeled DNAs was obtained by titrating a fixed amount of 3HCnt-labeled duplex by the protein and monitoring the fluorescence intensity and anisotropy signals, simultaneously. The affinity constants were determined by fitting the fluorescence anisotropy changes to the following equation:

$$r = \frac{vRr_t - r_d(v-1)}{1+Rv-v} \qquad eq.\,8.9$$

where r and r_t are the anisotropy values at a given and a saturating SRA concentration respectively, r_d is the anisotropy in the absence of protein. R is the ratio of the QYs of the bound to free forms, K_a is the apparent affinity constant, ν is the fraction of bound SRA calculated as:

$$v = \frac{(K_a^{-1}+nL_t+P_t) - \sqrt{(K_a^{-1}+nL_t+Pt)^2 - 4nP_tL_t}}{2L_t} \qquad eq.\,8.10$$

where P_t and L_t are the concentrations of SRA and duplexes, respectively, and n is the number of SRA proteins bound per duplex (Lakowicz 2006; Rochel et al. 2011).

8.14 Isothermal titration calorimetry (ITC)

8.14.1 Physical meaning of the main thermodynamic parameters

Heat is one the most important physical quantities in biology. Biological systems and processes are highly heat-sensitive and will only function in relatively narrow temperature ranges. These ranges are largely defined by the effect of temperature on chemical processes and by the sensitivity of biopolymer structure to heat. Processes in which occurs heat exchange could be described by thermodynamic parameters

8.14.2 Enthalpy

The energy produced or absorbed by a reaction is called the change in enthalpy, ΔH. In endothermic reactions the enthalpy value, H, of the product is higher than that of the reactants while in exothermic reactions, it is the opposite. Enthalpy is defined as:

$$H = U + pV \qquad eq.8.11$$

where U is the internal energy of the molecule and V its volume at pressure, p. At constant pressure ($p = const$) ΔH can be directly determined in an isobaric calorimeter by direct measurement of reaction quantity of heat (q).

8.14.3 Entropy

Entropy (S) is another inherent thermodynamic parameter of all molecules including biomolecules. It expresses the level of disorder or randomness in the molecule or process. The Second Law of Thermodynamics states that a system will always undergo spontaneous change in such a way as to increase entropy. This is especially relevant to bio-macromolecules and more generally to biological systems, since these are unusually highly ordered and therefore constantly show a natural tendency to adopt more random forms.

Absorption of heat by a chemical system results in an increase in disorder and hence an increase in entropy (ΔS). This value is the ratio of the heat absorbed to the absolute temperature:

$$\Delta S = \frac{q}{T} \qquad eq.8.12$$

If T remains constant, such a process is isothermal. A consequence of the Second law of Thermodynamics is that ΔS_{total} for a spontaneous process must be greater than 0 where ΔS_{total} is the sum of the ΔS for the specific system plus the ΔS of its surroundings. If the reaction is exothermic, the system loses enthalpy to its surroundings. If the surroundings are sufficiently large, this does not result in an increase in temperature, then:

$$\Delta S_{total} - \frac{\Delta H}{T} > 0 \qquad eq.8.13$$

Thus, spontaneous reactions will occur generally when ΔH < T ΔS. Endothermic reactions will occur provided the ΔS value is sufficiently large to make TΔS greater than ΔH.

8.14.4 Free Energy

At given conditions, all molecules have different amounts of a specific type of energy defined as the energy available to do work, called the Gibbs free energy. Spontaneous chemical reactions always result in a decrease in G:

$$\Delta G = \Delta H - T\Delta S < 0 \qquad eq.8.14$$

8.14.5 Principle of isothermal titration calorimetry

ITC may be used directly to measure ΔH changes associated with processes such as ligand binding and complex formation. The principle of ITC measurements is shown on **Figure** 8.9. A typical experiment involves measurement of heat change as a function of the addition of small quantities of a reagent to the calorimeter cell containing other components of the system under investigation. For example, this reagent could be a protein ligand or substrate/inhibitor of an enzyme. At the beginning of the experiment, there is a large excess of protein compared to ligand. This means that ΔH values associated with each aliquot can be individually measured. Initially, these values are large but, as aliquots are progressively added, they decrease to values similar to the ΔH of dilution of ligand into the solution in the calorimeter cell. The ΔH measured is the total enthalpy change, which includes heat associated with processes such as formation of noncovalent bonds between interacting molecules and with other equilibria in the system such as conformational changes, ionization of polar groups (e.g. deprotonation) and changes due to interactions with solvent. Frequently, the results are reported as 'apparent ΔH' and compared to other experiments performed under identical conditions to allow identification of specific effects.

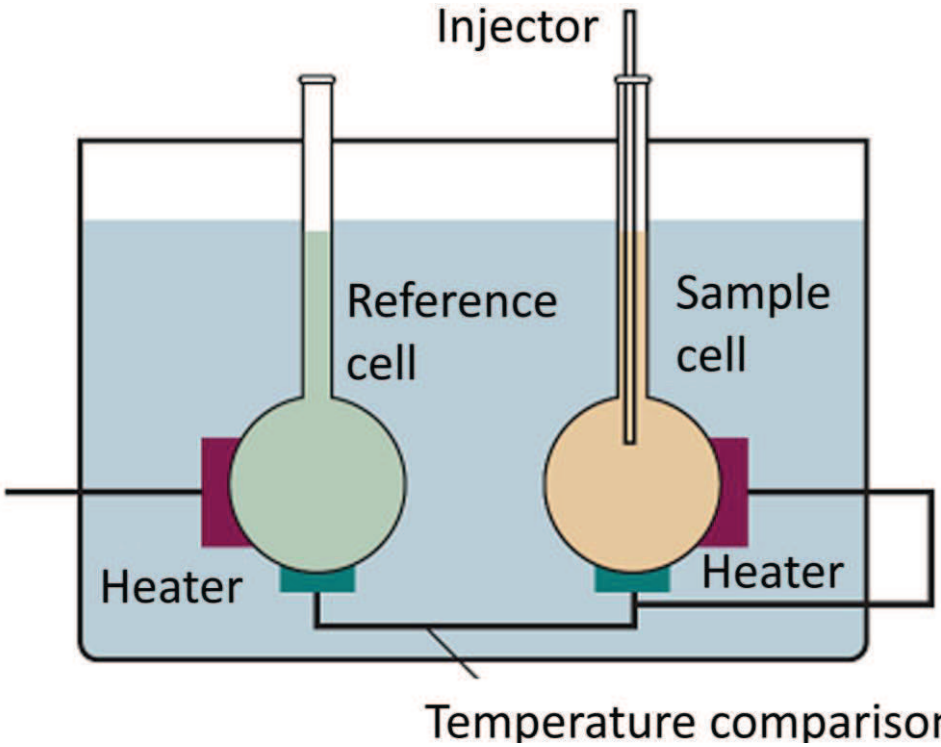

Figure 8.9. Schematic diagram for ITC measurement. Addition of a substance such as a protein ligand into the sample cell causes either a release or an absorption of a small amount of heat. This heat is compensated by the amount of heat produced by the "Heater" to thermo-stabilize both cells. This is electrically detected and analyzed. Several injections are made during a typical experiment.

8.14.6 ITC for stoichiometry determination

ITC provides a useful method for studying binding of a protein (P) to a ligand (L):

$$P + L \leftrightarrow PL \qquad eq.8.15$$

The dissociation constant (K_D) could be calculated as:

$$K_D = \frac{[P][L]}{[PL]} \qquad eq.8.16$$

K_D is related to ΔG by:

$$\Delta G = -RT\ lnK_D \qquad eq.8.17$$

Because the ΔH for the binding interaction decreases as the system approaches equilibrium, it is a sensitive probe for the extent of the binding interaction. Subtraction of heats of dilution gives a binding isotherm which can be used to calculate K_D. It is possible for binding of two individual ligands to a single protein to have similar K_D values (and consequently similar ΔGs

(Equation 8.17)) but quite different ΔH and ΔS values. ITC allows a direct determination of ΔH and therefore helps to confirm detailed differences in binding thermodynamics.

8.14.7 Experimental conditions of ITC experiments with SRA/DNA

The affinity of SRA to non-labeled DNA was determined by Isothermal titration calorimetry. The heat exchanged for the interaction of SRA with the hemimethylated duplex was analyzed in the spectroscopic buffer (without PEG) with a VP ITC microcalorimeter (Microcal, Northampton, MA, USA). Titration of SRA by the hemi-methylated duplex was performed by monitoring under constant stirring (310 rpm) the thermal power generated by repeated injections of 4 µL aliquots (in 4 min) of 40 µM DNA contained in the syringe into a 6 µM SRA solution contained in the 1.42 mL cell compartment of the instrument. The total heat resulting from an injection of titrant was calculated as the integral versus time of the experimental signal. A control experiment in which DNA was titrated into the buffer alone was done to determine the heat of dilution. Instrument control, data acquisition, and analysis were done with the VPViewer and Origin software provided by the manufacturer.

8.15 Stopped flow spectroscopy

The scheme of a stopped-flow apparatus is shown on **Figure** 8.10. The apparatus allows the rapid mixing of two or more solutions, which then flow into an observation cell while the previous contents are flushed and replaced with freshly mixed reactants. A stop syringe is used to limit the volume of solution expanded with each measurement and also serves to abruptly stop the flow and to trigger simultaneously the acquisition of the signal. The reaction is followed as the solution ages after flow stops. The time resolution of the method is limited by the time required for the reactants to flow from the point of mixing to the point of observation; this “dead time” is typically on the order of 1-4 ms. Thus half of the signal is lost at rates of 180 s^{-1} (4 ms dead time) to 700 s^{-1} (1 ms dead time).

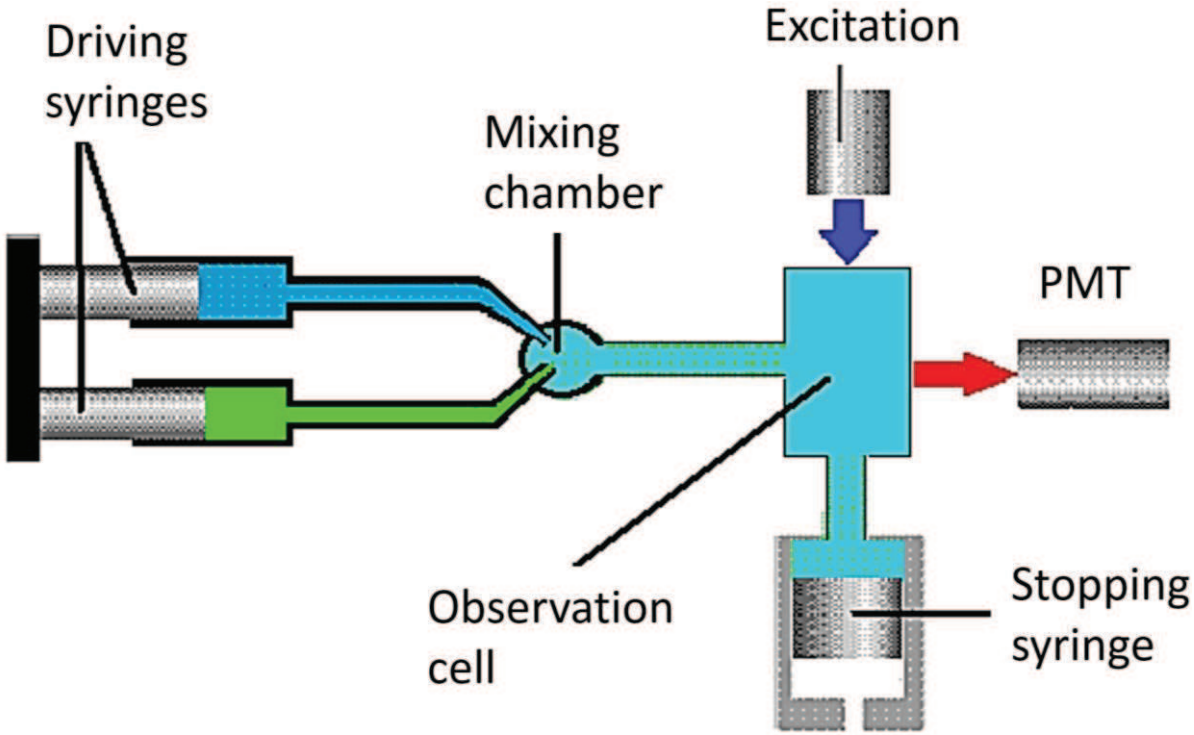

Figure 8.10. Schematic of stopped flow measurements

8.15.1 Analysis of stopped flow data

Kinetics studies determine the dynamics of chemical or biochemical reactions. The raw data are the measurements of rates of reactions, while the final goal is to find explanations of these rates in terms of a complete reaction mechanism. Complex mechanisms are usually expressed in sequences of simple reactions. In general, a reaction could be written as:

$$aA + bB + \cdots \xrightarrow{k} cC + dD + \cdots \qquad eq.8.18$$

the reaction rates for the individual components are:

$$-\frac{1}{a}\frac{d[A]}{dt}; -\frac{1}{b}\frac{d[B]}{dt}; +\frac{1}{c}\frac{d[C]}{dt}; -\frac{1}{d}\frac{d[D]}{dt} \qquad eq.8.19$$

Where square brackets denote to concentrations. In most cases only closed, homogenous systems are considered in which there is no gain or loss of material during the reaction. Reactions are assumed to proceed isothermally. The rate of reaction at a fixed temperature is proportional to concentration terms:

$$-\frac{1}{a}\frac{d[A]}{dt} = k([A]^{\alpha} + [B]^{\beta} + \cdots \qquad eq.8.20$$

The proportionality constant k is called the rate constant. The sum of the exponents of the concentrations $n = \alpha + \beta + \cdots$ is the overall order of the reaction, while α and β are the orders of the reaction with respect to A and B, respectively. In principle, the order of reaction for each

reacting compound must be determined experimentally since it cannot be deduced from the equation describing the reaction.

8.15.2 Determination of reaction order

Without knowing the order of the reaction it is impossible to determine any model for describing the reaction. There are several experimental methods for determination of the order of reaction (Capellos & Bielski 1980).

8.15.3 The half-life method

The half-life method is applicable for single component reactions and based on comparison of the time at which signal changed for 50% (half-life) with the expected half-life for specific order.

8.15.4 The initial rate method

A more general approach is the initial rate method. For a reaction of the nth order, the rate of reaction is given by:

$$R_1 = \frac{d[A]_1^n}{dt} = k_n[A]_1^n \qquad eq.8.21$$

where the subscript 1 refers to a particular initial rate. The order of reaction can be determined from measurements of initial rates R_1 and R_2 for different initial concentrations of A, since:

$$R_1 = k_n[A]_1^n \; and \; R_2 = k_n[A]_2^n \qquad eq.8.22$$

and the order could be determined from:

$$n = \left[\frac{\ln(R_1/R_2)}{\ln([A]_1/[A]_2)}\right] \qquad eq.8.23$$

8.15.5 The isolation method

In a second-order reaction when one of the reactants is present in large excess, the reaction will behave experimentally as if it were of first-order. Similarly, a third-order reaction behaves as if it were second-order if one reactant is in large excess, or it behaves as a first-order reaction if two reactants are in excess. The reason for such behavior (pseudo-order reactions) is that the concentration of species present in large excess will remain virtually constant during the course of the reaction, and the overall order of the reaction will be apparently reduced.

It is possible to isolate each of the reacting species by adjustment of the concentration of the other participating compounds. For example, for the reaction:

$$\frac{dx}{dt} = k([A]_0 - x)^a([B]_0 - x)^b([C]_0 - x)^c \qquad eq.8.24$$

where a, b and c are the unknown exponents, 0 denote to concentrations of reactants at t = 0. The individual exponents are determined by choice of the proper initial concentrations:

1. If $[A]_0 \; and \; [B]_0 \gg [C]_0$ equation 8.24 could be written as:

   $$\frac{dx}{dt} = k([A]_0)^a([B]_0)^b([C]_0 - x)^c \qquad eq.8.25$$

   and the reaction is of order *c*, since $k([A]_0)^a([B]_0)^b$ is constant.
2. If $[A]_0 \; and \; [C]_0 \gg [B]_0$ equation 8.24 becomes:

   $$\frac{dx}{dt} = k([A]_0)^a([C]_0)^c([B]_0 - x)^b \qquad eq.8.26$$

   and reaction is of order *b*;
3. Similarly if $[B]_0 \; and \; [C]_0 \gg [BA]_0$ the observed order would be *a*.

Thus, by using the isolation method, it is possible to determine the order of complex reactions.

8.15.6 Experimental conditions for measurements of kinetics of SRA/DNA interactions

The kinetics of SRA binding to the 3HCnt-labeled duplexes was monitored using a stopped-flow apparatus (SFM-3, Bio-Logic, Claix, France). The 3HCnt-labeled DNA was excited at 365 nm, and its fluorescence intensity was recorded above 530 nm with a long-pass filter (Melles Griot, France). The data recording frequency was 5 kHz for the first 200 ms and 2 kHz between 200 ms and 1200 ms. The dead time of the set-up was 2 ms (Maillot et al. 2014). The kinetic traces were recorded after fast mixing of 100 µL of each solution. The final concentration of labeled DNA was 0.3 µM and the concentration of SRA was adjusted to have 80% of DNA bound to protein. Blank experiments in which the SRA was omitted were performed under the same conditions. Dissociation experiments were performed by adding an excess of ctDNA to pre-formed complexes of SRA with HM or NM duplexes labeled with 3HCnt. The final concentration of SRA was adjusted to have 50% of DNA bound to protein. The signal acquisition and experimental setup parameters were as for association measurements. Data acquisition and processing were done with the Biokine software from the instrument manufacturer.

8.16 Time-resolved spectroscopy

Presently, the majority of the time-domain measurements are performed using time-correlated single-photon counting (TCSPC). In this technique, the sample is excited with a pulse of light (**Figure 8.**11). And the emitted photons are collected by a high-speed micro-channel plate photomultiplier.

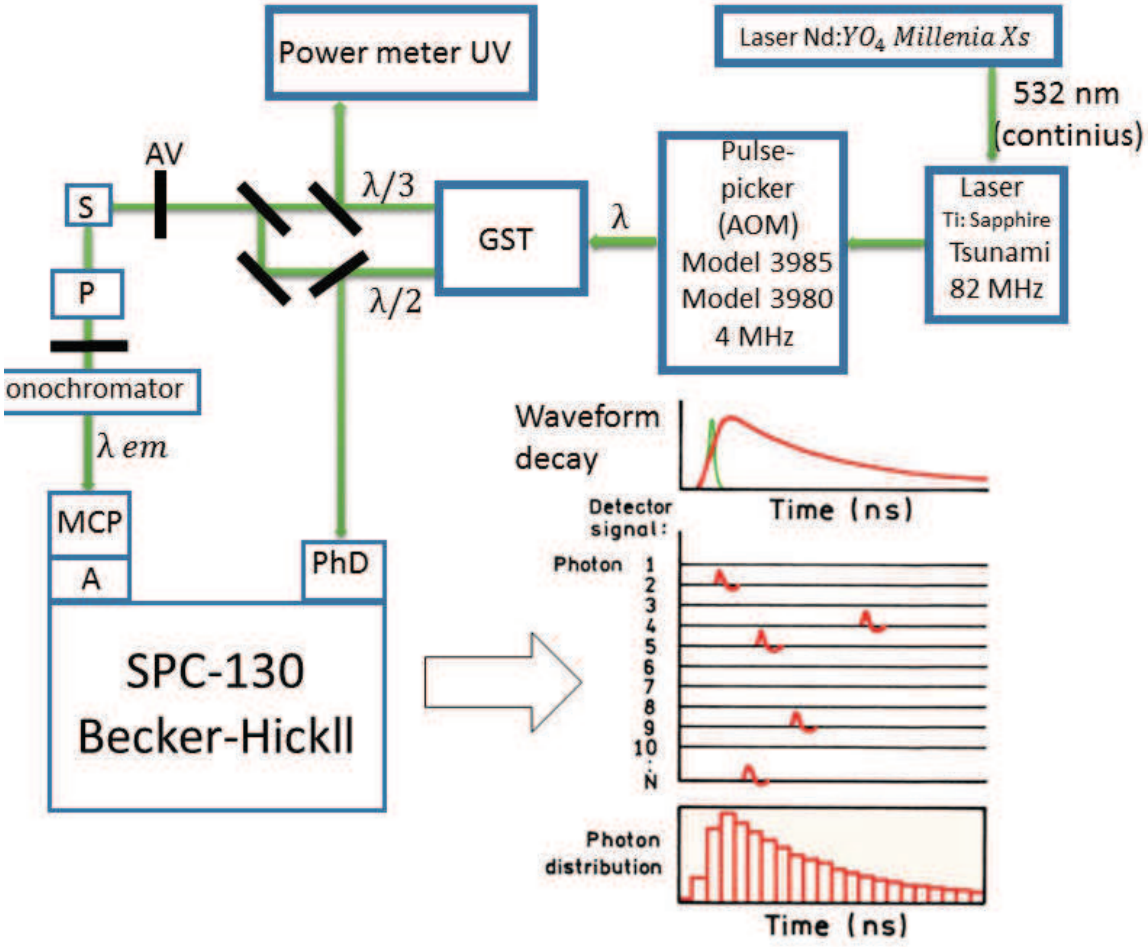

Figure 8.11. Schematic of Time-resolved spectroscopy measurements**.** GST – generator of second and third harmonics, AV – variable attenuator, S – sample, P – polarizer, PhD – photodiode, MCP - micro-channel plate photomultiplier, A – Preamplifier of pulses, SPC-130 – acquisition module.

For each collected photon, the time between the excitation pulse and the observed photon is stored in a histogram. The x-axis is the time difference and the y-axis the number of photons detected for this time difference. With a detection rate much less than 1 photon per excitation

pulse, this histogram represents the convolution of the fluorescence decay with the response function of the instrument.

Time-resolved fluorescence measurements were performed using the frequency-tripled output of a Ti-sapphire laser pumped by a Millenia X laser (Tsunami, Spectra Physics) **Figure** 8.11. The Ti-sapphire laser emits in region from 720 to 1080 nm and produces pulses with duration of 1 ps with a repetition frequency of 82 MHz. This frequency is reduced by a pulse-picker to 4MHz. After the pulse-picker, the laser pulse propagates through a system of nonlinear crystals - generator of second and third harmonic (GST). First, the laser pulse passes a crystal of LBO (lithium borate) and doubles its frequency. Then, the fundamental and doubled frequency beam passes a crystal of BBO (β - barium borate) in which the beam frequency is tripled. The nonlinear conversion allows to modulate the excitation wavelength without losing excitation laser properties and to excite organic molecules in the range 420-480 nm by using the second harmonic and in range 280-320 nm by using the third harmonic.

A fraction of doubled-frequency beam is redirected to the fast photodiode connected to a discriminator (Tennelec TC 454), which initiates (Start) a time-amplitude converter (TAC) (SPC-130 Becker-Hickl) and the beginning of condensator charging. Emitted photons from the sample are detected perpendicular to excitation by the micro-channel plate photomultiplier (PMT) (Hamamatsu R3809U) coupled with a preamplifier (HFAC Becker-Hickl) (A). The emission wavelength is selected by a monochromator (Jobin-Yvon) with adjustable slits (4-16 nm). A polarizer (P) set to 54,7^{o} allows the detection of the fluorescence independently on the movements of the excited molecules. The signal corresponding to the first detected photon serves as “Stop” for TAC which stops the condensator charging. Accumulated charge in TAC proportional to interval of time between excitation (Start) and emission photon (Stop). This charge is digitalized by the multichannel analyzer (SPC-130 Becker-Hickl). 4096 channels are used to obtain the histogram of arriving photons. The multichannel analyzer is controlled by SPCM software. To obtain a histogram which may represent the decay of multiple fluorophores, the detection of at least 10^6 photons is required.

8.16.1 Extraction of lifetimes from decay data

The final histogram obtained from the measurements is a convolution of the instrumental response function (IRF) and the fluorescence emission I:

$$F = I * IRF = \int_0^t I(\tau) IRF(t-\tau) d\tau \qquad eq. 8.27$$

The IRF is measured by using a polished aluminum reflector and is mainly determined by the physical properties of the detector.

The emission intensity is modeled as:

$$I(t) = \sum_{i=0}^{N} \alpha_i e^{-\frac{t}{\tau_i}} \qquad eq.8.28$$

where α_i are the amplitudes and τ_i the lifetimes. To get a proper fit, the intensity calculated by eq.8.28 $F_c(t_i)$ and the experimental value $F_e(t_i)$ must satisfy the χ^2 criteria:

$$\chi^2 = \frac{1}{M} \sum_{i=0}^{M} \{F_c(t_i) - F_e(t_i)\}^2 \frac{1}{\sigma_i} \sim 1.0 \qquad eq.8.29$$

where σ_i are the standard deviations for the data points and M is the number of data points. It happens that the good fit criterion of χ^2~1.0 could be obtained for different distributions of $\alpha(\tau)$. To find the optimum distribution, the Maximum Entropy Method (MEM) is used (Brochon 1994; Livesey & Brochon 1987). In this method, the optimum distribution is the one which fits the data adequately and maximizes the value of the Shannon-Jaynes entropy function S, as defined:

$$S = -\sum \frac{\alpha_i}{\sum \alpha_i} \log \frac{\alpha_i}{\sum \alpha_i} \qquad eq.8.30$$

The MEM method allows discriminating multiple components in the decay function without any prior knowledge.

Systems with multiple components in decays could also be characterized by a mean lifetime calculated as $\tau_m = \sum \alpha_i \tau_i$. In case of fluorescent nucleotides, highly quenched populations (dark species) are frequently observed. Their population, α_0, could be calculated as:

$$\alpha_0 = 1 - \frac{\tau_{free}}{\tau_{DNA} R_m} \qquad eq.8.31$$

where τ_{free} is the lifetime of the free fluorophore, τ_{DNA} is the measured mean lifetime of fluorescent base within the DNA and R_m is the ratio of their corresponding quantum yields. The

remaining amplitudes, α_{ic} then should be recalculated from the measured amplitudes according to $\alpha_{ic} = \alpha_i \cdot (1 - \alpha_0)$.

8.16.2 Experimental conditions of lifetime measurements of HCnt labelled DNAs

Time-resolved studies of the interaction of SRA and its mutants with 3HCnt labelled DNAs were performed in the Spectroscopic Buffer. The concentrations of DNAs were in range from 5-10 μM and concentrations of SRA and its mutants were adjusted to have about 80% of complex in solution. The excitation wavelength was set at 315 nm. The number of collected photons per measurement was 10^6. The instrumental response function was recorded using a polished aluminum reflector, and its full width at half- maximum was ~40 ps. The time-resolved decays obtained by using the maximum of entropy method with Pulse 5 software (Brochon 1994) (Maximum Entropy Data Consultants) allowed us to resolve fluorescence lifetimes down to ~20 ps. The goodness of the fit was evaluated from the χ^2 values, which ranged from 0.9 to 1.2, and from the plot of the residuals and the autocorrelation function.

IX Results

9.1 Direct study of SRA-induced base flipping by 5-methyl-2-pyrimidinone .

The SRA binding domain of UHRF1 has several structural features which allow this protein to specifically recognize and flip methylcytosine. To study this flipping, one obvious strategy is to use a fluorescent nucleotide analog of methylcytosine. This nucleotide should be isomeric to mC in order to satisfy the steric restrictions of the SRA binding pocket. The closest isomeric analog to mC is 5-methylpyrimidine (M5k), a derivative of 2`-deoxycytidine (**Figure** 9.1). The M5k nucleotide has absorption and emission maxima at 314 and 380 nm, respectively, with a quantum yield of ~ 10% when inserted into DNA (Singleton et al. 2001) Its fluorescence properties were shown to be sensitive to its microenvironment, so that M5k can serve as a reporter for monitoring DNA structural dynamics (Wu & Nordlund 1990; Singleton et al. 2001). When SRA induces the flipping of this nucleotide, the environment of the probe should change from a highly quenched state in DNA to a much less quenched one when the flipped nucleotide is accommodated in the binding pocket. Thus, it is expected that substitution by M5k nucleotide of the target mC should allow a direct detection of SRA binding and base flipping.

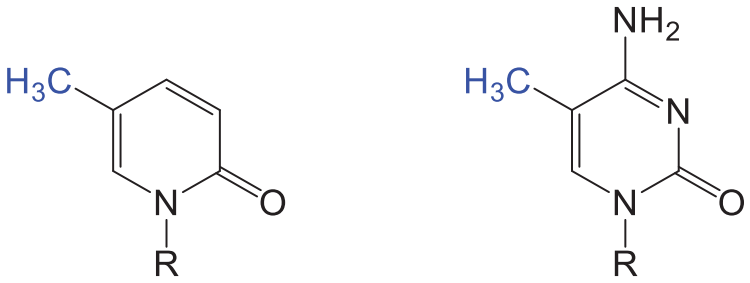

5-methylpyrimidin (M5k) 5-methyl-2-pyrimidinone

Figure 9.1. Comparison of 5-methylcytosine and 5-methyl-2-pyrimidinone structures.

9.1.1 Thermal denaturation studies of M5k labelled DNA

To test whether M5k could be flipped by SRA and whether its fluorescence response could be used to monitor this flipping, M5k was introduced in the target CpG site of the SRA domain, within the sequence 5'-GGG CCX GCA GGG-3' (X corresponding to M5k). To obtain a double stranded DNA, the M5k-labeled sequence and its complementary sequence were mixed in equal amounts and annealed. The effect of the M5k insertion on the duplex stability was checked by melting experiments. No significant difference in stability was observed between the wild-type and the M5k-labeled duplexes.

9.1.2 Steady state spectroscopy

Steady state spectroscopy measurements were performed with the M5k-labeled duplex and SRA. The emission spectrum of M5k-labeled DNAs was found to be in good agreement with previous reports (Singleton et al. 2001) showing an emission maximum at 375 nm.

Figure 9.2. Fluorescence spectra of DNA labeled with M5k at position 6 with (red curve) and without (black curve) SRA. Final DNA and SRA concentrations were 3 μM and 4 μM, respectively. Experiments were performed in the spectroscopic buffer.

Unfortunately, comparison of the emission spectra of M5k in free DNA and in presence of SRA showed that no fluorescence changes appeared in response to SRA (**Figure** 9.2). This suggests that M5K is likely insensitive to SRA binding and is probably not flipped by SRA.

The M5k fluorescent nucleotide mainly differs from mC by the absence of a NH_2 group at position 4. As discussed in chapter 2.3, two hydrogen bonds are thought to be established between two SRA residues (Asp 469 and Thr 479) and the nitrogen at position 4 of mC. The insensitivity of M5k to SRA interaction suggests that the absence of these hydrogen bonds significantly perturbs the SRA activity. This could be due either to SRA inability to flip M5k or because M5k, once flipped, cannot be accommodated a stable way in the binding pocket, leading to a reduced stability of the SRA/DNA complex. These data, together with previous

data obtained by using 2Ap as a probe to study SRA-induced base flipping (Greiner et al. 2015), show that the substitution of the target mC by fluorescent nucleotide analogs most likely will result in the absence of SRA base-flipping activity. As a consequence of the specific interactions between SRA residues and mC, it is likely that it is not possible to substitute the mC residue by any fluorescent nucleotide without perturbing the SRA activity. Moreover, our data with M5k suggest that mutagenesis studies of residues Asp 469 and Thr 479 of SRA could potentially be useful to understand how SRA can selectively recognize mC over other nucleotides.

9.2 Indirect study of SRA-induced base flipping by 8-vinyl-2'-deoxyguanosine

To study the SRA-induced base flipping without modifying its target nucleotide, it is possible to introduce a fluorescent nucleotide analog next to the flipping mC. Cytosine and mC are rather efficient fluorescence quenchers (Lakowicz 2006), so that once flipped out from the DNA duplex, the fluorescence of any neighboring probe could be partially restored. However, SRA specificity to CpG sites should be taken into account and again, only isomorphic nucleotide analogs could be envisioned as neighbors of the target mC.
8-vinyl-2'-deoxyguanosine (8VdG) (**Figure 9.3**), an environment sensitive fluorescent analog of G (Nadler et al. 2011), was used to substitute the G base in the CpG recognition motif.

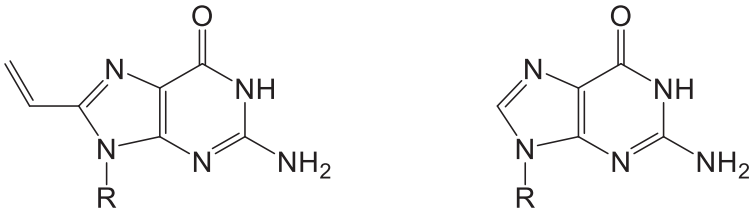

8-Vinyl-2'-deoxyguanosine Guanine

Figure 9.3. Comparison of 8-vinyl-2'-deoxyguanosine and Guanine structures.

The extinction coefficient of 8VdG at 277 nm is 7200 M^{-1} cm^{-1}, but it can be excited up to 325 nm, so that it can be used to site-specifically probe oligonucleotides in the presence of proteins. The quantum yield of free 8VdG is 72% and is unaffected by changes of pH within the physiological range pH 5–9.

8VdG-labelled sequences 5'-GGG CCY XCA GGG-3' (where X is 8VdG and Y is C or mC) were used to investigate if this probe could sense SRA-induced base flipping.

9.2.1 Thermal denaturation

The effect of the replacement of guanine at position 7 by 8VdG on the stability of ds DNA was studied by measuring UV melting curves, comparatively to wild type DNA. Our data showed that the substitution of guanine at position 7 by 8VdG decreases the thermal stability of model duplexes by 7°C. This significant decrease in the melting temperature may result from a steric penalty of the vinyl substituent and/or from the disruption of the spine of hydration in the major groove as was observed for the similar 8-vinyl-deoxyadenosine (Gaied 2005).

9.2.2 Steady-state spectroscopy

The ability of 8VdG to sense the interaction of SRA with ds DNA was investigated by steady-state and time-resolved fluorescence spectroscopy, using 8VdG-labeled DNA, in the absence and presence of SRA (**Figure 9.4**). Both labeled sequences show quantum yields close to 10%. This value is one order of magnitude higher than that of 2-Ap, indicating that 8VdG is either poorly quenched by its cytosine neighbors and/or is rejected toward the solvent in an extra-helical conformation. Addition of SRA to the sequences labeled at position 7 by 8-VdG gives only a small increase in the intensity, but without any differences for methylated and non-methylated DNAs. In presence of SRA, the quantum yield increased from ~ 9.5% to 12% for both sequences. This low increase could be explained by the fact that the quantum yield is already high in the absence of SRA. In these conditions, binding of SRA can hardly restrict the quenching by the neighbors bases, in contrast with 2Ap (Greiner et al. 2015).

Figure 9.4. Fluorescence spectra of DNA duplexes labelled at position 7 by 8-VdG. The spectra in black correspond to the spectra of the HM and NM duplexes in the absence of protein. The spectra in blue and red correspond to NM and HM duplexes in the presence of SRA. Final DNA and SRA concentrations were 3 μM and 4 μM, respectively. Experiments were done in 25 mM TRIS, 50 mM NaCl, 2mM TCEP, 0.04% PEG 20000, pH 7.5, 20 °C.

9.2.3 Time resolved spectroscopy

Time-resolved fluorescence measurements were performed on the 8VdG-labeled DNAs and their complexes with SRA. Lifetimes of 8VdG in HM and NM sequences are characterized by 3 components: 0.04 ns, 0.11 ns and about 2 ns (Table 1).

Table 1. Time-resolved spectroscopy data of 8VdG in free DNA and in SRA/DNA complex

Sample	τ_1, ns	a_1	τ_2, ns	a_2	τ_3, ns	a_3	Tau mean
HM	0.040	0.74	0.11	0.16	2.00	0.10	0.25
HM+SRA	0.038	0.70	0.11	0.22	2.70	0.08	0.27
NM	0.037	0.76	0.11	0.15	2.17	0.09	0.24
NM+SRA	0.038	0.70	0.11	0.22	2.56	0.08	0.26

Final DNA concentrations were 3 μM and concentration of SRA was 4 μM. Experiments were done in 25 mM TRIS, 50 mM NaCl, 2mM TCEP, 0.04 PEG 20000, pH 7.5, 25 °C. Emission was collected at 400nm.

The lifetimes were short, especially the long-lived lifetime which is markedly shorter than the long-lived lifetime of 2-Ap (10 ns), so that it is unlikely that 8VdG exhibits an extrahelical conformation.

The formation of SRA-DNA complex induces a small increase in the long-lived lifetime for both HM and NM DNAs, as well as a limited redistribution of their amplitudes.

9.2.4 Discussion

8VdG in our model DNA sequences shows a relatively high quantum yield of about 10%. The formation of SRA-DNA complex induces only limited changes in quantum yields and lifetimes. The quantum yield of 8vdG is already high in the absence of SRA, suggesting that it is not well quenched by the neighboring C bases. Addition of SRA decreases to some extent the quenching of 8VdG by its neighbors but this decrease it is too limited to use 8-VdG for further investigation of the SRA/DNA interaction. Moreover, no difference was observed between NM and HM duplexes. This limited response to interaction of SRA with DNA suggests that substitution of guanosine could perturb the recognition properties or the functions of SRA. This could result from a steric clash between vinyl group on 8vdG and V446, R433 and F432 residues of SRA (**Figure 8.6**). These residues in the NKR finger interact with the G7·C7' base pair through a combination of hydrogen bonds and favorable van der Waals interactions (Avvakumov et al. 2008). This steric clash probably prevent the NKR finger to flip mC or to stabilize the complex.

9.3 Investigation of SRA-induced base flipping by using 3HCnt

ESIPT possessing fluorescent nucleotides analogs are the most promising probes of DNA-protein interactions. In order to study the SRA-induced base flipping activity we labelled the structurally characterized 12-bp duplex (Avvakumov et al. 2008) with 2-thienyl-3-hydroxychromone. Due to ESIPT reaction, this highly responsive universal nucleobase analog displays environmentally sensitive normal (N*) and tautomeric (T*) emission bands. We introduce this probe in to various positions in either non-methylated (NM) or hemi-methylated (HM) duplexes. By performing thermal denaturation studies by UV spectroscopy we found that 3HCnt at most positions marginally destabilized duplexes. Further, we investigated if introduction of 3HCnt into the target DNA perturbs the SRA/DNA interaction. For this purpose, we performed binding studies of SRA to DNA first by using Isothermal Titration Calorimetry to determine the apparent affinities of SRA to non labelled HM DNA. Next, we determined the apparent affinities constant of SRA to 3HCnt labeled NM and HM DNAs. This was done by recording fluorescence anisotropy changes as the labeled duplex was titrated with increasing concentrations of SRA. By comparing results obtained from the two techniques we found that

introduction of 3HCnt affects SRA/DNA interaction in a site-specific manner. SRA bound up to 20 times stronger to labelled DNA when 3HCnt was introduced next to mC. This is in agreement with data obtained with using 8vdG nucleotide, confirming the CpG sequence sensitivity of SRA. Meanwhile, at positions outside the CpG site SRA binding was less perturbed and showed preferential binding to HM DNA as expected.

As a next step, we compared the SRA-induced changes in the emission spectra of the 3HCnt-labeled HM or NM duplexes. SRA binding increases the QY and decreases the N*/T* ratio of most HM and NM duplexes, but the changes were position dependent. The changes were the largest for positions next to mC , but equal for NM and HM DNAs. Significant differences between HM and NM duplexes modified at positions 8 and 5' were observed upon SRA binding. While SRA interaction with the HM duplex increases 3HCnt's QY up to 2 and 2.7 times for positions 8 and 5', respectively, the corresponding increase was only ~1.3 and 1.6 times, respectively for the NM duplex. As HM and NM duplexes differ only by a single methyl group at C6, we attribute the larger changes observed with HM duplexes to mC6 flipping. In order to strengthen this conclusion, we used a SRA mutant where the G448 residue has been replaced by a D residue. This G448D mutant was previously suggested to sterically hinder the flipping of the mC6 residue. In sharp contrast to the wild-type SRA, the G448D SRA mutant induces only a limited change in the emission spectra, comparable with that observed for the binding of both wild-type and mutant SRA to NM duplexes in agreement with our expectations.

To further characterize the SRA-induced flipping of mC6, we comparatively investigated the interaction of wild type and mutant SRA with the 5'- and 8-labeled HM and NM duplexes by stopped-flow. We observed the kinetics of SRA-induced flipping of mC by monitoring the intensity of the T* band of 3HCnt. We found that SRA interacts with NM and HM duplexes with rates that differ by several orders of magnitude. This difference was absent with the mutant SRA, confirming that the observed kinetic differences are related to flipping. To verify the specificity of 3HCnt response to SRA-induced flipping, we applied the isolation method of reaction order determination and performed dissociation studies. Based on our findings, we concluded that UHRF1 (through its SRA binding domain) might direct DNMT1 by increasing the residence time of UHRF1 on the HM CpG sites.

Our data show that the sensitivity of 3HCnt to mC flipping is a novel approach to study the activity of SRA, and therefore of UHRF1 with high sensitivity. This approach will allow investigating the complex dynamics of DNA methylation maintenance by the UHRF1/DNMT1 tandem, which was not possible before.

Publication 1: “Dynamics of methylated cytosine flipping by UHRF1”

Dynamics of methylated cytosine flipping by UHRF1

Vasyl Kilin ,[†] Nicolas P.F. Barthes,[‡] Benoît Y. Michel,[‡] Christian Boudier ,[†] Valeriy Yashchuk,[ħ] Marc Mousli,[†] Marc Ruff,[‖] Florence Granger,[‖] Yitzhak Tor,[§] Christian Bronner,[‖] Alain Burger,[‡] Yves Mély,[*,†]

[†] Laboratoire de Biophotonique et Pharmacologie, UMR 7213 CNRS, Université de Strasbourg, Faculté de pharmacie, 74 route du Rhin, 67401 Illkirch, France

[‡] Institut de Chimie de Nice, UMR 7272 CNRS, Université de Nice Sophia Antipolis, Parc Valrose, 06108 Nice Cedex 2, France

[ħ] Department of Physics, Kiev National Taras Shevchenko University, Kiev, Ukraine

[‖] Institut de Génétique et de Biologie Moléculaire et Cellulaire (IGBMC), INSERM U964 CNRS UMR 7104, Université de Strasbourg, Illkirch, France

[§] Department of Chemistry and Biochemistry, University of California, San Diego, La Jolla, California 92093-0358, United States

Abstract

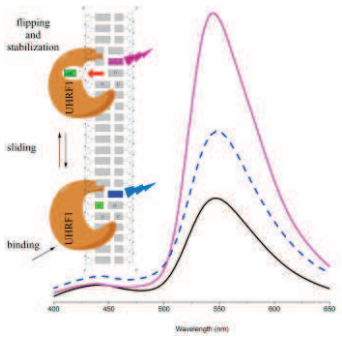

DNA methylation patterns, which are critical for gene expression, are replicated by DNA methyltransferase 1 (DNMT1) and Ubiquitin-like with PHD and Ring Finger 1 (UHRF1) proteins. This replication is initiated by the recognition of hemi-methylated CpG sites and further flipping of methylated cytosines (mC) by the Set and Ring Associated (SRA) domain of UHRF1. Though crystallography studies have shed light on the SRA mechanism, additional tools are required to monitor in real time how SRA reads DNA and flips mC. To reach this aim, we incorporated 2-thienyl-3-hydroxychromone (3HCnt), a fluorescent nucleobase analog, into hemi-methylated (HM) and non-methylated (NM) DNA duplexes. Large fluorescence changes were associated with mC flipping in HM duplexes, showing this probe's outstanding sensitivity to the small structural changes accompanying base flipping. Importantly, at positions where 3HCnt was responsive to base flipping, it marginally affected the structure of the duplex and its affinity for SRA, illustrating it is a unique non-perturbing probe for monitoring such events. Using this tool, stopped-flow studies revealed fast kinetics

of SRA binding and sliding to NM duplexes consistent with its reader role. In contrast, the kinetics of mC flipping was found to be much slower, substantially increasing the lifetime of UHRF1 bound to a CpG site in HM duplexes and thus, the probability of recruiting DNMT1 in order to faithfully duplicate the DNA methylation profile. The 3HCnt-based approach provides a key step toward the mechanistic characterization of the UHRF1/DNMT1 tandem and the development of assays for the identification of base flipping inhibitors

1. INTRODUCTION

The last decade has seen an explosion in our understanding of the underlying molecular mechanisms that govern gene expression, with epigenetics, a term once used to describe inexplicable phenomena, taking center stage. Epigenetics refer to the heritable phenotypic changes that occur without altering the DNA sequence. Major epigenetic markers include DNA methylation, post-translational modifications of histones, histone variants and nucleosome positioning[1–12]. DNA methylation is a heritable cytosine modification, mediated by DNA methyltransferases (DNMTs),[13] which methylate cytosine's C5, mainly in a symmetrical CpG context[14–16]. One of the first steps of the reproduction of the DNA methylation profile involves recognition of hemi-methylated (HM) CpG sites (*i.e.,* only one DNA strand is methylated) generated after DNA replication, which is subsequently fully methylated through the action of DNMT1. The preference of DNMT1 for HM CpG sites is insufficient, however, to explain the high fidelity in the replication of DNA methylation patterns. In this context, UHRF1 (Ubiquitin-like containing PHD and RING finger 1) plays a key role since it guides DNMT1 to its DNA target. This is achieved by specifically recognizing HM DNA [17–23] and flipping methylated cytosines (mCs) via its SRA (Set and Ring Associated) domain.

Crystallographic studies have shed light on the selective recognition of HM CpG sites and the mechanism of mC flipping, [17,18,20] which is facilitated by a specific binding hemisphere of 2Å radius in SRA, able to perfectly accommodate a methyl group. The flipped mC is stacked between Tyr 466 and Tyr 478 and further stabilized by H bonding with Asp469 and Thr479[17] (**Figure** 1a). Importantly, Gly448 plays a crucial role at the entry of the pocket. Its mutation drastically decreases the affinity of SRA for HM DNA and prevents mC flipping[17].

While crystallography reveals the "static" structural elements of the SRA/HM DNA complex, other techniques are required to monitor in real time how SRA reads DNA and flips mC. Towards this end, fluorescence-based techniques are particularly attractive, since they are

highly sensitive and information-rich. They rely, however, on fluorescent probes, which should respond sensitively and selectively to the molecular event of interest. The most obvious strategy for nucleic acids is the site-specific incorporation of fluorescent nucleobase analogues. Monitoring base flipping is, however, especially challenging due to several constraints. The highly confined SRA binding pocket limits the choices of mC substitutes. Moreover, substitution of a nucleobase in the vicinity to mC should not affect the binding of SRA, nor the stability or conformation of the duplexes. Recently, incorporation of 2-aminopurine (2-Ap) close to mC was found to partly fulfill these criteria. This emissive nucleoside was able to monitor the binding of SRA to HM and non methylated duplexes, but was insufficiently sensitive for reporting mC flipping[24].

In the present study, we labelled the structurally characterized 12-bp duplex[17] with 2-thienyl-3-hydroxychromone (3HC, **Figure** 1b), a highly responsive nucleobase surrogate[25,26] behaving as an universal nucleobase and displaying environmentally sensitive normal (N*) and tautomeric (T*) emission bands, due to an excited-state intramolecular proton transfer[27–29]. Strategic positions, close to the central CpG recognition site, were labeled in either non-methylated (NM) or hemi-methylated (HM) duplexes. When 3HCnt replaces G5' or C8, we observe a much larger change in emission quantum yield (QY) and N*/T* ratio on SRA binding to HM duplexes, as compared to NM duplexes. This large change vanishes when a SRA mutant unable to perform base flipping was used. Stopped-flow studies reveal that the comparatively slow kinetics of mC flipping significantly increases the lifetime of the SRA/HM DNA complex as compared to the SRA/NM DNA counterpart. These observations advance the mechanistic understanding of UHRF1 and its role in the replication of DNA methylation patterns and provide a potential platform for developing screening assays aimed at targeting UHRF1.

2. EXPERIMENTAL SECTION

2.1. 2.1 Materials

The SRA domain of hUHRF1 (SRA, residues 408-643) was expressed in *Escherichia coli* BL21-pLysS (DE3) and purified as previously described[30]. The mutant G448D SRA was produced as described elsewhere[31]. Unmodified oligonucleotides (DNAs) were synthesized and HPLC-purified by IBA GmbH Nucleic Acids Product Supply (Germany). 3HCnt and DNAs labeled by 3HCnt were produced as described previously[25]. The sequence of the 12-bp duplex was 5'-GGGCCXGCAGGG-3'/5'-CCCTGCGGGCCC-3' with a single CpG site that

was either nonmethylated (X = C) or hemi-methylated (X = 5mC). The 3HCnt was selectively introduced at different positions (3, 5, 6, 7, 8, 9, 6' or 5') within this sequence[25]. The duplexes were prepared by mixing the complementary strands in equal molar amounts in 20 mM phosphate buffer pH 7.5 containing 50 mM NaCl and 1 mM EDTA (referred to as the buffer) and annealing them by heating to 90°C for 5 min, followed by cooling down to room temperature. Samples were then kept on ice. EDTA was critical to avoid the formation of the anionic form of 3HCnt[32,33].

The lyophilized calf thymus DNA (ctDNA) from Sigma Aldrich was solubilized overnight at 10°C and its molar concentration in nucleotides was determined from its absorption at 260 nm using an extinction coefficient of 6600 M^{-1} cm^{-1}.

2.2 Absorption spectroscopy

Absorption spectra were recorded on a Cary 400 spectrophotometer (Varian). Extinction coefficients between 85,500 and 107,300 $M^{-1}cm^{-1}$ were used to determine the concentrations of the duplexes at 260 nm. All experiments were performed at 20°C in the buffer containing 2.5 mM TCEP and PEG 20,000 to prevent protein adsorption on the cuvette walls[34].

Melting curves of the duplexes (2 μM of each strand in the buffer) were recorded by following the temperature-dependence of the absorbance changes at 260 nm with a Cary 400 spectrophotometer (Varian) equipped with a Peltier thermostated cell holder. The optical path length of the cell was 1 cm. The temperature range was 20 – 80° C, with a speed of heating of 0.5°C/min. The melting temperatures were extracted from melting curves as described elsewhere[35].

2.3 Steady-state fluorescence spectroscopy

Fluorescence spectra were recorded at 20°C on a FluoroLog spectrofluorometer (Jobin Yvon) equipped with a thermostated cell compartment. Excitation wavelength was set at 374 nm. Spectra were corrected for buffer fluorescence, lamp fluctuations, and detector spectral sensitivity. QYs of the labeled duplexes in the absence or presence of the SRA protein were determined by using quinine sulfate (QY=0.577 in 0.5 M H_2SO_4) as a reference[36]. Measurements were performed using SRA concentrations ensuring that at least 80% of the 3HCnt-labeled duplexes are bound to SRA.

Anisotropy measurements were performed on the same instrument. Excitation wavelength was at 374 nm and emission was collected at 556 nm, which corresponds to the T* band

emission. Anisotropy values were obtained by averaging 10 measurements. The affinity of wild-type SRA and its G448D mutant to labeled DNAs was obtained by titrating a fixed amount of 3HCnt-labeled duplex by the protein and monitoring the fluorescence intensity and anisotropy signals, simultaneously. The affinity constants were determined by fitting the fluorescence anisotropy changes to the following equation:

$$r = \frac{vRr_t - r_d(v-1)}{1+Rv-v} \quad (1)$$

where r and r_t are the anisotropy values at a given and a saturating SRA concentration respectively, r_d is the anisotropy in the absence of protein. R is the ratio of the QYs of the bound to free forms, K_a is the apparent affinity constant, ν is fraction of bound SRA calculated as:

$$v = \frac{(K_a^{-1}+nL_t+P_t) - \sqrt{(K_a^{-1}+nL_t+Pt)^2 - 4nP_tL_t}}{2L_t} \quad (2)$$

where P_t and L_t are the concentrations of SRA and duplexes, respectively, and n is the number of SRA proteins bound per duplex[37,38].

2.3 Isothermal titration calorimetry (ITC)

Affinity of SRA for non-modified HM DNA was also determined by Isothermal titration calorimetry. The heat exchanged during the interaction was analyzed at 20 ^{0}C in the buffer with a VP ITC microcalorimeter (Microcal, Northampton, MA, USA). Titration was performed by monitoring under constant stirring (310 rpm) the thermal power generated by repeated injections (interval of 4 min) of 4 µL aliquots (0.5 µL.s $^{-1}$) of 40 µM HM DNA contained in the syringe into a 6 µM SRA solution contained in the 1.42 mL cell compartment of the instrument. The total heat resulting from an injection of titrant was calculated as the integral versus time of the experimental signal. A control experiment in which DNA was titrated into the buffer alone was done to determine the heat of dilution. Instrument control, data acquisition, and analysis were done with the VPViewer and Origin software provided by the manufacturer.

2.4 Stopped flow spectroscopy

The kinetics of SRA's binding to the 3HCnt-labeled duplexes was monitored using a stopped-flow apparatus (SFM-3, Bio-Logic, Claix, France). The 3HCnt was excited at 365 nm, and its fluorescence intensity was recorded above 530 nm with a long-pass filter (Melles Griot, France). The data recording frequency was 5 kHz for the first 200 ms and 2 kHz between 200 ms and 1200 ms. The dead time of the set-up was 2 ms[39]. The kinetic traces were recorded after

fast mixing of 100 µL of each solution. The final concentration of labeled DNA was 0.3 µM and the concentration of SRA was adjusted to have 80% of DNA bound to protein. Blank experiments in which the SRA was omitted were performed under the same conditions. Dissociation experiments were performed by adding an excess of ctDNA to pre-formed complexes of SRA with HM or NM duplexes labeled with 3HCnt. The final concentration of SRA was adjusted to have 50% of DNA bound to protein. The signal acquisition and experimental setup parameters were as for association measurements. Data acquisition and processing were done with the Biokine software from the instrument manufacturer.

3. RESULTS

3.1 Labeling position strategy and spectroscopic characterization of labeled duplexes

Based on the reported structure of SRA complexed to a 12 bp duplex (**Figure** 1a) [17], the latter was labeled with 3HCnt (**Figure** 1b) at positions 5, 6, 7, 8, 9, 5' and 6'. These sites were selected for their proximity to the methylcytosine (mC) at position 6 and their direct interaction with SRA. Positions 3 and 9, not in contact with SRA, were also labeled. The corresponding 3HCnt-labeled NM duplexes with a cytosine at position 6 were also synthesized for systematic comparison with HM duplexes.

Thermal denaturation measurements show all 3HCnt-labeled duplexes to have a minimal T_m drop (≤ 3°C) with the exception of the duplex modified at position 3 (**Figure** S1 and Table S1 in the Supporting Information). Since the observed destabilization is lower than a single mismatch, the large surface area of 3HCnt must partially compensate for the lack of base pairing[25]. We note that even the duplex modified close to its 5'-end at position 3 predominates at 20 ºC, the working temperature (data not shown).

Incorporation of the emissive nucleoside into duplexes significantly shifts its N* and T* bands, and strongly decreases their ratio in comparison with the free 3HCnt (**Figure** 1c). Both changes are consistent with intraduplex stacking of 3HCnt and exclusion of bulk water [25]. The emission QYs were rather low (0.5 – 2%; Table S2 in the Supporting Information), likely due to the neighboring G and/or C residues, which act as efficient fluorescence quenchers [25]. Importantly, the methylation of the cytosine at position 6 had negligible effect on the spectroscopic properties of 3HCnt at all used positions (Table S2 in the Supporting Information).

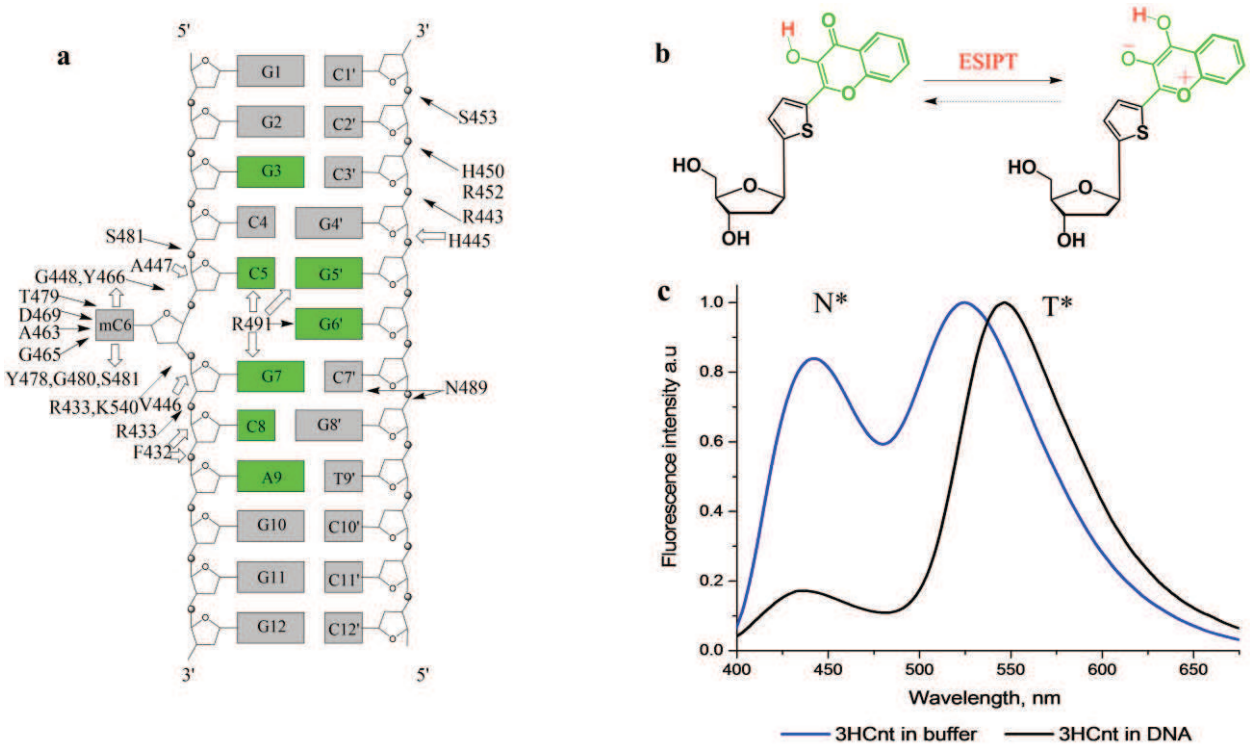

Figure 1. Structure of the used duplex and 3HCnt. (a) Structure of the duplex. The interactions of the duplex with SRA, as determined by X-ray crystallography [17] are indicated by arrows. Hydrogen bonding and van der Waals interactions are indicated by black and white arrows, respectively. Positions substituted by 3HCnt are highlighted in green. (b) Structure of the normal (N*) and tautomer (T*) forms of 3HCnt and ESIPT reaction. (c) Fluorescence spectra of 3HCnt either free (blue curve) or incorporated at position 5 in the duplex (black curve); N* and T* forms generate the higher and lower energy emission bands, respectively. Experiments were done in phosphate buffer 20 mM, NaCl 50 mM, TCEP 2.5 mM, PEG 0.05%, pH 7.5, at T=20°C. The spectra were normalized at the T* band maximum.

3.2 Binding of SRA to DNA

To investigate whether 3HCnt alters the binding of SRA to the duplexes, fluorescence anisotropy changes were recorded as the labeled duplex was titrated with increasing concentrations of SRA (**Figure** 2a). Assuming a 1:1 binding model, K_{app} values were found to depend on the 3HCnt position in the duplex (**Figure** 2b and Table S3 in the Supporting Information). The K_{app} values for duplexes modified at positions 3, 8, 9, or 5', are close to the values obtained by ITC with the non-labeled HM duplex (**Figure** S2 in the Supporting Information) and the values reported in the literature [21,24], suggesting 3HCnt minimally affecting the binding of SRA. This conclusion is further strengthened by the observation that the affinity of SRA for HM duplex modified at positions 8 and 5' is ~5 and ~8 times higher than for NM duplex (**Figure** 2c), in line with previous reports [17–23].

In contrast, 3HCnt at position 5 or 7 increases the affinity of the labeled HM duplex to SRA by 4- to 14-fold as compared to the non-labeled HM duplex. As numerous contacts were

evidenced between these positions and SRA in the SRA/DNA complex [17], the complexes are likely stabilized through direct interaction between the 3HCnt and SRA amino acids. The loss of differential affinity of SRA to HM and NM duplexes in this case further suggests, however, that SRA may interact similarly with C6 and mC6 in NM and HM duplexes, respectively. At position 6', the 3HCnt also substantially stabilizes the complexes with SRA, but differences in the binding constants to HM and NM duplexes are still observed (**Figure** 2c).

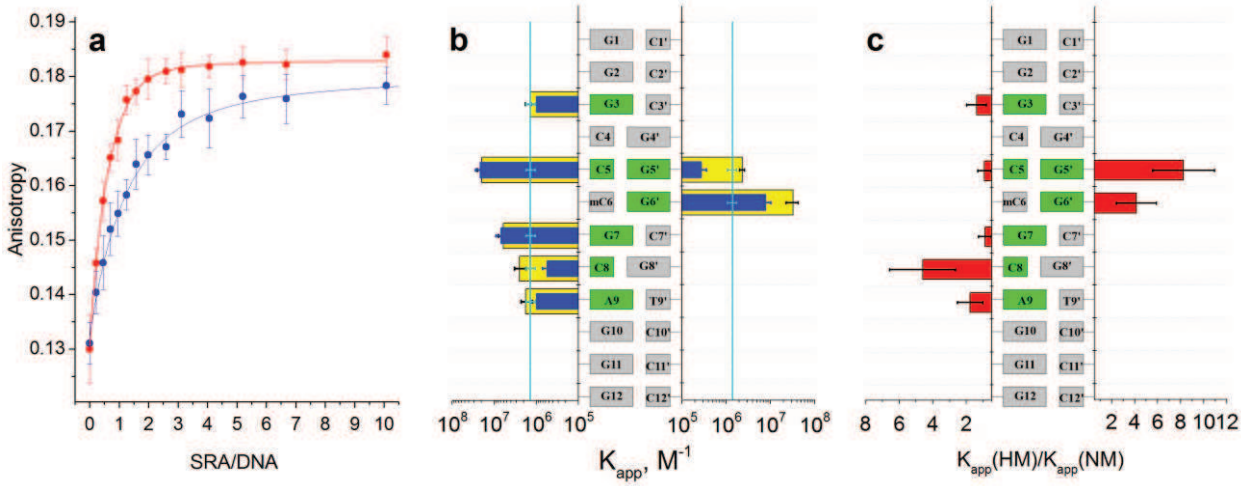

Figure 2. Binding of SRA to 3HCnt-labeled HM and NM duplexes, as monitored by fluorescence anisotropy. (a) Anisotropy titration curves for HM (red) and NM (blue) duplexes labeled by 3HCnt at position 5'. The concentration of duplexes was 2 μM in the same buffer as in **Figure** 1. The lines correspond to the best fits of the experimental points to equations 1 and 2. Experimental points are expressed as means ± standard deviation for n = 2 independent experiments. (b) Plot of the apparent affinity constants K_{app} for 3HCnt-labeled HM (yellow) and NM (blue) duplexes. The cyan line describes the affinity of SRA to the non-labeled HM duplex, as determined by ITC in **Figure** S2 in the Supporting Information. (c) Effect of C6 methylation on the affinity constants of SRA to the duplexes. At each position, the ratio of the K_{app} value for HM duplex to that for NM duplex is given. Data in (b) and (c) are expressed as means ± standard deviation for n = 3 independent experiments.

3.3 Monitoring SRA-DNA interaction by steady-state spectroscopy measurements

To determine whether 3HCnt could be used to monitor SRA binding and the resulting flipping of mC at position 6, we compared the SRA-induced changes in emission spectra of the 3HCnt-labeled HM or NM duplexes. SRA binding increases the QY and decreases the N*/T* ratio of most HM and NM duplexes, but the changes were position dependent (**Figure** 3 and 4, and Table S2 in the Supporting Information). Interestingly, significant differences between HM and NM duplexes modified at positions 8 and 5' are observed upon SRA binding (**Figure** 3a and b). Indeed, while SRA interaction with the HM duplex increases 3HCnt's QY up to 2 and 2.7 times for positions 8 and 5', respectively, the corresponding increase was only ~1.3 and 1.6 times, respectively for the NM duplex (**Figure** 3a and b). Concurrently, while the N*/T* ratio

decreases of 30% and 69% for positions 8 and 5' in the HM duplex, respectively, a drop of 7% and 25%, is observed for the NM duplex. As HM and NM duplexes differ only by a single methyl group at C6, the larger changes observed with HM duplexes are likely related to mC6 flipping.

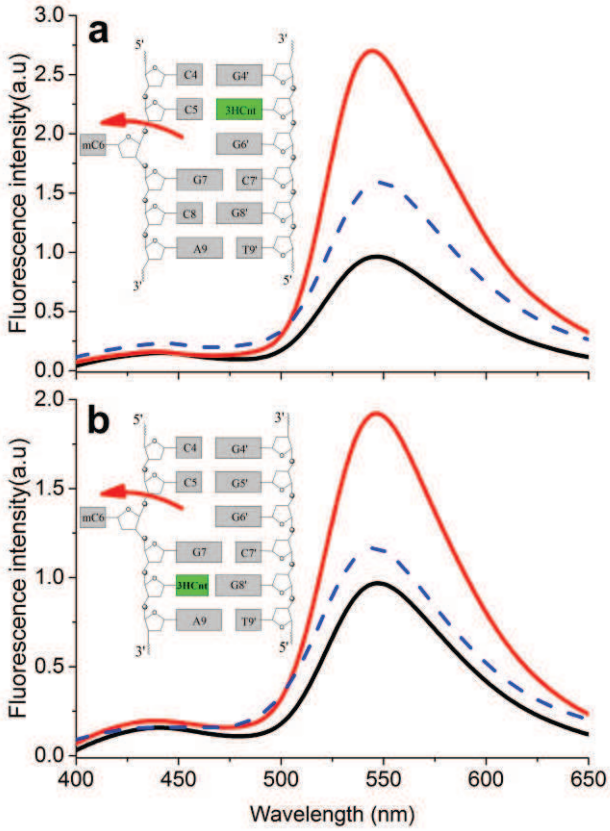

Figure 3. Fluorescence spectra of HM and NM duplexes labeled by 3HCnt at positions 8 (a) and 5' (b). Black lines - spectra of free labeled duplexes (HM and NM are superimposable), blue lines – spectra of NM duplex bound with SRA, red lines - spectra of HM duplex bound with SRA. Buffer was as in **Figure** 1. Concentration of labeled duplexes was 1 μM, while the SRA concentration was adjusted to complex at least 80% of the DNA molecules.

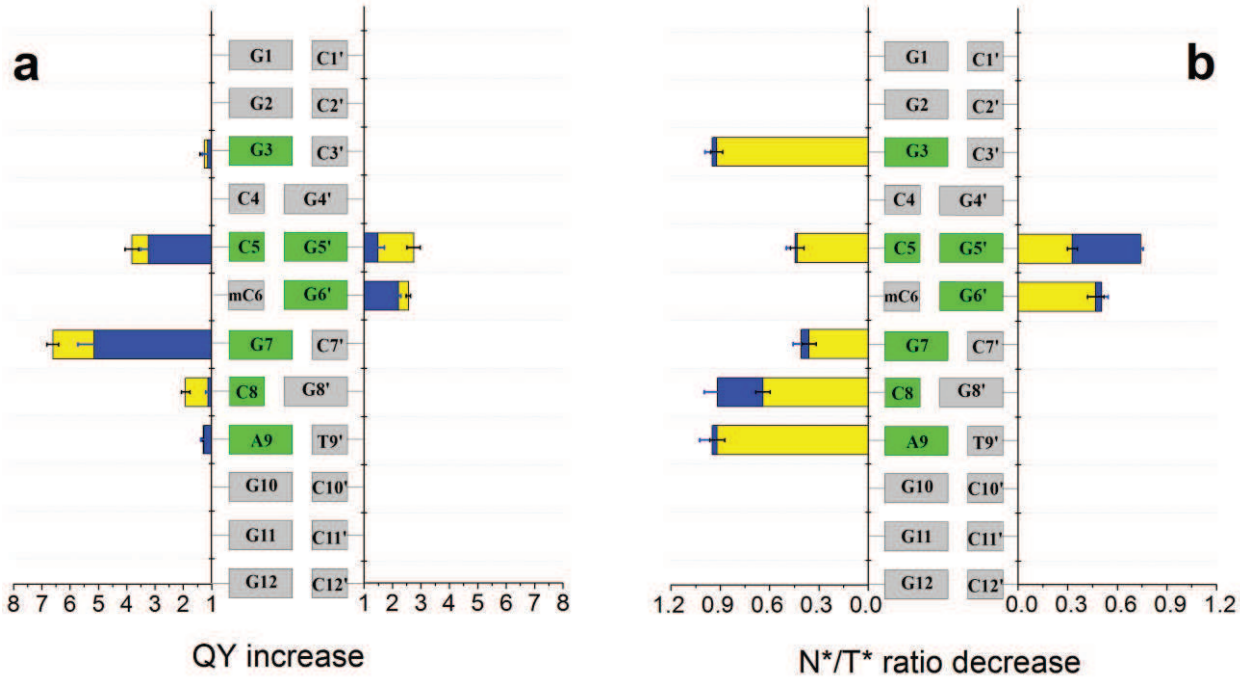

Figure 4. SRA-induced changes in the QY (a) and N*/T* ratio (b) of 3HCnt-labeled NM (blue bars) and HM (yellow bars) duplexes. Experiments were performed as described in **Figure** 3. The QY increase in (a) corresponds to the ratio of the QY of 3HCnt in the SRA/duplex complex to that of 3HCnt in the free DNA. The N*/T* ratio decrease in (b) was calculated by dividing the N*/T* ratio value of 3HCnt in the DNA/SRA complex by that in the free DNA. Data are expressed as means ± standard deviation for n = 5 independent experiments.

The largest changes in QY and N*/T* ratios are observed for positions 5, 7 and 6' (Table S2 in the Supporting Information), immediately next or opposite to position 6, confirming that 3HCnt at these positions likely interacts directly with SRA and thus, stabilizes the SRA/duplex (**Figure** 2b). This stabilization may in turn affect the proper interaction of SRA with the mC6 or C6 residues in HM and NM duplexes, respectively, as suggested by the marginal differences between the binding constants and spectroscopic properties of HM and NM duplexes (**Figure** 2c and **Figure** 4). Finally, only limited changes in QY and N*/T* ratios were observed at positions 3 and 9, in line with the marginal interaction of SRA with both positions in the crystal structure[17]. Taken together, the binding and spectroscopy data indicate that incorporating 3HCnt into positions 8 and 5' does not alter the binding of SRA to both HM and NM duplexes and allows monitoring the flipping of mC6.

3.4 Interaction of 3HCnt-labeled HM and NM duplexes with G448D SRA mutant

To substantiate our conclusion that the distinct responses of the 5'- and 8-labeled HM and NM duplexes to SRA binding reflect flipping of the mC6 nucleobase, we employed a SRA mutant where the G448 residue has been replaced by a D residue. This G448D mutant was previously suggested to sterically hinder the flipping of the mC6 residue[17,31]. Interestingly, a significant decrease in the affinity of this SRA mutant to HM duplexes (**Figure** 5a) is seen, in line with previous observations[17]. Moreover, the G448D mutation also eliminates the preferential binding to HM duplexes, as the affinities of G448D to both HM and NM duplexes were found to be similar and comparable to those seen for binding of the native SRA to the NM duplexes. In sharp contrast to the wild-type SRA, the G448D SRA mutant induces only a limited increase in the QY (**Figure** 5b) and decrease in N*/T* ratio (data not shown) of the HM duplex, comparable with that observed for binding of both wild-type and mutant SRA to NM duplexes. These data support that 3HCnt at positions 8 and 5' senses the SRA-induced flipping of mC6 and that SRA's preferential affinity to HM duplexes likely relies on its ability to flip the mC6 residue into its binding pocket [17,18,20].

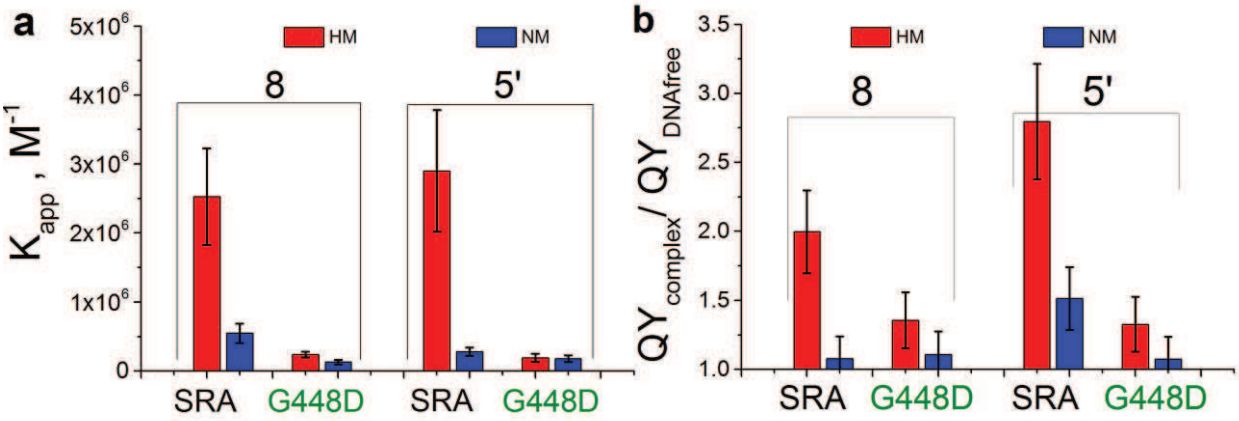

Figure 5. Comparison of the interaction of wild-type SRA and G448D SRA with HM and NM duplexes labeled with 3HCnt at positions 8 and 5'. (a) Affinity constants of wild-type and mutant SRA to the labeled NM and HM duplexes. (b) Changes in the QY of the labeled NM and HM duplexes on binding to wild-type and mutant SRA. The concentration of duplexes was 1 μM. The concentration of proteins was adjusted to ensure 80% of binding. Experimental conditions were as in **Figure** 2.

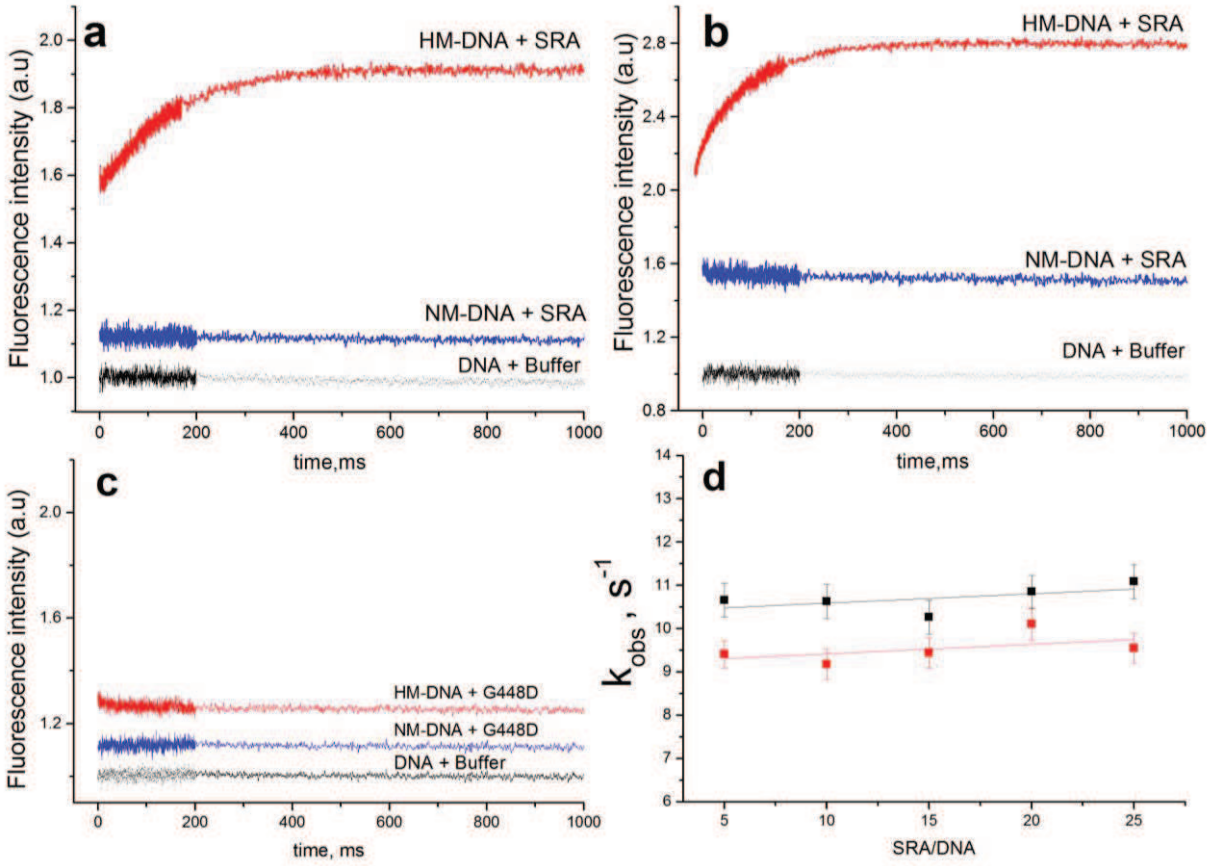

Figure 6. Interaction kinetics of wild-type SRA and G448D SRA mutant with HM and NM duplexes labeled at position 8 and 5', as monitored by stopped-flow. (a) Kinetic traces obtained with duplexes labeled by 3HCnt at position 8. The black curve corresponds to HM- or NM-duplexes mixed with the buffer. The blue and red solid lines are the kinetic traces for the interaction of SRA with NM- and HM-duplexes, respectively. (b) Kinetic traces with duplexes labeled at position 5'. Color codes are as in (a). (c) Kinetic traces of the interaction of the G448D SRA mutant with HM and NM duplexes labeled at position 5'. Color codes are as in (a). (d) Observed rate constants of the interaction of SRA with HM-duplexes labeled at positions 8 (red) and 5' (black) as a function of the SRA/DNA ratio.

3.5 Kinetics of base flipping

To further characterize the SRA-induced flipping of mC6, we comparatively investigated the interaction of wild type and mutant SRA with the 5'- and 8-labeled HM and NM duplexes by stopped-flow. The interaction kinetics were monitored through the changes in the fluorescence intensity of the T* band of 3HCnt. For NM duplexes, a non resolvable fluorescence increase was observed upon mixing with SRA, indicating the reaction was essentially completed within the dead time (2 ms) of the instrument and thus, that the apparent bimolecular rate constant of the reaction is > 10^9 M^{-1} s^{-1} (**Figure** 6a and b). This very fast kinetics with an apparent rate constant greater than the "diffusion-limited" one is typical of binding of proteins to nucleic acids[40,41]. For HM duplexes, a similar non resolvable component was observed, but was followed by a much slower exponential increase of the fluorescence

intensity that was completed in 0.5 s (**Figure** 6a and b). At the end of the process, the final fluorescence increase was fully consistent with the QY increase seen in **Figure** 4a. This slow component, but not the initial non resolvable component, disappeared when the HM duplexes were mixed with the G448D mutant (**Figure** 6c), strongly indicating that this slow component can be attributed to the kinetics of mC6 base flipping. To further corroborate this attribution, we monitored the interaction kinetics of SRA with the 3HCnt-labeled HM duplexes, using SRA/DNA ratios varying from 5:1 to 25:1, and fitted the kinetic traces to single exponential functions. The observed rate constants were found to be independent of the concentration of SRA (**Figure** 6d), indicating that the flipping is a first-order reaction. This reaction order was fully expected as the flipping reaction can be envisioned as a conformational rearrangement that occurs after formation of the intermolecular complex of SRA with the HM duplex.

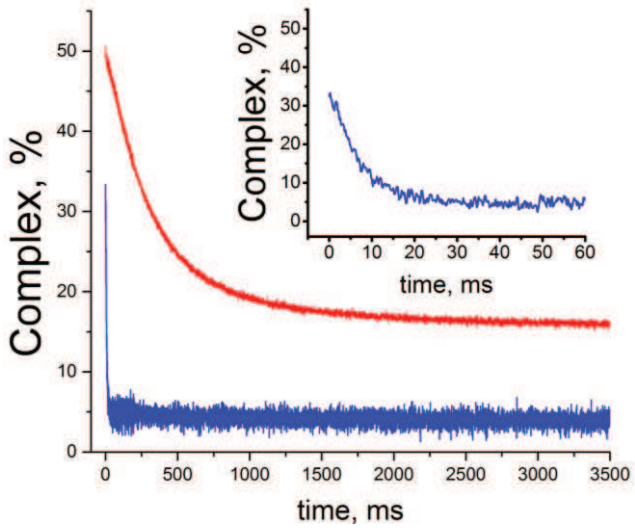

Figure 7. Dissociation kinetics of the complexes of SRA with HM (red) and NM (blue) duplexes labeled with 3HCnt at position 5'. The kinetics traces were recorded by stopped-flow after addition of an excess of ctDNA to the complexes. The concentration of HM or NM duplexes was 0.3 µM. The SRA concentration was 1.8 and 3.6 µM for having ~50% of complex with HM and NM duplexes, respectively. The concentration of ctDNA was 600 µM, as expressed in nucleotides. The measured fluorescence intensity was converted in percentage of 3HCnt-labeled duplexes bound to SRA. Inset: Highlight of the kinetic trace recorded with the NM-labeled duplex during the first 60 ms.

Next, we performed dissociation experiments by adding an about 80-fold excess of calf thymus DNA (ctDNA) to preformed complexes of SRA with HM or NM duplexes labeled at the 5' position (**Figure** 7). Addition of ctDNA to a SRA/NM complex leads to a fast fluorescence decrease, likely related to its dissociation, with a rate constant of 150 s^{-1}. Under similar conditions, a much slower rate constant of 2.9 s^{-1} was observed when ctDNA was added to a complex of SRA with HM duplex. This observed rate constant was found to be only weakly dependent on ctDNA concentration (data not shown), indicating that the slower reaction rate

can be considered as first order, and likely describes the flipping back of the mC6 into the HM duplex. Comparison of the dissociation curves obtained with HM and NM duplexes further suggests that the flipping back of the mC6 residue is the rate-limiting step and is immediately followed by the dissociation of the complex. Taken together, the kinetic data clearly confirm that the 3HCnt at position 8 and 5' can monitor the SRA-induced flipping of the mC6 residue, allowing for the first time, the determination of the rate constants associated with the flipping reaction as well as its back reaction.

4. DISCUSSION

Base flipping in nucleic acids is a fundamental phenomenon. Here we were able, for the first time, to monitor in diluted solution and real time the flipping of the mC6 residue of a HM duplex promoted by the SRA domain of UHRF1. This was achieved by inserting an environment-sensitive fluorescent nucleotide analogue 3HCnt at either position 8 or 5'. The 3HCnt probe at these two positions marginally perturbs the binding of SRA and preserves the preferential binding to HM over NM duplex (**Figure** 2). The flipping of the mC6 residue in HM duplexes was observed to strongly increase the T* emission band and decrease the N*/T* ratio of 3HCnt at these positions (**Figure** 3 and 4). Stopped-flow studies further reveal that the kinetics of mC6 flipping is much slower than the kinetics of SRA binding to the duplex (**Figure** 6). Importantly, the strong spectroscopic changes as well as the slow component in the kinetic traces disappear when the HM duplex is replaced by a NM duplex or the SRA domain by a G448D SRA mutant unable to execute base flipping (**Figure** 5), clearly supporting that the observed spectroscopic changes upon SRA binding were related to base flipping.

As the 3HCnt undergoes an irreversible ESIPT reaction with a fast proton transfer rate constant [42] leading to rapid accumulation of the T* form, the observed spectroscopic changes with SRA likely result from a decrease of the stacking interactions of the T* form of the probe with G and C neighbors[25]. These decreased stacking interactions could be rationalized by considering the 3D structure of the complex of SRA with the HM duplex[17]. In this complex, the Arg491 residue of SRA is inserted into the void left by the flipped mC6 residue in DNA and forms tight contacts with the C5 and G7 residues, as well as with the G5' and G6' residues. Thus, when 3HCnt is at position 8, the contacts of Arg491 with G7 likely reduce its ability to dynamically quench the 3HCnt probe, explaining the increase in the emission quantum yield of 3HCnt. Similarly, when 3HCnt is at 5' position, the interaction of Arg491 with G6' likely restricts the dynamic quenching of 3HCnt by this residue.

This strong sensitivity of 3HCnt to mC6 base flipping appears quite unique, since 2-aminopurine, an established probe, did not sense the base flipping induced by UHRF1[24]. Nevertheless, 3HCnt's duplex position is critical to observe relevant response. Indeed, by labeling positions 5, 7 or 6', 3HCnt was found to clearly increase the affinity for SRA and suppress the preferential binding to HM duplex, likely as a result of the multiple contacts of the nucleobases at these positions with the SRA amino acids[17]. These multiple contacts may restrict the dynamic quenching of 3HCnt by its neighbors, explaining the strong changes in the QY and N*/T* ratio at these positions for both HM and NM duplexes.

Using 3HCnt at position 8 or 5', we were able to monitor the kinetics of interaction of SRA with its DNA target and reveal, for the first time, the kinetics of base flipping. The interaction of SRA with the duplexes was found to be faster than a "diffusion-limited" reaction, suggesting that it proceeds through a two-step "bind-and slide" mechanism (scheme 1), as classically described for protein/DNA interactions [40,41,43].

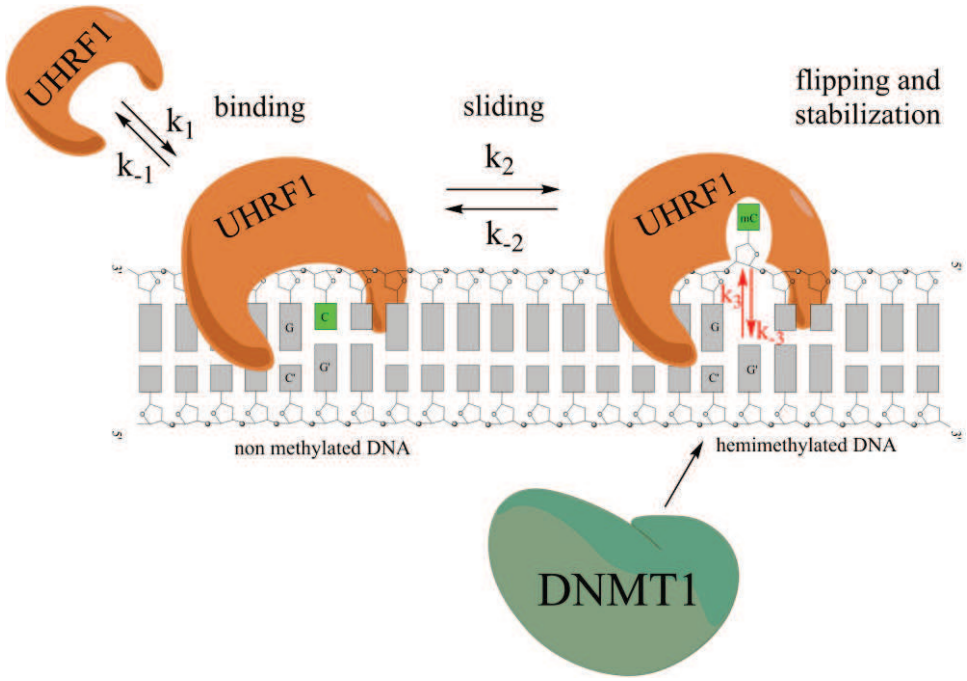

Scheme 1. Proposed mechanism for the interaction of SRA with DNA duplexes. SRA interacts with the duplexes through a fast two-step "bind-and slide" mechanism. At CpG recognition sites, SRA flips the methylated cytosines with rate-limiting kinetics that stabilize the binding of SRA to the CpG sites and allows recruiting DNMT1.

In this mechanism, the protein binds nonspecifically to the duplex, and then slides to the CpG recognition site. As the sliding corresponds to a one-dimensional diffusion, this mechanism reduces the dimensionality of the search, explaining why apparent rate constants faster than diffusion-limited rate constants, are obtained. Due to the inability to kinetically resolve the binding reaction, we could not determine the values of k_1, k_2, k_{-1} and k_{-2}. In contrast,

as the flipping reaction was much slower, it could be represented as the third step in scheme 1. The kinetic rate constants were determined to be $k_3 = 10\ s^{-1}$ and $k_{-3} = 2.9\ s^{-1}$. From the ratio of these values, it can be deduced that the flipping step and the accompanying conformational changes stabilize the complex by about 3.5-fold. This stabilization is in very good agreement with the four-fold increase in affinity observed for HM over NM duplex[24]. Importantly, comparison of the dissociation experiments with NM and HM duplexes (**Figure** 7) indicates that the k_{-3} value is much smaller than the k_{-2} and k_{-1} values. This suggests that the lifetime of UHRF1 bound to a CpG site in HM duplexes is much longer than in NM duplexes. This obviously increases the probability of recruiting DNMT1, in order to duplicate the DNA methylation profile. In contrast, the much shorter lifetime of SRA bound to NM duplexes is consistent with a reader role of SRA, which is able to slide rapidly along the DNA to scan for hemi-methylated CpG sites [44,45].

In conclusion, the environmentally sensitive fluorescent nucleoside analogue 3HCnt appears to be a unique tool for the high sensitivity monitoring of SRA-induced flipping of methylcytosine and its dynamics. This tool will likely facilitate studying the cooperation of SRA with other domains of UHRF1, *e.g.,* the tandem tudor domain (TTD) that shows affinity for the methylated lysine at position 9 of histone H3 [46]. As UHRF1 ensures a link between DNA methylation and histone methylation thanks to the readout capacities of both its SRA domain and TTD [22,44,47], questions whether the different structural domains cooperate to regulate the affinity of each domain to its target site arise. Consequently, there is a great need to investigate how the SRA domain flips out the methylated cytosine in connection with other putative domains of the UHRF1 protein and/or its partners, such as DNMT1. Tools, such as 3HCnt, will likely shed light on these events and will be of help to find inhibitors of mC flipping by UHRF1. Such inhibitors may be useful to prevent DNA methylation pattern inheritance in cancer cells leading for instance to re-expression of tumor suppressor genes through the hindrance to UHRF1 functions[48,49].

ASSOCIATED CONTENT

Supporting Information

Thermal denaturation, quantum yield, N*/T* ratio, and isothermal titration calorimetry analytical data. This material is available free of charge via the Internet at http:// pubs.acs.org.

AUTHOR INFORMATION

Corresponding Author

*yves.mely@unistr.fr

ACKNOWLEDGEMENTS

We thank the ANR (ANR-12-BS08-0003-02) and the FRM (DCM20111223038) for financial support and fellowships to V.K. and N.P.F.B, as well as the French Infrastructure for Integrated Structural Biology (FRISBI) ANR-10-INSB-05-01.

REFERENCES

(1) Feinberg, A. P.; Tycko, B. *Nat. Rev. Cancer* **2004**, *4*, 143.

(2) Esteller, M. *N. Engl. J. Med.* **2008**, *358*, 1.

(3) Jones, P. a.; Baylin, S. B. *Cell* **2007**, *128*, 683.

(4) Laird, P. W. *Nat. Rev. Cancer* **2003**, *3*, 253.

(5) Ng, H.; Bird, A. *Genet. Dev.* **1999**, *9*, 158.

(6) Jenuwein, T.; Allis, C. D. *Science* **2001**, *293*, 1074.

(7) Berger, S. L.; Kouzarides, T.; Shiekhattar, R.; Shilatifard, A. *Genes Dev.* **2009**, *23*, 781.

(8) Berger, S. L. *Nature* **2007**, *447*, 407.

(9) Lorincz, M. C.; Dickerson, D. R.; Schmitt, M.; Groudine, M. *Nat. Struct. Mol. Biol.* **2004**, *11*, 1068.

(10) Kouzarides, T. *Cell* **2007**, *128*, 693.

(11) Li, B.; Carey, M.; Workman, J. L. *Cell* **2007**, *128*, 707.

(12) Spruijt, C. G.; Vermeulen, M. *Nat. Struct. Mol. Biol.* **2014**, *21*, 949.

(13) Bestor, T. H.; Ingram, V. M. *PNAS* **1983**, *80*, 5559.

(14) Bird, A. *Genes Dev.* **2002**, *16*, 6.

(15) Jeltsch, A. *Nat. Struct. Mol. Biol.* **2008**, *15*, 1003.

(16) Straussman, R.; Nejman, D.; Roberts, D.; Steinfeld, I.; Blum, B.; Benvenisty, N.; Simon, I.; Yakhini, Z.; Cedar, H. *Nat. Struct. Mol. Biol.* **2009**, *16*, 564.

(17) Avvakumov, G. V; Walker, J. R.; Xue, S.; Li, Y.; Duan, S.; Bronner, C.; Arrowsmith, C. H.; Dhe-Paganon, S. *Nature* **2008**, *455*, 822.

(18) Hashimoto, H.; Horton, J. R.; Zhang, X.; Bostick, M.; Jacobsen, S. E.; Cheng, X. *Nature* **2008**, *455*, 826.

(19) Bostick, M.; Kim, J. K.; Estève, P.-O.; Clark, A.; Pradhan, S.; Jacobsen, S. E. *Science* **2007**, *317*, 1760.

(20) Arita, K.; Ariyoshi, M.; Tochio, H.; Nakamura, Y.; Shirakawa, M. *Nature* **2008**, *455*, 818.

(21) Qian, C.; Li, S.; Jakoncic, J.; Zeng, L.; Walsh, M. J.; Zhou, M. M. *J. Biol. Chem.* **2008**, *283*, 34490.

(22) Rottach, A.; Frauer, C.; Pichler, G.; Bonapace, I. M.; Spada, F.; Leonhardt, H. *Nucleic Acids Res.* **2009**, *38*, 1796.

(23) Frauer, C.; Hoffmann, T.; Bultmann, S.; Casa, V.; Cardoso, M. C.; Antes, I.; Leonhardt, H. *PLoS One* **2011**, *6*, 1.

(24) Greiner, V. J.; Kovalenko, L.; Humbert, N.; Richert, L.; Birck, C.; Ruff, M.; Zaporozhets, O. A.; Dhe-Paganon, S.; Bronner, C.; Mély, Y. *Biochemistry* **2015**, *54*, 6012.

(25) Dziuba, D.; Postupalenko, V. Y.; Spadafora, M.; Klymchenko, A. S.; Guérineau, V.; Mély, Y.; Benhida, R.; Burger, A. *J. Am. Chem. Soc.* **2012**, *134*, 10209.

(26) Kuznetsova, A. a.; Kuznetsov, N. a.; Vorobjev, Y. N.; Barthes, N. P. F.; Michel, B. Y. B. Y.; Burger, A.; Fedorova, O. S. *PLoS One* **2014**, *9*, e100007.

(27) Klymchenko, A. S.; Demchenko, A. P. *J. Am. Chem. Soc.* **2002**, *124*, 12372.

(28) Kilin, V.; Glushonkov, O.; Herdly, L.; Klymchenko, A.; Richert, L.; Mely, Y. *Biophys. J.* **2015**, *108*, 2521.

(29) Demchenko, A. P.; Tang, K. C.; Chou, P. T. *Chem. Soc. Rev.* **2013**, *42*, 1379.

(30) Delagoutte, B.; Lallous, N.; Birck, C.; Oudet, P.; Samama, J. P. *Acta Crystallogr. Sect. F Struct. Biol. Cryst. Commun.* **2008**, *64*, 922.

(31) Achour, M.; Mousli, M.; Alhosin, M.; Ibrahim, A.; Peluso, J.; Muller, C. D.; Schini-Kerth, V. B.; Hamiche, A.; Dhe-Paganon, S.; Bronner, C. *Biochem. Biophys. Res. Commun.* **2013**, *430*, 208.

(32) Tomin, V. I.; Jaworski, R. **2014**, *81*, 360.

(33) Tomin, V. I.; Javorski, R. *Opt. Spectrosc.* **2007**, *103*, 952.

(34) Vuilleumier, C.; Maechling-Strasser, C.; Gérard, D.; Mély, Y. *Anal. Biochem.* **1997**, *244*, 183.

(35) Breslauer, K. J. In *Energetics of Biological Macromolecules*; Michael L. Johnson, G. K. A. B. T.-M. in E., Ed.; Academic Press: New Jersey, USA., 1995; Vol. 259, pp 221–242.

(36) Spadafora, M.; Postupalenko, V. Y.; Shvadchak, V. V.; Klymchenko, A. S.; Mély, Y.; Burger, A.; Benhida, R. *Tetrahedron* **2009**, *65*, 7809.

(37) Rochel, N.; Ciesielski, F.; Godet, J.; Moman, E.; Roessle, M.; Peluso-Iltis, C.; Moulin, M.; Haertlein, M.; Callow, P.; Mély, Y.; Svergun, D. I.; Moras, D. *Nat. Struct. Mol. Biol* **2011**, *18*, 564.

(38) Lakowicz, J. R. *Principles of Fluorescence Spectroscopy*; Springer: New York, NY, USA, 2006.

(39) Maillot, S.; Carvalho, A.; Vola, J.-P.; Boudier, C.; Mély, Y.; Haacke, S.; Léonard, J. *Lab Chip* **2014**, *14*, 1767.

(40) Von Hippel, P. H.; Berg, O. G. *J. Biol. Chem.* **1989**, *264*, 675.

(41) Berg, O. G.; Winter, R. B.; von Hippel, P. H. *Biochemistry* **1981**, *20*, 6929.

(42) Dziuba, D.; Karpenko, I. A.; Barthes, N. P. F.; Michel, B. Y.; Klymchenko, A. S.; Benhida, R.; Demchenko, A. P.; Mely, Y.; Burger, A. *Chemistry* **2014**, *20*, 1998.

(43) Winter, R. B.; Berg, O. G.; von Hippel, P. H. *Biochemistry* **1981**, *20*, 6961.

(44) Bronner, C.; Fuhrmann, G.; Chedin, F. L.; Macaluso, M.; Dhe-Paganon, S. *Genet. Epigenet.* **2010**, *2009*, 29.

(45) Hashimoto, H.; Vertino, P. M.; Cheng, X. *Epigenomics* **2010**, *2*, 657.

(46) Rothbart, S. B.; Krajewski, K.; Nady, N.; Tempel, W.; Xue, S.; Badeaux, A. I.; Barsyte-lovejoy, D.; Martinez, J. Y.; Bedford, M. T.; Fuchs, S. M.; Arrowsmith, C. H.; Strahl, B. D. *Nat. Struct. Mol. Biol* **2012**, *19*, 1155.

(47) Liu, X.; Gao, Q.; Li, P.; Zhao, Q.; Zhang, J.; Li, J.; Koseki, H.; Wong, J. *Nat. Commun.* **2013**, *4*, 1563.

(48) Alhosin, M.; Sharif, T.; Mousli, M.; Etienne-Selloum, N.; Fuhrmann, G.; Schini-Kerth, V. B.; Bronner, C. *J. Exp. Clin. Cancer Res.* **2011**, *30*, 41.

(49) Bronner, C.; Krifa, M.; Mousli, M. *Biochem. Pharmacol.* **2013**, *86*, 1643.

Supporting Information

Dynamics of methylated cytosine flipping by UHRF1

Vasyl Kilin,[†] Nicolas P.F. Barthes,[‡] Benoît Y. Michel,[‡] Christian Boudier ,[†] Valeriy Yashchuk,[ħ] Marc Mousli,[†] Marc Ruff,[ǁ] Florence Granger,[ǁ] Yitzhak Tor,[§] Christian Bronner,[ǁ] Alain Burger,[‡] Yves Mély,[*,†]

Thermal denaturation measurements

The melting curves were monitored by the absorbance changes at 260 nm and converted into a plot of α versus temperature, where α represents the fraction of strands in the duplex state. The melting temperatures were extracted by fitting the first derivative of these curves by a Gaussian (Table S1).

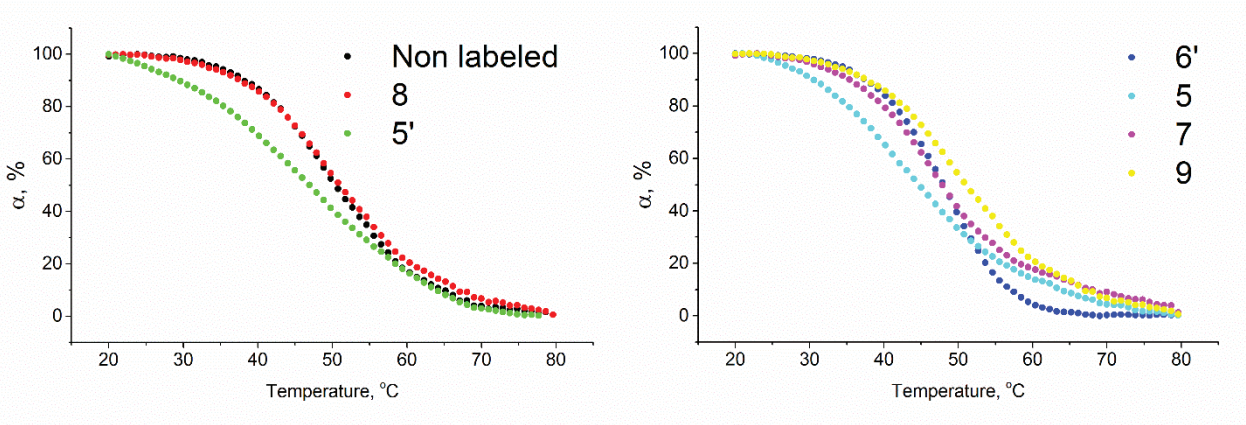

Figure S1. Thermal denaturation curves. The curves are expressed in fraction α of strands in the duplex state versus temperature for the non labeled duplex (A, black) and the duplexes labeled by 3HCnt at various positions (A and B). The concentration of duplexes was 2 μM in 20 mM PBS buffer, 50 mM NaCl, EDTA 1 mM, pH = 7.4.

Table S1. Melting temperatures of 3HCnt-labeled duplexes

Position	Non labeled	5	7	8	9	5’	6’
Tm, °C	50	48	47	48	51	47	48
ΔTm , °C	-	2	2	2	-1	3	2

Quantum yield and N*/T* ratio of the 3HCnt-labeled duplexes

Table S2. Quantum yield and N*/T* ratio of 3HCnt-labeled DNAs in the absence and the presence of SRA[1]

Position	Methylation status	QY,% $_{DNA}$ free[2]	QY,% $_{SRA/DNA}$ complex[2]	$\frac{QY_{SRA/DNA}}{QY_{DNA}}$	N*/T* $_{DNA}$ free	N*/T* $_{SRA/DNA}$ complex	$\frac{N/T_{SRA/DNA}}{N/T_{DNA}}$
Free 3HC		5.5			0.84		
G3	HM	0.55	0.7	1.3	0.19	0.18	0.95
	NM	0.45	0.5	1.1	0.20	0.18	0.90
C5	HM	1.2	4.6	3.8	0.17	0.08	0.47
	NM	1.2	3.9	3.2	0.17	0.08	0.47
G7	HM	1.2	7.85	6.6	0.14	0.05	0.36
	NM	1.2	6.0	5.1	0.136	0.06	0.44
C8	HM	0.9	1.7	1.9	0.145	0.10	0.69
	NM	0.8	0.9	1.1	0.15	0.14	0.93
A9	HM	2.2	2.8	1.25	0.11	0.10	0.91
	NM	2.1	2.7	1.3	0.115	0.10	0.87
G5'	HM	0.5	1.4	2.7	0.19	0.06	0.32
	NM	0.5	0.7	1.45	0.19	0.14	0.74
G6'	HM	1.9	4.9	2.55	0.12	0.06	0.50
	NM	1.9	4.3	2.2	0.12	0.06	0.50

[1]Values are average of 5 experiments. Standard deviations are equal or less than 20 %,
[2] Quantum yield for labeled DNA was calculated with free 2-thienyl-3-hydroxychromone in buffer as a reference.

Binding of SRA to the non labeled HM duplex, as monitored by ITC

The binding of SRA with the non-labeled HM duplex was characterized by ITC. The binding reaction was found exothermic (Fig. S2 top), showing a 1:1 stoichiometry and an apparent affinity constant, $K_{app} = 1.4(\pm 0.3)\times10^6$ M^{-1} (Fig. S2 bottom), in good agreement with the values in the literature [21,24].

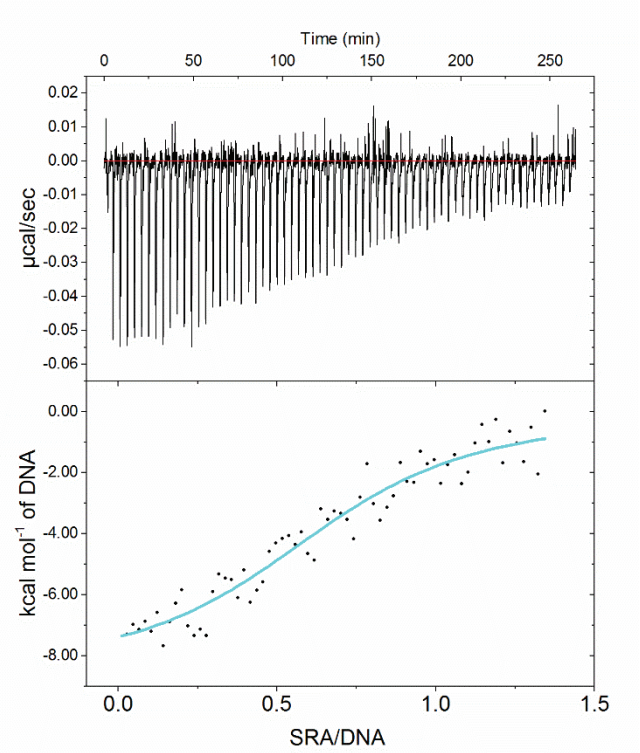

Figure S2. Binding of SRA to non-labeled HM duplex, as monitored by ITC. Heat release as a function of the injection time (top) and the SRA/duplex molar ratio (bottom). The cyan line corresponds to the fit with a 1:1 binding model and the binding constant given in the text.

Binding parameters of SRA and its G448D mutant for the 3HCnt-labeled duplexes

Table S3. Apparent affinity constants of SRA and its G448D mutant for the 3HCnt-labeled DNAs

Position	Methylation status of C6	Ka SRA ($\times 10^{-6}$), M^{-1}	$\frac{K_{a\ labeled}}{K_{a\ nonlabeled}}$	Ka SRA-G448D ($\times 10^{-6}$), M^{-1}
Non modified	HM	1.4	1.0	
G3	HM	1.4	1.0	
	NM	1.0		
C5	HM	20	14	
	NM	21		
G7	HM	6.1	4.3	
	NM	6.9		
C8	HM	2.5	1. 8	0.24
	NM	0.55		0.13
A9	HM	1.8	1.25	
	NM	1.0		
G5'	HM	2.3	1.6	0.19
	NM	0.28		0.18
G6'	M	33	23	
	NM	7.9		

Values are average of 3 experiments. Standard deviations are equal or less than 20 %. $K_{a\ labeled}/K_{a\ non\ labeled}$ describes the ratio of the apparent affinity constant of SRA for the labeled duplex as compared to the non labeled duplex.

9.4 Mechanism of 3HCnt sensitivity to SRA-induced base flipping

As it was discussed in Publication 1, the quantum yield and N/*T* ratio of 3HCnt were found to be sensitive to the SRA-induced flipping of 5-methylcytosine. The N*/T* ratio changes were found to be related mostly to the T* band intensity changes. The equation which describes the ESIPT reaction equilibrium using eq.6.4 and eq.6.5 could be written as:

$$\frac{N^*}{T^*} = \frac{k_R^T + k_{nR}^T + k_- + k_Q}{k_+} \qquad eq.9.1$$

The predominance of the T* band in the emission spectra suggests that the direct proton transfer rate is significantly greater than the sum of the rates describing the deactivation of the T* excited state $k_+ \gg k_R^N + k_{nR}^N + k_Q > k_-$.

The observed spectroscopic changes likely result from a decrease of the stacking interactions with the T* form of the probe, as the 3HCnt residue is highly quenched by stacking interactions with its G and C neighbors (Dziuba et al. 2012), and as it undergoes an irreversible ESIPT reaction with a fast proton transfer rate constant (Dziuba et al. 2014) leading to rapid accumulation of the T* form. These decreased stacking interactions could be rationalized by considering the 3D structure of the complex of SRA with the HM duplex (Avvakumov et al. 2008). In this complex, the Arg491 residue of SRA is inserted into the void left by the flipped mC6 residue in DNA and forms tight contacts with the C5 and G7 residues, as well as with the G5' and G6' residues. Thus, when 3HCnt is at position 8, the contacts of Arg491 with G7 likely reduce its ability to dynamically quench the 3HCnt residue, explaining the increase in the emission quantum yield of 3HCnt. Similarly, when 3HCnt is at 5' position, the interaction of Arg491 with G6' likely restricts the dynamic quenching of 3HCnt by this residue.

In order to further clarify the mechanism of 3HCnt sensitivity to SRA-induced base flipping, time-resolved measurements were performed. For HM and NM DNA containing 3HCnt at position 8 or 5', decays were recorded at the T* band. For all samples, up to 4 fluorescence lifetimes were recovered in line with the multiexponential decay reported earlier for this chromophore (Das et al. 2009) Comparison of the mean lifetime and quantum yield values further revealed the presence of very large amounts (~90%) of dark species.

Table 2. Time-resolved spectroscopy data of 3HCnt in free DNA and in the SRA/DNA complex

Sample	Labelling position	τ_1, ns	a_1	τ_2, ns	a_2	τ_3, ns	a_3	τ_4, ns	a_4	Tau mean	a_0
free DNAs	8, NM	0.02	**-1.00**	0.15	**0.080**	0.64	**0.039**	2.83	**0.012**	0.31	**0.869**
	8, HM	0.03	**-1.00**	0.20	**0.092**	0.75	**0.053**	3.32	**0.011**	0.40	**0.844**
	5', NM	0.04	**-1.00**	0.59	**0.043**	0.34	**0.018**	3.40	**0.004**	0.52	**0.943**
	5', HM	0.03	**-1.00**	0.19	**0.042**	0.69	**0.029**	3.08	**0.007**	0.39	**0.922**
Complex	8, NM+SRA	0.02	**-1.00**	0.25	**0.024**	1.22	**0.017**	4.87	**0.013**	0.65	**0.946**
	8, HM+SRA	0.03	**-1.00**	0.14	**0.058**	0.57	**0.068**	2.67	**0.044**	0.37	**0.830**
	5', NM+SRA	0.05	**-1.00**	0.29	**0.031**	1.38	**0.014**	5.18	**0.008**	0.63	**0.947**
	5', HM+SRA	0.03	**-1.00**	0.27	**0.062**	1.18	**0.044**	4.00	**0.016**	0.65	**0.878**

Final DNA concentrations were 4 µM and concentration of SRA was adjusted to have 80% of complex. Experiments were performed in the Spectroscopic Buffer. Emission was collected at maximum of T* band.

These values are comparable to those usually observed with 2Ap (Godet et al, 2011) and can be explained by the presence of neighboring G residues, which strongly quench the fluorescence of 3HCnt. As expected for an excited-state reaction such as ESIPT (Kilin et al. 2013), a short lifetime corresponding to a fast-rise component associated with a negative amplitude was observed for the T* form. Its value indicated that the ESIPT reaction occurs faster or within ~30 ps (corresponding to k_+), so that the T* form accumulated rapidly. This component was found to be independent on the presence of SRA, but it should be noted that the ~30ps value is close to the resolution of our set-up. Therefore, we cannot exclude that this parameter may be affected by SRA binding and base flipping. The longer lifetime components of 3HCnt were found to be similar in both HM and NM DNAs at 8 and 5' positions of labeling (Table 2). The interaction of SRA with 3HCnt-labelled DNAs induced only small changes in the lifetime values and their amplitudes. The observed changes appear rather erratic and can hardly be correlated with the changes in quantum yield. This is likely the consequence of the low emission of the labeled duplexes. In fact, the presence of more than 98% of species characterized by lifetimes shorter than 1 ns and the presence of a negative component likely hinder the accurate recovery of the short components. Therefore, our lifetime data in their current form do not provide further information on the mechanism of sensitivity of 3HCnt to base flipping. Femtosecond pump-probe and fluorescence down-conversion experiments will be required to

get more information on the system and the mechanism that governs the 3HCnt sensitivity to base flipping.

9.5 Mutagenesis studies

Crystallography studies of SRA/DNA complex unveiled a number of SRA residues interacting with DNA nucleotides and with 5-methylcytosine (Avvakumov et al. 2008). Among them, several were suggested to be of potential interest for mutagenesis studies (Avvakumov et al. 2008). For example, a mutation of Glycine 448, which is at the entrance of the binding pocket, could block the SRA flipping. Also two other residues, Arginine 491 and Asparagine 489, were suggested to be directly involved in the flipping of 5-methylcytosine or in the SRA ability to discriminate between hemi-methylated and symmetrically methylated DNAs. These three residues were mutated and their role in SRA-induced base flipping were studied by using 3HCnt-labeled HM and NM DNAs.

9.5.1 Mutant G448D SRA

Substitution of Glycine 448 by Aspartic acid (Mutant G448D) resulted in significant changes of SRA functions. The detailed studies of the interaction of G448D with the 3HCnt-labeled HM and NM DNAs are presented in Publication 1. Our data show that this mutant is able to bind DNA, but cannot flip methylcytosine.

Figure 9.5. Structure of the SRA binding pocket: simulation of Gly448 replacement by an Asp residue. (A) Wild-type SRA with accommodated 5-methylcytosine. In (B), the Gly 448 residue was replaced by an Asp. This creates a steric clash with the 5-methylcytosine in the pocket. The binding pocket is shown as a solvent-accessible surface.

In order to simulate the structure of this mutant, we used the PyMOL software. By replacing the Gly 448 residue with the relatively bigger Asp residue in the structure of the SRA/DNA

complex, we evidenced a steric clash between the Asp residue and mC (**Figure** 9.5). As a result, the Asn448 probably blocks the insertion of 5-methylcytosine in the binding pocket, explaining the inability of the G448D mutant to flip the mC residue.

9.5.2 Mutant R491A and N489A SRAs

In order to determine if Arginine 491 (**Figure 9.6**) and Asparagine 489 (**Figure 9.7**) residues play a key role in the SRA flipping function, we mutated these residues in SRA.

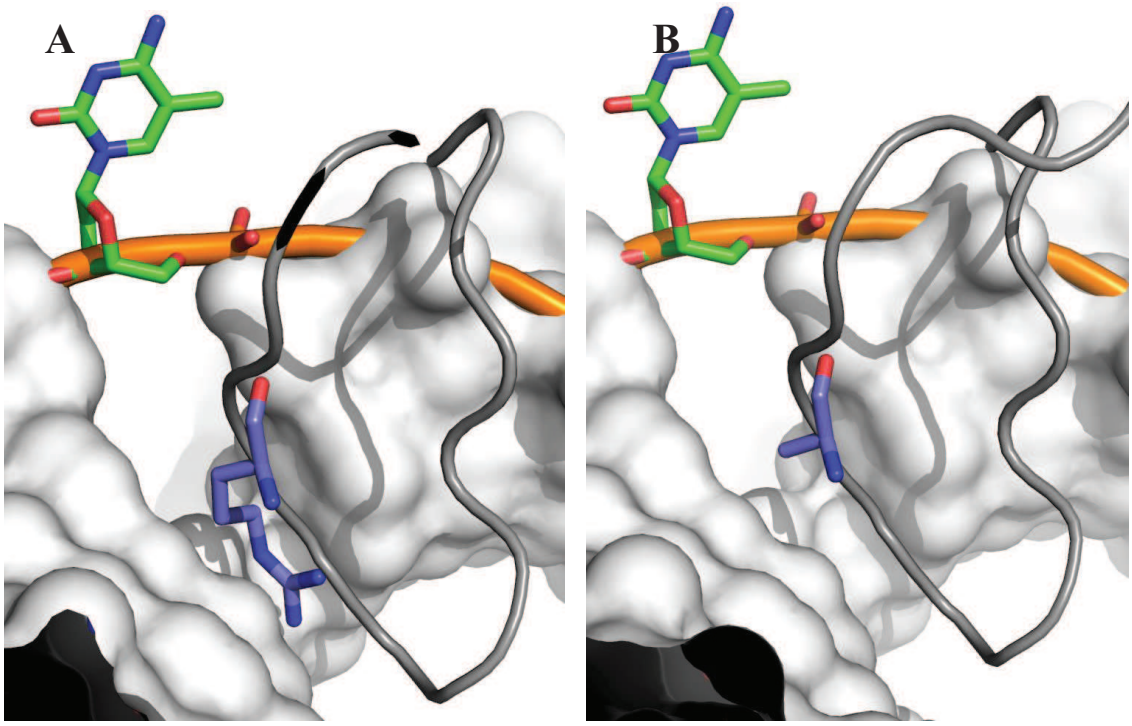

Figure 9.6. Simulation of Arg491 replacement by an Ala residue on the structure of SRA in interaction with DNA. (**A**) Wild-type SRA with higlighted Arginine 491 in blue color and NKR finger in light gray. (**B**) The same structure where Arginine 491 is substituted by an Alanine residue. The white surface represents solvent-accessible surface areas of DNA.

First of all, we performed binding studies of SRA mutants with DNA (**Figure 9.8**). The determined K_{app} values were in agreement with those obtained for the wild-type SRA, suggesting that these two mutations do not impact binding of SRA to DNA.
Next, the interaction of R491A SRA and N489A SRA with 3HCnt-labelled HM and NM DNAs was studied by steady-state (**Figure 9.9**) and time-resolved (data not shown) spectroscopy. The fluorescence response of 3HCnt to the interaction of R491A SRA and N489A SRA with HM and NM DNAs was similar to that of the wild-type SRA.

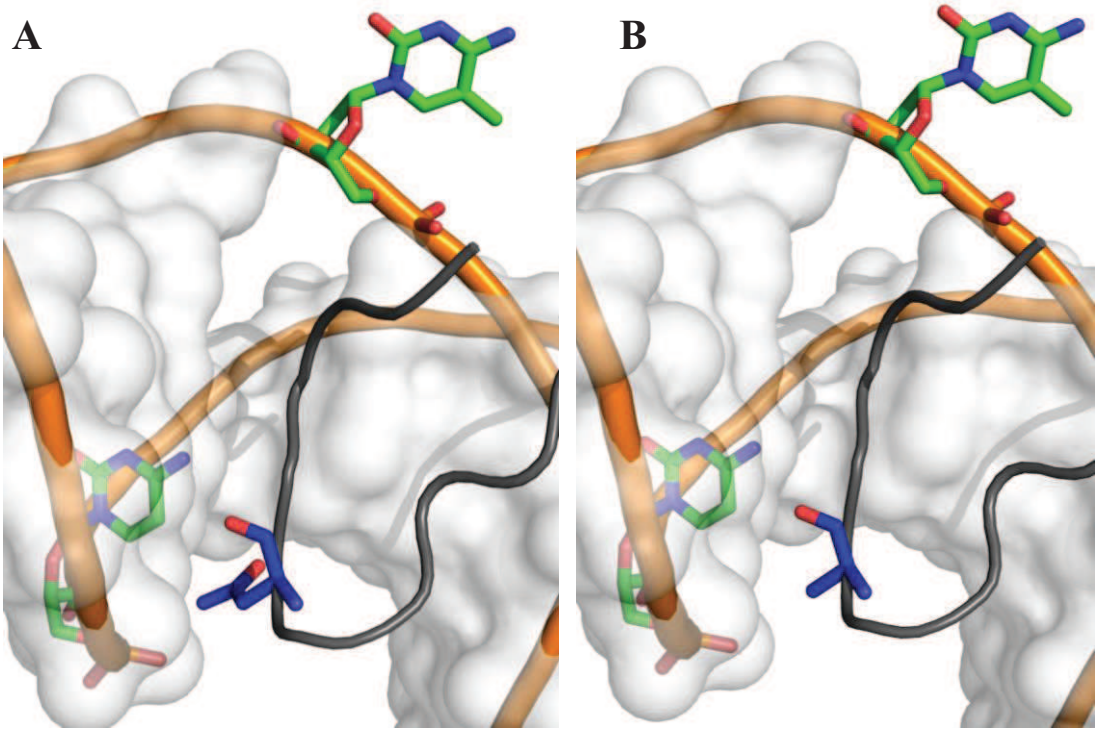

Figure 9.7. Simulation of Asn489 replacement by an Ala residue on the structure of SRA in interaction with DNA. (**A**) Wild-type SRA with higlighted Asparagine 489 in blue color, NKR finger in light gray. (**B**) The same structure where Asparagine 489 is substituted by Alanine residue. The white surface represents solvent-accessible surface areas of DNA. The 489 residue is close to the cytosine residue in the complementary strand of the HM duplex, which is the target for DNMT1.

Figure 9.8. Comparison of the apparent affinities of wild-type and mutant SRAs for 3HCnt-labeled HM and NM DNAs. Labelling positions were 8 (A) and 5' (B).

Similarly, the fluorescence lifetimes of 3HCnt in DNAs interacting with these mutants were in agreement with those obtained for the interaction with the wild-type SRA, suggesting that these two mutants are able to flip 5-methylcytosine.

Figure 9.9. Comparison of quantum yield changes upon interaction of wild-type and mutant SRA for 3HCnt-labeled HM and NM DNAs. Positions of labelling were 8 (**A**) and 5' (**B**).

Figure 9.10. Comparison of base flipping kinetics of wild-type and mutant SRAs on 3HCnt-labeled HM DNAs. Positions of labelling were 8 (**A**) and 5' (**B**).

To further investigate the role of Arg 491 and Asn 489 residues, we performed stopped-flow measurements. The base flipping kinetics of R491A SRA and N489A SRA on 3HCnt-labeled HM DNAs were found to be comparable to those of the wild-type SRA. The only noticeable

difference is the two-fold increase in flipping rate observed for R491A SRA as compared to the wild-type SRA (**Figure 9.10**)

Our data suggest that the Arg491 and Asn489 residues are not critical for the 5-methylcytosine flipping. As was shown by X-ray crystallography studies, Arg 491 interacts non-specifically with nucleotides in the vicinity of the gap created after mC flipping. Thus, Alanine at this position is likely able to induce similar nonspecific interactions. The increased flipping rate for R491A mutant may be related to the smaller size of Ala as compared to Arg (**Figure 9.6**) which may facilitate the insertion of the NKR finger in the DNA gap.

9.6 Interaction of SRA with symmetrically methylated 3HCnt-labelled DNA

The ability of SRA to distinguish between non-methylated, hemi-methylated and symmetrically methylated (BM) DNAs is critical for UHRF1 function as a fidelity factor of DNMT1.

Figure 9.11. Comparison of quantum yield changes upon interaction of wild-type and mutant SRAs with 3HCnt-labelled HM (red bars), NM (blue bars) and BM (cyanine bars) DNAs. Position of labelling was 8.

During replication of methylation patterns, the UHRF1 is expected to report on the methylation status of DNA to other proteins involved in DNA methylation maintenance. Our data showed that UHRF1 can signal hemi-methylated CpG sites through an increase in its residence time, when it is bound to these sites. In order to check if SRA binds to HM and BM by the same mechanism, we performed studies with BM DNA labelled at position 8.

As for other type of DNAs, we performed binding studies of wild type SRA and its mutants with BM DNA (data not shown). The determined K_{app} values were comparable with those shown on **Figure** 9.8 for HM DNAs, suggesting that SRA binds with similar affinities to HM and BM DNAs.

Steady-state spectroscopy showed that interaction of SRA with BM DNAs induce similar changes in quantum yield (**Figure 9.11**), suggesting that flipping of 5-methylcytosine may also occur in symmetrically methylated DNAs. According to the changes in quantum yields, it may be concluded that base flipping affects the same mC residue at position 6 than in HM duplexes. Nevertheless, it cannot be excluded that the mC at position 7' at the opposite strand may induce the same changes in the quantum yield.

Figure 9.12. Interaction kinetics of SRA derivatives with HM and BM DNAs. (A) Kinetics of interaction of wild–type SRA with HM and NM DNAs. (B) Kinetics of interaction of wild-type and mutant SRAs with BM DNA.

The kinetics of interaction of wild-type SRA and its mutants with BM and HM DNAs were comparatively studied by stopped-flow measurements (**Figure 9.12 A and B**). The main difference between HM and BM DNAs is the absence of slow kinetics on interaction with wild–type, R491A, and N489A SRAs. This suggests that base flipping is no more a rate-limiting kinetic step in BM DNAs. One possible explanation is that the mC at position 7' destabilizes the mC at position 6, so that the latter can be flipped immediately when the SRA slides along

the DNA sequence. As a result, the lifetime of SRA/BM-DNA complex is thought to be significantly shorter than that of SRA/HM-DNA complex, so that DNMT1 will not be recruited. Thus, a slow flipping kinetics by UHRF1 is selective for HM duplexes. This strengthened our kinetically-driven mechanism, where recruitment of proteins needed for maintenance of the methylation pattern only occurs for HM duplexes.

X Conclusions and perspectives

The biodiversity of organisms as well as the cellular differentiation within an individual organism are determined by epigenetic mechanisms that regulate the activity of the genome. These mechanisms lead to the establishment of epigenetic marks on DNA without affecting its sequence. These marks play a key role in gene expression, which strongly depends on the environment during development and life. In addition, changes in epigenetic patterns are involved in many common diseases, including cancers (Burdge & Lillycrop 2010). Among the epigenetic marks, DNA methylation is a heritable modification of the cytosine base, realized by covalent addition of a methyl group. This DNA methylation leads to specific silencing of gene expression and determines the uniqueness of the epigenome. Methylation patterns are copied during cell division. During DNA replication, the methylation pattern of the parent strand is transferred to the newly synthesized strand through the action of the DNA methyltransferase DNMT1 to give fully methylated DNA (bimethylated DNA, BM-DNA). A critical role in this respect is provided by UHRF1 that through its base flipping domain SRA directs DNMT1 onto the appropriate sites to faithfully reproduce the methylation pattern. Although a general mechanism was proposed, the different steps of DNA methylation involving UHRF1 and DNMT1 remain to be elucidated. Our project was to apply original environment-sensitive nucleobase analogs to address unanswered questions on the molecular mechanisms of DNA methylation by UHRF1.

In order to monitor the flipping of the methylated cytosine that is mediated by the SRA domain of UHRF1, we used several labelling strategies, which showed that only labelling outside of target methylated CpG has no effect on SRA-DNA interaction. Direct substitution of 5-methylcytosine by its structural fluorescent analog 5-methyl-2-pyrimidinone confirmed the high specificity of SRA for methylated cytosine evidenced by X-ray crystallography studies (Avvakumov et al. 2008), and particularly the importance of the hydrogen bonds between SRA and the NH_2 group at position 4 of 5-methylcytosine. Both our data and the previous attempt using 2Ap (Greiner et al. 2015) suggest that 5-methylcytosine can probably not be replaced by any fluorescent analog in the target CpG site to study the SRA-induced base flipping. By using 8-vinyl-2'-deoxyguanosine, a weakly quenched fluorescent nucleoside substituting G in the target methylated CpG site, we found that this probe could sense SRA/DNA interaction, but with low sensitivity to SRA induced base flipping. Probably, the steric clash between the vinyl group of 8vdG and residues of SRA prevent the NKR finger to flip mC. This indicated that in order to obtain a good response to SRA base flipping activity, the fluorescent nucleoside analog should possess outstanding environment sensitivity and minimally perturb the binding site.

These requirements were satisfied by using an environment-sensitive fluorescent nucleoside analog based on 2-thienyl-3-hydroxychromone (3HCnt) (Dziuba et al. 2012), which acts as a universal nucleoside. Due to an excited state intramolecular proton transfer (ESIPT), this fluorescent nucleobase exhibits two excited-state forms, namely the initially excited normal (N*) and tautomeric (T*) forms, which are highly sensitive to environment changes. This 3HC-based nucleoside analog was inserted at various positions in hemi-methylated DNAs (HM-DNA), as well as in the corresponding non-methylated (NM-DNA) sequences used as controls. Comparison of the responses obtained on HM and NM sequences on binding to the SRA domain of UHRF1 revealed that the probe response was specifically sensitive to the flipping of the methylated cytosine at certain positions. This conclusion was strengthened by using SRA mutants unable to flip the methylcytosines. Correlation of these data with the reported crystallographic structure of the SRA-DNA complex (Avvakumov et al. 2008) suggested that the observed response resulted from the sensitivity of the 3HC-based nucleoside to the flipping of methylcytosine. Thus, to our knowledge, we built up for the first time an assay able to sensitively monitor the UHRF1-induced base flipping.

Moreover, we monitored the kinetics of SRA interaction with DNA. Using the 3HCnt-labeled DNA, we were able for the first time to measure the kinetics of interaction of SRA with its DNA target as well as the kinetics of base flipping. The presence of a single methyl group on the target cytosine was found to remarkably modulate the kinetics of SRA/DNA interaction. Association and dissociation stopped-flow studies showed that SRA interaction with DNA is initiated by a non-specific binding of the SRA domain to the duplex, followed by sliding to the CpG recognition site. Only recognition sites with methylated cytosines were found to be associated with a rate-limiting base flipping. As a consequence, the lifetime of the complex of UHRF1 bound to a CpG site in HM duplexes is much longer than in NM duplexes or BM duplexes. This obviously increases the time and the probability to recruit DNMT1, in order to duplicate the DNA methylation profile (**Figure 9.13**). Therefore, our kinetic study constitute a first experimental demonstration on how UHRF1 could serve as a fidelity factor of DNMT1.

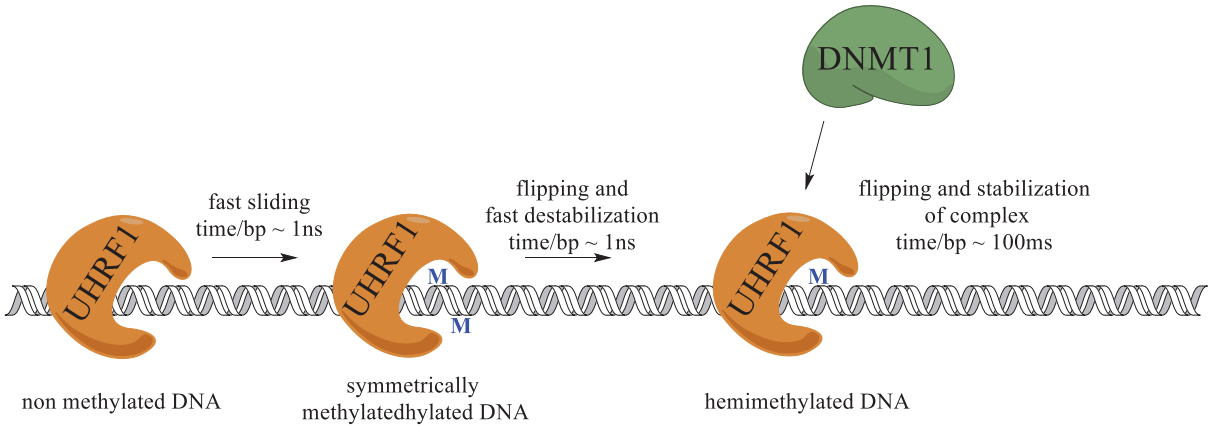

Figure 9.13. Schematic representation of the mechanism by which UHRF1 directs DNMT1 to hemimethylated DNA. Time/bp denotes the time spent by UHRF1 per base pair. For NM and BM duplexes, this time is estimated from typical rates of 1D protein diffusion on DNA (Bloomfield 2001).

In conclusion, the environment-sensitive 3HCnt fluorescent nucleoside analog appears as a unique tool to monitor with high sensitivity the SRA-induced flipping of methylcytosine and its dynamics. This approach will allow monitoring the role of the other domains of UHRF1 in base flipping as well as the cooperation of SRA with other proteins involved in DNA epigenetic pattern regulations. In particular, the UHRF1/DNMT1 tandem could be studied to determine the mechanism of both proteins in base flipping. In addition, 3HCnt-labeled DNAs could be used to study with high sensitivity the activity of the UHRF2 protein, which is thought to recognize and flip hydroxymethylcytosine. Thus, the 3HCnt nucleotide appears as a multiparametric probe that could sense conformational changes in CpG sites, without perturbing the activity of CpG specific proteins and enzymes. By extension, the response of 3HCnt to base flipping could potentially be used to monitor the activity of any methyltransferase.

In addition, kinetic studies showed new insights on the mechanism by which UHRF1 could recruit the Dnmt1 enzyme in the duplication of DNA methylation patterns. The increased residence time of SRA on HM CpG sites could be potentially used to map DNA methylation patterns by single-molecule techniques, using SRA labeled with a bright fluorescent probe (Alexa648, Cy3). The labeled SRA will slide rapidly through NM regions and will be stabilized on HM CpG sites. Due to the high sliding rates of SRA on NM DNA and the set up limitations, the fluorescence from the labeled SRA will be detected only when SRA will be stabilized on a HM CpG site. The binding/unbinding of SRA proteins on different methylated CpG sites in

single molecule experiments will result in intensity traces with blinking events. Thus, blinking super resolution techniques (Steinhauer et al. 2013) should be able to identify methylated profiles with single nucleotide resolution.

The specific response of 3HCnt to SRA-induced base flipping will also be helpful to find inhibitors of mC flipping by UHRF1. Increasing number of studies suggest that UHRF1 plays central role in the maintenance of DNA methylation patterns (Avvakumov et al. 2008; Arita et al. 2008; Bronner et al. 2009), in synergy with multiple partners (Bronner et al. 2013). Thus, inhibition of UHRF1 activity might have a significant effect on DNA methylation replication. Such inhibitors may be useful to prevent DNA methylation pattern inheritance in cancer cells leading for instance to re-expression of tumor suppressor genes (Alhosin et al. 2011; Bronner et al. 2013). Application of 3HCnt-based assays for search of UHRF1 inhibitors could be extended to other proteins with base flipping activity. Additionally, since 3HCnt labeled DNA allows the study of the UHRF1/DNMT1 tandem, it is possible to search inhibitors of DNMT1 through inhibiting DNMT1/UHRF1 interaction which would be of great interest as alternative to already developed inhibitors of DNMT1/DNA interaction.

Thus, 3HCnt nucleotide opens a wide range of applications and potentially allows the design of assays for identifying therapeutic molecules.

Appendix

In addition to my dissertation work, I had the opportunity to collaborate on other projects that are presented in papers shortly introduced below:

1) Proceedings Article: "Two photon fluorescence imaging of lipid membrane domains and potentials using advanced fluorescent probes"

The development of dyes for sensing biomembrane properties is one of the main research topics of our research team. Fluorophores sensitive to the surface charge in lipid bilayers are useful in many ways, and notably for apoptosis detection. In the present study, we showed that the lifetimes of the 3HC-based membrane probe F2N12S that was designed to label the external leaflet of the plasma membrane, could be used to sensitively probe the composition and the physicochemical properties of model and biological lipid membranes. Due to both an ESIPT reaction and hydration by the solvent, F2N12S shows three different excited-state forms, namely N*, H-N* and T* that exhibit different spectral properties. Moreover, the relative concentrations of these three forms are exquisitely sensitive to the environment, and notably to the polarity, the electric field and the order of the lipid bilayer. As a consequence, the ratio of the emission bands as well as the fluorescence lifetimes appear as sensitive parameters to report on the membrane environment. Using model lipid bilayers (LUVs, GUVs), we have shown that these parameters depend on the lipid surface charge and the lipid order. Using two-photon ratiometric imaging and FLIM, F2N12S was studied in living cells in order to determine, whether this probe can be used to monitor changes in the plasma membrane composition and physicochemical properties.

2) Article "Fluorescence Lifetime Imaging of Membrane Lipid Order with a Ratiometric Fluorescent Probe"

Based on the aforementioned sensitivity of lifetimes of F2N12S probe to the composition and the physicochemical properties of model and biological lipid membranes, we used this probe to monitor lateral segregation of lipids into liquid-ordered (Lo) and -disordered (Ld) phases in lipid membranes. A variety of plasma membrane biological functions, such as regulation of membrane protein activity, membrane trafficking, and signal transduction, are thought to be related to the lateral segregation of lipids into phases. In the present work, we showed that these two phases could be discriminated by the time-resolved parameters of F2N12S in model and cell membranes. We performed a detailed study of the time-resolved fluorescence parameters of this probe in lipid vesicles of controlled lipid composition by using time-resolved

spectroscopy. Both the long and mean lifetime values of the T* form of F2N12S were found to differ by two-fold between Ld and Lo phases. To understand the mechanism of sensitivity of lifetimes to lipid phases, we performed Decay Associated Spectra (DAS) measurements. These experiments showed that the sensitivity of time-resolved parameters towards lipid phases results from the restriction in the relative motions of the two aromatic moieties of F2N12S imposed by the highly packed Lo phase. This differs from the changes in the ratio of the two emission bands between the two phases, which mainly resulted from the decreased hydration in the Lo phase. Next, we showed that the strong difference in lifetimes between the two phases allows performing high contrast imaging by fluorescence lifetime imaging microscopy (FLIM) on giant unilamellar vesicles (GUVs). As a consequence of the clear difference in lifetimes between the two phases, the partition coefficient of F2N12S between the two phases was calculated from GUVs images. Finally, we performed FLIM imaging of F2N12S-labeled live HeLa cells and confirmed that the plasma membrane was mainly in a Lo-like phase. Furthermore, the two phases were found to be homogeneously distributed all over the plasma membrane, indicating that they are highly mixed at the spatiotemporal resolution of the FLIM setup. Further, we showed that time-resolved parameters could be used to monitor changes in the composition of cell membranes and to detect apoptosis.

3) Article “Counterion-enhanced cyanine dye loading into lipid nano-droplets for single-particle tracking in zebrafish”

The availability of nanomaterials for imaging purposes has generated a variety of methods for imaging, with features including improved brightness, inertness to their microenvironment and a more even distribution. Nanoparticles (NPs), in contrast to molecular probes, are not cytotoxic in most cases and do not suffer from nonspecific binding by cellular biomacromolecules or unwanted sequestration. All known NPs have photo-stabilities that are distinctly better than those of molecular probes. Many NPs can be easily internalized into cells and tissues and can be even targeted to specific sites. They are many types of NPs made from silica and organically-modified silica, hydrophobic and hydrophilic organic polymers, semiconducting organic polymers, quantum dots, carbonaceous nanomaterials including carbon (quantum) dots, carbon nano-clusters and nanotubes, nano-diamonds, up-conversion materials, metal particles, metal oxides and others. The discussion on the potential cytotoxity of NPs remains actual, and numerous studies have been performed to investigate the effects of NPs on physiological

systems. However, most of inorganic nanoparticles show a lack of biodegradability. Self-assembling nano-emulsions encapsulating high concentrations of organic dyes are an attractive alternative combining simplicity of synthesis with the loading of multiple fluorophores. Moreover, they could be prepared from biodegradable and non-toxic materials. The development of highly bright fluorescent nano-emulsion is complicated by the poor solubility of classical fluorescent dyes in the loading matrix and their tendency to form non-fluorescent aggregates . In the present study, these problems were solved by considering a cationic cyanine dye (DiI) and substituting its perchlorate counterion by a bulky and hydrophobic tetraphenylborate counterion. This new dye salt, due to its exceptional solubility, could be loaded at 8 wt% concentration into nano-droplets formed by spontaneous nano-emulsification from oil matrix (Labrafac CC®, biodegradable) and lipid-like shell (Cremophor ELP®, biodegradable). We performed a detailed characterization of NPs nano-emulsions by steady-state spectroscopy, dynamic light scattering (DLS) and fluorescence correlation spectroscopy (FCS). Our data showed that spontaneous nano-emulsification allows to obtain NPs of controlled sizes in range 20-140 nm and that the counterion exchange allows to obtain an outstanding dye loading without affecting the spectroscopic properties of the dye. Our 90 nm droplets, which contained > 10,000 cyanine molecules, were > 100-fold brighter than quantum dots. We perform comparative single particle studies of nano-emulsions with commercially available organic non-biodegradable NPs (Fluorospheres, Red-orange) and found that our nano-emulsions could be up to 16 times brighter. As cytotoxicity is a key issue for biological applications of nanoparticles, we investigated the cytotoxicity of our nano- emulsions using the MTT assay. These experiments confirmed that our fluorescent nano-emulsions do not have any cytotoxicity as they are built up from non-toxic biodegradable materials.

Next, these ultra-bright fluorescent organic NPs were used to perform imaging of live animals. The extreme brightness allowed, for the first time, a single-particle tracking in the blood flow of live zebrafish embryo, revealing both the slow and fast phases of the cardiac cycle. The concept of counterion-based dye loading provided a new effective route to ultra-bright lipid nanoparticles, which enabled tracking single particles in live animals, a new dimension of in-vivo imaging.

Publication 2: “Two photon fluorescence imaging of lipid membrane domains and potentials using advanced fluorescent probes”

Two photon fluorescence imaging of lipid membrane domains and potentials using advanced fluorescent probes

Vasyl Kilin, Zeinab Darwich, Ludovic Richert, Pascal Didier, Andrey Klymchenko and Yves Mély
[a] Biophotonics and Pharmacology Laboratory, UMR 7213 CNRS, Faculté de Pharmacie, 67401 Illkirch, France

*yves.mely@unistra.fr; phone +33 (0)3 68 85 42 63; fax +33 (0)3 68 85 43 12.

ABSTRACT

Biomembranes are ordered and dynamic nanoscale structures critical for cell functions. The biological functions of the membranes strongly depend on their physicochemical properties, such as electrostatics, phase state, viscosity, polarity and hydration. These properties are essential for the membrane structure and the proper folding and function of membrane proteins. To monitor these properties, fluorescence techniques and notably, two-photon microscopy appear highly suited due to their exquisite sensitivity and their capability to operate in complex biological systems, such as living cells and tissues. In this context, we have developed multiparametric environment-sensitive fluorescent probes tailored for precise location in the membrane bilayer. We notably developed probes of the 3-hydroxychromone family, characterized by an excited state intramolecular proton transfer reaction, which generates two tautomeric emissive species with well-separated emission bands. As a consequence, the response of these probes to changes in their environment could be monitored through changes in the ratios of the two bands, as well as through changes in the fluorescence lifetimes. Using two-photon ratiometric imaging and FLIM, these probes were used to monitor the surface membrane potential, and were applied to detect apoptotic cells and image membrane domains.

Keywords: two-photon microscopy, FLIM, environment-sensitive probes, lipid domains, apoptosis, ratiometric probes

1. INTRODUCTION

Cell plasma membranes play important roles in cell biology. They maintain the cellular shape by anchoring the cytoskeleton, and due to their permeability, allow the incoming and the outgoing of materials between the intracellular and extracellular media. As a consequence, they are critical for communication with the outer world by enabling the transfer of compounds needed for cell metabolism and for chemical and electrical signaling. Biological membranes consist of lipids, proteins and sugars. Lipids and proteins are held together mainly by non-covalent interactions, while carbohydrates are attached to the outer side of the membrane by covalent bonds to protein or lipid molecules. Plasma membranes may contain hundreds and even thousands of different lipid species differing in their hydrocarbon chain length, insaturation and structure of headgroup [1]. These lipids, which are mainly synthesized in the endoplasmic reticulum, as essential components of cell membrane are not only important for energy storage but they also play active roles as first and second messengers in signal transduction. They may be considered as amphiphilic molecules with a polar head on one side and lipophilic apolar alkyl chains on the opposite side. There are three major types of lipids found in biological membranes. The first type consists of glycerophospholipids, which are the dominant lipids in eukaryotic membranes, having diacylglycerol (glycerol linked to two fatty acid chains) as a backbone carrying a phosphate (phosphatidic acid PA) esterified by a choline in phosphatidylcholine (PC), serine in phosphatidylserine (PS), ethanolamine in phosphatidylethanolamine (PE) and inositol in phosphatidylinositol (PI). PC is the major component (> 50%) of biological membranes, with most PC molecules having one unsaturated fatty acyl chain. The second type consists of sphingolipids that participate in plasma membrane structure, with ceramide as a hydrophobic part. Sphingomyelin with a saturated fatty acyl chain (SM) and glycosphingolipids are the major sphingolipids in the membrane of mammalian cells. iii) The third type of lipids consists of sterols with cholesterol being the most frequent representative in membranes of mammalian cells. Their structure differs from that of phospholipids, as it contains a four-ring steroid structure with a short hydrocarbon chain and a hydroxyl group [2]. Due to their amphiphilic properties, lipids self-assemble in aqueous media forming different nanostructures, including the lipid bilayers, which are the natural structure of biological membranes. Another key property of biological membranes is the asymmetric distribution of lipids between the leaflets, the outer (non-cytosolic) leaflet containing mainly SM and PC, while PS and PE predominate in the inner (cytosolic) leaflet [3], [4]. This asymmetry confers to the inner leaflet a negatively charged surface, while the

Multiphoton Microscopy in the Biomedical Sciences XIII, edited by Ammasi Periasamy, Karsten König, Peter T. C. So,
Proc. of SPIE Vol. 8588, 85880S · © 2013 SPIE · CCC code: 1605-7422/13/$18 · doi: 10.1117/12.2001492

upper leaflet is more neutral. This asymmetry is maintained by the activity of flippase, an ATP-dependent aminophospholipid translocase that transports PS and PE from the outer to the inner leaflet [5].

In addition to this transmembrane asymmetry, lateral segregation of lipids in domains has also been described. These lipid domains, which have been largely investigated, seem to play critical roles in a number of cell functions ranging from regulation of membrane protein activity to membrane trafficking, sorting and signal transduction [6-8]. However, the detection and visualization of these domains is not a simple task. Even their definition is controversial, and seems to depend on the method that has been used for their observation [9] and [10]. Lipid domains are enriched in saturated lipids (mainly sphingolipids) and sterols (mainly cholesterol) that form a liquid ordered (Lo) phase. The separation between Lo phase and liquid disordered (fluid) phase (Ld) can be observed in model membranes, where the former is perceived as rafts floating in a sea, constituted by the loosely-packed Ld phase enriched in unsaturated phospholipids [6, 11, 12]. Various amounts of Lo phase (from 10 to 80%) and a rather large range of Lo domain sizes (from 10 to 1000 nm) were reported within cell plasma membranes, depending on the technique used to evidence them [13-18].

Fluorescence probes are largely used to monitor membrane physicochemical properties [19]. A large number of these probes were developed to monitor the various membrane potentials (transmembrane, dipolar and surface potentials) and to visualize lipid domains on cell membranes. For the latter, the developed probes are either highly selective for a particular phase or they partition evenly into Lo and Ld phases providing a different fluorescence response in each phase. One of the most used probe is the fluorescently labeled protein Cholera toxin-B (CT-B) from Vibrio cholerae, which binds selectively to the ganglioside GM1 associated with Lo phase domains [14, 20, 21]. Unfortunately, most of the other molecular membrane probes, and notably the lipid-like probes are not suited for staining Lo phase domains, due to their exclusion from the tightly packed Lo phase [7]. Nonetheless, as exceptions to this rule, a few saturated lipids, fluorescently labeled at their head groups [11, 15], as well as a limited number of fluorescent dyes with long alkyl chains, such as LcTMA-DPH [22] or diI-C20 [23], preferentially partition in Lo domains. However, this partition depends on the lipid composition of the Lo domain [24] .

Alternatively, lipid domains can be investigated by environment-sensitive molecular probes, such as Laurdan [24, 25] and its derivatives [26, 27] as well as di-4-ANEPPDHQ [28]. These probes distribute in both Ld and Lo phases and their spectroscopic properties (emission color, intensity, and lifetime) depend on the local membrane properties (polarity, hydration or fluidity), that in turn are related to the phase state of the membrane. Therefore, this sensitivity to the membrane properties can be used to visualize the membrane lateral heterogeneities. In this context, we have developed new membrane probes of the family of 3-hydroxyflavones (3HFs) for monitoring membrane properties and imaging lipid domains in membrane models and biological membranes [19]. These probes exhibit a dual emission due to their excited-state intramolecular proton transfer (ESIPT) reaction. Due to this reversible ESIPT reaction, the commonly observed normal (N∗) excited state is in equilibrium with a tautomer (T∗) excited state. Interestingly, both forms are emissive, but the emission of the T* form is largely red-shifted in respect with the emission of the N* form, so that a two-band emission spectrum is observed. The relative energies of these states control their relative intensities [29]. Moreover, due to an internal charge transfer from the 4′-dialkylamino to the 4-carbonyl group, the N∗ state exhibits a large dipole moment, similar to that observed in solvatochromic dyes such as Prodan. As a consequence, the position of the N* emission band is an indicator of the polarity. In contrast, the ESIPT product T∗ state exhibits a much smaller dipole moment and is thus, far less sensitive to polarity. Moreover, as an additional consequence of its large dipole moment, the N* state can be stabilized by intermolecular interactions and external electric fields, which results in a shift of the ESIPT equilibrium and a redistribution of fluorescence intensity between the two bands. Therefore, the intensity ratio (N∗/T∗) between the two bands is sensitive not only to membrane polarity [30], but also to membrane electrostatics [31].

In addition to lipid domains and membrane potentials, efforts have been done to develop tools able to monitor membrane changes in various biological processes. This is notably the case for apoptosis, which is defined as a programmed and physiological cell death in multicellular organisms [32]. During apoptosis, various changes occur, including cell shrinkage, chromatin condensation, nuclear fragmentation and membrane blebbing, ultimately resulting in the formation of apoptotic bodies. These changes result from a cascade of events requiring the involvement and regulation of a large number of proteins at different levels [33, 34]. Moreover, a loss of the plasma membrane asymmetry occurs in the early steps of apoptosis, as a result of cleavage of flippase and/or activation of scramblase, which lead to a flip of PS from the inner to the outer leaflet. This exposure of PS to the cell surface constitutes a signal for macrophages to clear cells undergoing apoptosis [35]. Importantly, in spite of these modifications, the plasma membrane integrity is preserved during apoptosis. This constitutes a major difference with cell necrosis, where the integrity of the plasma membrane is compromised from the beginning, resulting in the release of the intracellular medium to the extracellular medium. To

detect changes at the plasma membrane during apoptosis, and thus detect apoptosis itself, one of the most popular assays is based on fluorescently labeled annexinV that recognizes specifically PS exposed at the plasma membrane outer leaflet of apoptotic cells [36]. Alternatively, organic ligands complexed with Zn ions can also be used to recognize the exposed PS lipids [37]. In addition to PS exposure to the cell surface, the loss of membrane asymmetry may alter several other properties of the cell plasma membrane, such as its surface charge, lipid packing, fraction of the Lo phase, hydration, etc. Therefore, it was tempting to design and apply 3HF probes in order to sense the changes in plasma membranes occurring during apoptosis. In this respect, we developed the N-[[4′-N,N-diethylamino-3-hydroxy-6-flavonyl]-methyl]-N-methyl-N-(3-sulfopropyl)-1-dodecanaminium, inner salt (F2N12S) probe in which the 3HF fluorophore was conjugated to an ionic headgroup and a long alkyl chain to anchor the probe at the plasma membrane outer leaflet and to provide a well-defined depth and orientation to the fluorophore [38]. This probe was shown to be sensitive to both the surface charge and the lipid order of lipid bilayers. Therefore, it was applied to monitor the changes in the upper leaflet of the plasma membrane during apoptosis, by using two photon ratiometric imaging, as well as two photon Fluorescence Lifetime Imaging Microscopy (FLIM).

2. MATERIALS AND METHODS

2.1 Materials

All chemicals and solvents for synthesis were from Sigma-Aldrich. F2N12S was synthesized as previously described [38]. The probe was pure according to thin layer chromatography, 1H-NMR data, absorption and fluorescence spectra in organic solvents.

2.2 Model membranes

Large unilamellar vesicles (LUVs) were obtained by the extrusion method. Briefly, a suspension of multilamellar vesicles was extruded by using a Lipex Biomembranes extruder (Vancouver, Canada). The size of the filters was first 0.2 μm (7 passages) and thereafter 0.1 μm (10 passages). This generates monodisperse LUVs with a mean diameter of 0.11 μm, as measured with a Malvern Zetamaster 300 (Malvern, UK). A 20 mM phosphate buffer pH 7.4 was used in these experiments. LUVs were labeled by adding aliquots of probe stock solutions in dimethylsulfoxide (DMSO) to 1 mL solutions of vesicles. Concentrations of the probes and lipids were chosen to get a ratio of 1 fluorophore per 100 lipids.

Giant unilamellar vesicles (GUVs) were generated by electroformation in a home-built liquid cell (University of Odense, Denmark), using previously described procedures [39-41]. A 1 mM solution of lipids in chloroform was deposited on the platinum wires of the chamber and the solvent was evaporated under vacuum for 30 min. The chamber, thermostated at 55 °C, was filled with a 300 mM sucrose solution, and a 2-V, 10-Hz alternating electric current was applied for ca 2 h. Then, 50 mL of the obtained stock solution of GUVs in sucrose (cooled down to room temperature) was added to 200 mL of 0.1% (w/w) agarose solution at 60°C and incubated at 40°C for 30 min and then cooled down to room temperature to give the final suspension of GUVs. Staining of GUVs was performed by addition of an aliquot of the probe stock solution in DMSO to obtain a 0.5 μM final probe concentration (final DMSO volume < 0.25%).

2.3 Cell lines, culture conditions and treatment

HeLa cells were grown in Dulbecco's modified Eagle medium (D-MEM, high glucose, Gibco-invitrogen) supplemented with 10% (v/v) fetal bovine serum (FBS, Lonza), 1% antibiotic solution (penicillin-streptomycin, Gibco-invitrogen) in a humidified incubator with 5% CO_2 atmosphere at 37°C. A cell concentration of 5×10^4 cells/mL was maintained by removal of a portion of the culture and replacement with fresh medium, three times per week.

Cholesterol was depleted with methyl-β-cyclodextrin (MβCD) (Sigma-Aldrich). In short, a stock solution of MβCD in Dulbecco's Phosphate Buffered Saline (DPBS) was prepared at an appropriate concentration, filtered by a Millipore filter (0.22 μm) and added to the cells to a final concentration of 5 mM. Treated cells were kept in the incubator at 37 °C for 2 h. To induce apoptosis, cells were treated with actinomycin D (0.5 μg/ml) for 18h at 37 °C.

In fluorescence spectroscopy experiments, cells were trypsinated to detach them from the dish surface. Old culture medium was first removed from the culture dish and cells were washed two times with DPBS. Trypsin 10x (LONZA) solution was diluted 10 times with DPBS and added to the cells at 37 °C for 3 minutes. The trypsinated cells in solution were then diluted by HBSS (Hank's Balanced Salt Solution), transferred to Falcon tubes and centrifuged at 1500 rpm for 5 min, two times. For staining, an aliquot of probe stock solution in DMSO was added to 0.5 mL of HBSS buffer and

after vortexing, the solution was immediately added to 0.5 mL of the cell suspension (1×10^6 cells/mL) to obtain a final F2N12S concentration of 0.1 μM (< 0.25% DMSO). It should be noted that only freshly prepared solutions of F2N12S in HBSS should be used (< 1 min) for cell staining, because of its slow aggregation in water. The cell suspension was incubated with the probe for 7 min at room temperature in the dark, before recording spectra. For microscopy experiments, cells were seeded onto a chambered coverglass (IBiDi) at a density of 5×10^4 cells/IBiDi. After 18-24h, cells were washed with Opti-MEM and then stained by adding a freshly prepared solution of F2N12S in Opti-MEM to the cells to a final concentration of 0.5 μM (< 0.25% DMSO volume) and incubated for 7 min in the dark at room temperature.

2.4 Steady-state and time-resolved fluorescence spectroscopy

Absorption spectra were recorded on a Cary 4 spectrophotometer (Varian) and fluorescence spectra on a FluoroMax 3.0 (Jobin Yvon, Horiba) spectrofluorometer. Fluorescence emission spectra were recorded, using a 315 nm excitation wavelength at room temperature. All the spectra were corrected from the fluorescence of the corresponding blank (suspension of cells or lipid vesicles without the probe).

Deconvolution of F2N12S emission spectra into three bands (N*, H–N* and T*) was performed using the Siano software provided by A.O. Doroshenko (Kharkov, Ukraine), as described [42, 43]. The program is based on an iterative nonlinear least-squares method, where the individual emission bands were approximated by a log-normal function accounting for several parameters: maximal amplitude, I_{max}, spectral maximum position, ν_{max}, and position of half-maximum amplitudes, ν_1 and ν_2, for the blue and red parts of the band, respectively. These parameters determine the shape parameters of the log-normal function, namely full width at the half-maximum, FWHM = $\nu_1 - \nu_2$, and band asymmetry, $P = (\nu_1 - \nu_{max})/(\nu_{max} - \nu_2)$. The resulting fluorescence intensities of the separated N*, H–N* and T* bands (I_{N*}, I_{H-N*} and I_{T*}) were used to calculate the hydration parameter, which is given by the ratio of the peak emission intensity of the hydrated (H–N*) form to the summed intensities of the non-hydrated (N* and T*) forms. Knowing that the FWHM for the T* band is ca 2.5-fold narrower than for the N* and H–N* bands, the hydration parameter was estimated as $I_{H-N*}/(I_{N*} + 0.4 \times I_{T*})$. The polarity parameter is given by I_{N*}/I_{T*}.

Time-resolved fluorescence measurements were performed with the time-correlated, single-photon counting (TCSPC) technique using the frequency-doubled output of a Ti-sapphire laser (Tsunami, Spectra Physcs) pumped by a Millenia X laser (Tsunami, Spectra Physics) [44]. Excitation wavelength was set at 315 nm. The fluorescence decays were collected at the magic angle (54.7◦) of the emission polarizer in order to avoid artifacts due to vertically polarized excitation beam. The single-photon events were detected with a micro-channel plate photomultiplier (Hamamatsu) either coupled to a pulse pre-amplifier (Philips) and recorded on a multi-channel analyser (Ortec) calibrated at 25.5 ps/channel or coupled to a pulse pre-amplifier HFAC (Becker-Hickl) and recorded on a SPC-130 board (Becker-Hickl). The instrumental response function (IRF) was recorded using a polished aluminium reflector, and its full-width at half-maximum was ∼40 ps. The time-resolved decays were analyzed together with instrument response functions using an iterative reconvolution method which provided an effective time resolution of ∼15 ps. The goodness of the fit was evaluated from the values and plot of the residuals and the autocorrelation function.

2.5 Two photon ratiometric imaging and FLIM

Two photon fluorescence microscopy was performed by using a home-built two-photon laser scanning set-up based on an Olympus IX70 inverted microscope with an Olympus 60× 1.2NA water immersion objective [45, 46] Two-photon excitation was provided by a titanium-sapphire laser (Tsunami, Spectra Physics) and photons were detected with Avalanche Photodiodes (APD SPCM-AQR-14-FC, Perkin Elmer) connected to a counter/timer PCI board (PCI6602, National Instrument). Imaging was carried out using two fast galvo mirrors in the descanned fluorescence collection mode. Typical power of excitation was around 2.5 mW (λ=830 nm) at the sample. For getting ratiometric images, we recorded simultaneously images corresponding to the short-wavelength and the long-wavelength emission bands using a dichroic mirror (Beamsplitter 550 DCXR) and two band-pass filters (BrightlineHC 520/20 and HQ 585/40) in front of two APDs. The images were processed with a home-made program under ImageJ that generates ratiometric images by dividing the image of the short-wavelength channel by that of the long-wavelength channel. For each pixel, a pseudo-color scale was used for coding the ratio, while the pixel intensity corresponded to the integral intensity recorded for both channels at the corresponding pixel. Time-correlated single-photon counting FLIM was performed in parallel on the same set-up. The two APDs were connected to the single photon counting (TCSPC) module (SPC830, Becker & Hickl, Germany), which operates in the reversed start-stop mode. The samples were scanned continuously to achieve appropriate photon statistics to analyze the fluorescence decays. Data were analyzed using a commercial software

package (SPCImage V2.8, Becker & Hickl, Germany), which uses an iterative reconvolution method to recover the lifetimes from the fluorescence decays.

3. RESULTS AND DISCUSSION

3.1 Large Unilamellar vesicles labeled by F2N12S

To investigate the sensitivity of F2N12S to the physicochemical properties of lipid bilayers, we used first large unilamellar vesicles (LUV), as model membranes with controlled composition. DOPC and DOPS LUVs were used to model liquid disordered (Ld) phases, with neutral and negative surface charge, respectively. LUVs composed of SM and cholesterol (SM/Chol 2/1 mol/mol) were used to model liquid ordered (Lo) phase. Finally, LUVs composed of DOPC, SM and cholesterol (SM/DOPC/Chol 1/1/1 molar ratio) were used to model lipid bilayers where Lo and Ld phases coexist. Addition of F2N12S at a ratio of 1 probe per 100 lipids to the four different types of LUVs was found to provide a dual emission in all cases. Though the position of the long-wavelength band was similar in the four types of LUVs, the position of the short-wavelength band and the ratio of the two bands were found to vary significantly (Figure 1A and Table 1). In SM/chol LUVs figuring Lo phase, the short-wavelength band was strongly blue-shifted, so that the two emission bands were well separated. In contrast, the short-wavelength band was red-shifted in the Ld phase models (DOPC and DOPS LUVs) and thus, the two emission bands were less resolved. Though, the position of the short-wavelength band was similar in both Ld phase LUVs, its intensity was markedly higher in the negatively charged DOPS LUVs as compared to the neutral DOPC LUVs. Finally, as expected, the position of the short-wavelength band in SM/DOPC/Chol LUVs and the N*/T* ratio where both phases coexist were intermediate to those observed with pure Ld and Lo phases.

To further analyze the spectral data for describing the properties of the lipid bilayers, we deconvoluted the spectra using the methodology previously developed for probe F2N8, a close analogue of F2N12S [42]. This method decomposes the probe emission spectrum into three bands corresponding to normal (N*), H-bonded normal (H–N*) and tautomer (T*) forms of the dye.

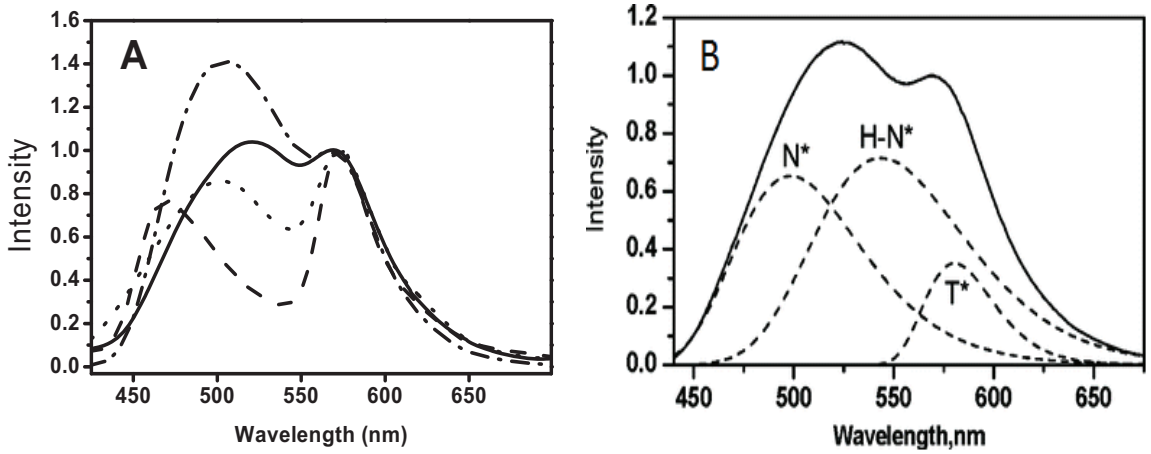

Figure 1. Fluorescence spectra of F2N12S in LUVs of different compositions. (A) Emission spectra of LUVs composed of DOPC (solid curve), DOPS (dash-dotted), Sm/Ch (dashed curve) and DOPC/SM/Ch (dotted curve). (B) Decomposition of the F2N12S spectrum into three bands. Concentrations of lipids and probe were 200 μM, and 2 μM, respectively. Excitation wavelength was 315 nm.

The application of this methodology to F2N12S in DOPC LUVs is shown in Figure 1B. The deconvolution evidences that the red-shift of the short-wavelength band results from the strong contribution of the H-N* form. In sharp contrast, this form is nearly negligible in SM/chol LUVs (data not shown). From the separated bands, the hydration and polarity parameters could be estimated, as described in the materials and methods section. The polarity estimated through the

N*/T* ratio of the non H-bonded forms of the probe correlates well with the surface charge of the vesicles, as this parameter strongly increases in anionic DOPS vesicles as compared to the corresponding neutral DOPC vesicles (Table 1). In contrast to the polarity parameter, the hydration parameter, deduced from the relative contribution of the H-bonded H-N* form is critically dependent on the lipid phase. In Lo phase SM/Chol vesicles, the hydration parameter is much lower than in Ld phase vesicles (Table 1), indicating that the Lo phase is strongly dehydrated. Unsurprisingly, the hydration and polarity parameters of the probe in SM/DOPC/Chol LUVs were intermediate to those observed in DOPC and SM/DOPC/Chol LUVs.

Table 1. Spectroscopic data and estimated values of polarity and hydration for F2N12S in model membranes and cells.

Sample	λ_{SW}, nm	I_{SW}/I_{LW}	Hydration	Polarity
DOPC	512	1.00	0.61	1.63
DOPS	505	1.41	0.38	3.24
SM/Chol	470	0.70	0.01	0.88
SM/DOPC/Chol	494	0.84	0.32	1.22
Intact cells	478	0.83	0.18	0.86
Cells-MβCD	497	1.18	0.58	1.07
Apoptotic cells	489	1.38	0.34	1.47

λ_{SW} describes the position of the emission maximum of the short-wavelength band, I_{SW}/I_{LW} describes the intensity ratio of the short- to the long-wavelength bands at their maxima. Hydration and polarity were estimated from the deconvolution of the emission spectra into three bands, as shown in Fig. 1B. Cells-MβCD correspond to cells where cholesterol was extracted with 5 mM MβCD for 2 h. Spectroscopic values are an average of two to three independent measurements. The estimated errors are $\lambda_{SW} \pm 2$ nm for vesicles and ± 3 nm for cells; $I_{SW}/I_{LW} \pm 2\%$ for vesicles and ± 3% for cells; hydration ± 5% for vesicles and ± 7% for cells; Polarity ± 3% for vesicles and ± 5% for cells.

As it was previously demonstrated with the related F2N8 probe [42], the obtained data could be rationalized by assuming that the N* and H-N* forms differ in their position and orientation in the bilayer. The N* form shows a limited tilt of the 3HF fluorophore in respect with the phospholipid acyl chains, so that the C=O and O-H groups involved in the ESIPT reaction are located deep in the leaflet, at the level of the glycerol group of the phospholipids. Accordingly, the polarity parameter is thought to estimate the polarity at this level. In the H-N* form, the 3HF fluorophore is thought to be nearly perpendicular to the lipid acyl chains, so that the C=O and O-H groups are close to the phospholipid head groups and can be easily hydrated. Due to this hydration, an intermolecular H bond forms between the O-H group of the 3HF fluorophore and water molecules. This intermolecular H bond competes with the intramolecular H bond that is normally present in the N* form, so that the ESIPT reaction is thought to be prevented. Due to the nearly perpendicular orientation of the 3HF fluorophore, this form occupies a larger volume than the N* form. As a result, the H-N* form can only accumulate at significant concentration in the loosely packed Ld phase, but is strongly restricted in the highly packed Lo phase. Moreover, comparison between DOPS and DOPC LUVs indicates a stronger accumulation of the H-N* form in the former. This may indicate a higher hydration of the probe in the negatively charged LUVs or alternatively, a stabilization of its H-N* form by the electric field generated by the negatively charged surface of the DOPS LUVs.

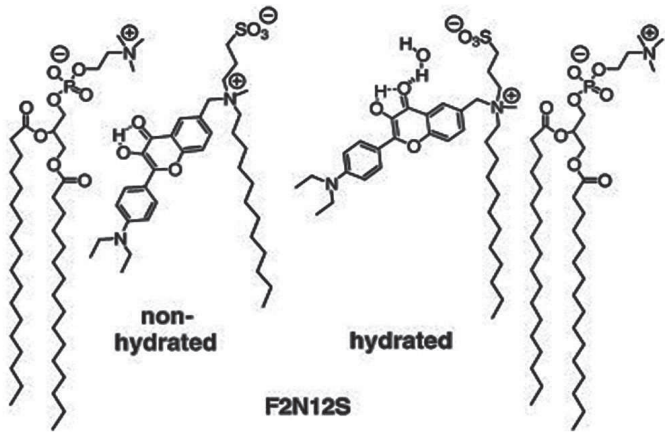

Figure 2. Estimated location of H-bonded and H-bond-free forms of the F2N12S probe in a lipid bilayer.

In a next step, we performed time-resolved fluorescence spectroscopy measurements of F2N12S in the four different types of LUVs in solution. The experiments were performed using the TCSPC technique, with a set-up that allows recording as much as one million of photons for each decay curve, which ensures excellent statistics. For each LUV, decays were recorded at six different emission wavelengths, ranging from 490 to 610 nm. As shown from Figure 3, the fluorescence decays are clearly multi-exponential and show strong differences in their long-lived lifetimes. The decay observed in DOPS LUVs was close to that in DOPC LUVs and was thus not represented.

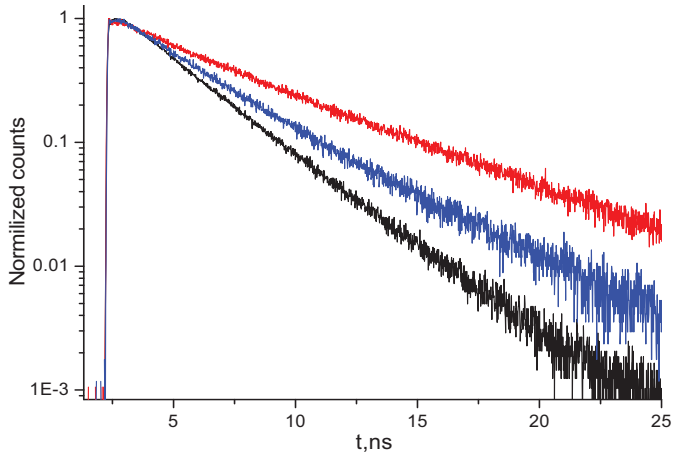

Figure 3. Time-dependent emission decays of F2N12S in LUVs composed of DOPC (black), SM/Cholesterol (red) and DOPC/SM/Cholesterol (blue). Concentrations of lipids and probes were 200 μM, and 2 μM, respectively. Excitation and emission wavelengths were 315 nm and 580 nm, respectively.

Three to five lifetimes were observed for F2N12S in the different LUVs, at the various emission wavelengths (Table 2). As expected for an excited-state reaction, such as ESIPT [47], a fast rise component associated with a negative amplitude was observed for emission wavelengths where the T* form is predominant. This component further indicates that the ESIPT reaction occurs within 30 ps, so that the equilibrium between N and T* forms is reached very rapidly.

For all types of LUVs, the emission decays were strongly wavelength-dependent, showing a progressive decrease of the amplitudes associated with the short-lived components to the benefit of the amplitudes associated with the long-lived lifetimes. Moreover, as observed from Fig. 3, the emission decays of the Ld and Lo phases strongly differed by the values of their long-lived lifetimes. While the Ld phase is characterized by a ~ 3 ns long-lived component, the Lo phase

is characterized by a much longer component of ~ 6 ns. F2N12S in the Lo phase exhibits also a ~ 2ns component, but with a rather low amplitude. Therefore, both due its low amplitude and its significantly lower value, this component can hardly be mixed up with the ~ 3 ns component of the Ld phase. Thus, the long-lived lifetimes in Lo and Ld phases constitute clear signatures of these two phases, and can thus be used to discriminate them. As the amplitudes of these long-lived lifetimes increased with the emission wavelength, reaching nearly 80% at wavelengths ≥ 590 nm, we selected these emission wavelengths for further measurements.

Table 2. Time-resolved spectroscopy data of F2N12S in LUVs of different composition.

	λ, nm	τ_1	a_1	τ_2	a_2	τ_3	a_3	τ_4	a_4	τ_5	a_5	τ_m
DOPC	490	0	0	0.23	0.54	0.98	0.23	2.73	0.23	0	0	0.97
	510	0	0	0.29	0.4	1.28	0.22	2.93	0.38	0	0	1.51
	530	0	0	0.4	0.2	1.62	0.16	2.96	0.64	0	0	2.23
	570	0.032	-1	0.27	0.22	1.1	0.11	3.1	0.67	0	0	2.25
	590	0.033	-1	0.26	0.195	1.23	0.04	2.74	0.765	0	0	2.19
	610	0.054	-1	0.24	0.16	1.15	0.06	2.87	0.78	0	0	2.34
Sm/Ch-1:1	490	0	0	0.13	0.62	1.05	0.1	2.8	0.07	5.9	0.21	1.62
	510	0	0	0.096	0.67	0.74	0.085	2.06	0.08	5.48	0.165	1.19
	530	0	0	0.12	0.58	0.82	0.08	2.19	0.13	5.31	0.21	1.53
	570	0.03	-1	0.2	0.215	1.05	0.05	1.96	0.07	5.77	0.665	4.06
	590	0.031	-1	0.14	0.19	1.11	0.04	2.59	0.14	6.49	0.63	4.52
	610	0.021	-1	0	0	0	0	2.06	0.19	6.2	0.81	5.41
DOPC/SM/ Ch-1:1:1	490	0	0	0.074	0.41	0	0	2.86	0.18	6.2	0.41	3.08
	510	0	0	0.17	0.44	0.86	0.2	2.83	0.29	5.6	0.07	1.45
	530	0	0	0.23	0.27	1.1	0.14	2.95	0.51	5.75	0.08	2.18
	570	0.025	-1	0.28	0.18	1.17	0.17	3.23	0.56	5.89	0.09	2.58
	590	0.026	-1	0.075	0.07	0.82	0.026	3.06	0.77	6.06	0.134	3.19
	610	0.028	-1	0.2	0.05	1.23	0.086	3.26	0.76	6.36	0.104	3.25

Experiments were performed at room temperature, with an excitation wavelength of 315 nm. Lifetimes are in ns. The mean lifetime $\tau_m = \Sigma\alpha_i\tau_i$

As an alternative to the long-lived lifetimes, the values of the mean lifetime τ_m appear also discriminating, especially in the T* emission band. While a 2.2-2.3 ns was observed with DOPC LUVs, a more than twice higher value (4.5-5.4 ns) was seen with SM/Chol LUVs. As expected from the data on pure phases, the two lifetime signatures were observed in the ternary mixture (DOPC/SM/Chol), where both phases coexist, further highlighting that lifetime measurements

constitute a powerful mean to discriminate the two phases. Noticeably, the amplitude associated with the 3 ns component was significantly higher as compared to that of the 6 ns component, suggesting either that the Ld phase is predominant in these LUVs and/or that F2N12S preferentially binds to the Ld phase. In further line with this conclusion, the τ_m value in the ternary mixture was much closer to the corresponding value in Ld phase than in Lo phase.

3.2 Giant Unilamellar vesicles labeled by F2N12S

In a next step, F2N12S was used to label Giant Unilamellar Vesicles (GUVs) and image them by two photon ratiometric imaging. Images were recorded simultaneously at 520 and 580 nm, using a linearly polarized infra-red femtosecond laser as a two-photon excitation source. From these images, ratiometric images were obtained, where the color of each pixel was associated with the I520/I580 intensity ratio, while its intensity is associated with the number of counted photons (Figure 4). A strong polarization effect was observed with the Lo phase. Due the vertical orientation of the fluorophore imposed by the highly ordered fatty acid chains of lipids, no excitation of the dyes could be achieved when their absorption transition moment is perpendicular to the light emission field, explaining the absence of emission in the equatorial region of the GUVs. In contrast, due the much more limited constraints imposed by the lipid chains in the Ld phase, the probes can sample various orientations, so that excitation is always possible and a uniform emission is observed in all parts of the GUVs. Importantly, the two phases could be well discriminated by their ratio in GUVs composed of SM/DOPC/cholesterol, as illustrated by the coexistence of blue and green areas on their ratiometric images.

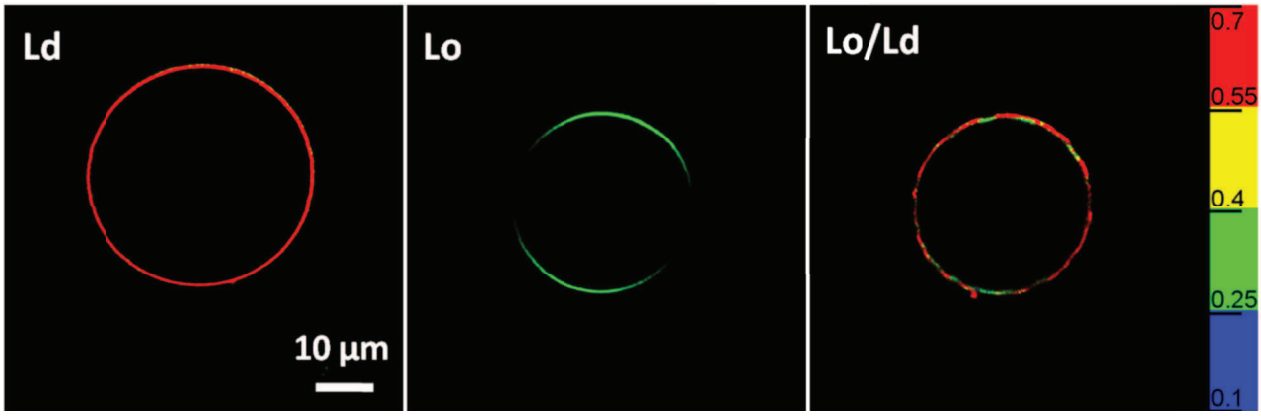

Figure 4. Fluorescence ratiometric images of GUVs composed of DOPC, SM/Chol 2/1 and DOPC/SM/Chol 1/1/0.7. The ratio between the green (520/35 nm) and red (585/40 nm) channels was calculated and converted according to the color code in the right axis. Dye concentration was 0.5 µM. Incubation time was 5 min at 20 °C.

In a next step, the F2N12S-labelled GUVs were imaged by FLIM. In this scanning technique, a fluorescence decay is recorded at each pixel, in order to extract the fluorescence lifetimes and converted them into a color code. Therefore, the contrast of the obtained images is given by the lifetime values. In contrast to solution measurements, FLIM does not allow to record more than a few thousand of photons per pixel, giving thus poor statistics which preclude analyzing the decays with more than one or two lifetime components. As we are using APD as detectors with very broad response functions of 0.5 ns, we expect to be insensitive to lifetimes shorter than this value. Taking into account that we are monitoring the emission centered at 580 nm, we should according to Table 2, only be able to detect the ~ 3 ns component in GUVs with Ld phase and the ~ 6 ns component with some moderate contribution of the 2 ns component in the case of GUVs with Lo phase. In excellent agreement with our expectations, by imaging the τ_m value (Figure 5A), we observe rather narrow lifetime distributions centered at 2.8 ns for DOPC GUVs and 6.5 ns for SM/chol GUVs (Figure 5B). Moreover, as for ratiometric images, a strong polarization effect could be observed for the Lo phase. Using GUVs with ternary SM/DOPC/cholesterol composition, regions with lifetimes about 5 ns (blue) and below 3 ns (orange) could be clearly distinguished, confirming that FLIM could be used to discriminate the two phases (Fig. 5C). Nevertheless, due to

the longer acquisition times as compared with ratiometric imaging, the images appeared somewhat blurry (likely as a result of the fluctuating motions of GUV bilayers in this time frame) and τ_m values intermediate to those obtained with Ld and Lo phases were observed, especially at the boarders between the phase domains, likely as the consequence of the dynamic motions of the phases in this time scale.

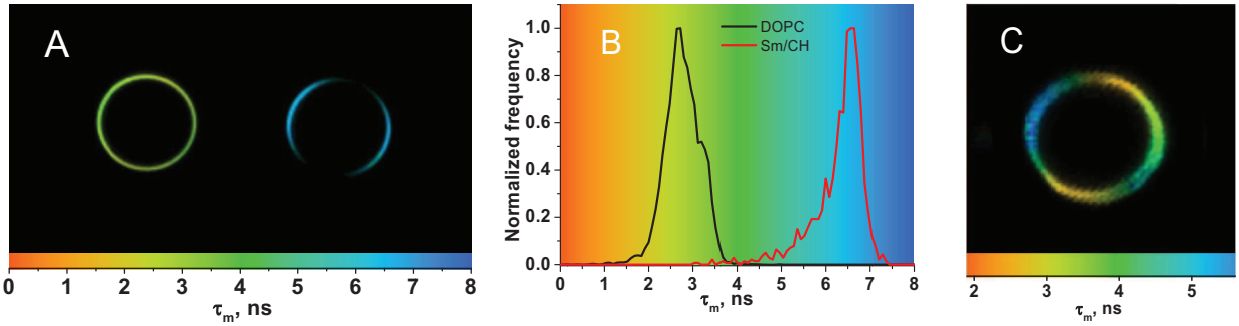

Figure 5: FLIM images and lifetime distribution of GUVs of different composition. A) FLIM images of DOPC (left) and SM/chol (right) GUVs. FLIM images were recorded using a HQ 585/40 filter. The colors of the pixels describe the τ_m values. B) Distribution of the τ_m lifetime values for the two types of GUVs. C) FLIM image of a GUV with SM/DOPC/cholesterol composition. Two-photon excitation wavelength was at 830 nm. Sizes of the GUV were ~22 µm. Probe concentration was 0.5 µM.

3.3 Cells labeled by F2N12S

In a next step, F2N12S was used to label living cells in order to determine, whether this probe can be used to monitor changes in the plasma membrane composition and physicochemical properties. To reach this aim, intact HeLa cells were compared with cholesterol-depleted cells and apoptotic cells. F2N12S in Opti-MEM was added to the cells to a final concentration of 0. 5µM (< 0.25% DMSO volume) and incubated for 7 min in the dark at room temperature.

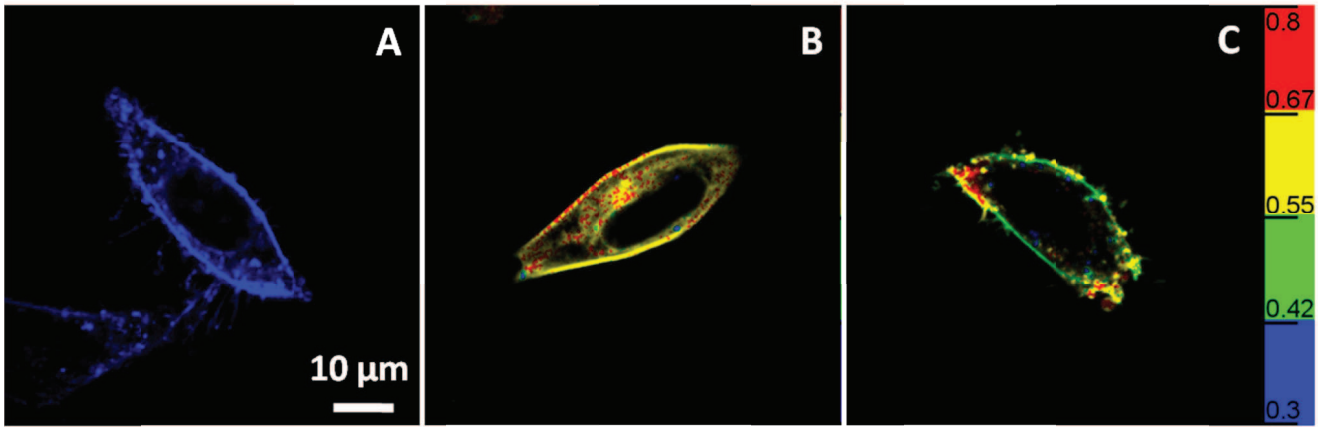

Figure 6. Two-photon fluorescence ratiometric images of intact (A), cholesterol-depleted (B), and apoptotic (C) HeLa cells stained with F2N12S. The ratio between the green (520/35 nm) and red (585/40 nm) channels was calculated and converted using the color scale on the right axis. Dye concentration was 0.5 µM. Incubation time was 7 min at 20 °C.

Using two-photon ratiomeric imaging, the ratio of two emission bands derived from the images was constant all over the cellular membrane for the intact cells (Figure 6A), indicating that membrane heterogeneity cannot be observed on the timescale of seconds with the resolution of our microscope [43]. Surprisingly, in line with the spectral data on cell suspensions (Table 1), the observed ratio of the two bands was much closer to that observed with Lo phase than with Ld phase, suggesting that the Lo phase may be dominant, in variance with the classical view that Lo domains are floating on a sea of Ld phase. Cholesterol depletion by M-ß-CD produced an increase in the green/red ratio, in full line with the

spectroscopic data in cell suspensions (Table 1). This increase in the ratio is fully consistent with the loss of Lo phase that is expected in the upper leaflet of the plasma membrane, after cholesterol extraction. Induction of apoptosis by incubation with actinomycin D was found also to increase the green/red ratio, suggesting that a loss in Lo domain may also occur in the outer leaflet of the plasma membrane of apoptotic cells. Since SM is a major component of Lo domains and since SM is largely concentrated in the outer leaflet of intact cells, apoptosis should induce a massive flip of SM lipids to the inner leaflet, which will obviously lead to a loss of the Lo domains in the outer leaflet. Moreover, as the spectroscopic parameters of apoptotic cells were close to those of DOPS vesicles (Table 1), it may be further deduced that the change in the surface charge of the outer plasma membrane in apoptotic cells, due to the flip of the negatively charged lipids to the outer leaflet, also contributes to the observed signal.

FLIM images of F2N12S-labelled intact cells (Figure 7) are characterized by a mean lifetime of ~5.3 ns, which confirms that Lo domains appear predominant in the membrane of intact cells. Cholesterol depletion performed using MβCD led to a homogeneous decrease of τ_m to 3 ns, in full line with a loss of Lo domains in the outer leaflet of the plasma membrane. Induction of apoptosis by actinomycin D (0.5 µg/mL) for 18 h at 37°C was observed to induce a distribution of lifetimes, suggesting that Ld phase regions appear but more ordered regions are still present.

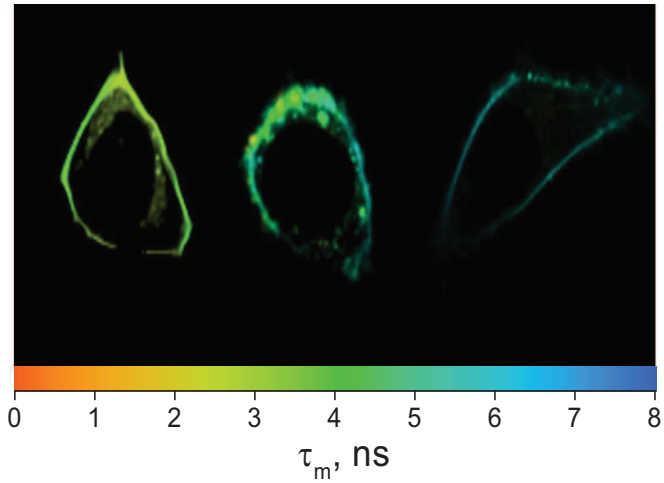

Figure 7. FLIM images of cholesterol-depleted (left), apoptotic (middle) and intact (right) Hela cells. FLIM images were recorded by using a 580 nm filter. In the images, the color of the pixels represents the τ_m value. Two-photon excitation wavelength was at 830 nm. Sizes of the images were 50 x 50 µm. Probe concentration was 0.5 µM.

4. CONCLUSION

In present work, we have shown that the membrane probe F2N12S that was designed to label the external leaflet of the plasma membrane could be used to sensitively probe the composition and the physicochemical properties of model and biological lipid membranes. Due to an ESIPT reaction and hydration by the solvent, F2N12S shows three different excited-state forms, namely N*, H-N* and T* that exhibit different spectral properties. Moreover, the relative concentrations of these three forms are exquisitely sensitive to the environment, and notably to the polarity, electric field and order of the neighbor molecules. As a consequence, the ratio of the emission bands as well as the fluorescence lifetimes appear as sensitive parameters to report on the environment. Using model lipid bilayers (LUVs, GUVs), we have shown that these parameters depend on the lipid surface charge and the lipid order. Using two-photon ratiometric imaging and FLIM, these parameters were further shown to be useful for characterizing the outer leaflet of the cell plasma membranes and to monitor its changes on cholesterol-depletion and apoptosis. This probe appears thus as a convenient substitute to annexinV-derived probes to monitor apoptosis as well as a promising tool to visualize Lo domains with appropriate microscopy tools.

REFERENCES

[1] O. G. Mouritsen, "Lipidology and lipidomics-quo vadis? A new era for the physical chemistry of lipids," Physical Chemistry Chemical Physics, 13(43), 19195-19205 (2011).

[2] G. van Meer, D. R. Voelker, and G. W. Feigenson, "Membrane lipids: where they are and how they behave," Nature Reviews Molecular Cell Biology, 9(2), 112-124 (2008).

[3] G. V. Meer, "Lipid Traffic in Animal Cells," Annu Rev Cell Biol, 5(1), 247-275 (1989).

[4] G. W. Feigenson, "Phase boundaries and biological membranes," Annu Rev Biophys Biomol Struct, 36, 63-77 (2007).

[5] P. Williamson, and R. A. Schlegel, "Back and forth - the regulation and function of transbilayer phospholipid movement in eukaryotic cells," Molecular Membrane Biology, 11(4), 199-216 (1994).

[6] D. A. Brown, and J. K. Rose, "Sorting of GPI-anchored protrins to glycolipid-enriched membrane subdomains during transport to the apical cell-surface," Cell, 68(3), 533-544 (1992).

[7] G. Vanmeer, and K. Simons, "Lipid polarity and sorting in epithelial-cells " Journal of Cellular Biochemistry, 36(1), 51-58 (1988).

[8] K. Simons, and D. Toomre, "Lipid rafts and signal transduction," Nature Reviews Molecular Cell Biology, 1(1), 31-39 (2000).

[9] P. H. M. Lommerse, H. P. Spaink, and T. Schmidt, "In vivo plasma membrane organization: results of biophysical approaches," Biochimica Et Biophysica Acta-Biomembranes, 1664(2), 119-131 (2004).

[10] L. J. Pike, "Rafts defined: a report on the Keystone Symposium on Lipid Rafts and Cell Function," Journal of Lipid Research, 47(7), 1597-1598 (2006).

[11] C. Dietrich, L. A. Bagatolli, Z. N. Volovyk *et al.*, "Lipid rafts reconstituted in model membranes," Biophysical Journal, 80(3), 1417-1428 (2001).

[12] S. L. Veatch, and S. L. Keller, "Organization in lipid membranes containing cholesterol," Physical Review Letters, 89(26), 268101 (2002).

[13] A. Pralle, P. Keller, E. L. Florin *et al.*, "Sphingolipid-cholesterol rafts diffuse as small entities in the plasma membrane of mammalian cells," Journal of Cell Biology, 148(5), 997-1007 (2000).

[14] C. Dietrich, B. Yang, T. Fujiwara *et al.*, "Relationship of lipid rafts to transient confinement zones detected by single particle tracking," Biophysical Journal, 82(1), 274-284 (2002).

[15] G. J. Schutz, G. Kada, V. P. Pastushenko *et al.*, "Properties of lipid microdomains in a muscle cell membrane visualized by single molecule microscopy," Embo Journal, 19(5), 892-901 (2000).

[16] P.-F. Lenne, L. Wawrezinieck, F. Conchonaud *et al.*, "Dynamic molecular confinement in the plasma membrane by microdomains and the cytoskeleton meshwork," Embo Journal, 25(14), 3245-3256 (2006).

[17] P. Sharma, R. Varma, R. C. Sarasij *et al.*, "Nanoscale organization of multiple GPI-anchored proteins in living cell membranes," Cell, 116(4), 577-589 (2004).

[18] M. J. Swamy, L. Ciani, M. Ge *et al.*, "Coexisting domains in the plasma membranes of live cells characterized by spin-label ESR spectroscopy," Biophysical Journal, 90(12), 4452-4465 (2006).

[19] A. P. Demchenko, Y. Mely, G. Duportail *et al.*, "Monitoring Biophysical Properties of Lipid Membranes by Environment-Sensitive Fluorescent Probes," Biophysical Journal, 96(9), 3461-3470 (2009).

[20] P. W. Janes, S. C. Ley, and A. I. Magee, "Aggregation of lipid rafts accompanies signaling via the T cell antigen receptor," Journal of Cell Biology, 147(2), 447-461 (1999).

[21] A. K. Kenworthy, N. Petranova, and M. Edidin, "High-resolution FRET microscopy of cholera toxin B-subunit and GPI-anchored proteins in cell plasma membranes," Molecular Biology of the Cell, 11(5), 1645-1655 (2000).

[22] X. L. Xu, R. Bittman, G. Duportail *et al.*, "Effect of the structure of natural sterols and sphingolipids on the formation of ordered sphingolipid/sterol domains (rafts)," Journal of Biological Chemistry, 276(36), 33540-33546 (2001).

[23] J. Korlach, P. Schwille, W. W. Webb *et al.*, "Characterization of lipid bilayer phases by confocal microscopy and fluorescence correlation spectroscopy," Proceedings of the National Academy of Sciences of the United States of America, 96(15), 8461-8466 (1999).

[24] L. A. Bagatolli, "To see or not to see: Lateral organization of biological membranes and fluorescence microscopy," Biochimica Et Biophysica Acta-Biomembranes, 1758(10), 1541-1556 (2006).

[25] T. Parasassi, E. Gratton, W. M. Yu *et al.*, "Two-photon fluorescence microscopy of Laurdan generalized polarization domains in model and natural membranes," Biophysical Journal, 72(6), 2413-2429 (1997).
[26] H. M. Kim, H.-J. Choo, S.-Y. Jung *et al.*, "A two-photon fluorescent probe for lipid raft imaging: C-laurdan," Chembiochem, 8(5), 553-559 (2007).
[27] H. M. Kim, B. H. Jeong, J.-Y. Hyon *et al.*, "Two-photon fluorescent turn-on probe for lipid rafts in live cell and tissue," Journal of the American Chemical Society, 130(13), 4246 (2008).
[28] L. Jin, A. C. Millard, J. P. Wuskell *et al.*, "Characterization and application of a new optical probe for membrane lipid domains," Biophysical Journal, 90(7), 2563-2575 (2006).
[29] A. P. Demchenko, K. C. Tang, and P. T. Chou, "Excited-state proton coupled charge transfer modulated by molecular structure and media polarization," Chem Soc Rev, in press DOI: 10.1039/C2CS35195A (2012).
[30] M. M. Hao, S. Mukherjee, and F. R. Maxfield, "Cholesterol depletion induces large scale domain segregation in living cell membranes," Proceedings of the National Academy of Sciences of the United States of America, 98(23), 13072-13077 (2001).
[31] B. C. Lagerholm, G. E. Weinreb, K. Jacobson *et al.*," Detecting microdomains in intact cell membranes, " Annual Review of Physical Chemistry, 56, 309-336 (2005).
[32] G. F. Erickson, "Defining apoptosis: Players and systems," Journal of the Society for Gynecologic Investigation, 4(5), 219-228 (1997).
[33] N. A. Thornberry, and Y. Lazebnik, "Caspases: Enemies within," Science, 281(5381), 1312-1316 (1998).
[34] G. S. Salvesen, and V. M. Dixit, "Caspases: Intracellular signaling by proteolysis," Cell, 91(4), 443-446 (1997).
[35] R. F. A. Zwaal, and A. J. Schroit, "Pathophysiologic implications of membrane phospholipid asymmetry in blood cells," Blood, 89(4), 1121-1132 (1997).
[36] I. Vermes, C. Haanen, H. Steffensnakken *et al.*, "A novel assay for apoptosis - flow cytometric detection of phosphatidylserine expression on early apoptotic cells using fluorescein-labeled annesin-v " Journal of Immunological Methods, 184(1), 39-51 (1995).
[37] A. Q. Truong-Tran, J. Carter, R. E. Ruffin *et al.*, "The role of zinc in caspase activation and apoptotic cell death," Biometals, 14(3), 315-330 (2001).
[38] V. V. Shynkar, A. S. Klymchenko, C. Kunzelmann *et al.*, "Fluorescent biomembrane probe for ratiometric detection of apoptosis," Journal of the American Chemical Society, 129(7), 2187-2193 (2007).
[39] M. I. Angelova, and D. S. Dimitrov, "Liposome electroformation," Faraday Discussions, 81, 303 (1986).
[40] M. Fidorra, L. Duelund, C. Leidy *et al.*, "Absence of fluid-ordered/fluid-disordered phase coexistence in ceramide/POPC mixtures containing cholesterol," Biophysical Journal, 90(12), 4437-4451 (2006).
[41] N. Kahya, D. Scherfeld, K. Bacia *et al.*, "Probing lipid mobility of raft-exhibiting model membranes by fluorescence correlation spectroscopy," Journal of Biological Chemistry, 278(30), 28109-28115 (2003).
[42] A. S. Klymchenko, G. Duportail, A. P. Demchenko *et al.*, "Bimodal distribution and fluorescence response of environment-sensitive probes in lipid bilayers," Biophysical Journal, 86(5), 2929-2941 (2004).
[43] S. Oncul, A. S. Klymchenko, O. A. Kucherak *et al.*, "Liquid ordered phase in cell membranes evidenced by a hydration-sensitive probe: Effects of cholesterol depletion and apoptosis," Biochimica Et Biophysica Acta-Biomembranes, 1798(7), 1436-1443 (2010).
[44] J. Godet, N. Ramalanjaona, K. K. Sharma *et al.*, "Specific implications of the HIV-1 nucleocapsid zinc fingers in the annealing of the primer binding site complementary sequences during the obligatory plus strand transfer," Nucleic Acids Research, 39(15), 6633-6645 (2011).
[45] J. P. Clamme, J. Azoulay, and Y. Mely, "Monitoring of the formation and dissociation of polyethylenimine/DNA complexes by two photon fluorescence correlation spectroscopy," Biophysical Journal, 84(3), 1960-1968 (2003).
[46] J. Azoulay, J. P. Clamme, J. L. Darlix *et al.*, "Destabilization of the HIV-1 complementary sequence of TAR by the nucleocapsid protein through activation of conformational fluctuations," J Mol Biol, 326(3), 691-700 (2003).
[47] V. V. Shynkar, Y. Mely, G. Duportail *et al.*, "Picosecond time-resolved fluorescence studies are consistent with reversible excited-state intramolecular proton transfer in 4 '-(dialkylaminoe)-3-hydroxyflavones," Journal of Physical Chemistry A, 107(45), 9522-9529 (2003).

Publication 3 “Fluorescence Lifetime Imaging of Membrane Lipid Order with a Ratiometric Fluorescent Probe”

Article

Fluorescence Lifetime Imaging of Membrane Lipid Order with a Ratiometric Fluorescent Probe

Vasyl Kilin,[1] Oleksandr Glushonkov,[1] Lucas Herdly,[1] Andrey Klymchenko,[1] Ludovic Richert,[1] and Yves Mely[1,*]
[1]Laboratoire de Biophotonique et Pharmacologie, UMR 7213 CNRS, Faculté de Pharmacie, Université de Strasbourg, Illkirch Cedex, France

ABSTRACT To monitor the lateral segregation of lipids into liquid-ordered (Lo) and -disordered (Ld) phases in lipid membranes, environment-sensitive dyes that partition in both phases but stain them differently have been developed. Of particular interest is the dual-color F2N12S probe, which can discriminate the two phases through the ratio of its two emission bands. These bands are associated with the normal (N*) and tautomer (T*) excited-state species that result from an excited-state intramolecular proton transfer. In this work, we investigated the potency of the time-resolved fluorescence parameters of F2N12S to discriminate lipid phases in model and cell membranes. Both the long and mean lifetime values of the T* form of F2N12S were found to differ by twofold between Ld and Lo phases as a result of the restriction in the relative motions of the two aromatic moieties of F2N12S imposed by the highly packed Lo phase. This differed from the changes in the ratio of the two emission bands between the two phases, which mainly resulted from the decreased hydration of the N* form in the Lo phase. Importantly, the strong difference in lifetimes between the two phases was preserved when cholesterol was added to the Ld phase. The two phases could be imaged with high contrast by fluorescence lifetime imaging microscopy (FLIM) on giant unilamellar vesicles. FLIM images of F2N12S-labeled live HeLa cells confirmed that the plasma membrane was mainly in the Lo-like phase. Furthermore, the two phases were found to be homogeneously distributed all over the plasma membrane, indicating that they are highly mixed at the spatiotemporal resolution of the FLIM setup. Finally, FLIM could also be used to sensitively monitor the change in lipid phase upon cholesterol depletion and apoptosis.

INTRODUCTION

Plasma membrane (PM) bilayers contain a large number of lipid species that differ in their hydrocarbon chain length, saturation, and headgroup (1). A variety of PM biological functions, such as regulation of membrane protein activity, membrane trafficking, and signal transduction, are thought to be related to the lateral segregation of lipids into domains (2–4). Lipid domains enriched in saturated lipids (mainly sphingolipids) and sterols (mainly cholesterol (Chol)) are believed to form a liquid-ordered (Lo)-like phase with strongly packed lipids. These domains may behave as rafts floating on a sea constituted by the loosely packed liquid-disordered (Ld)-like phase enriched in unsaturated phospholipids (2,5,6). However, detection and visualization of these domains is not a simple task (7,8). Various percentages of Lo phase (10–80%) and a rather large range of Lo domain sizes (10–1000 nm) in PMs have been reported depending on the technique used to detect them (9–14).

To noninvasively investigate these domains, investigators have developed fluorescence labels that are selective for a particular phase (15), such as the fluorescently labeled protein cholera toxin-B (CT-B) from *Vibrio cholerae*, which binds rather selectively to the ganglioside GM1 associated with Lo-phase domains, but can induce lipid domains by itself due to its tendency to aggregate (10,16,17). Unfortunately, most molecular membrane probes, notably lipid-like probes, are not suited for staining Lo-phase domains due to their exclusion from the tightly packed Lo phase (3). Nonetheless, as exceptions to this rule, a few saturated lipids that are fluorescently labeled at their headgroups (5,11) and a small number of fluorescent dyes with long alkyl chains, such as LcTMA-DPH (18) and diI-C20 (19), preferentially partition in Lo domains. However, this partition depends on the lipid composition of the Lo domain (20). Molecular rotors such as BODIPY-FL-C_{12}, BODIDY-FL-DHPE, and $DiOC_{18}$ (21) are powerful tools for monitoring microscopic viscosity (22–25) and can also discriminate Lo and Ld phases, but suffer from their preferential partitioning in the Ld phase. Alternatively, lipid domains can be investigated by environment-sensitive probes such as Laurdan (20,26) and its derivatives (27,28), as well as di-4-ANEPPQ (29,30) and NR12S (31). These probes partition in both Lo and Ld phases but change their emission color in response to changes in the lipid phase, which can be detected by ratiometric techniques (26,32). Of particular interest is N-[[4′-N,N-diethylamino-3-hydroxy-6-flavonyl]-methyl]-N-methyl-N-(3-sulfopropyl)-1-dodecanaminium, inner salt (F2N12S), which is highly sensitive to the lipid order of lipid bilayers (33,34). F2N12S is a 3-hydroxyflavone (3HF) probe that exhibits a dual emission as a result of an excited-state intramolecular

Submitted January 13, 2015, and accepted for publication April 3, 2015.
*Correspondence: yves.mely@unistra.fr
Editor: Tobias Baumgart.

0006-3495/15/05/2521/11 $2.00
http://dx.doi.org/10.1016/j.bpj.2015.04.003

proton transfer (ESIPT) reaction generating two different excited-state species (34). Being conjugated to a zwitterion headgroup and a long alkyl chain, the F2N12S fluorophore is selectively anchored at the PM outer leaflet (33), whereas its fluorophore moiety is thought to adopt two slightly different positions and orientations (Fig. 1) (35).

The deepest and more vertical orientation is thought to be associated with a hydrogen (H)-bond-free form that can undergo ESIPT, thus providing the normal (N*) and tautomer (T*) excited-state forms. The more shallow location and tilted orientation is associated with an H-bonded form in which the fluorophore forms an intermolecular H-bond with water. This H-bond is thought to prevent the ESIPT reaction, so only the H-bonded normal form (H-N*) can emit. The emission spectra of the three forms (N*, H-N*, and T*) can be obtained by deconvolution (34,36), which allows one to characterize the polarity of the H-bond-free form through the N*/T* ratio, as well as the hydration parameter through the relative contribution of the H-N* form. In model membranes, F2N12S is highly sensitive to the lipid order and surface charge (33,34). Whereas the Ld-to-Lo transition drastically decreases the hydration parameter, a change in the surface charge mainly affects the polarity parameter. F2N12S was successfully used to monitor changes in the lipid phase of the PM of live cells upon Chol extraction and apoptosis (33). So far, all applications of F2N12S, and notably its imaging in cells, have relied on ratiometric measurements. Although ratiometric imaging is sensitive, it requires a calibration step with model systems of pure phase, as well as a precise alignment of detectors at two different wavelengths (32,37). An alternative is fluorescence lifetime imaging microscopy (FLIM), which registers the fluorescence lifetime values in each pixel of the image independently of the instrumentation used and with no need for a calibration step. Previous studies have shown the advantages of using fluorescence lifetimes to investigate lipid phases in cells (38–40), in particular using Laurdan to estimate the fraction of Lo-like phase in the PM of live cells (41).

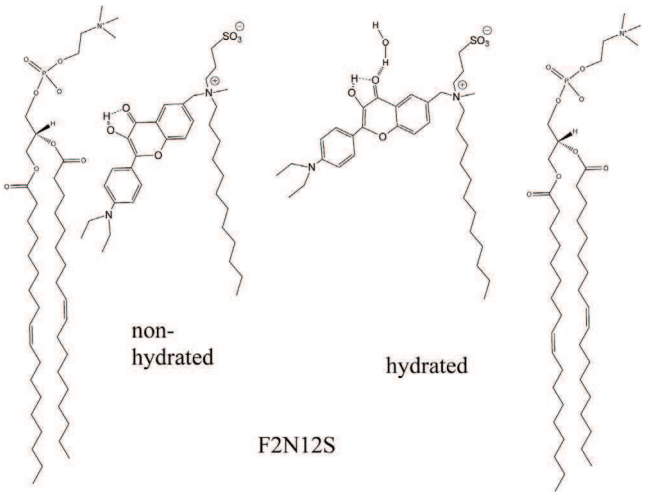

FIGURE 1 Location and orientation of the hydrated and nonhydrated forms of the F2N12S probe in a lipid bilayer.

In this context, our objective in this work was to determine the sensitivity of F2N12S time-resolved fluorescence parameters to the lipid phase and Chol content in large unilamellar vesicles (LUVs) and giant unilamellar vesicles (GUVs), and to validate FLIM as a method for monitoring lipid phases in cells. Our data show that the long and mean lifetimes of the T* band of F2N12S differ by a factor of 2 between the Lo and Ld phases, and thus can be used by FLIM to sensitively and straightforwardly monitor the changes in lipid phase in cells.

MATERIALS AND METHODS

Materials

All chemicals and solvents used in this work were obtained from Sigma-Aldrich. F2N12S was synthesized as previously described (33). The probe was pure according to thin-layer chromatography, ^{1}H-NMR data, absorption, and fluorescence spectra in organic solvents.

Model membranes

LUVs and GUVs were obtained by extrusion and electroformation, respectively (42–44), as described in the Supporting Material.

Cell lines, culture conditions, and treatment

HeLa cells were grown in Dulbecco's modified Eagle's medium (DMEM, high glucose; GIBCO-Invitrogen) supplemented with 10% (v/v) fetal bovine serum (Lonza) and 1% antibiotic solution (penicillin-streptomycin; GIBCO-Invitrogen) in a humidified incubator with 5% CO_2 atmosphere at 37°C.

Chol was depleted with methyl-β-cyclodextrin (MβCD) (Sigma-Aldrich). In short, a stock solution of MβCD in Dulbecco's PBS was prepared at an appropriate concentration, filtered by a Millipore filter (0.22 μm), and added to the cells to a final concentration of 5 mM. Treated cells were kept in the incubator at 37°C for 30 min and then washed with PBS buffer. A stock solution of F2N12S in DMSO was diluted in PBS and added to the cells to a final concentration of 0.1 μM per 10^6 cells (<0.25% DMSO volume), and the cells were incubated for 2 min in the dark at 37°C. To induce apoptosis, the cells were treated with actinomycin D (0.5 μg/mL) for 18 h at 37°C.

In steady-state and time-resolved fluorescence experiments, cells were trypsinized to detach them from the dish surface. The culture medium was first removed from the culture dish and then the cells were washed two times with PBS buffer. Trypsin 10× (Lonza) solution was diluted 10 times with PBS and added to the cells at 37°C for 3 min. The trypsinized cells in solution were then diluted by Hank's balanced salt solution (HBSS), transferred to Falcon tubes, and centrifuged two times at 1500 rpm for 5 min. For staining, an aliquot of probe stock solution in DMSO was added to 0.5 mL of HBSS buffer, and after vortexing, the solution was immediately added to 0.5 mL of the cell suspension (10^6 cells/mL) to obtain a final F2N12S concentration of 0.1 μM (<0.25% DMSO). It should be noted that only freshly prepared solutions of F2N12S in HBSS (<1 min old) should be used for cell staining, because of its slow aggregation in water. The cell suspension was incubated with the probe for 7 min at room temperature in the dark before spectra were recorded or time-resolved fluorescence experiments were performed.

For microscopy experiments, cells were seeded onto a chambered coverglass (IBiDi) at a density of 5×10^4 cells/IBiDi. After 18–24 h, the cells were washed with PBS and then stained by adding a freshly prepared solution of F2N12S in PBS to a final concentration of 0.1 μM per 10^6 cells

(<0.25% DMSO volume), and incubated for 2 min in the dark at room temperature. The cells were then washed again with PBS buffer.

Steady-state and time-resolved fluorescence spectroscopy

Absorption and fluorescence spectra were recorded on a Cary 4000 spectrophotometer (Varian) and a FluoroMax 3.0 (Jobin Yvon, Horiba) spectrofluorometer, respectively. Fluorescence emission spectra were recorded using a 315 nm excitation wavelength at room temperature. All of the spectra were corrected for the fluorescence of the corresponding blank (suspension of cells or lipid vesicles without the probe) and the wavelength dependence of the optical elements in the emission pathway. Deconvolution of F2N12S fluorescence spectra into three bands (N*, H-N*, and T*) was carried out (36) using the PeakFit 4 software as described in the Supporting Material.

We performed single-point time-resolved fluorescence measurements in cuvettes using the time-correlated, single-photon counting (TCSPC) technique with the frequency-tripled output of a Ti-sapphire laser pumped by a Millenia X laser (Tsunami; Spectra Physics) (45). The excitation wavelength was set at 315 nm. The fluorescence decays were collected at the magic angle (54.7°) of the emission polarizer to avoid artifacts due to the vertically polarized excitation beam. Single-photon events were detected with a microchannel plate photomultiplier (R3809-U; Hamamatsu) coupled to a pulse preamplifier (HFAC; Becker & Hickl) and recorded on an SPC-130 board (Becker & Hickl). The instrumental response function was recorded using a polished aluminum reflector, and its full width at half-maximum was ~40 ps. We analyzed the time-resolved decays using the maximum of entropy method (46,47) with Pulse 5 software (Maximum Entropy Data Consultants), which allowed us to resolve fluorescence lifetimes down to ~20 ps. The goodness of the fit was evaluated from the χ^2 values, which ranged from 0.9 to 1.2, and from the plot of the residuals and the autocorrelation function. The mean lifetime was calculated by $\tau_m = \sum \alpha_i \tau_i$, using the lifetimes τ_i associated with positive α_i amplitudes. Decay-associated spectra (DAS) were calculated by : $I_i(\lambda) = a_i\tau_i I(\lambda)/\sum a_i(\lambda)\tau_i$, where $I(\lambda)$ is the steady-state emission spectrum and $a_i(\lambda)$ are the wavelength-dependent amplitudes.

Two-photon FLIM

We performed two-photon fluorescence microscopy at 20°C by using an in-house-built two-photon laser scanning setup based on an Olympus IX70 inverted microscope with an Olympus 60× 1.2NA water immersion objective and two fast galvo mirrors in the descanned fluorescence collection mode (48,49). Two-photon excitation was provided by a titanium-sapphire laser (Tsunami; Spectra Physics) or an Insight DeepSee laser (Spectra Physics). The typical excitation power was ~2.5 mW (λ = 830 nm) at the sample. Photons were detected using an avalanche photodiode (SPCM-AQR-14-FC; Perkin Elmer) coupled to an HQ 585/40 bandpass filter and a single-photon-counting TCSPC module (SPC830; Becker & Hickl) operating in the reversed start-stop mode. Acquisition times were adjusted to achieve 1000 photons per pixel. The minimum fluorescence lifetime detectable with this setup is ~300 ps. FLIM data were analyzed with a binning of one using the SPCImage V4.6 software (Becker & Hickl), which uses an iterative reconvolution method to recover the lifetimes from the fluorescence decays (50). The goodness of the fit was evaluated from the χ^2 values, which ranged from 0.9 to 1.2, and from the plot of the residuals.

RESULTS

LUVs labeled by F2N12S

As the first step in characterizing the dependence of the time-resolved fluorescence parameters on the lipid phase, we investigated the fluorescence intensity decays of F2N12S in LUVs of a controlled lipid composition (Fig. S1). LUVs were chosen as model membranes because they can be easily prepared with any composition. LUVs composed of DOPC lipids were used as models of the Ld phase, and LUVs composed of sphingomyelin (SM) and Chol at a ratio of 2:1 were used as models of the Lo phase. We performed time-resolved fluorescence measurements using the TCSPC technique with a setup that allowed us to record as much as 1 million photons for each decay curve, ensuring excellent statistics. For each type of LUV, decays were recorded at six different emission wavelengths, ranging from 490 to 610 nm (Fig. 2, *A* and *B*; Table S1). For LUVs of both lipid phases, up to five fluorescence lifetimes were recovered, in line with the multiexponential decay reported earlier for this probe in an Ld model membrane (51). As expected for an excited-state reaction such as ESIPT (52), a short lifetime (~30 ps) with a positive amplitude was observed for the N* band, and a corresponding fast-rise component associated with a negative amplitude was observed for the T* form in both phases. This shortest component was almost independent of the phase state. Its value indicated that the ESIPT reaction occurred within 30 ps, so the equilibrium between the N* and T* forms was reached very rapidly in both lipid phases. The values of the intermediate lifetimes (0.1–0.3 ns) and (0.7–1.1 ns) were found to be reasonably close in the two lipid phases (Fig. 2, *A* and *B*). In sharp contrast, the two phases clearly differed with regard to the F2N12S long lifetimes. The Ld phase was characterized by a 2.8 ($\pm$ 0.2) ns component (Fig. 2 *A*), whereas the Lo phase was characterized by a much longer component of 6.0 ($\pm$ 0.2) ns (Fig. 2 *B*). Importantly, the amplitudes of these long lifetimes were observed to strongly increase with the emission wavelength, reaching ~80% at wavelengths $\geq$ 590 nm, so these emission wavelengths were selected for further measurements.

Interestingly, the long lifetime value in the Lo phase (6.0 ns) was very close to that reported for the T* band of a 3HF-based amino acid when it was included in a polystyrene film or when, being part of a peptide, it was stacked with nucleobases in a peptide/oligonucleotide complex (53). For this 3HF-based amino acid, the ~6-ns-long lifetime was clearly related to the restriction of the relative motions of the two aromatic moieties of the 3HF fluorophore, as result of stacking interactions with the polystyrene aromatic rings or the nucleobases, which favored the more planar and emissive 3HF conformation. Therefore, we assumed that the relative motions of the two aromatic rings of the F2N12S fluorophore were also restricted by the highly packed Lo phase, explaining the appearance of the 6.0 ns component as a result of a decrease in the nonradiative deactivation rates. Due to the less constrained packing of lipids in the Ld phase, the restriction in the relative motions of the F2N12S aromatic moieties was certainly less stringent, readily explaining the lower value (2.8 ns) of the long

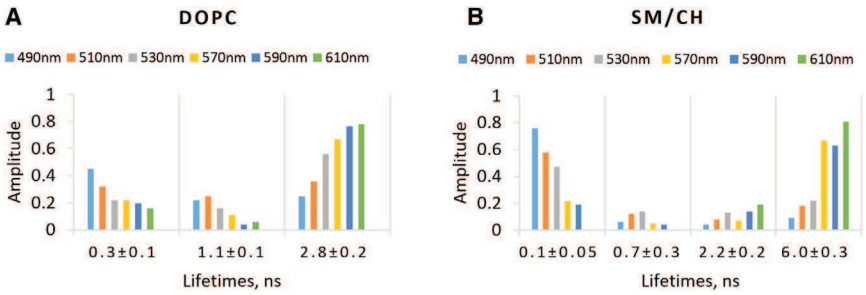

FIGURE 2 Dependence on the emission wavelength of the time-resolved fluorescence parameters of F2N12S in LUVs of Ld and Lo phases. (*A* and *B*) Time-resolved emission decays of F2N12S were recorded in cuvettes for LUVs composed of (*A*) DOPC (Ld phase) and (*B*) SM/Chol (Lo phase). The ~30 ps component describing the ESIPT reaction was omitted in the graph. The emission wavelengths are indicated by the color code. The excitation wavelength was 315 nm. To see this figure in color, go online.

lifetime in this case. Notably, a 2.2 (± 0.1) ns component was also observed in the Lo phase. However, due to its low amplitude (<19%), this 2.2 ns component is expected to only marginally interfere with the determination of the Lo and Ld phases in systems where both phases are present.

As an alternative to the long lifetimes, the values of the mean lifetime τ_m can also be used to discriminate the two phases. These values are especially selective for the T* band at high emission wavelengths. Indeed, we obtained τ_m values of 2.3 (± 0.1) ns and 5.4 (± 0.5) ns for DOPC LUVs and SM/Chol LUVs, respectively, using the decay parameters at 590 and 610 nm (Fig. S2). Thus, both the long and mean lifetime values differ by a factor of 2 between the Lo and Ld phases, and the two phases can be discriminated with high contrast using FLIM.

The strong dependence of the lifetime amplitudes on the wavelength suggests that the different lifetimes may be associated with different excited-state species. As was shown in previous studies (34,36), three emissive species (N*, H-N*, and T*) contribute to the F2N12S emission spectrum. To attribute the lifetime components to these species, we drew the DAS for all lifetime components and compared them with the spectra of the three species obtained by deconvolution of the emission spectra (Fig. 3) (36). Notably, the emission spectra of F2N12S in DOPC and SM/Chol LUVs differed slightly from those reported in our previous studies (34,54), since they were corrected from the wavelength dependence of the optical elements in the emission pathway. A comparison of the deconvoluted spectra of F2N12S in Ld and Lo phases (Fig. 3, *A* and *B*) indicated that the spectra differed mainly by the large contribution of H-N* in the Ld phase. The absence of the H-N* form in the Lo phase could be readily explained by the strong packing and poor hydration of this phase (36,55), which did not favor this hydrated and tilted form.

A comparison of the deconvoluted emission spectra with the DAS for each lifetime component indicates that the emission of F2N12S in SM/Chol LUVs was largely dominated by the 6.0 ns component (Fig. 3 *A*, *green diamonds*). This finding was fully expected for the T* form, where the amplitude and thus the population associated with the 6.0 ns component represented up to 81% (Fig. 2 *B*), and its fractional contribution to the fluorescence intensity calculated by the product of the component by its amplitude divided by the mean lifetime represented up to 92%. The 6.0 ns component also dominated the emission of the N* band, although its population represented less than 20% in this band (Fig. 2 *B*). The strong contribution of this component in the N* emission resulted from the fact that the most populated component (0.1 ns) of the N* form is very poorly fluorescent and thus contributes little to the N* emission (Fig. 3 *A*, *orange disks*). In DOPC LUVs, the emission spectrum of F2N12S was dominated by the emission associated with the 2.8 ns component. This component was particularly dominant in the case of the H-N* and T* forms, as could be seen from the DAS spectra. In contrast, the emission of the N* band was mainly contributed by the 0.3 ns and 1.1 ns components. The short-decay components (0.1–0.3 ns) with high amplitude observed for the N* band in both Ld and Lo phases are likely due to fast photophysical

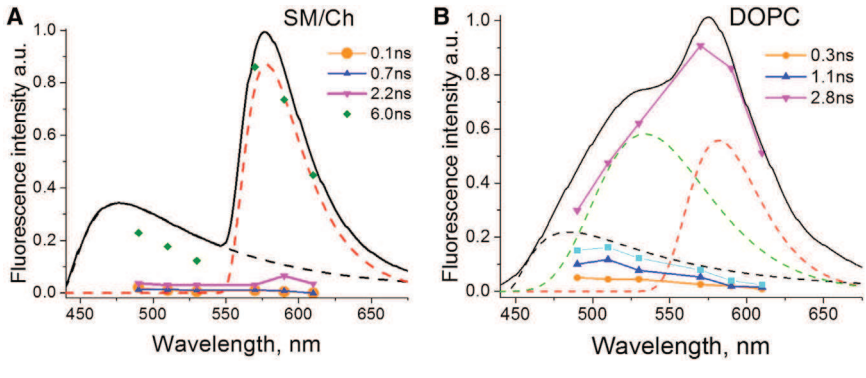

FIGURE 3 (*A* and *B*) DAS overlapped with steady-state spectra and deconvoluted bands of F2N12S in SM/Chol (*A*) and DOPC (*B*) LUVs. Steady-state spectra are represented as solid lines. Deconvoluted spectra of N*, H-N*, and T* bands are drawn with black, green, and red dashed lines, respectively. The DAS for the 0.1 ns, 0.7 ns, and 2.2 ns components in (*A*) and the 0.3 ns, 1.1 ns, and 2.8 ns components in (*B*) are plotted with orange disks, blue triangles, and magenta inverted triangles, respectively. The DAS for the 6 ns component in (*A*) is plotted with green diamonds. The sum of the DAS for 0.3 ns and 1.1 ns components in (*B*) is plotted with cyan squares. To see this figure in color, go online.

processes related to the charge and proton transfer properties of the highly dipolar N* form. On the other hand, the intermediate-decay component (~1 ns) observed for the N* form in DOPC LUVs could be related to the slow relaxation of its lipid environment, as suggested in earlier studies (51,56).

Next, we investigated the dependence of F2N12S time-resolved fluorescence parameters in the Ld phase on the presence of Chol. Chol is a major component of cell membranes, representing up to 50% of their lipid composition (57–59). Its presence in model membranes of the Ld phase was shown to affect the response of Prodan, Laurdan, and di-4-ANEPPDHQ probes (20,26,29,60,61), suggesting that it can affect both membrane order (31,41,54,62) and hydration (36,55). By using Ld LUVs composed of DOPC and increasing Chol fractions, we observed a progressive and substantial decrease of the H-N* band in the F2N12S emission spectra (Fig. 4 *A*). From the deconvoluted spectra, we observed a Chol-induced decrease in the hydration parameter of F2N12S by up to 50% (Fig. 4 *A*, *inset*) at the highest Chol fraction tested (32%), in line with the well-known dehydration effect of Chol in lipid membranes (34,55). However, there was far less dehydration in the Ld phase than in the Lo phase, where the H-N* band was absent.

The time-resolved intensity decays of the DOPC/Chol LUVs were characterized by five lifetime components (Fig. 4 *B*; Table S2). Whereas the long lifetime was identical to that of SM/Chol LUVs (Lo phase), all other lifetimes were similar to those observed in DOPC LUVs (Ld phase). Even at low concentrations, Chol significantly affected the F2N12S environment, as shown by the sharp decrease in the amplitude associated with the 3 ns component, which was mainly to the benefit of the 1 ns component. It can be speculated that a low Chol content in DOPC would induce some disorder in the probe environment, and thus the relative motions between the two aromatic moieties of F2N12S would be less restricted. At higher Chol concentrations, we observed a progressive increase in the amplitude of the 3 ns lifetime, indicating that the probe accumulates in more packed lipid regions, which form as a result of the favorable packing interactions of Chol with lipids. Some of these regions may be rigid enough to allow the 6 ns component to be perceived. However, the amplitude of this 6 ns component ($<-11\%$) is far below that observed in the Lo phase (63%), suggesting that the DOPC/Chol clusters around the F2N12S probe are much more dynamic than the SM/Chol ones. Therefore, the relative amplitudes associated with the 3 and 6 ns components appear to be reliable parameters for discriminating the Lo phase from the Ld phase in both the absence and presence of Chol.

GUVs labeled by F2N12S

LUVs were not appropriate to use for FLIM experiments due to their small size (0.11 μm); therefore, we used GUVs, whose sizes (~10 μm) are perfectly suited for microscopy measurements. In the FLIM technique, a fluorescence decay is recorded at each pixel to extract the fluorescence lifetimes and convert them into a color code. Therefore, the contrast of the obtained images is given by the lifetime values. In contrast to solution measurements, FLIM does not allow recording of more than a few thousand photons per pixel. This results in poor statistics, which precludes analysis of decays with more than one or two lifetime components (50). By monitoring the emission centered at 580 nm, where the contribution of lifetimes of $\leq$2.2 ns are negligible (Fig. 3, *A* and *B*), we should only be able to detect the 2.8 ns component in DOPC GUVs of the Ld phase and the 6 ns component in SM/Chol GUVs of the Lo phase.

In line with our expectations, FLIM measurements (Fig. 5 *A*, *top*) provided rather narrow lifetime distributions centered at 2.7 $\pm$ 0.5 ns for DOPC GUVs and 6.6 $\pm$ 0.6 ns for SM/Chol GUVs (Fig. 5 *B*), which correspond to the long lifetime signatures of the Ld and Lo phases, respectively. Notably, as was found for the ratiometric images, a strong polarization effect could be observed for the Lo phase due to the restricted vertical orientation of F2N12S fluorophore in the lipid bilayer (35,63). Due to the much less constrained environment in the Ld phase, the probe can sample a larger range of orientations, so at each pixel of the GUV bilayer, at least a fraction of the dyes are not perpendicular to the electric field of the laser beam. In GUVs composed of

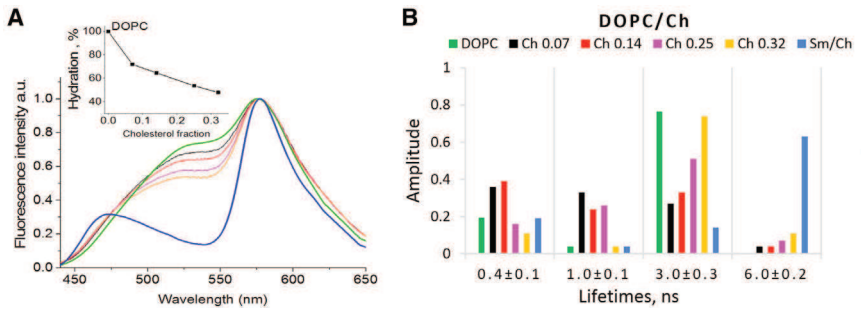

FIGURE 4 Steady-state and time-resolved fluorescence spectroscopy of F2N12S in DOPC/Chol LUVs. (*A*) Steady-state spectra of F2N12S in DOPC/Chol LUVs with increasing fractions of Chol: 0.07 (*black*), 0.14 (*red*), 0.25 (*magenta*), and 0.32 (*orange*). Spectra of F2N12S in DOPC and SM/Chol are in green and blue, respectively. The spectra are normalized at the T* band maximum. (*Inset*) Dependence of the hydration parameter of F2N12S on the Chol fraction in DOPC/Chol LUVs. The probe hydration in DOPC was taken as 100%. (*B*) Time-resolved fluorescence parameters of F2N12S in DOPC/Chol LUVs with increasing Chol fraction. Experiments were performed in cuvettes. Color code as in (*A*). The ~30 ps component describing the ESIPT reaction was omitted in the graph. Emission was recorded at 590 nm. To see this figure in color, go online.

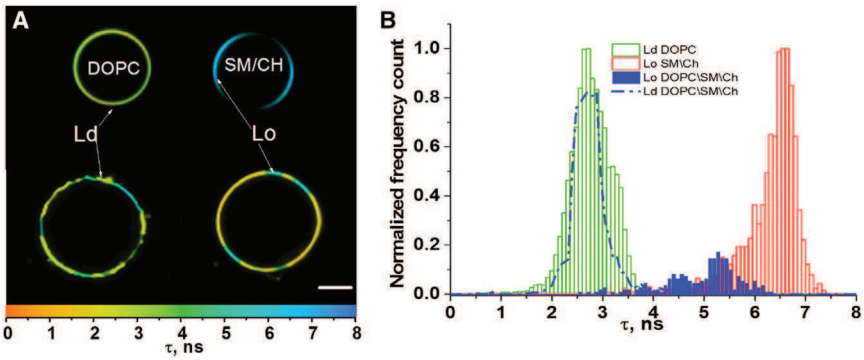

FIGURE 5 FLIM images and lifetime distribution of GUVs of different compositions. (*A*) FLIM images of DOPC (Ld) and SM/Chol (2:1) (Lo) GUVs (*top*). FLIM image of GUVs with SM/DOPC/Chol (1:1:0.7) composition (Lo+Ld) (*bottom*). For each pixel, the lifetime value is coded using the color scale given at the bottom. The scale bar is 10 μm. (*B*) Distribution of lifetime values for the three types of GUVs. To see this figure in color, go online.

DOPC/SM/Chol (1:1:0.7), where the Lo and Ld phases coexist, the two phases could be easily distinguished through their lifetimes, highlighting the ability of the FLIM technique to discriminate the two phases with high contrast. The lifetime of the Ld phase (2.7 $\pm$ 0.5 ns) was found to be very similar to the lifetimes of the DOPC GUVs (Fig. 5 *B*) and the DOPC/Chol (2:1) LUVs (Fig. 4 *B*). In contrast, the lifetime of the Lo phase (5.2 $\pm$ 1 ns) was somewhat shorter than that of the SM/Chol (2:1) GUVs, suggesting that the Lo phase was slightly less ordered in the ternary mixture. This lower-order level probably resulted from the presence of DOPC in the Lo phase of the ternary mixture, which may somewhat reduce the tight packing between SM and Chol in this phase. As a consequence of the clear difference in lifetimes between the two phases, the partition coefficient of F2N12S between the two phases could be estimated. For this purpose, we first measured the size of both domains using ImageJ software (64) on 10 GUVs to estimate the fractional amounts of Lo and Ld phases in these GUVs. We obtained a 75:25 ratio of Ld/Lo phases, in excellent agreement with the 70:30 ratio expected from the phase diagram for GUVs of this composition (65). Next, using SPCimage software, we integrated the number of photons, N_o and N_d, emitted for each of the two phases. We then calculated the partition coefficient of F2N12S between the two phases, P = [Lo]/[Ld], as

$$P = \frac{N_o \phi_d}{N_d \phi_o} \frac{C_d}{C_o}, \quad (1)$$

where ϕ_o (26.5 $\pm$ 3%) and ϕ_d (30 $\pm$ 3%) are the quantum yields of F2N12S in the Lo and Ld phases, respectively, and C_d/C_o is the ratio of the two phases in the GUVs. A p value of 0.17 $\pm$ 0.04 was obtained, indicating a clear preference of F2N12S for the Ld phase.

Cells labeled by F2N12S

Next, we used time-resolved fluorescence approaches to characterize F2N12S-labeled cell membranes. First, we characterized suspensions of intact and Chol-depleted cells using the TCSPC technique. Chol-depleted cells were obtained by incubation with 5 mM MβCD at 37°C for 30 min (31,66). As previously reported for another cell line (U-87 MG) (31), Chol depletion was observed to increase the ratio of short- to long-wavelength bands and red-shift the short-wavelength band (Fig. 6 *A*). The value of the short lifetime associated with the negative amplitude (Table S3) was indistinguishable from the corresponding value in LUVs, indicating that the ESIPT process is only marginally altered by the cell membrane environment or by Chol depletion. Moreover, the amplitudes of the two intermediate lifetimes (0.2 $\pm$ 0.04 and 0.9 $\pm$ 0.2 ns) were low (<10%), so the decays recorded at 590 nm were largely dominated by the two long lifetimes, 3.3 $\pm$ 0.2 ns and 6.9 $\pm$ 0.1 ns, which corresponded to the signatures of the Ld and Lo phases, respectively (Fig. 6 *B*).

In intact cells, the two long lifetimes (3.3 and 6.9 ns) had similar amplitudes (Fig. 6 *B*), giving a mean lifetime of 4.5 $\pm$ 0.5 ns. Both the amplitudes associated with the two long lifetimes and the mean lifetime value are closer to those observed in Lo LUVs as compared with Ld LUVs, confirming that the Lo-like phase may be dominant in cell PMs (34,41,66). Depletion of Chol leads to a redistribution of the amplitudes of the two components (Fig. 6 *B*) with, as expected, a strong decrease of the amplitude of the lifetime associated with the Lo-like phase and thus a strong decrease of the mean lifetime to 2.6 $\pm$ 0.5 ns.

Next, we imaged F2N12S-labeled intact and Chol-depleted HeLa cells using FLIM. We first analyzed the images by employing a single-decay-component model. As previously reported for ratiometric images (31), the FLIM images of intact and Chol-depleted cells labeled with F2N12S showed a remarkable homogeneity in their pseudo-color distribution (Fig. 7 *A*), indicating that no clear phase separation could be perceived. The lifetime distributions were centered at 5.6 $\pm$ 0.9 ns and 3.6 $\pm$ 0.4 ns for intact and Chol-depleted cells, respectively (Fig. 7 *B*). Both lifetimes were intermediate between those observed for the Ld and Lo phases in GUVs (Fig. 5 *B*), suggesting that the two phases may be present in both types of cells. As these two phases could not be discriminated in the FLIM images (Fig. 7 *A*), this suggests that the Lo-like and Ld-like domains are smaller than the ~300 nm resolution

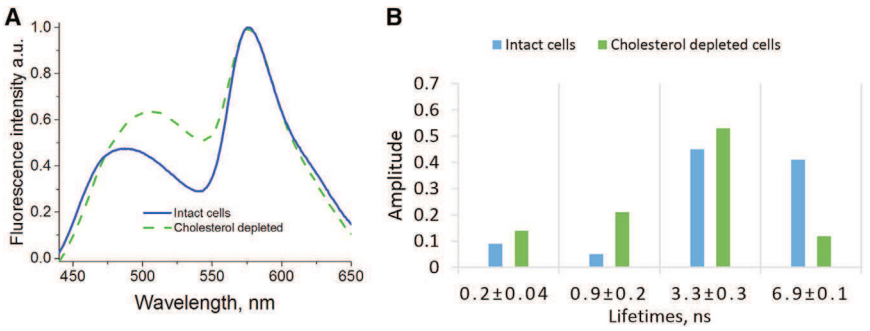

FIGURE 6 (*A* and *B*) Emission spectra (*A*) and time-resolved fluorescence parameters (*B*) of F2N12S-labeled intact (*blue*) and Chol-depleted (*green*) HeLa cells. Time-resolved fluorescence parameters were obtained by TCSPC measurements at 590 nm emission wavelength on cell suspensions in cuvettes. The excitation wavelength was 315 nm. To see this figure in color, go online.

limit of our two-photon excitation microscope and/or that the domains are highly dynamic and thus cannot be resolved in the timescale (approximately seconds) of the FLIM measurements. This is in sharp contrast to the DOPC/SM/Chol GUVs (Fig. 5 *A*), where the separated lipid domains could be easily observed due to their large size and slow dynamics (5,20,35).

As both Lo-like and Ld-like phases are likely present in intact and Chol-depleted cells, we next analyzed the FLIM images using a two-component model to recover the lifetimes and amplitudes associated with the two phases. For intact cells, we obtained $\tau_1 = 3.4 \pm 0.7$ ns and $\tau_2 = 6.4 \pm 0.9$ ns components (Fig. 8, *A* and *B*), which are consistent with the lifetimes of Ld and Lo phases in model systems and the lifetimes recovered by TCSPC measurements on suspensions of the same cells. The two lifetimes recovered by FLIM were found to be homogeneously distributed all over the PM, confirming that the two phases are mixed, at least at the spatiotemporal resolution of the setup. For Chol-depleted HeLa cells, the two lifetime components of F2N12S were $\tau_1 = 2.7 \pm 0.4$ ns and $\tau_2 = 5.4 \pm 0.7$ ns, respectively (Fig. 8, *A* and *B*). The 5.4 ns value for the long lifetime was significantly lower than the 6.9 ns value in TCSPC measurements. This is likely a consequence of there being too few photons in several pixels of the FLIM image, so the analysis could not resolve the two components. In spite of this limitation, it is still obvious from the τ_1 and τ_2 images of Chol-depleted cells (Fig. 8 *A*) that the two phases largely overlap all over the cell PM, suggesting that Chol depletion is not able to unmix the two phases, at least at the spatiotemporal resolution of our FLIM setup.

To further illustrate the potency of our lifetime-based imaging approach, we monitored PM remodeling during apoptosis induced by actinomycin D (0.5 μg/mL; Fig. 9). Using a single-component analysis, we found that apoptotic cells exhibit a lifetime value of 5.1 ± 0.6 ns, which is intermediate between the 5.6 ± 0.9 ns and 3.6 ± 0.4 ns values shown by intact and Chol-depleted cells, respectively. This indicated a decrease in the Lo-like phase (34,62), which probably resulted from the loss of transmembrane asymmetry (67) and the SM hydrolysis into ceramide that occurred during apoptosis (68). A further decreased lifetime value (4.4 ± 0.3 ns) and thus a further decrease in lipid order were observed in vesicles (Fig. 9, *arrows*), which may be attributed to apoptotic blebs (69,70). This decrease in lipid order in apoptotic blebs is fully consistent with the Ld-like phase that Kreder et al. (70) recently described for these blebs by ratiometric imaging using Nile-red based probes.

DISCUSSION

In this work, we investigated the potency of time-resolved fluorescence techniques to discriminate lipid phases in model and cell membranes, using the ratiometric membrane probe F2N12S. Despite the complex multiexponential decay of F2N12S (51), we found that the Lo phase could be discriminated from the Ld phase with high contrast, by the values of its long and mean fluorescence lifetimes. The best sensitivity was observed at the red edge of the F2N12S emission spectrum, where the T* form is dominant. The twofold higher values of the F2N12S long and mean lifetimes in the Lo phase as compared with the Ld

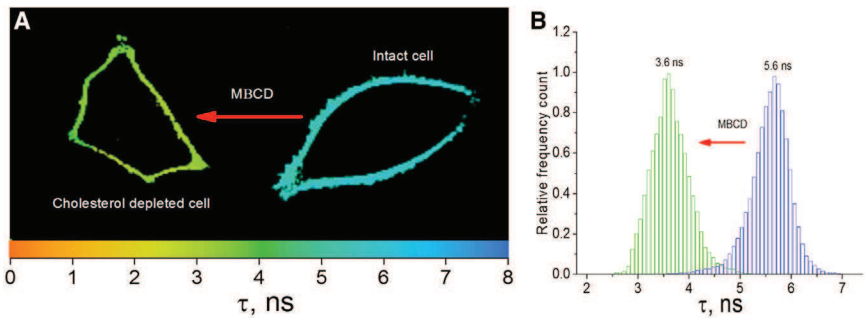

FIGURE 7 FLIM images and lifetime distribution of intact and Chol-depleted HeLa cells, analyzed by a single decay component model. (*A*) FLIM images of Chol-depleted (*left*) and intact (*right*) HeLa cells. The pixel colors describe the lifetime values according to the color scale on the *X* axis. (*B*) Lifetime distribution for intact (*blue*) and Chol-depleted (*green*) cells. The distributions were obtained from measurements on 20 cells. Two-photon excitation was at 830 nm. To see this figure in color, go online.

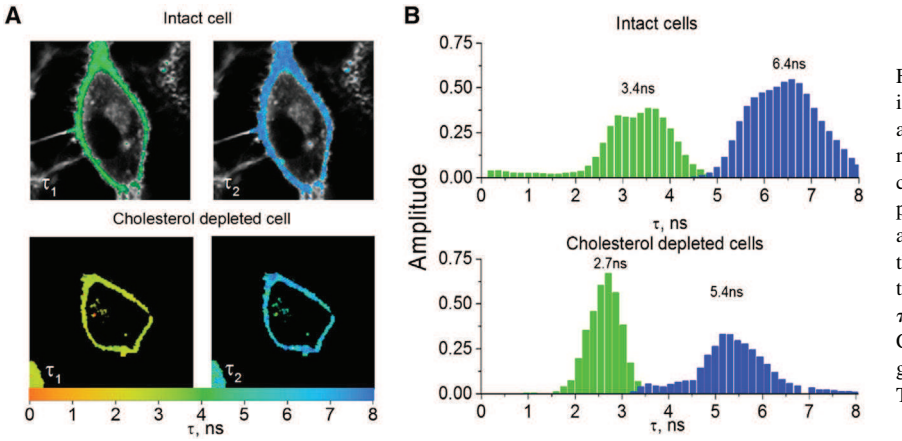

FIGURE 8 FLIM images of F2N12S-labeled intact and Chol-depleted HeLa cells, analyzed by a two-component model. (*A*) FLIM images were recorded as in Fig. 7 and analyzed with a two-component (τ1 and τ2) model. The colors of the pixels describe the values of the τ1 (*left panels*) and τ2 (*right panels*) components according to the color scale on the *X* axis. (*B*) Distribution of the amplitudes associated with the τ1 (*green*) and τ2 (*blue*) components for intact (*top panel*) and Chol-depleted (*bottom panel*) cells. The histograms resulted from measurements on 20 cells. To see this figure in color, go online.

phase were attributed to the restriction in the relative motions of the two aromatic moieties of F2N12S imposed by the highly packed Lo phase, which favored the more planar and more emissive conformation of the 3HF fluorophore (53). Addition of Chol to DOPC LUVs was also found to induce the appearance of the ~6 ns lifetime component, which is characteristic of the Lo phase, but only at low amplitude. This is likely related to the inability of Chol to induce in the Ld phase the strong packing of lipids that characterizes the Lo phase and efficiently restricts the relative motions of the two aromatic moieties of F2N12S. Therefore, the lifetime signatures of the Ld and Lo phases (~3 ns and ~6 ns, respectively) appear to be sensitive tools for distinguishing the two phases even in the presence of Chol. This was confirmed by FLIM images of SM/DOPC/Chol GUVs, where the large and stable Ld and Lo phases could be easily discriminated by their lifetime signatures, although Chol was likely distributed in both phases (Fig. 5). The capacity to distinguish between the Lo and Ld phases in Chol-containing lipid compositions is an important advantage of F2N12S over a number of other environment-sensitive probes, such as Laurdan, in which case the presence of Chol in the Ld phase decreases the contrast with respect to the Lo phase (71).

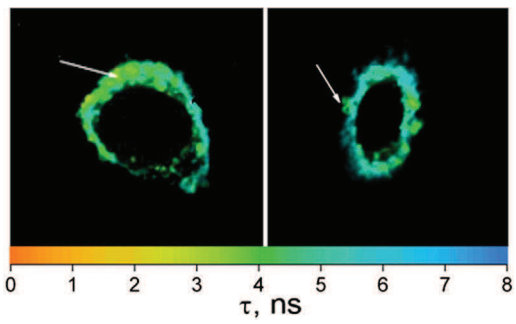

FIGURE 9 FLIM images of apoptotic HeLa cells analyzed by a single-decay-component model. The pixel colors describe the lifetime values according to the color scale on the *X* axis. The arrows show vesicles that can be assigned to blebs. The lifetime values of the blebs suggest that they exhibit an Ld-like phase. To see this figure in color, go online.

The contrast in lifetimes between the two phases observed with F2N12S was found to be significantly higher than that observed for various fluorescence-labeled phospholipids, such as BODIPY-PC (72), Rhod-DOPE (73), and C6-NBD-PC (38,74). Although the last compound was also quite sensitive, showing a 70% difference in lifetime values between the two phases, it provided a much smaller change (<10%) in response to Chol depletion as compared with F2N12S (~60%) and suffered also from low photostability (38). F2N12S also showed improved sensitivity compared with perylene monoimide derivatives, which are highly bright and photostable, but undergo a smaller change (35%) in their lifetime between Ld and Lo phases and suffer from their tendency to aggregate (39).

The ~2-fold variation in F2N12S lifetimes between Lo and Ld phases is comparable to the variation in the general polarization or the two-band ratio values observed with Laurdan (41), PY series (40), di-4-ANEPPDHQ (30,38,39), and NR12S (31) probes. However, since fluorescence lifetimes are absolute parameters that are independent of the instrumentation used, no calibration is required, in contrast to ratiometric methods, which are based on intensity measurements (26,31,33,75). Moreover, a key feature of F2N12S is its capacity to bind specifically to the outer leaflet of the PM. This is of crucial importance for two reasons. First, since the PM is asymmetric, with the outer leaflet being highly enriched in SM, Lo domains are particularly important in this leaflet. As a result, the information revealed by F2N12S at the PM is not complicated by staining of the inner leaflet. Second, since F2N12S is anchored at the outer leaflet, it does not diffuse rapidly inside the cell to stain the inner lipid membranes. As a result, the contrast of the FLIM images at the PM is not decreased by photons coming from inner compartments close to the PM. A frequently used alternative to FLIM imaging is the phasor plot approach (76,77). Although this method is also based on fluorescence decays, it requires a calibration step with

compounds exhibiting single lifetimes (41,77). The contrast obtained by F2N12S lifetime analysis is also comparable to that reported for the ratio of its two emission bands (34). More importantly, the contrast offered by the lifetime analysis and the intensity ratio differs according to its origin. Whereas ratiometric measurements are mainly sensitive to F2N12S hydration, fluorescence lifetimes mainly reflect the local dynamics of F2N12S in its lipid environment. The F2N12S fluorescence lifetimes measured at 580 nm are poorly sensitive to hydration or solvent relaxation effects because the T* form, in contrast to the N* form, exhibits low dipole moment in its excited state (78–80). Therefore, FLIM and ratiometric imaging with F2N12S are two complementary approaches for studying lipid membranes. Remarkably, when the Lo and Ld phases are compared, these two parameters correlate because the increase in the membrane rigidity (observed by lifetimes) is a result of tight packing in the Lo phase, which expels water from the membrane (observed by the ratio).

Whereas the time-resolved fluorescence parameters of F2N12S in the Ld phase were only moderately sensitive to Chol, it nevertheless appears that DOPC LUVs, which are frequently used as an Ld phase standard (34,41), do not appropriately mimic the Chol-rich Ld-like phase in cell membranes. It is likely that other lipids (in particular, partially unsaturated ones such as POPC) may also affect the local dynamics of F2N12S, making it difficult to find the appropriate lipid composition that will faithfully mimic the behavior of F2N12S in the Ld-like phase of cell membranes. The same conclusion likely applies also for the Lo phase. Further complication arises from the fact that, to our knowledge, the exact lipid composition of both phases in cell membranes is still not known. In these conditions, it appears to be very difficult to use this kind of tool to accurately determine the phase composition in cell membranes. Whereas an accurate quantitative determination of the two phases appears unrealistic, the large difference in the lifetimes of the two phases allowed us to reveal by FLIM that both Lo-like and Ld-like phases were distributed all over the PM of intact and Chol-depleted live cells. No separation of the two phases could be observed, suggesting that the two phases are mixed over the PM in our measurement conditions. This suggests that the two phases are highly dynamic on the timescale of the measurements (seconds) and/or that one or both phases show subdiffraction sizes (<250 nm), supporting the notion that lipid domains in cell membranes may be small and highly dynamic (81,82). In line with previous reports (31,34,41,54,62,66,83), the Lo-like phase was clearly dominant in live cells, whereas Chol depletion or apoptosis was found to increase the Ld-like phase. Thus, our data on the coexistence of the two phases and the prevalence of the Lo-like phase in intact cells are in line with a previous model suggesting that the PM may be constituted by a continuous Lo-like phase filled with Ld-like holes or, alternatively, by a continuous Ld-like phase containing a large number of Lo domains that cannot be spatially resolved (41).

Taken together, our data indicate that the use of F2N12S with lifetime-based approaches allows one to distinguish Lo from Ld phases with high contrast. We successfully used this technique to monitor membrane remodeling in F2N12S-labeled cells during various physiological processes, such as apoptosis. Further characterization of the membrane phases will require techniques with either faster acquisition rates than FLIM, such as fluorescence lifetime-transient scanning (FLITS, with a millisecond acquisition time (50)), or higher spatial resolution, such as single-particle tracking (82) and stimulated emission depletion-fluorescence correlation spectroscopy (STED-FCS) (81,84). Experiments using these techniques are currently being conducted on F2N12S-labeled cells.

SUPPORTING MATERIAL

Supporting Materials and Methods, two figures, and three tables are available at http://www.biophysj.org/biophysj/supplemental/S0006-3495(15)00349-5.

AUTHOR CONTRIBUTIONS

V.K., O.G., and L.H. performed research and analyzed the data. Y.M. designed research. V.K., A.K., L.R., and Y.M. wrote the article.

ACKNOWLEDGMENTS

We thank Nicolas Humbert, Ny Hanitra Andriamora, and Sule Oncul for technical assistance.

This work was supported by the University of Strasbourg and CNRS.

REFERENCES

1. Mouritsen, O. G. 2011. Lipidology and lipidomics—quo vadis? A new era for the physical chemistry of lipids. *Phys. Chem. Chem. Phys.* 13:19195–19205.
2. Brown, D. A., and J. K. Rose. 1992. Sorting of GPI-anchored proteins to glycolipid-enriched membrane subdomains during transport to the apical cell surface. *Cell.* 68:533–544.
3. van Meer, G., and K. Simons. 1988. Lipid polarity and sorting in epithelial cells. *J. Cell. Biochem.* 36:51–58.
4. Simons, K., and D. Toomre. 2000. Lipid rafts and signal transduction. *Nat. Rev. Mol. Cell Biol.* 1:31–39.
5. Dietrich, C., L. A. Bagatolli, …, E. Gratton. 2001. Lipid rafts reconstituted in model membranes. *Biophys. J.* 80:1417–1428.
6. Veatch, S. L., and S. L. Keller. 2002. Organization in lipid membranes containing cholesterol. *Phys. Rev. Lett.* 89:268101.
7. Lommerse, P. H., H. P. Spaink, and T. Schmidt. 2004. In vivo plasma membrane organization: results of biophysical approaches. *Biochim. Biophys. Acta.* 1664:119–131.
8. Pike, L. J. 2006. Rafts defined: a report on the Keystone Symposium on Lipid Rafts and Cell Function. *J. Lipid Res.* 47:1597–1598.
9. Pralle, A., P. Keller, …, J. K. H. Hörber. 2000. Sphingolipid-cholesterol rafts diffuse as small entities in the plasma membrane of mammalian cells. *J. Cell Biol.* 148:997–1008.

10. Dietrich, C., B. Yang, …, K. Jacobson. 2002. Relationship of lipid rafts to transient confinement zones detected by single particle tracking. *Biophys. J.* 82:274–284.

11. Schütz, G. J., G. Kada, …, H. Schindler. 2000. Properties of lipid microdomains in a muscle cell membrane visualized by single molecule microscopy. *EMBO J.* 19:892–901.

12. Lenne, P. F., L. Wawrezinieck, …, D. Marguet. 2006. Dynamic molecular confinement in the plasma membrane by microdomains and the cytoskeleton meshwork. *EMBO J.* 25:3245–3256.

13. Sharma, P., R. Varma, …, S. Mayor. 2004. Nanoscale organization of multiple GPI-anchored proteins in living cell membranes. *Cell.* 116:577–589.

14. Swamy, M. J., L. Ciani, …, J. H. Freed. 2006. Coexisting domains in the plasma membranes of live cells characterized by spin-label ESR spectroscopy. *Biophys. J.* 90:4452–4465.

15. Demchenko, A. P., Y. Mély, …, A. S. Klymchenko. 2009. Monitoring biophysical properties of lipid membranes by environment-sensitive fluorescent probes. *Biophys. J.* 96:3461–3470.

16. Janes, P. W., S. C. Ley, and A. I. Magee. 1999. Aggregation of lipid rafts accompanies signaling via the T cell antigen receptor. *J. Cell Biol.* 147:447–461.

17. Kenworthy, A. K., N. Petranova, and M. Edidin. 2000. High-resolution FRET microscopy of cholera toxin B-subunit and GPI-anchored proteins in cell plasma membranes. *Mol. Biol. Cell.* 11:1645–1655.

18. Xu, X., R. Bittman, …, E. London. 2001. Effect of the structure of natural sterols and sphingolipids on the formation of ordered sphingolipid/sterol domains (rafts). Comparison of cholesterol to plant, fungal, and disease-associated sterols and comparison of sphingomyelin, cerebrosides, and ceramide. *J. Biol. Chem.* 276:33540–33546.

19. Korlach, J., P. Schwille, …, G. W. Feigenson. 1999. Characterization of lipid bilayer phases by confocal microscopy and fluorescence correlation spectroscopy. *Proc. Natl. Acad. Sci. USA.* 96:8461–8466.

20. Bagatolli, L. A. 2006. To see or not to see: lateral organization of biological membranes and fluorescence microscopy. *Biochim. Biophys. Acta.* 1758:1541–1556.

21. Wu, Y., M. Stefl, …, M. K. Kuimova. 2013. Molecular rheometry: direct determination of viscosity in Lo and Ld lipid phases via fluorescence lifetime imaging. *Phys. Chem. Chem. Phys.* 15:14986–14993.

22. Kuimova, M. K., G. Yahioglu, …, K. Suhling. 2008. Molecular rotor measures viscosity of live cells via fluorescence lifetime imaging. *J. Am. Chem. Soc.* 130:6672–6673.

23. Levitt, J. A., M. K. Kuimova, …, D. Phillips. 2009. Membrane-bound molecular rotors measure viscosity in live cells via fluorescence lifetime imaging. *J. Phys. Chem. C.* 113:11634–11642.

24. Kuimova, M. K., S. W. Botchway, …, P. R. Ogilby. 2009. Imaging intracellular viscosity of a single cell during photoinduced cell death. *Nat. Chem.* 1:69–73.

25. Haidekker, M. A., and E. A. Theodorakis. 2007. Molecular rotors—fluorescent biosensors for viscosity and flow. *Org. Biomol. Chem.* 5:1669–1678.

26. Parasassi, T., E. Gratton, …, M. Levi. 1997. Two-photon fluorescence microscopy of laurdan generalized polarization domains in model and natural membranes. *Biophys. J.* 72:2413–2429.

27. Kim, H. M., H.-J. Choo, …, B. R. Cho. 2007. A two-photon fluorescent probe for lipid raft imaging: C-laurdan. *ChemBioChem.* 8:553–559.

28. Kim, H. M., B. H. Jeong, …, B. R. Cho. 2008. Two-photon fluorescent turn-on probe for lipid rafts in live cell and tissue. *J. Am. Chem. Soc.* 130:4246–4247.

29. Jin, L., A. C. Millard, …, L. M. Loew. 2005. Cholesterol-enriched lipid domains can be visualized by di-4-ANEPPDHQ with linear and nonlinear optics. *Biophys. J.* 89:L04–L06.

30. Owen, D. M., P. M. Lanigan, …, A. I. Magee. 2006. Fluorescence lifetime imaging provides enhanced contrast when imaging the phase-sensitive dye di-4-ANEPPDHQ in model membranes and live cells. *Biophys. J.* 90:L80–L82.

31. Kucherak, O. A., S. Oncul, …, A. S. Klymchenko. 2010. Switchable nile red-based probe for cholesterol and lipid order at the outer leaflet of biomembranes. *J. Am. Chem. Soc.* 132:4907–4916.

32. Krasnowska, E. K., E. Gratton, and T. Parasassi. 1998. Prodan as a membrane surface fluorescence probe: partitioning between water and phospholipid phases. *Biophys. J.* 74:1984–1993.

33. Shynkar, V. V., A. S. Klymchenko, …, Y. Mely. 2007. Fluorescent biomembrane probe for ratiometric detection of apoptosis. *J. Am. Chem. Soc.* 129:2187–2193.

34. Oncul, S., A. S. Klymchenko, …, Y. Mély. 2010. Liquid ordered phase in cell membranes evidenced by a hydration-sensitive probe: effects of cholesterol depletion and apoptosis. *Biochim. Biophys. Acta.* 1798:1436–1443.

35. Klymchenko, A. S., S. Oncul, …, Y. Mély. 2009. Visualization of lipid domains in giant unilamellar vesicles using an environment-sensitive membrane probe based on 3-hydroxyflavone. *Biochim. Biophys. Acta.* 1788:495–499.

36. M'Baye, G., Y. Mély, …, A. S. Klymchenko. 2008. Liquid ordered and gel phases of lipid bilayers: fluorescent probes reveal close fluidity but different hydration. *Biophys. J.* 95:1217–1225.

37. Parasassi, T., G. De Stasio, …, E. Gratton. 1990. Phase fluctuation in phospholipid membranes revealed by Laurdan fluorescence. *Biophys. J.* 57:1179–1186.

38. Stöckl, M. T., and A. Herrmann. 2010. Detection of lipid domains in model and cell membranes by fluorescence lifetime imaging microscopy. *Biochim. Biophys. Acta.* 1798:1444–1456.

39. Margineanu, A., J. Hotta, …, J. Hofkens. 2007. Visualization of membrane rafts using a perylene monoimide derivative and fluorescence lifetime imaging. *Biophys. J.* 93:2877–2891.

40. Kwiatek, J. M., D. M. Owen, …, K. Gaus. 2013. Characterization of a new series of fluorescent probes for imaging membrane order. *PLoS ONE.* 8:e52960.

41. Owen, D. M., D. J. Williamson, …, K. Gaus. 2012. Sub-resolution lipid domains exist in the plasma membrane and regulate protein diffusion and distribution. *Nat. Commun.* 3:1256.

42. Angelova, M. I., and D. S. Dimitrov. 1986. Liposome electroformation. *Faraday Discuss.* 81:303–311.

43. Fidorra, M., L. Duelund, …, L. A. Bagatolli. 2006. Absence of fluid-ordered/fluid-disordered phase coexistence in ceramide/POPC mixtures containing cholesterol. *Biophys. J.* 90:4437–4451.

44. Kahya, N., D. Scherfeld, …, P. Schwille. 2003. Probing lipid mobility of raft-exhibiting model membranes by fluorescence correlation spectroscopy. *J. Biol. Chem.* 278:28109–28115.

45. Godet, J., N. Ramalanjaona, …, Y. Mély. 2011. Specific implications of the HIV-1 nucleocapsid zinc fingers in the annealing of the primer binding site complementary sequences during the obligatory plus strand transfer. *Nucleic Acids Res.* 39:6633–6645.

46. Livesey, A. K., and J. C. Brochon. 1987. Analyzing the distribution of decay constants in pulse-fluorimetry using the maximum entropy method. *Biophys. J.* 52:693–706.

47. Brochon, J. C. 1994. Maximum entropy method of data analysis in time-resolved spectroscopy. *Methods Enzymol.* 240:262–311.

48. Clamme, J. P., J. Azoulay, and Y. Mély. 2003. Monitoring of the formation and dissociation of polyethylenimine/DNA complexes by two photon fluorescence correlation spectroscopy. *Biophys. J.* 84:1960–1968.

49. Azoulay, J., J. P. Clamme, …, Y. Mély. 2003. Destabilization of the HIV-1 complementary sequence of TAR by the nucleocapsid protein through activation of conformational fluctuations. *J. Mol. Biol.* 326:691–700.

50. Becker, W., V. Shcheslavkiy, …, I. Slutsky. 2014. Spatially resolved recording of transient fluorescence-lifetime effects by line-scanning TCSPC. *Microsc. Res. Tech.* 77:216–224.

51. Das, R., A. S. Klymchenko, …, Y. Mély. 2008. Excited state proton transfer and solvent relaxation of a 3-hydroxyflavone probe in lipid bilayers. *J. Phys. Chem. B.* 112:11929–11935.

52. Shynkar, V. V., Y. Mely, …, A. P. Demchenko. 2003. Picosecond time-resolved fluorescence studies are consistent with reversible excited-state intramolecular proton transfer in 4′-(dialkylaminoe)-3-hydroxyflavones. *J. Phys. Chem. A.* 107:9522–9529.

53. Sholokh, M., O. M. Zamotaiev, …, Y. Mély. 2015. Fluorescent amino acid undergoing excited state intramolecular proton transfer for site-specific probing and imaging of peptide interactions. *J. Phys. Chem. B.* 119:2585–2595.

54. Kilin, V., Z. Darwich, …, Y. Mely. 2013. Two photon fluorescence imaging of lipid membrane domains and potentials using advanced fluorescent probes. *Proc. SPIE.* 8588:13.

55. Parasassi, T., M. Di Stefano, …, E. Gratton. 1994. Cholesterol modifies water concentration and dynamics in phospholipid bilayers: a fluorescence study using Laurdan probe. *Biophys. J.* 66:763–768.

56. Kułakowska, A., P. Jurkiewicz, …, M. Hof. 2010. Fluorescence lifetime tuning—a novel approach to study flip-flop kinetics in supported phospholipid bilayers. *J. Fluoresc.* 20:563–569.

57. Chen, L., Z. Yu, and P. J. Quinn. 2007. The partition of cholesterol between ordered and fluid bilayers of phosphatidylcholine: a synchrotron X-ray diffraction study. *Biochim. Biophys. Acta.* 1768:2873–2881.

58. Huang, J., J. T. Buboltz, and G. W. Feigenson. 1999. Maximum solubility of cholesterol in phosphatidylcholine and phosphatidylethanolamine bilayers. *Biochim. Biophys. Acta.* 1417:89–100.

59. Bloch, K. E. 1979. Speculations on the evolution of sterol structure and function. *CRC Crit. Rev. Biochem.* 7:1–5.

60. Gaus, K., E. Gratton, …, W. Jessup. 2003. Visualizing lipid structure and raft domains in living cells with two-photon microscopy. *Proc. Natl. Acad. Sci. USA.* 100:15554–15559.

61. Massey, J. B. 1998. Effect of cholesteryl hemisuccinate on the interfacial properties of phosphatidylcholine bilayers. *Biochim. Biophys. Acta.* 1415:193–204.

62. Darwich, Z., A. S. Klymchenko, O. A. Kucherak, L. Richert, and Y. Mely. 2012. Detection of apoptosis through the lipid order of the outer plasma membrane leaflet. *Biochim. Biophys. Acta.* 1818:3048–3054.

63. Barucha-Kraszewska, J., S. Kraszewski, …, M. Hof. 2010. Numerical studies of the membrane fluorescent dyes dynamics in ground and excited states. *Biochim. Biophys. Acta.* 1798:1724–1734.

64. Schneider, C. A., W. S. Rasband, and K. W. Eliceiri. 2012. NIH Image to ImageJ: 25 years of image analysis. *Nat. Methods.* 9:671–675.

65. Bezlyepkina, N., R. S. Gracià, …, R. Dimova. 2013. Phase diagram and tie-line determination for the ternary mixture DOPC/eSM/cholesterol. *Biophys. J.* 104:1456–1464.

66. Hao, M., S. Mukherjee, and F. R. Maxfield. 2001. Cholesterol depletion induces large scale domain segregation in living cell membranes. *Proc. Natl. Acad. Sci. USA.* 98:13072–13077.

67. Zwaal, R. F., and A. J. Schroit. 1997. Pathophysiologic implications of membrane phospholipid asymmetry in blood cells. *Blood.* 89:1121–1132.

68. Tepper, A. D., P. Ruurs, …, W. J. van Blitterswijk. 2000. Sphingomyelin hydrolysis to ceramide during the execution phase of apoptosis results from phospholipid scrambling and alters cell-surface morphology. *J. Cell Biol.* 150:155–164.

69. Charras, G. T., M. Coughlin, …, L. Mahadevan. 2008. Life and times of a cellular bleb. *Biophys. J.* 94:1836–1853.

70. Kreder, R., K. A. Pyrshev, …, A. S. Klymchenko. 2015. Solvatochromic Nile Red probes with FRET quencher reveal lipid order heterogeneity in living and apoptotic cells. *ACS Chem. Biol.* Published online March 6: 2015. http://dx.doi.org/10.1021/cb500922m.

71. Parasassi, T., M. Di Stefano, …, E. Gratton. 1994. Influence of cholesterol on phospholipid bilayers phase domains as detected by Laurdan fluorescence. *Biophys. J.* 66:120–132.

72. Ariola, F. S., D. J. Mudaliar, …, A. A. Heikal. 2006. Dynamics imaging of lipid phases and lipid-marker interactions in model biomembranes. *Phys. Chem. Chem. Phys.* 8:4517–4529.

73. de Almeida, R. F., J. Borst, …, A. J. Visser. 2007. Complexity of lipid domains and rafts in giant unilamellar vesicles revealed by combining imaging and microscopic and macroscopic time-resolved fluorescence. *Biophys. J.* 93:539–553.

74. Stöckl, M., A. P. Plazzo, …, A. Herrmann. 2008. Detection of lipid domains in model and cell membranes by fluorescence lifetime imaging microscopy of fluorescent lipid analogues. *J. Biol. Chem.* 283:30828–30837.

75. Balogh, G., G. Maulucci, …, L. Vígh. 2011. Heat stress causes spatially-distinct membrane re-modelling in K562 leukemia cells. *PLoS ONE.* 6:e21182.

76. Jameson, D. M., E. Gratton, and R. D. Hall. 1984. The measurement and analysis of heterogeneous emissions by multifrequency phase and modulation fluorometry. *Applied Spec. Rev.* 20:55–106.

77. Digman, M. A., V. R. Caiolfa, …, E. Gratton. 2008. The phasor approach to fluorescence lifetime imaging analysis. *Biophys. J.* 94:L14–L16.

78. Klymchenko, A. S., and A. P. Demchenko. 2002. Electrochromic modulation of excited-state intramolecular proton transfer: the new principle in design of fluorescence sensors. *J. Am. Chem. Soc.* 124:12372–12379.

79. Kenfack, C. A., A. S. Klymchenko, …, Y. Mély. 2012. Ab initio study of the solvent H-bonding effect on ESIPT reaction and electronic transitions of 3-hydroxychromone derivatives. *Phys. Chem. Chem. Phys.* 14:8910–8918.

80. Demchenko, A. P., K. C. Tang, and P. T. Chou. 2013. Excited-state proton coupled charge transfer modulated by molecular structure and media polarization. *Chem. Soc. Rev.* 42:1379–1408.

81. Eggeling, C., C. Ringemann, …, S. W. Hell. 2009. Direct observation of the nanoscale dynamics of membrane lipids in a living cell. *Nature.* 457:1159–1162.

82. Sahl, S. J., M. Leutenegger, …, C. Eggeling. 2010. Fast molecular tracking maps nanoscale dynamics of plasma membrane lipids. *Proc. Natl. Acad. Sci. USA.* 107:6829–6834.

83. Darwich, Z., O. A. Kucherak, …, A. S. Klymchenko. 2013. Rational design of fluorescent membrane probes for apoptosis based on 3-hydroxyflavone. *Methods Appl. Fluoresc.* 1:025002.

84. Honigmann, A., V. Mueller, …, C. Eggeling. 2014. Scanning STED-FCS reveals spatiotemporal heterogeneity of lipid interaction in the plasma membrane of living cells. *Nat. Commun.* 5:5412.

Publication 4: “Counterion-enhanced cyanine dye loading into lipid nano-droplets for single-particle tracking in zebrafish”

Biomaterials 35 (2014) 4950–4957

Contents lists available at ScienceDirect

Biomaterials

journal homepage: www.elsevier.com/locate/biomaterials

Counterion-enhanced cyanine dye loading into lipid nano-droplets for single-particle tracking in zebrafish

Vasyl N. Kilin [a,1], Halina Anton [a,1], Nicolas Anton [b], Emily Steed [c], Julien Vermot [c], Thierry F. Vandamme [b], Yves Mely [a], Andrey S. Klymchenko [a,*]

[a] Laboratoire de Biophotonique et Pharmacologie, UMR 7213 CNRS, Université de Strasbourg, Faculté de Pharmacie, 74, Route du Rhin, 67401 Illkirch, France
[b] Laboratoire de Conception et Application de Molecules Bioactives, UMR CNRS 7199, Université de Strasbourg, Faculté de Pharmacie, 74, Route du Rhin, 67401 Illkirch, France
[c] IGBMC (Institut de Génétique et de Biologie Moléculaire et Cellulaire), Inserm U964, CNRS UMR7104, Université de Strasbourg, 1 rue Laurent Fries, 67404 Illkirch, France

ARTICLE INFO

Article history:
Received 10 February 2014
Accepted 25 February 2014
Available online 21 March 2014

Keywords:
lipid
nanoparticle
nano-emulsion
fluorescence
counterion-assisted dye loading
singleparticle tracking

ABSTRACT

Superior brightness of fluorescent nanoparticles places them far ahead of the classical fluorescent dyes in the field of biological imaging. However, for *in vivo* applications, inorganic nanoparticles, such as quantum dots, are limited due to the lack of biodegradability. Nano-emulsions encapsulating high concentrations of organic dyes are an attractive alternative, but classical fluorescent dyes are inconvenient due to their poor solubility in the oil and their tendency to form non-fluorescent aggregates. This problem was solved here for a cationic cyanine dye (DiI) by substituting its perchlorate counterion for a bulky and hydrophobic tetraphenylborate. This new dye salt, due to its exceptional oil solubility, could be loaded at 8 wt% concentration into nano-droplets of controlled size in the range 30–90 nm. Our 90 nm droplets, which contained >10,000 cyanine molecules, were >100-fold brighter than quantum dots. This extreme brightness allowed, for the first time, single-particle tracking in the blood flow of live zebrafish embryo, revealing both the slow and fast phases of the cardiac cycle. These nano-droplets showed minimal cytotoxicity in cell culture and in the zebrafish embryo. The concept of counterion-based dye loading provides a new effective route to ultra-bright lipid nanoparticles, which enables tracking single particles in live animals, a new dimension of *in vivo* imaging.

1. Introduction

Fluorescent nanoparticles have been a dramatic surge in the recent years due their unique properties, placing them far ahead of the classical fluorescent dyes in the field of biological imaging. Thus, quantum dots [1,2], dye-doped silica nanoparticles [3,4], and nanodiamonds [5,6] show significantly higher brightness than fluorescent dyes together with possibility of multiple surface modifications for specific targeting. They were particularly important for techniques that require super-sensitive detection, namely, single-particle tracking (SPT) and *in vivo* animal imaging. SPT with fluorescent nanoparticles was successfully used for monitoring diffusion of biomolecules in live cells and flow in biological fluids [7–11]. However, it remains a challenge to perform SPT in live animals due to the insufficient brightness of the nano-objects and the strong light absorption and scattering of the tissues. The experiments in animals reported so far deal with *in vivo* imaging of large populations of nanoparticles [12–15], so that behavior of individual nanoparticles was not addressed. One rare example showed the possibility to monitor the pathway of individual quantum dots *in vivo*, to clarify the mechanism of their interaction and internalization into tumors [16]. It is obvious that SPT experiments require ultra-high brightness. Moreover, *in vivo* applications request biodegradability, which is not the case for the well-established inorganic nanoparticles. An attractive alternative is offered by organic nanoparticles, which being composed of organic materials, lipids or polymers, can be intrinsically non-toxic and biodegradable [12,17–19]. Moreover, they can encapsulate a large quantity of organic dyes, so that particles of exceptional brightness, close or even superior to quantum dots can be obtained [20–24].

In this respect, lipid nano-emulsions, composed of nano-droplets with liquid-core, are of particular interest for biological

* Corresponding author. Tel.: +33 368 85 42 55; fax: +33 390 24 43 13.
E-mail address: andrey.klymchenko@unistra.fr (A.S. Klymchenko).
[1] These authors contributed equally.

http://dx.doi.org/10.1016/j.biomaterials.2014.02.053
0142-9612/

imaging [21,25–27]. Firstly, nano-emulsions are composed of non-toxic components, which are biodegradable and/or readily eliminated from the animal body. Secondly [28–31], the oily core of nano-droplets is a perfect reservoir for encapsulation of lipophilic dyes, in contrast to the solid-core particles, where the distribution and fluorescent properties of the dyes are difficult to control [32]. The other advantage is their simple and rapid preparation based on spontaneous nano-emulsification [28,30,31], allowing a sharp control of the size and composition of the nano-droplets. However, examples of highly fluorescent lipid nano-droplets and their application for bioimaging are limited. In one report, Texier et al. prepared lipid nanocarriers encapsulating cyanine dyes bearing long hydrophobic chains [20]. The authors encapsulated up to 53 molecules per particle of 35 nm diameter, which corresponded to a 3.9 mM concentration of the dye in the droplets and showed their successful application for cellular and *in vivo* animal imaging [25]. Recently, we designed lipophilic fluorescent derivatives of 3-alkoxyflavone and Nile Red. For the non-planar 3-alkoxyflavone dye, 170 mM loading was achieved with no sign of self-quenching, which corresponds to ~830 dyes per 40-nm droplet. In contrast for the Nile Red derivative, self-quenching was observed already above 17 mM, indicating that its planar structure favors its aggregation at high concentrations [21]. Achieving high encapsulation efficiency for cyanine dyes, as for the 3-alkoxyflavone, would be of particular importance, because they show ~10-fold larger absorption coefficient compared to 3-alkoxyflavones. However, the cationic nature of cyanines limits their solubility in the apolar oils of the nano-emulsions. Moreover, at high concentrations, cyanines tend to form non-emissive π-stacked structures, so-called H-aggregates [33], which are responsible for strong self-quenching. We hypothesized that these problems could be solved by replacing a small hydrophilic counterion (i.e. perchlorate) of a cationic cyanine dye with a bulky hydrophobic tetraphenylborate (TPB) anion (Fig. 1). Salts of TPB are known to be soluble in organic solvents and used as ionophores in polymer matrix, to generate ionic sites in cation-sensitive electrodes [34,35]. Moreover, a recently proposed "ion-association" method uses TPB derivatives to precipitate water soluble cationic organic dyes into fluorescent nanoparticles [36].

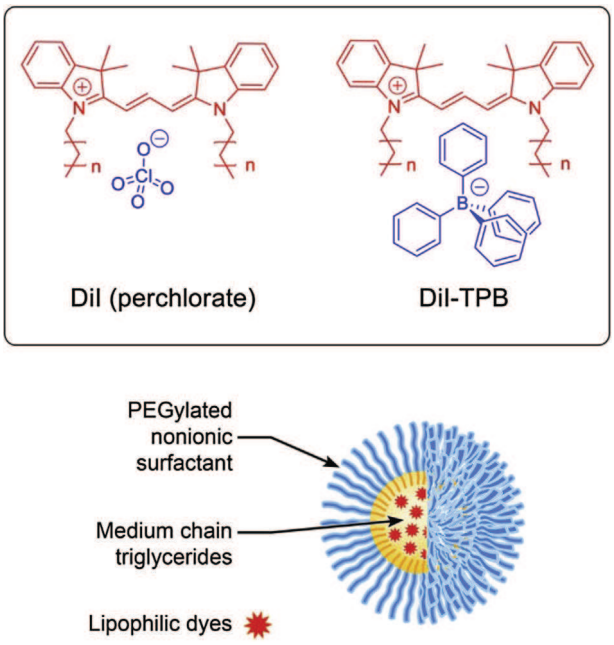

Fig. 1. Chemical structures of DiI perchlorate and DiI-TPB and schematic presentation of nano-droplet encapsulating them.

However to date, this method has never been applied for increasing the encapsulation efficiency of cationic dyes into lipid nanocarriers.

In the present work, we used fluorescent nano-emulsion as a nanocarrier of hydrophobic cyanine dye 1,1′-dioctadecyl-3,3,3′,3′-Tetramethylindocarbocyanine (DiI) and proposed an innovative approach to drastically improve the dye encapsulation efficiency by replacing its perchlorate counterion with a bulky hydrophobic TPB (Fig. 1). After detailed characterization of the obtained nano-droplets of different size in solutions, they were studied in the blood circulatory system of zebrafish at the single-particle level. This work opens a new route to biodegradable organic nano-objects of exceptional fluorescence brightness, which enable single-particle tracking *in vivo*.

2. Materials and methods

All chemicals and solvents for synthesis were from Sigma–Aldrich. Nonionic surfactants (Cremophor ELP®) are of parenteral grade, and consist of a PEG chain (M_w = 1500 g/mol^{-1}) grafted onto a triglyceride (castor oil). They were obtained from BASF (Ludwigshafen, Germany) kindly gifted from Laserson (Etampes, France). Medium chain triglycerides (Labrafac CC®) were obtained from Gattefossé (Saint-Priest, France). Ultrapure® water was obtained using a Milli-Q filtration system (Millipore, Saint-Quentin-en-Yvelines, France). Culture reagents were obtained from Sigma (St. Louis, USA), Lonza (Verviers, Belgium) and Gibco-Invitrogen (Grand Island, USA).

2.1. Synthesis of DiI-TPB

100 mg of 1,1′-dioctadecyl-3,3,3′,3′-tetramethylindocarbocyanine (DiI) perchlorate (Life Technologies) was mixed with 3.6 g (100 mol eq) of sodium tetraphenylborate in ethyl acetate, which dissolved readily both salts. The formation of the desired salt was confirmed by thin layer chromatography, where the product moved much faster than the starting DiI perchlorate (dichloromethane/methanol, 95/5). After solvent evaporation the product (DiI-TPB) was purified by column chromatography (dichloromethane/methanol, 95/5).

2.2. Formulation and characterization of nano-emulsions

Nano-emulsions were prepared by spontaneous nano-emulsification. Briefly, DiI-TPB was dissolved in Labrafac CC®. Then, Cremophor ELP® was added and the mixture was homogenized under magnetic stirring at 35 °C. Nano-emulsions were formed by adding ultrapure (Milli-Q) water. Two sizes of nano-droplets were prepared by varying the proportions between the different components (Table 1). Formulation A, giving nano-droplets of *ca* 30-nm diameter contained 20 mg of Labrafac CC®, 80 mg of Cremophor ELP® and 230 mg of water. Formulation B, giving nano-droplets of *ca* 90-nm diameter contained 55 mg of Labrafac CC®, 45 mg of Cremophor ELP® and 230 mg of water.

The size distribution of the nano-emulsions was determined by dynamic light scattering on a Zetasizer® Nano series DTS 1060 (Malvern Instruments S.A., Worcestershire, UK) using the following specifications: medium viscosity, 0.8872 cP; refractive index (RI) medium, 1.33; RI of nano-droplets 1.454; scattering angle, 90°; temperature, 25 °C.

2.3. Fluorescence spectroscopy

Absorption and fluorescence spectra were recorded on a Cary 4 spectrophotometer (Varian) and a Fluorolog (Jobin Yvon, Horiba) spectrofluorometer, respectively. Fluorescence emission spectra were recorded at room temperature with

Table 1
Characterization of the nano-droplets encapsulating cyanine dyes by DLS and fluorescence measurements.

% surfactant	Dye	[Dye], wt%	Size, nm	PDI	Dyes/droplet	QY
70	–	0	27	0.07	–	–
50	–	0	87	0.17	–	–
70	DiI-ClO4	0.1	36	0.11	8	0.50
70	DiI-TPB	0.1	23	0.13	2	0.49
70	DiI-TPB	1	28	0.02	33	0.31
70	DiI-TPB	4	24	0.19	75	0.17
70	DiI-TPB	8	31	0.13	384	0.13
50	DiI-TPB	8	87	0.16	12,052	0.14

% surfactant is the concentration of Cremophor (wt%) in the mixture with Labrafac, used in the formulation; *[Dye]* is the dye concentration (wt%); *size* is the hydrodynamic diameter of nano-droplets (nm); *PDI* is the polydispersity index; *Dyes/droplet* is estimated number of dyes per droplet; *QY* is the fluorescence quantum yield.

520 nm excitation wavelengths. All fluorescence measurements were done using solutions with absorbance ≤0.1. Fluorescence quantum yields (QY) of DiI perchlorate and DiI-TPB loaded nano-droplets were measured using Rhodamine B in methanol (QY = 0.68) as a reference [37].

2.4. Single-particle measurements

Nano-droplets (90 nm diameter with 8% of DiI-TPB) and fluorescent polystyrene nanoparticles (FluoSpheres, Red-orange, 565/580 nm, 45 nm diameter) were immobilized in 1% agarose (Aldrich) gel. For this purpose, nano-droplets and FluoSpheres were diluted 5×10^4 and 10^5 times, respectively, from their original formulation into a warm gel solution. The dilution was made in order to achieve close concentrations of the two types of particles. After 30 min of incubation, the obtained gels were ready for fluorescence microscopy studies. Fluorescence images were taken on a Leica TSC SPE confocal microscope, using a 561 nm laser source. The particle displacement in the gel was negligible during the acquisition time (10 s per image).

For the determination of the molar absorption coefficient per nano-droplet, FluoSpheres® red-orange (diameter 0.04 μm, carboxylate modified, Invitrogen) were used as a reference. From the micrographs, the mean fluorescence intensity of the FluoSpheres I_{FS} was determined. Their quantum yield ($QY_{FS} = 0.57$) and per particle molar absorption coefficient ($\varepsilon_{FS} = 2.66 \times 10^7$ M^{-1} cm^{-1} at 561 nm) were determined in independent measurements. From this, molar absorption coefficient per nano-droplet was obtained according to:

$$\varepsilon_{ND} = \frac{I_{ND}}{I_{FS}} \cdot \frac{\varepsilon_{FS} \cdot QY_{FS}}{QY_{ND}} \quad (1)$$

where ε_{ND} is the molar absorption coefficient per nano-droplet, I_{ND} is the mean emission intensity of the DiI-loaded nano-droplets, and QY_{ND} is the quantum yield of the nano-droplets.

2.5. Cytotoxicity studies

HeLa cells were seeded in 96-well plates at a concentration of 1.10^4 cells per well in 100 μL of the DMEM growth medium and then incubated overnight at 37 °C in humidified atmosphere containing 5% CO_2. Next, the lipid nano-droplets containing 8 wt% DiI-TPB were added, by substituting the culture medium for a similar one containing variable dilutions of the nano-droplets. After incubation for 24 h, the medium was removed and the adherent cell monolayers were washed with PBS. Then, the wells were filled with cell culture medium containing MTT, incubated for 4 h at 37 °C, and the formazan crystals formed were dissolved by adding 100 μL of 10% of sodium dodecyl sulfate (SDS), 0.01 M hydrochloric acid solution. The absorbance was then measured at 570 nm with a microplate reader (Xenius, Safas). The remaining absorbance from DiI-TPB was negligible compared to the formazan absorbance in all cases. Experiments were carried out in triplicate, and expressed as a percentage of viable cells compared to the control group.

2.6. In vivo imaging on zebrafish

Zebrafish were kept at 28 °C and bred under standard conditions. The transgenic zebrafish *Tg(fli1:eGFP)^{y1}*, expressing eGFP specifically in the endothelial cells, was used in order to visualize the vasculature [38]. For the angiography, the embryos, 3 days after fertilization, were anaesthetized in Danieau 0.3% containing 0.04% Tricaine and 0.05% Phenylthiourea (Sigma–Aldrich) and immobilized in 0.8% low melting point agarose (Sigma). The injections were performed using a Nanoject microinjector (Drummond Scientific, Broomall, PA, USA). The glass capillary was filled with DiI-TPB nano-emulsions (8 wt% in oil) in 5 mM Hepes and 2.3 nL were injected in the sinus venosus of the embryos as described elsewhere [39]. The dilutions used were 1000× for the microangiography experiments and 1,000,000× for the single-particle tracking experiments. The nano-emulsion was immediately distributed in all the vasculature. The injected embryos were placed on the microscope stage and imaged within 5 min after injection. The microangiography imaging was performed on a Leica SP5 Fixed stage direct microscope with a 25× (NA 0.95) and 10× (NA 0.3) water immersion objectives. 488 nm argon and 561 nm supercontinuum laser lines were used to excite both eGFP and the DiI-TPB dyes, respectively. Fluorescence emission was detected by two separate PMTs in the spectral range 500–530 nm for green and 600–650 nm for the red channel. In these conditions, no cross-talk between the channels was observed.

Single-particle tracking experiments were performed on a Zeiss 780 inverted microscope with a 40× (NA 1.2) water immersion objective. eGFP and the nano-droplets were excited by 488 nm and 561 nm laser lines, respectively. In order to increase to the maximum the acquisition speed (20 frames per second), the time-lapses were recorded sequentially in red and green channel and superimposed post acquisition.

The embryos were imaged during 1 h post injection and no toxicity due to the injection or to the illumination was observed. To avoid any influence of the temperature on the heart rate and blood velocity profile, the microscope stage was placed in a heated box and the temperature maintained at 28 °C. All experiments performed with zebrafish complied with the European directive 86/609/CEE and IGBMC guidelines validated by the regional committee of ethics.

Confocal z-stacks and time-lapse sequences were treated by the ImageJ software (http://rsbweb.nih.gov/ij/). The blood flow in the dorsal aorta is highly pulsatile. During the systole, the peak velocity may reach 2000 μm/s while during the diastole the blood cells are almost stationary. The dynamic range of the particle velocities is very large and therefore, two different approaches were applied to analyze the particle velocities during the whole heart cycle. During the diastole, the flow speed was low, so that individual particles were followed in several consecutive frames and the particle velocities were determined by manual tracking. In the frames where the blood flow was high, the moving particles were visualized as “tilted lines”. In fact, the particles were moving too fast and were thus captured by the scanning laser beam in different positions. Therefore, the velocity of the particle was calculated by measuring the distance of the particle trace between two lines and dividing it by the time that the laser beam took to scan one line (0.75 ms) in a similar way to the kymograph analysis. This combined analysis permitted us to measure the velocity value during the whole heart beat cycle.

3. Results and discussion

3.1. Ion exchange and solubility in oil

DiI-TPB was synthesized by ion exchange using DiI perchlorate (DiI-ClO4) with 100-fold molar excess of sodium TPB in ethyl acetate. The formation of the desired salt was confirmed by thin layer chromatography, where the product moved much faster than the starting DiI perchlorate. After solvent evaporation, the product (DiI-TPB) was purified by column chromatography.

To encapsulate the dyes into nano-droplets, they should be first dissolved in the corresponding oil. In our preparations, Labrafac CC® (Labrafac), a medium chain triglyceride, was used. To obtain solution of DiI-ClO4 in Labrafac, it was first dissolved in acetone, then mixed with Labrafac and finally evaporated to obtain theoretically a 1.0 weight % (wt%) solution of the dye. However, after acetone evaporation DiI-ClO4 precipitated in Labrafac. After removing the excess of dye by centrifugation, the supernatant corresponding to the saturated solution of DiI-ClO4 showed only 0.2 wt% concentration according to photometry measurements. This concentration is close to that used by Texier et al. to prepare lipid nanoparticles with the highest possible loading of analogous cyanine dyes [20]. In contrast, DiI-TPB was readily soluble in Labrafac, as we could easily prepare 8 wt% concentration of DiI-TPB (higher concentrations were possible but were not studied). Thus, substitution of perchlorate anion with TPB improves drastically the solubility of DiI in the oil (>40-fold). The obtained 8 wt% solution and its dilutions to 4, 1 and 0.1 wt% were used to further prepare nano-droplets.

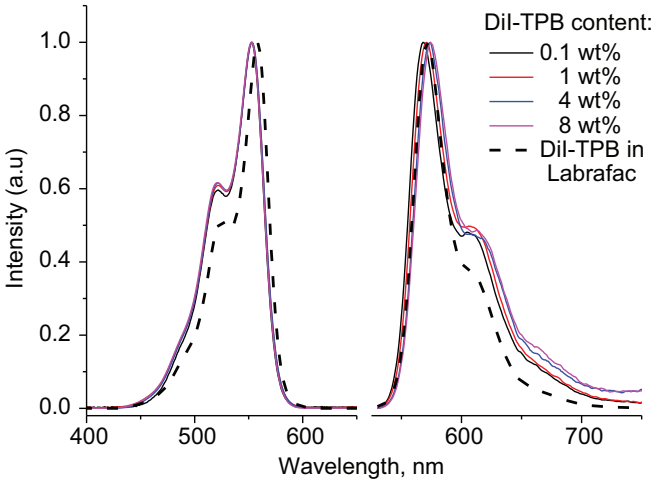

Fig. 2. Absorption and fluorescence spectra of DiI-TPB loaded nano-emulsions at different weight content (wt%) in Labrafac.

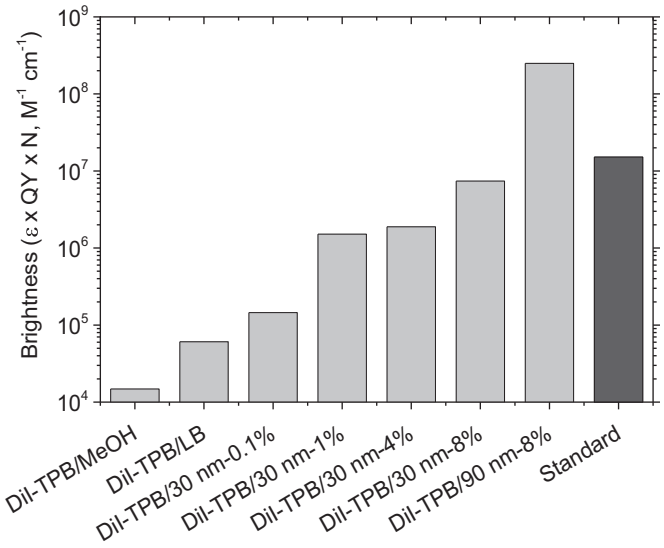

Fig. 3. Estimated brightness of fluorescent nano-droplets in comparison to DiI-TPB in solution and standard fluorescent nanoparticles (FluoSpheres, Red-orange, 565/580 nm, 45 nm diameter). The brightness is expressed as $\varepsilon \times QY \times N$ [40], where ε is the absorption coefficient of the dye; QY – quantum yield; N – number of dyes per particle.

3.2. Preparation of nano-droplets

The dye solution in Labrafac was first thoroughly mixed with Cremophor ELP® surfactants (Cremophor, polyethylene-glycol (35) ricinoleate) at a constant temperature of 35 °C. Then, nano-emulsions were generated after sudden addition of Milli-Q water to this mixture under gentle stirring. Two formulations were made with different oil-surfactant weight ratio, and droplet mean diameter around 30 and 90 nm, according to dynamic light scattering (DLS) measurements (Table 1). Remarkably, nano-droplets encapsulating DiI-TPB at all studied concentrations showed nearly the same polydispersity and size as the blank nano-droplets.

3.3. Optical properties

Photometric measurements showed that the dye concentration in the various formulations corresponded closely to the one expected from their preparation (not shown), suggesting quantitative solubilization of the fluorophore in the nano-emulsions. This result was expected, taking into account the extremely high hydrophobicity of the DiI-TPB dye, which remains in the oil phase during the nano-droplet preparation.

Remarkably, the absorption spectra of nano-droplets are independent of the DiI-TPB concentration inside the nano-droplets (expressed in wt% with respect to Labrafac). Even at 8 wt% loading, the shape of the spectrum is represented by a narrow band centered at 553 nm (Fig. 2), which indicates that even at this high dye concentration no dye aggregation is observed. However, these spectra slightly differ from that in neat Labrafac, indicating that the environment of the droplets is different probably due to the Cremophor-based shell.

Fluorescence spectra also showed a single emission band, which shifts marginally to the red with an increase in the dye concentration and matches closely the maximum emission wavelength in neat Labrafac. At low dye loading, the fluorescence quantum yield of the nano-emulsion is very high and close to that observed for DiI-ClO4 and DiI-TPB in Labrafac. The up to 5-fold larger QY values in Labrafac and nano-droplets as compared to methanol are related to their very low viscosity, which decreases the non-radiative deactivation due to the fluorophore motion. With increase in the DiI-TPB dye loading, QY values decreased gradually (Table 1). This phenomenon is typical for highly concentrated dye solutions, where different quenching phenomena may take place. However, this decrease is relatively moderate, as an increase in the concentration by 80-fold (from 0.1 to 8 wt%) leads to a decrease in QY by only a factor of 3.5. As the brightness of the nano-droplets is proportional to the dye concentration and QY, the particle brightness at 8 wt% should increase by about 80/3.5 – *ca* 23-fold compared to the particle encapsulating 0.1 wt% of the dye. Based on the QY values, absorption coefficient and the calculated approximate number of fluorophores per nano-droplet (based on dye wt% and mass of the nano-droplets with a given hydrodynamic diameter), we estimated the brightness of our nano-droplets and compared it with DiI dye and standard fluorescent nanoparticles of known brightness (Fig. 3).

To confirm experimentally the brightness of our nano-droplets, we performed fluorescence imaging of our largest nano-droplets (90 nm) with the heaviest DiI-TPB loading (8 wt%), which are the most attractive candidates for SPT *in vivo* (see below). Confocal microscopy images of these nano-droplets immobilized in agarose gel were compared with those of polystyrene nanoparticles of similar absorption and fluorescence properties (FluoSpheres, Red-orange, 565/580 nm, 45 nm diameter, quantum yield 0.57 and molar absorption coefficient per particle of 2.7×10^7 м$^{-1}$ cm^{-1} at 561 nm), used as a standard. From the fluorescence images, our nano-droplets are clearly brighter than the standard polystyrene nanoparticles (Fig. 4). Statistical analysis of the images revealed a

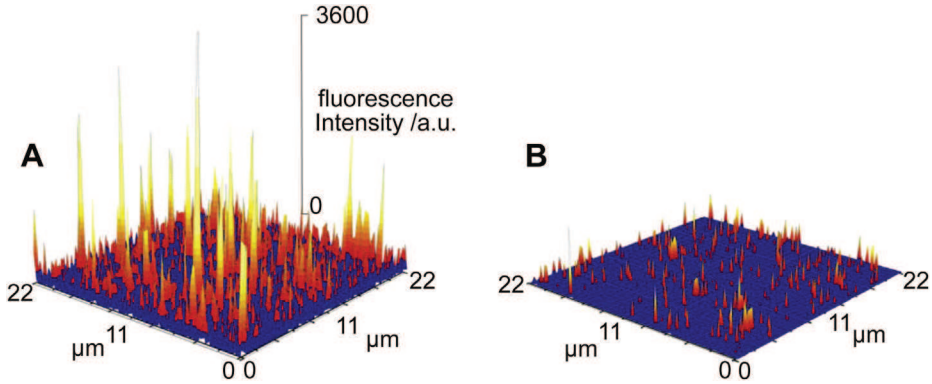

Fig. 4. Confocal images of nano-droplets loaded with DiI-TPB at 8 wt% (A) and standard polystyrene fluorescent nanoparticles (FluoSpheres, Red-orange, 565/580 nm, 45 nm diameter) of similar spectroscopic properties (B) in agarose gel recorded at the same experimental conditions.

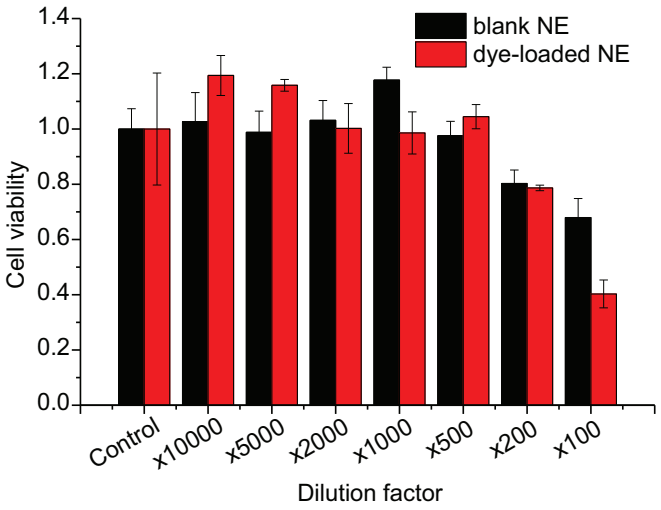

Fig. 5. Cytotoxicity tests of nano-emulsions (NE) loaded with DiI-TPB. Cell viability was measured by MTT assay on HeLa cells incubated for 24 h with 90-nm size nano-emulsions droplets without and with 8 wt% of DiI-TPB at different dilutions from the original formulation.

5.3-fold difference in the brightness (Fig. S1 in SI), in reasonable agreement with the 16-fold difference in the estimated brightness (Fig. 3). Thus, we deduced that our particles, having a quantum yield of 0.14, show an extinction coefficient of 5.7×10^8 M^{-1} cm^{-1}, that corresponds to the expected value based on the theoretical number of fluorophores per droplet (1.8×10^9 M^{-1} cm^{-1}). The experimental brightness value (i.e. QY $\times$ absorption coefficient of droplet) is more than 100-fold higher than that of quantum dots of similar emission wavelength, which typically show molar absorption coefficient $\sim 1 \times 10^6$ M^{-1} cm^{-1} at the long-wavelength maximum and quantum yield ~ 0.5 [41]. The brightness of our nano-droplets is comparable only with fluorescent polystyrene beads of similar size (from Life technologies), but the latter are not biodegradable and have thus limited applications *in vivo*.

3.4. Cytotoxicity

As cytotoxicity is the key issue for biological applications of nanoparticles, we investigated the cytotoxicity of our nano-emulsions using the MTT assay. In most of the dilutions from the original highly concentrated formulation, the cytotoxicity was not detectable (Fig. 5). It starts only to be observed for dilution factors below 200, which corresponds to 0.15% mass content of the principle constituents of the nano-emulsion (oil and surfactant). The presence of 8 wt% of DiI-TPB dye in the nano-emulsions did not change the observed low cytotoxicity for all studied dilutions, except at 100-fold dilution, where a higher toxicity was observed. Moreover, for all concentrations studied in the presence and absence of DiI-TPB, microscopy observations did not reveal any increase in the number of the dead (detached) cells with respect to the alive ones (data not shown). This indicates that even at the highest concentration used, the nano-emulsions probably did not kill the cells but just slowed down their division. It should be noted that cell viability was decreased for dilutions that correspond to 21 μM DiI dye concentration, which is >20-fold larger than the dye concentration usually used in biological samples (<1 μM). These encouraging results can be explained by the fact that our nano-emulsions are built from non-toxic elements. Moreover, it appears that at the concentrations used, the DiI dye salt with a hydrophobic TPB counterion inside the nano-emulsion droplets is not toxic. This important result shows the great potential of these nano-emulsions for bioimaging applications, especially *in vivo*, where low toxicity is a crucial requirement.

3.5. Microangiography in zebrafish embryos

Having obtained ultra-bright fluorescent nano-droplets, we further tested their suitability for *in vivo* microangiography imaging on living zebrafish embryos. Nano-emulsions of 30- or 90-nm nano-droplets containing 8 wt% DiI-TPB were injected in the sinus venosus of the embryos, and the embryos were imaged by confocal microscopy (Fig. 6 and Fig. S2 in SI). The nano-droplets were immediately distributed in all the vascular system and the obtained staining patterns did not change within the 5–30 min period after

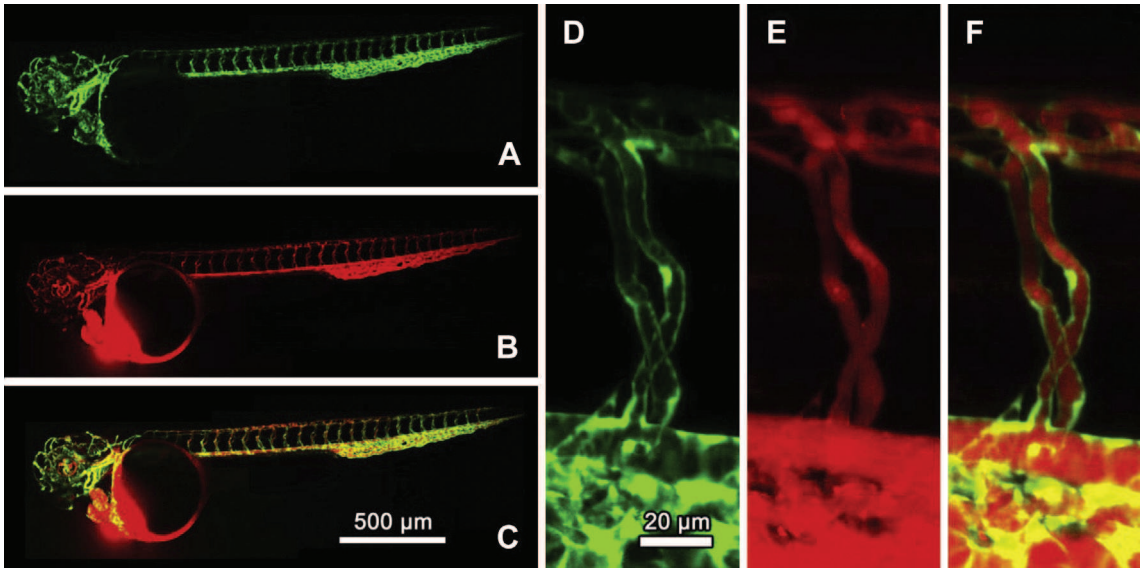

Fig. 6. Zebrafish microangiography using 90-nm nano-droplets containing 8 wt% of DiI-TPB injected in *Tg(fli1:eGFP)*^{y1} embryons 3 days post fertilization. Images present the global view (A–C) and a zoom in of the trunk vasculature (D–F). Images in green (A and D) present endothelial cells expressing eGFP, while images in red present the fluorescence of DiI-TPB, 30 min after injection of the nano-emulsion. The merged images (C and F) show no colocalization of DiI-TPB with the endothelial cells.

injection. Fig. 6 shows typical examples of angiography using 90 nm nano-emulsion droplets. The eGFP-expressing endothelial cells [38], which constitute the vessel walls, were visualized in the green channel (Fig 6A and D), while nano-droplets were observed in the red one (Fig. 6B and E). The DiI-TPB fluorescence was detected exclusively in the lumen of the vessels, as shown in Fig. 6 D–F. No labeling of the endothelial cells by DiI was visible even 60 min after injection, indicating that DiI-TPB loaded nano-droplets remain in the blood circulation without interacting with the vessel wall and without dye leakage from the nano-droplets. Previously, we showed that Nile Red loaded in similar nano-droplets diffused and accumulated in endothelial cells, while its highly hydrophobic derivative NR668 remained in the blood circulation [21]. The presently observed stability of DiI-TPB in the blood circulatory system is clearly connected with the very high hydrophobicity of this dye salt, which prevents its leakage from the low-polar nano-droplet core. Noticeably, other *in vivo* studies on similar nanocarrier systems showed their sufficiently long circulation half-life in the blood

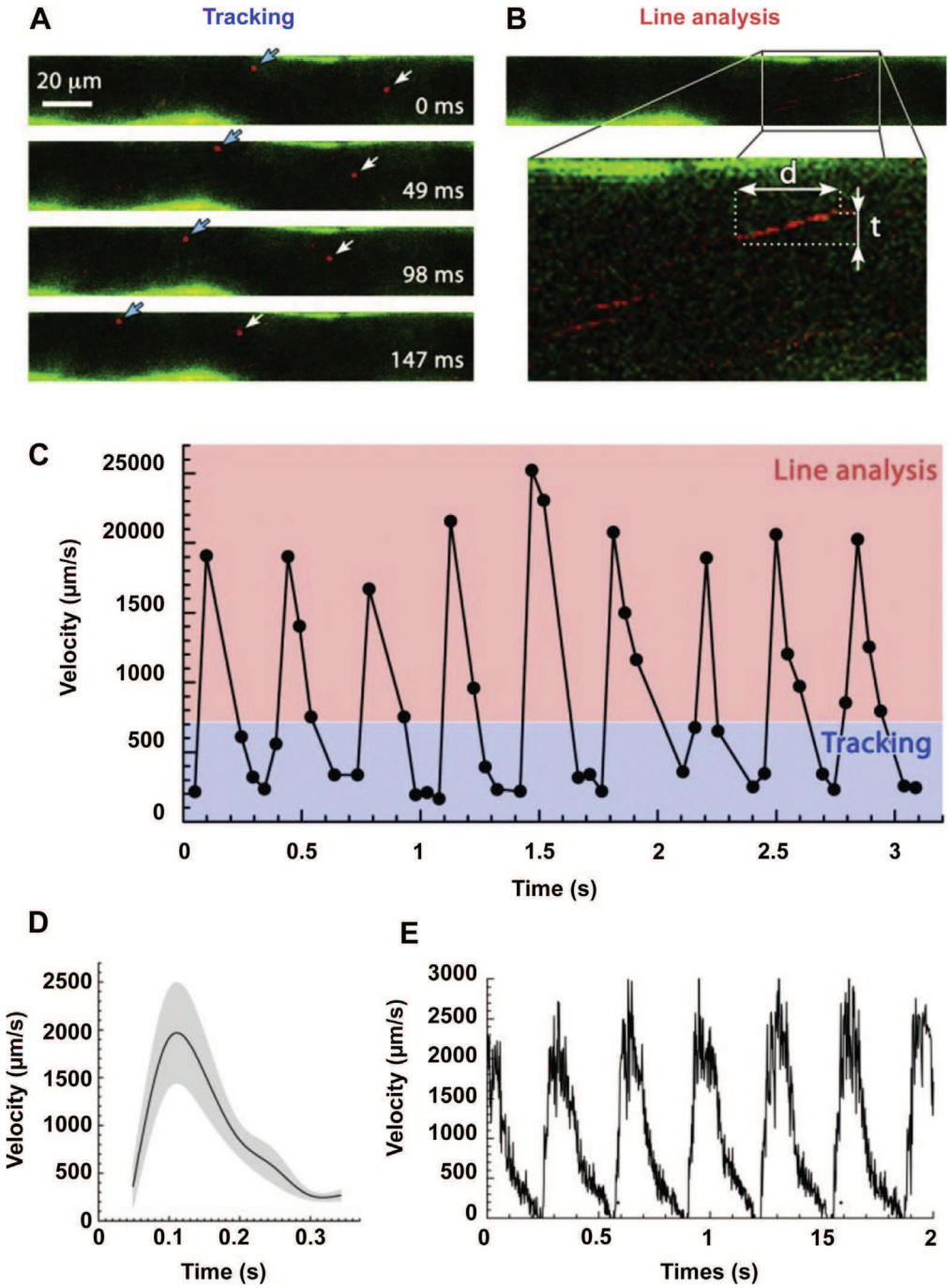

Fig. 7. Single-particle tracking of DiI-TPB nano-droplets in zebrafish vessels. During the diastole single particles were followed in consecutive frames (A). During the systole, the velocity was calculated from the shape of the line, which is a result of the movement of the particles during the line scanning (B). Reconstruction of the blood flow profile (C). The velocities during the diastole (lower part < 500 µm/s) were determined by manual tracking (A) while the peak velocities (>500 µm/s) were deduced from the line profiles (B), where ***d*** and ***t*** define the particle displacement and the required time, respectively. Average velocity profile of 10 pulses shown in panel C (D). Example of velocity profile of the blood flow in the dorsal aorta determined by tracking the blood cells (E).

stream of Wistar rats (over 2 h) [42], which confirms their potential for targeted labeling and long-time observations.

In this context, the DiI-TPB loaded nano-droplets represent a tool perfectly adapted for microangiography imaging and appear advantageous over fluorescent microbeads [39] or quantum dots [43], which show relatively fast accumulation in endothelial cells and are not biodegradable.

3.6. Single-particle tracking to monitor blood flow

Blood flow velocity *in vivo* is typically derived from measuring the displacement of the circulating blood cells, which are about 10 μm in size. The use of QDs for blood flow measuring has been proposed though never really realized [43] mainly because of their interactions with the vessel walls and their insufficient signal to noise ratio. The use of 90-nm nano-droplets loaded with 8 wt% DiI-TPB, which should be two orders of magnitude as bright as QDs, could solve this problem. To show their potential in this application, a highly diluted nano-emulsion (10^6-fold) of the 90-nm droplets was injected into the embryo circulation and the particles were imaged and tracked. The resulting time-lapse video is shown in Supplementary material (Movie 1). Because of the high velocity of the blood flow, the main challenge in these experiments was to detect the single nano-droplets even at high acquisition rates (20 frames per second, limited by the experimental setup). In the confocal microscope, the laser beam scans the whole image during 50 ms, which means that the effective detection time is only a few microseconds per particle. Despite the high acquisition speed the signal to noise ratio was ~50, allowing tracking of individual DiI-TPB loaded nano-droplets (Fig. 7).

Measurements realized by tracking individual blood cells (Fig. 7E) have shown that the velocity profile of the blood flow in the Dorsal Aorta is pulsatile with a large dynamic range. Erythrocytes are almost stationary during the diastole, but their velocity peaks at 2500 μm/s during the heart contraction. As a consequence of these large changes in velocity, the tracked individual DiI-TPB nano-droplets appeared on the frames as a moving bright spots during the slow phase (Fig. 7A) and as "tilted" lines during the systole (Fig. 7B). These lines are the result of the fast movement of the particle during line scanning of the laser. The velocities during the diastole (<500 μm/s) were determined by manual tracking, while the peak velocities (>500 μm/s) were deduced from the line profiles. Their shapes can be analyzed in a similar way to the kymographs [44], where the angle of the tilt is proportional to the velocity of the particle. Knowing the time of the line scan (0.75 ms) and the pixel size, the velocity value can be directly calculated by dividing the overall displacement $\boldsymbol{d}$ by the corresponding displacement time $\boldsymbol{t}$ (Fig. 7B). The time-lapse sequence analyzed and the final reconstruction of 3 s long velocity profile of the blood flow is shown in Fig. 7C. Interestingly, the average pulse profile along with the standard deviation, represented in Fig. 7D, perfectly matches the velocity profile measured by blood cell tracking in the same conditions (Fig. 7E).

The newly proposed protocol of blood flow measurement in zebrafish embryo is the first alternative to the "classical" approach based on blood cell tracking. The use of nano-droplets is advantageous as the flow of the blood cells may be influenced by their size and shape. Moreover, our approach can be used in cases where blood cells are absent, such as during the early stages of the development of cardio-vascular system, where the heart contractions start several hours prior to the release of the blood cells into the circulation. Since the shear stress and mechanical forces generated by the flow were shown to be crucial parameters for the heart and vessel morphogenesis branching and lumenization [45–48], it would be of particular interest to monitor the flow profiles during this period. Similarly, the study of the flow during the lumen opening or in narrow vessel connections during the vascular morphogenesis or in mutants lacking blood cells would be of particular interest.

4. Conclusion

To achieve extreme fluorescence brightness of lipid nano-droplets, organic dyes should be confined inside the oil core at very high concentrations, which is not possible with conventional dyes due to their poor solubility and formation non-fluorescent aggregates. In the present work, an original solution was developed for a cationic cyanine dye by substituting its perchlorate counterion for a bulky and hydrophobic tetraphenylborate. This approach allowed us encapsulation of 8 wt% of this new dye salt in nano-droplets of the size range 30–90 nm. For the 90 nm droplets, which theoretically contained ~12,000 cyanine molecules, we experimentally found a fluorescence quantum yield of 0.14 and a molar extinction coefficient of 5.7×10^8 M^{-1} cm^{-1}, so that they are >100-fold brighter than corresponding quantum dots. This extreme brightness enabled for the first time to realize single-particle tracking in order to monitor the blood flow *in vivo* (zebrafish embryo) revealing both the slow and fast phases resulting from the cardiac cycle. These nano-droplets showed minimal cytotoxicity in cell culture and no dye leakage in zebrafish. The concept of counterion-based dye loading could be extended to other ionic dyes and counterions, opening a new effective route to ultra-bright organic nanoparticles. Moreover, we showed that ultra-bright nano-droplets enable tracking single particles inside live animals, which is a new dimension of *in vivo* imaging.

Acknowledgment

This work was supported by CNRS, Université de Strasbourg, ANR JCJC (ANR-11-JS07-014-01), National Institute of Health and Medical Research and Marie Curie FP7 (256549). We thank to R. Vauchelles from PIQ imaging platform for help with fluorescence imaging. We also thank the IGBMC imaging and zebrafish facilities for excellent technical help.

Appendix A. Supplementary data

Supplementary data associated with this article and the full color images can be found, in the online version, at http://dx.doi.org/10.1016/j.biomaterials.2014.02.053

References

[1] Medintz IL, Uyeda HT, Goldman ER, Mattoussi H. Quantum dot bioconjugates for imaging, labelling and sensing. Nat Mater 2005;4:435.
[2] Michalet X, Pinaud FF, Bentolila LA, Tsay JM, Doose S, Li JJ, et al. Quantum dots for live cells, in vivo imaging, and diagnostics. Science 2005;307:538–44.
[3] Bonacchi S, Genovese D, Juris R, Montalti M, Prodi L, Rampazzo E, et al. Luminescent silica nanoparticles: extending the frontiers of brightness. Angew Chem Int Ed Engl 2011;50:4056–66.
[4] Kumar R, Roy I, Ohulchanskyy TY, Goswami LN, Bonoiu AC, Bergey EJ, et al. Covalently dye-linked, surface-controlled, and bioconjugated organically modified silica nanoparticles as targeted probes for optical imaging. ACS Nano 2008;2:449–56.
[5] Fu CC, Lee HY, Chen K, Lim TS, Wu HY, Lin PK, et al. Characterization and application of single fluorescent nanodiamonds as cellular biomarkers. Proc Natl Acad Sci U S A 2007;104:727–32.
[6] Liu K-K, Wang C-C, Cheng C-L, Chao J-I. Endocytic carboxylated nanodiamond for the labeling and tracking of cell division and differentiation in cancer and stem cells. Biomaterials 2009;30:4249–59.
[7] Braeckmans K, Buyens K, Bouquet W, Vervaet C, Joye P, Vos FD, et al. Sizing nanomatter in biological fluids by fluorescence single particle tracking. Nano Lett 2010;10:4435–42.

[8] Filipe V, Poole R, Kutscher M, Forier K, Braeckmans K, Jiskoot W. Fluorescence single particle tracking for the characterization of submicron protein aggregates in biological fluids and complex formulations. Pharm Res 2011;28:1112–20.
[9] Levi V, Gratton E. Exploring dynamics in living cells by tracking single particles. Cell Biochem Biophys 2007;48:1–15.
[10] Tada H, Higuchi H, Wanatabe TM, Ohuchi N. In vivo real-time tracking of single quantum dots conjugated with monoclonal anti-HER2 antibody in tumors of mice. Cancer Res 2007;67:1138–44.
[11] Liu S-L, Zhang Z-L, Sun E-Z, Peng J, Xie M, Tian Z-Q, et al. Visualizing the endocytic and exocytic processes of wheat germ agglutinin by quantum dot-based single-particle tracking. Biomaterials 2011;32:7616–24.
[12] Brigger I, Dubernet C, Couvreur P. Nanoparticles in cancer therapy and diagnosis. Adv Drug Deliv Rev 2002;54:631.
[13] Liong M, Lu J, Kovochich M, Xia T, Ruehm SG, Nel AE, et al. Multifunctional inorganic nanoparticles for imaging, targeting, and drug delivery. ACS Nano 2008;2:889.
[14] Santra S, Wang K, Tapec R, Tan W. Development of novel dye-doped silica nanoparticles for biomarker application. J Biomed Opt 2001;6:160.
[15] Sharma P, Brown S, Walter G, Santra S, Moudgil B. Nanoparticles for bioimaging. Adv Colloid Interface Sci 2006;123–126:471.
[16] Hamada Y, Gonda K, Takeda M, Sato A, Watanabe M, Yambe T, et al. In vivo imaging of the molecular distribution of the VEGF receptor during angiogenesis in a mouse model of ischemia. Blood 2011;118:e93–100.
[17] Feng SS, Mu L, Win KY, Huang G. Nanoparticles of biodegradable polymers for clinical administration of paclitaxel. Curr Med Chem 2004;11:413–24.
[18] Torchilin VP. Recent advances with liposomes as pharmaceutical carriers. Nat Rev Drug Discov 2005;4:145–60.
[19] Vrignaud S, Benoit J-P, Saulnier P. Strategies for the nanoencapsulation of hydrophilic molecules in polymer-based nanoparticles. Biomaterials 2011;32:8593–604.
[20] Texier I, Goutayer M, Silva AD, Guyon L, Djaker N, Veronique Josserand I, et al. Cyanine-loaded lipid nanoparticles for improved in vivo fluorescence imaging. J Biomed Opt; 2009:14.
[21] Klymchenko AS, Roger E, Anton N, Anton H, Shulov I, Vermot J, et al. Highly lipophilic fluorescent dyes in nano-emulsions: towards bright non-leaking nano-droplets. RSC Adv 2012;2:11876–86.
[22] Wagh A, Qian SY, Law B. Development of biocompatible polymeric nanoparticles for in vivo NIR and FRET imaging. Bioconjug Chem 2012;23:981–92.
[23] Wu C, Bull B, Szymanski C, Christensen K, McNeill J. Multicolor conjugated polymer dots for biological fluorescence imaging. ACS Nano 2008;2:2415–23.
[24] Navarro JRG, Lerouge F, Cepraga C, Micouin G, Favier A, Chateau D, et al. Nanocarriers with ultrahigh chromophore loading for fluorescence bioimaging and photodynamic therapy. Biomaterials 2013;34:8344–51.
[25] Goutayer M, Dufort S, Josserand V, Royere A, Heinrich E, Vinet F, et al. Tumor targeting of functionalized lipid nanoparticles: assessment by in vivo fluorescence imaging. Eur J Pharm Biopharm 2010;75:137.
[26] Ding J, Wang Y, Ma M, Zhang Y, Lu S, Jiang Y, et al. CT/fluorescence dual-modal nanoemulsion platform for investigating atherosclerotic plaques. Biomaterials 2013;34:209–16.
[27] Li X, Anton N, Zuber G, Zhao M, Messaddeq N, Hallouard F, et al. Iodinated α-tocopherol nano-emulsions as non-toxic contrast agents for preclinical X-ray imaging. Biomaterials 2013;34:481–91.
[28] Anton N, Benoit JP, Saulnier P. Design and production of nanoparticles formulated from nano-emulsion templates-A review. J Control Release 2008;128:185.
[29] Fryd MM, Mason TG. Advanced nanoemulsions. Annu Rev Phys Chem 2012;63:493–518.
[30] Anton N, Vandamme TF. Nano-emulsions and micro-emulsions: clarifications of the critical differences. Pharm Res 2011;28:978–85.
[31] McClements DJ. Nanoemulsions versus microemulsions: terminology, differences, and similarities. Soft Matter 2012;8:1719–29.
[32] Tikekar RV, Nitin N. Effect of physical state (solid vs. liquid) of lipid core on the rate of transport of oxygen and free radicals in solid lipid nanoparticles and emulsion. Soft Matter 2011;7:8149–57.
[33] Würthner F, Kaiser TE, Saha-Möller CR. J-aggregates: from serendipitous discovery to supramolecular engineering of functional dye materials. Angew Chem Int Ed Engl 2011;50:3376–410.
[34] Chen LD, Mandal D, Pozzi G, Gladysz JA, Bühlmann P. Potentiometric sensors based on fluorous membranes doped with highly selective ionophores for carbonate. J Am Chem Soc 2011;133:20869–77.
[35] Bakker E, Pretsch E. Lipophilicity of tetraphenylborate derivatives as anionic sites in neutral carrier-based solvent polymeric membranes and lifetime of corresponding ion- selective electrochemical and optical sensors. Anal Chim Acta 1995;309:7–17.
[36] Yao H, Ashiba K. Highly fluorescent organic nanoparticles of thiacyanine dye: a synergetic effect of intermolecular H-aggregation and restricted intramolecular rotation. RSC Adv 2011;1:834–8.
[37] Magde D, Brannon JH, Cremers TL, Olmsted J. Absolute luminescence yield of cresyl violet. A standard for the red. J Phys Chem 1979;83:696–9.
[38] Lawson ND, Weinstein BM. In vivo imaging of embryonic vascular development using transgenic zebrafish. Dev Biol 2002;248:307–18.
[39] Weinstein BM, Stemple DL, Driever W, Fishman MC. Gridlock, a localized heritable vascular patterning defect in the zebrafish. Nat Med 1995;1:1143–7.
[40] Lavis LD, Raines RT. Bright ideas for chemical biology. ACS Chem Biol 2008;3:142–55.
[41] Dabbousi BO, Rodriguez-Viejo J, Mikulec FV, Heine JR, Mattoussi H, Ober R, et al. (CdSe)ZnS core-shell quantum dots: synthesis and characterization of a size series of highly luminescent nanocrystallites. J Phys Chem B 1997;101:9463–75.
[42] Lacoeuille F, Hindre F, Moal F, Roux J, Passirani C, Couturier O, et al. In vivo evaluation of lipid nanocapsules as a promising colloidal carrier for paclitaxel. Int J Pharm 2007;344:143–9.
[43] Rieger S, Kulkarni RP, Darcy D, Fraser SE, Köster RW. Quantum dots are powerful multipurpose vital labeling agents in zebrafish embryos. Dev Dyn 2005;234:670–81.
[44] Jones EAV, Baron MH, Fraser SE, Dickinson ME. Measuring hemodynamic changes during mammalian development. Am J Physiol Heart Circ Physiol 2004;287:H1561–9.
[45] Le Noble F, Fleury V, Pries A, Corvol P, Eichmann A, Reneman RS. Control of arterial branching morphogenesis in embryogenesis: go with the flow. Cardiovasc Res 2005;65:619–28.
[46] Jones EAV, Le Noble F, Eichmann A. What determines blood vessel structure? Genetic prespecification vs. hemodynamics. Physiol (Bethesda) 2006;21:388–95.
[47] Vermot J, Forouhar AS, Liebling M, Wu D, Plummer D, Gharib M, et al. Reversing blood flows act through klf2a to ensure normal valvulogenesis in the developing heart. PLoS Biol; 2009:7.
[48] Buschmann I, Pries A, Styp-Rekowska B, Hillmeister P, Loufrani L, Henrion D, et al. Pulsatile shear and Gja5 modulate arterial identity and remodeling events during flow-driven arteriogenesis. Development 2010;137:2187–96.

References

Achour, M. et al., 2008. The interaction of the SRA domain of ICBP90 with a novel domain of DNMT1 is involved in the regulation of VEGF gene expression. *Oncogene*, 27(15), pp.2187–2197.

Agris, P.F., 1996. The Importance of Being Modified: Roles of Modified Nucleosides and Mg2+ in RNA Structure and Function. *Progress in Nucleic Acid Research and Molecular Biology*, 53, pp.79–129. Available at: http://www.sciencedirect.com/science/article/pii/S0079660308601439.

Alhosin, M. et al., 2011. Down-regulation of UHRF1, associated with re-expression of tumor suppressor genes, is a common feature of natural compounds exhibiting anti-cancer properties. *Journal of experimental & clinical cancer research : CR*, 30, p.41. Available at: http://www.pubmedcentral.nih.gov/articlerender.fcgi?artid=3096999&tool=pmcentrez&rendertype=abstract.

Allan, B.W. & Reich, N.O., 1996. Targeted base stacking disruption by the EcoRI DNA methyltransferase. *Biochemistry*, 35(47), pp.14757–14762.

Ameer-Beg, S. et al., 2001. Ultrafast Measurements of Excited State Intramolecular Proton Transfer (ESIPT) in Room Temperature Solutions of 3-Hydroxyflavone and Derivatives. *The Journal of Physical Chemistry A*, 105(15), pp.3709–3718. Available at: http://dx.doi.org/10.1021/jp0031101.

Arima, Y. et al., 2004. Down-regulation of nuclear protein ICBP90 by signals contributes to cell cycle arrest at G1 / S transition. *Genes to Cells*, 9, pp.131–142.

Arita, K. et al., 2008. Recognition of hemi-methylated DNA by the SRA protein UHRF1 by a base-flipping mechanism. *Nature*, 455, pp.818–821.

Arnaut, L.G. & Formosinho, S.J., 1993. Excited-state proton transfer reactions I. Fundamentals and intermolecular reactions. *Journal of Photochemistry and Photobiology A: Chemistry*, 75(1), pp.1–20.

Ashraf, S.S. et al., 2000. Role of modified nucleosides of yeast tRNAPhe in ribosomal binding. *Cell Biochemistry and Biophysics*, 33(3), pp.241–252.

Avvakumov, G. V et al., 2008. Structural basis for recognition of hemi-methylated DNA by the SRA domain of human UHRF1. *Nature*, 455, pp.822–825.

Badran, A.H. et al., 2011. Evaluating the global CpG methylation status of native DNA utilizing a bipartite split-luciferase sensor. *Analytical Chemistry*, 83(18), pp.7151–7157.

Ball, M.P. et al., 2009. Targeted and genome-scale strategies reveal gene-body methylation signatures in human cells. *Nature biotechnology*, 27(4), pp.361–8. Available at: http://www.pubmedcentral.nih.gov/articlerender.fcgi?artid=3566772&tool=pmcentrez&rendertype=abstract.

Bernstein, B.E. et al., 2012. An integrated encyclopedia of DNA elements in the human genome. *Nature*, 489(7414), pp.57–74. Available at: http://dx.doi.org/10.1038/nature11247.

Bestor, T.H., 2000. The DNA methyltransferases of mammals. *Human molecular genetics*,

9(16), pp.2395–2402.

Bianchi, C. & Zangi, R., 2012. How to distinguish methyl-cytosine from cytosine with high fidelity. *Journal of Molecular Biology*, 424(3-4), pp.215–224. Available at: http://dx.doi.org/10.1016/j.jmb.2012.09.024.

Bind, M.-A. et al., 2013. Air pollution and markers of coagulation, inflammation, and endothelial function: associations and epigene-environment interactions in an elderly cohort. *Epidemiology*, 23(2), pp.332–340.

Bird, A., 2002. DNA methylation patterns and epigenetic memory. *Genes & development*, 16(1), pp.6–21.

Bird, A.P. & Wolffe, A.P., 1999. Methylation-Induced Repression— Belts, Braces, and Chromatin. *Cell*, 99(5), pp.451–454.

Birks, J.B., 1970. *Photophysics of aromatic molecules*, London; New York: Wiley-Interscience.

Bloomfield, V.A., 2001. *Nucleic Acids: Structures, Properties, and Function.*, Springer-Verlag. Available at: http://dx.doi.org/10.1007/s00897000456a.

Bostick, M. et al., 2007. UHRF1 plays a role in maintaining DNA methylation in mammalian cells. *Science (New York, N.Y.)*, 317, pp.1760–1764.

Boudier, C. et al., 2009. Local environment perturbations in alpha1-antitrypsin monitored by a ratiometric fluorescent label. *Photochemical & photobiological sciences : Official journal of the European Photochemistry Association and the European Society for Photobiology*, 8(6), pp.814–821.

Breslauer, K.J., 1995. [10] Extracting thermodynamic data from equilibrium melting curves for oligonucleotide order-disorder transitions. In G. K. A. B. T.-M. in E. Michael L. Johnson, ed. *Energetics of Biological Macromolecules*. New Jersey, USA.: Academic Press, pp. 221–242. Available at: http://www.sciencedirect.com/science/article/pii/0076687995590463.

Brochon, J.C., 1994. Maximum entropy method of data analysis in time-resolved spectroscopy. *Methods in Enzymology*, 240, pp.262–311.

Bronner, C., Chataigneau, T., et al., 2007. The "Epigenetic Code Replication Machinery", ECREM: a promising drugable target of the epigenetic cell memory. *Current medicinal chemistry*, 14(25), pp.2629–2641.

Bronner, C., Achour, M., et al., 2007. The UHRF family: Oncogenes that are drugable targets for cancer therapy in the near future? *Pharmacology and Therapeutics*, 115(3), pp.419–434.

Bronner, C. et al., 2009. UHRF1 Links the Histone code and DNA Methylation to ensure Faithful Epigenetic Memory Inheritance. *Genetics and Epigenetics*, 2009(2), pp.29–36.

Bronner, C., Krifa, M. & Mousli, M., 2013. Increasing role of UHRF1 in the reading and inheritance of the epigenetic code as well as in tumorogenesis. *Biochemical Pharmacology*, 86, pp.1643–1649. Available at: http://dx.doi.org/10.1016/j.bcp.2013.10.002.

Buck-Koehntop, B. a. & Defossez, P.-A., 2013. On how mammalian transcription factors recognize methylated DNA. *Epigenetics*, 8(2), pp.131–137. Available at: http://www.tandfonline.com/doi/abs/10.4161/epi.23632.

Burdge, G.C. & Lillycrop, K.A., 2010. Nutrition, epigenetics, and developmental plasticity: implications for understanding human disease. *Annual review of nutrition*, 30, pp.315–339.

Capellos, C. & Bielski, B.H.J., 1980. *Kinetic systems : mathematical description of chemical kinetics in solution*, Huntington, N.Y.: R.E. Krieger Pub. Co.

Chen, L. et al., 1991. Direct identification of the active-site nucleophile in a DNA (cytosine-5)-methyltransferase. *Biochemistry*, 30(46), pp.11018–11025.

Christine, K.S., 2002. Cyclobutylpyrimidine Dimer Base Flipping by DNA Photolyase. *Journal of Biological Chemistry*, 277(41), pp.38339–38344. Available at: http://www.jbc.org/cgi/doi/10.1074/jbc.M206531200.

Clouaire, T. et al., 2010. Recruitment of MBD1 to target genes requires sequence-specific interaction of the MBD domain with methylated DNA. *Nucleic Acids Research*, 38(14), pp.4620–4634. Available at: http://nar.oxfordjournals.org/lookup/doi/10.1093/nar/gkq228.

Colot, V. & Rossignol, J.L., 1999. Eukaryotic DNA methylation as an evolutionary device. *BioEssays : news and reviews in molecular, cellular and developmental biology*, 21(5), pp.402–411.

Corces, V.G., 1995. Chromatin insulators. Keeping enhancers under control. *Nature*, 376(6540), pp.462–463.

Dai, Z. et al., 2001. Global Methylation Profiling of Lung Cancer Identifies Novel Methylated Genes. *Neoplasia*, 3(4), pp.314–323. Available at: http://linkinghub.elsevier.com/retrieve/pii/S1476558601800348.

Das, R. et al., 2009. Unusually slow proton transfer dynamics of a 3-hydroxychromone dye in protic solvents. *Photochemical & photobiological sciences : Official journal of the European Photochemistry Association and the European Society for Photobiology*, 8(11), pp.1583–9.

Delagoutte, B. et al., 2008. Expression, purification, crystallization and preliminary crystallographic study of the SRA domain of the human UHRF1 protein. *Acta Crystallographica Section F: Structural Biology and Crystallization Communications*, 64, pp.922–925.

Dziuba, D. et al., 2012. A universal nucleoside with strong two-band switchable fluorescence and sensitivity to the environment for investigating DNA interactions. *Journal of the American Chemical Society*, 134, pp.10209–10213.

Dziuba, D. et al., 2014. Rational design of a solvatochromic fluorescent uracil analogue with a dual-band ratiometric response based on 3-hydroxychromone. *Chemistry (Weinheim an der Bergstrasse, Germany)*, 20, pp.1998–2009.

Enander, K. et al., 2008. A peptide-based, ratiometric biosensor construct for direct fluorescence detection of a protein analyte. *Bioconjugate chemistry*, 19(9), pp.1864–70. Available at: http://www.ncbi.nlm.nih.gov/pubmed/18693760.

Erlanson, D. a., Chen, L. & Verdine, G.L., 1993. DNA methylation through a locally unpaired intermediate. *Journal of the American Chemical Society*, 115(26), pp.12583–12584. Available at: http://pubs.acs.org/doi/abs/10.1021/ja00079a047.

Fisher, T.E., Marszalek, P.E. & Fernandez, J.M., 2000. Stretching single molecules into novel

conformations using the atomic force microscope. *Nature Structural Biology*, 7(9), pp.719–724.

Flusberg, B. a et al., 2010. Direct detection of DNA methylation during single-molecule, real-time sequencing. *Nature Methods*, 7(6), pp.461–465. Available at: http://www.nature.com/doifinder/10.1038/nmeth.1459.

Gaied, N.B., 2005. 8-Vinyl-Deoxyadenosine, an Alternative Fluorescent Nucleoside Analog To 2'-Deoxyribosyl-2-Aminopurine With Improved Properties. *Nucleic Acids Research*, 33(3), pp.1031–1039.

Gerasimait, R., Merkiene, E. & Klimašauskas, S., 2011. Direct observation of cytosine flipping and covalent catalysis in a DNA methyltransferase. *Nucleic Acids Research*, 39(9), pp.3771–3780.

Glick, G.D. & Matsuda, A., 2001. Chemical and Enzymatic Probes for Nucleic Acid Structure. In *Current Protocols in Nucleic Acid Chemistry*. John Wiley & Sons, Inc. Available at: http://dx.doi.org/10.1002/0471142700.nc0600s33.

Goto, T. & Monk, M., 1998. Regulation of X-chromosome inactivation in development in mice and humans. *Microbiology and molecular biology reviews : MMBR*, 62(2), pp.362–378.

Greiner, V.J. et al., 2015. Site-Selective Monitoring of the Interaction of the SRA Domain of UHRF1 with Target DNA Sequences Labeled with 2-Aminopurine. *Biochemistry*, 54, pp.6012–6020. Available at: http://pubs.acs.org/doi/10.1021/acs.biochem.5b00419.

Gross, E., Bedlack, R.S. & Loew, L.M., 1994. Dual-wavelength ratiometric fluorescence measurement of the membrane dipole potential. *Biophysical journal*, 67(1), pp.208–216.

Hart, J.R., 2000. Ethylenediaminetetraacetic Acid and Related Chelating Agents. In *Ullmann's Encyclopedia of Industrial Chemistry*. Wiley-VCH Verlag GmbH & Co. KGaA. Available at: http://dx.doi.org/10.1002/14356007.a10_095.

Hashimoto, H. et al., 2008. The SRA domain of UHRF1 flips 5-methylcytosine out of the DNA helix. *Nature*, 455, pp.826–829.

Hashimoto, H. et al., 2009. UHRF1, a modular multi-domain protein, regulates replication-coupled crosstalk between DNA methylation and histone modifications. *Epigenetics*, 4(1), pp.8–14.

Hayatsu, H. et al., 1970. Reaction of sodium bisulfite with uracil, cytosine, and their derivatives. *Biochemistry*, 9(14), pp.2858–2865.

Ho, K.L. et al., 2008. MeCP2 Binding to DNA Depends upon Hydration at Methyl-CpG. *Molecular Cell*, 29(4), pp.525–531. Available at: http://linkinghub.elsevier.com/retrieve/pii/S1097276508000968.

Holliday, R. & Pugh, J.E., 1975. DNA modification mechanisms and gene activity during development. *Science (New York, N.Y.)*, 187(4173), pp.226–232.

Hopfner, R. et al., 2000. ICBP90, a novel human CCAAT binding protein, involved in the regulation of topoisomerase IIalpha expression. *Cancer research*, 60(1), pp.121–128.

Hosfield, D.J. et al., 1999. Structure of the DNA repair enzyme endonuclease IV and its DNA complex: double-nucleotide flipping at abasic sites and three-metal-ion catalysis. *Cell*, 98(3), pp.397–408. Available at: http://www.ncbi.nlm.nih.gov/pubmed/10458614.

Ikegami, K. et al., 2009. Interplay between DNA methylation, histone modification and

chromatin remodeling in stem cells and during development. *The International journal of developmental biology*, 53(2-3), pp.203–214.

Itoh, M. et al., 1982. Time-resolved and steady-state fluorescence studies of the excited-state proton transfer in 3-hydroxyflavone and 3-hydroxychromone. *Journal of the American Chemical Society*, 104(15), pp.4146–4150. Available at: http://www.scopus.com/inward/record.url?eid=2-s2.0-0000059355&partnerID=tZOtx3y1.

Itoh, Tanimoto & Tokumura, 2015. Transient Absorption Study of the Intramolecular Excited-State and Ground-State Proton Transfer in 3-Hydroxyflavone and 3-Hydroxychromone Michiya. *The effects of brief mindfulness intervention on acute pain experience: An examination of individual difference*, 1(9), pp.3339–3340.

Jaenisch, R. & Bird, A., 2003. Epigenetic regulation of gene expression: how the genome integrates intrinsic and environmental signals. *Nature genetics*, 33 Suppl(march), pp.245–254.

Jean, J.M. & Hall, K.B., 2001. 2-Aminopurine fluorescence quenching and lifetimes: role of base stacking. *Proceedings of the National Academy of Sciences of the United States of America*, 98(1), pp.37–41.

Jeanblanc, M. et al., 2005. The retinoblastoma gene and its product are targeted by ICBP90: a key mechanism in the G1/S transition during the cell cycle. *Oncogene*, 24(49), pp.7337–7345.

Jones, P.L. et al., 1998. Methylated DNA and MeCP2 recruit histone deacetylase to repress transcription. *Nature genetics*, 19(2), pp.187–191.

Kamakura, M., 2012. Royalactin induces queen differentiation in honeybees. *Seikagaku*, 84(12), pp.994–1003. Available at: http://dx.doi.org/10.1038/nature10093.

Kilin, V. et al., 2015. Fluorescence Lifetime Imaging of Membrane Lipid Order with a Ratiometric Fluorescent Probe. *Biophysical Journal*, 108, pp.2521–2531. Available at: http://linkinghub.elsevier.com/retrieve/pii/S0006349515003495.

Kilin, V. et al., 2013. Two photon fluorescence imaging of lipid membrane domains and potentials using advanced fluorescent probes. In Periasamy, A and Konig, K and So, PTC, ed. *MULTIPHOTON MICROSCOPY IN THE BIOMEDICAL SCIENCES XIII*. Proceedings of SPIE. SPIE-INT SOC OPTICAL ENGINEERING.

Kim, J.K. et al., 2009. UHRF1 binds G9a and participates in p21 transcriptional regulation in mammalian cells. *Nucleic Acids Research*, 37(2), pp.493–505.

Klose, R.J. et al., 2005. DNA Binding Selectivity of MeCP2 Due to a Requirement for A/T Sequences Adjacent to Methyl-CpG. *Molecular Cell*, 19(5), pp.667–678. Available at: http://linkinghub.elsevier.com/retrieve/pii/S1097276505015091.

Klymchenko, A.S. et al., 2003. Ultrasensitive two-color fluorescence probes for dipole potential in phospholipid membranes. *Proceedings of the National Academy of Sciences of the United States of America*, 100(20), pp.11219–11224.

Klymchenko, A.S. & Demchenko, A.P., 2002. Electrochromic modulation of excited-state intramolecular proton transfer: the new principle in design of fluorescence sensors. *J. Am. Chem. Soc.*, 124, pp.12372–12379. Available at: http://www.ncbi.nlm.nih.gov/pubmed/12371881.

Klymchenko, A.S. & Demchenko, A.P., 2003. Multiparametric probing of intermolecular interactions with fluorescent dye exhibiting excited state intramolecular proton transfer. , pp.461–468.

Klymchenko, A.S. & Mely, Y., 2013. Fluorescent environment-sensitive dyes as reporters of biomolecular interactions. *Progress in molecular biology and translational science*, 113, pp.35–58. Available at: http://www.sciencedirect.com/science/article/pii/B9780123869326000028 [Accessed December 17, 2015].

Kucharski, R. et al., 2008. Nutritional Control of Reproductive Status in Honeybees via DNA Methylation. *Science*, 319(5871), pp.1827–1830. Available at: http://www.sciencemag.org/cgi/doi/10.1126/science.1153069.

Kundaje, A. et al., 2015. Integrative analysis of 111 reference human epigenomes. *Nature*, 518(7539), pp.317–330.

Kuznetsova, A. a. et al., 2014. New environment-sensitive multichannel DNA fluorescent label for investigation of the protein-DNA interactions. *PLoS ONE*, 9, p.e100007.

Laget, S. et al., 2010. The Human Proteins MBD5 and MBD6 Associate with Heterochromatin but They Do Not Bind Methylated DNA. *PLoS ONE*, 5(8), p.e11982. Available at: http://dx.plos.org/10.1371/journal.pone.0011982.

Lakowicz, J.R., 2006. *Principles of Fluorescence Spectroscopy*, New York, NY, USA: Springer.

Larivière, L. & Moréra, S., 2002. A Base-flipping Mechanism for the T4 Phage β-Glucosyltransferase and Identification of a Transition-state Analog. *Journal of Molecular Biology*, 324(3), pp.483–490. Available at: http://linkinghub.elsevier.com/retrieve/pii/S0022283602010914.

Laszlo, a. H. et al., 2013. Detection and mapping of 5-methylcytosine and 5-hydroxymethylcytosine with nanopore MspA. *Proceedings of the National Academy of Sciences*, 110(47), pp.18904–18909. Available at: http://www.pnas.org/cgi/doi/10.1073/pnas.1310240110.

Laws, W.R. & Brand, L., 1979. Analysis of Two-State Excited-State Reactions. The Fluorescence Decay of 2-Naphthol William. *Society*, 83(7), pp.795–802.

Lenz, T. et al., 2007. 2-Aminopurine Flipped into the Active Site of the Adenine-Specific DNA Methyltransferase M.TaqI: Crystal Structures and Time-Resolved Fluorescence. *Journal of the American Chemical Society*, 129(19), pp.6240–6248. Available at: http://www.ncbi.nlm.nih.gov/pubmed/17455934\nhttp://pubs.acs.org/doi/abs/10.1021/ja069366n.

Leonard, S.M. et al., 2012. Oncogenic human papillomavirus imposes an instructive pattern of DNA methylation changes which parallel the natural history of cervical HPV infection in young women. *Carcinogenesis*, 33(7), pp.1286–1293. Available at: http://www.carcin.oxfordjournals.org/cgi/doi/10.1093/carcin/bgs157.

Li, E., Beard, C. & Jaenisch, R., 1993. Role for DNA methylation in genomic imprinting. *Nature*, 366(6453), pp.362–365.

Li, E., Bestor, T.H. & Jaenisch, R., 1992. Targeted mutation of the DNA methyltransferase gene results in embryonic lethality. *Cell*, 69(6), pp.915–926.

Lister, R. et al., 2009. Human DNA methylomes at base resolution show widespread epigenomic differences. *Nature*, 462(7271), pp.315–322. Available at: http://dx.doi.org/10.1038/nature08514.

Liu, L. et al., 2003. Aging, cancer and nutrition: the DNA methylation connection. *Mechanisms of ageing and development*, 124(10-12), pp.989–998.

Liu, Y. et al., 2012. An atomic model of Zfp57 recognition of CpG methylation within a specific DNA sequence. *Genes & development*, 26(21), pp.2374–2379. Available at: http://eutils.ncbi.nlm.nih.gov/entrez/eutils/elink.fcgi?dbfrom=pubmed&id=23059534&retmode=ref&cmd=prlinks\npapers2://publication/doi/10.1101/gad.202200.112.

Livesey, A.K. & Brochon, J.C., 1987. Analyzing the distribution of decay constants in pulse-fluorimetry using the maximum entropy method. *Biophys. J.*, 52(5), pp.693–706. Available at: http://www.ncbi.nlm.nih.gov/pubmed/19431708.

Madrigano, J. et al., 2012. Longitudinal changes in gene-specific DNA methylation Aging and epigenetics © 2012 Landes Bioscience . Do not distribute . © 2012 Landes Bioscience . , (January), pp.63–70.

Maillot, S. et al., 2014. Out-of-equilibrium biomolecular interactions monitored by picosecond fluorescence in microfluidic droplets. *Lab on a chip*, 14, pp.1767–1774.

Maleszka, R., 2008. Epigenetic integration of environmental and genomic signals in honey bees: the critical interplay of nutritional, brain and reproductive networks. *Epigenetics*, 3(4), pp.188–192. Available at: http://www.tandfonline.com/doi/abs/10.4161/epi.3.4.6697.

Mandal, P.K. & Samanta, A., 2003. Evidence of ground-state proton-transfer reaction of 3-hydroxyflavone in neutral alcoholic solvents. *Journal of Physical Chemistry A*, 107(32), pp.6334–6339.

Marks, D. et al., 1997. Solvent dependence of (sub)picosecond proton transfer in photo-excited [2,2′-bipyridyl]-3,3′-diol. *Chemical Physics Letters*, 2614(August), pp.370–376. Available at: http://www.sciencedirect.com/science/article/pii/S0009261497007409 [Accessed October 23, 2015].

Maunakea, A.K. et al., 2010. Conserved role of intragenic DNA methylation in regulating alternative promoters. *Nature*, 466(7303), pp.253–257. Available at: http://www.nature.com/doifinder/10.1038/nature09165.

Mclean, M.J. et al., 1987. Reaction conditions affect the specfity of bromnoacetaldehyde as a probe for DNA cruciforms and B-Z junctions. *Nucleic for DNAAcidscruciforms Research*, 15(17), pp.6917–6935.

McMorrow, D. & Kasha, M., 1984. Intramolecular excited-state proton transfer in 3-hydroxyflavone. Hydrogen-bonding solvent perturbations. *The Journal of Physical Chemistry*, 88(11), pp.2235–2243. Available at: http://dx.doi.org/10.1021/j150655a012.

Meehan, R.R., Lewis, J.D. & Bird, a P., 1992. Characterization of MeCP2, a vertebrate DNA binding protein with affinity for methylated DNA. *Nucleic acids research*, 20(19), pp.5085–92. Available at: http://www.pubmedcentral.nih.gov/articlerender.fcgi?artid=334288&tool=pmcentrez&rendertype=abstract.

Min, J.-H. & Pavletich, N.P., 2007. Recognition of DNA damage by the Rad4 nucleotide

excision repair protein. *Nature*, 449(7162), pp.570–575. Available at: http://www.nature.com/doifinder/10.1038/nature06155.

Monk, M., Boubelik, M. & Lehnert, S., 1987. Temporal and regional changes in DNA methylation in the embryonic, extraembryonic and germ cell lineages during mouse embryo development. *Development (Cambridge, England)*, 99(3), pp.371–82. Available at: http://www.ncbi.nlm.nih.gov/pubmed/3653008.

Moore, D.S., 2015. *The Developing Genome*, Oxford University Press.

Nadler, A., Strohmeier, J. & Diederichsen, U., 2011. 8-Vinyl-2'-deoxyguanosine as a fluorescent 2'-deoxyguanosine mimic for investigating DNA hybridization and topology. *Angewandte Chemie (International ed. in English)*, 50(23), pp.5392–6. Available at: http://www.ncbi.nlm.nih.gov/pubmed/21542071.

Nan, X. et al., 1998. Transcriptional repression by the methyl-CpG-binding protein MeCP2 involves a histone deacetylase complex. *Nature*, 393(6683), pp.386–389. Available at: http://www.ncbi.nlm.nih.gov/entrez/query.fcgi?cmd=Retrieve&db=PubMed&dopt=Citation&list_uids=9620804\nhttp://www.nature.com/nature/journal/v393/n6683/pdf/393386a0.pdf.

Nan, X., Meehan, R.R. & Bird, a, 1993. Dissection of the methyl-CpG binding domain from the chromosomal protein MeCP2. *Nucleic acids research*, 21(21), pp.4886–4892.

Neely, R.K., 2005. Time-resolved fluorescence of 2-aminopurine as a probe of base flipping in M.HhaI-DNA complexes. *Nucleic Acids Research*, 33(22), pp.6953–6960. Available at: http://nar.oxfordjournals.org/lookup/doi/10.1093/nar/gki995.

O'Gara, M. et al., 1998. Structures of HhaI methyltransferase complexed with substrates containing mismatches at the target base. *Nat Struct Biol*, 5(10), pp.872–877.

Ohgane, J., Yagi, S. & Shiota, K., 2008. Epigenetics: The DNA Methylation Profile of Tissue-Dependent and Differentially Methylated Regions in Cells. *Placenta*, 29(SUPPL.), pp.29–35.

Ohki, I. et al., 2001. Solution structure of the methyl-CpG binding domain of human MBD1 in complex with methylated DNA. *Cell*, 105(4), pp.487–497.

Okamoto, A., 2007. 5-Methylcytosine-Selective Osmium Oxidation. *Nucleosides, Nucleotides and Nucleic Acids*, 26(10-12), pp.1601–1604. Available at: http://www.tandfonline.com/doi/abs/10.1080/15257770701548428.

Okamoto, A., Tainaka, K. & Kamei, T., 2006. Sequence-selective osmium oxidation of DNA: efficient distinction between 5-methylcytosine and cytosine. *Organic & Biomolecular Chemistry*, 4(9), p.1638. Available at: http://xlink.rsc.org/?DOI=b600401f.

Okano, M. et al., 1999. DNA methyltransferases Dnmt3a and Dnmt3b are essential for de novo methylation and mammalian development. *Cell*, 99(3), pp.247–257.

Parker, J.B. et al., 2007. Enzymatic capture of an extrahelical thymine in the search for uracil in DNA. *Nature*, 449(7161), pp.433–437. Available at: http://www.nature.com/doifinder/10.1038/nature06131.

Pivovarenko, V.G. et al., 2012. Quantification of local hydration at the surface of biomolecules using dual-fluorescence labels. *Journal of Physical Chemistry A*, 116(12), pp.3103–3109.

Plass, C. & Soloway, P.D., 2002. DNA methylation, imprinting and cancer. *European journal*

of human genetics : EJHG, 10(1), pp.6–16.

Porter, J.R. et al., 2008. A general and rapid cell-free approach for the interrogation of protein-protein, protein-DNA, and protein-RNA interactions and their antagonists utilizing split-protein reporters. *Journal of the American Chemical Society*, 130(20), pp.6488–6497.

Postupalenko, V.Y. et al., 2011. Biochimica et Biophysica Acta Monitoring membrane binding and insertion of peptides by two-color fl uorescent label. *BBA - Biomembranes*, 1808(1), pp.424–432. Available at: http://dx.doi.org/10.1016/j.bbamem.2010.09.013.

Prokhortchouk, a. et al., 2001. The p120 catenin partner Kaiso is a DNA methylation-dependent transcriptional repressor. *Genes and Development*, 15(13), pp.1613–1618.

Purnell, R.F., Mehta, K.K. & Schmidt, J.J., 2008. Nucleotide identification and orientation discrimination of DNA homopolymers immobilized in a protein nanopore. *Nano letters*, 8(9), pp.3029–3034.

Quenneville, S. et al., 2011. In Embryonic Stem Cells, ZFP57/KAP1 Recognize a Methylated Hexanucleotide to Affect Chromatin and DNA Methylation of Imprinting Control Regions. *Molecular Cell*, 44(3), pp.361–372. Available at: http://linkinghub.elsevier.com/retrieve/pii/S1097276511007659.

Rachofsky, E.L., Osman, R. & Ross, J.B., 2001. Probing structure and dynamics of DNA with 2-aminopurine: effects of local environment on fluorescence. *Biochemistry*, 40(4), pp.946–956.

Rajski, S.R. & Barton, J.K., 2001. How different DNA-binding proteins affect long-range oxidative damage to DNA. *Biochemistry*, 40(18), pp.5556–5564.

Reddy, Y.V.. & Rao, D.N., 2000. Binding of EcoP15I DNA methyltransferase to DNA reveals a large structural distortion within the recognition sequence. *Journal of Molecular Biology*, 298(4), pp.597–610. Available at: http://linkinghub.elsevier.com/retrieve/pii/S0022283600936738.

Reichardt, C., 1994. Solvatochromic dyes as solvent polarity indicators. *Chemical reviews*, 94, pp.2319–2358. Available at: http://pubs.acs.org/doi/abs/10.1021/cr00032a005.

Reichmann, M.E. et al., 1954. A Further Examination of the Molecular Weight and Size of Desoxypentose Nucleic Acid. *J. Am. Chem. Soc.*, 76(11), pp.3047–3053. Available at: <Go to ISI>://A1954UB50000067.

Riggs, A.D., 1989. DNA methylation and cell memory. *Cell biophysics*, 15(1-2), pp.1–13.

Riggs, A.D., 1975. X inactivation, differentiation, and DNA methylation. *Cytogenetics and cell genetics*, 14(1), pp.9–25.

Roberts, R.J. & Cheng, X., 1998. Base flipping. *Annual review of biochemistry*, 67, pp.181–98. Available at: http://www.ncbi.nlm.nih.gov/pubmed/9783745.

Rochel, N. et al., 2011. Common architecture of nuclear receptor heterodimers on DNA direct repeat elements with different spacings. *Nat. Struct. Mol. Biol*, 18, pp.564–570. Available at: http://dx.doi.org/10.1038/nsmb.2054.

Rottach, A., Leonhardt, H. & Spada, F., 2009. Cellular Biochemistry. , 51(June), pp.43–51.

Rüegg, U.T. & Rudinger, J., 1977. *Reductive cleavage of cystine disulfides with tributylphosphine*, Elsevier. Available at: http://www.sciencedirect.com/science/article/pii/0076687977470125 [Accessed October

10, 2015].

Santi, D. V, Garrett, C.E. & Barr, P.J., 1983. On the mechanism of inhibition of DNA-cytosine methyltransferases by cytosine analogs. *Cell*, 33(1), pp.9–10.

Sarraf, S. a. & Stancheva, I., 2004. Methyl-CpG binding protein MBD1 couples histone H3 methylation at lysine 9 by SETDB1 to DNA replication and chromatin assembly. *Molecular Cell*, 15(4), pp.595–605.

Scarsdale, J.N. et al., 2011. Solution structure and dynamic analysis of chicken MBD2 methyl binding domain bound to a target-methylated DNA sequence. *Nucleic Acids Research*, 39(15), pp.6741–6752. Available at: http://nar.oxfordjournals.org/lookup/doi/10.1093/nar/gkr262.

Seidel, C. a M., Schulz, A. & Sauer, M.H.M., 1996. Nucleobase-Specific Quenching of Fluorescent Dyes. 1. Nucleobase One-Electron Redox Potentials and Their Correlation with Static and Dynamic Quenching Efficiencies. *The Journal of Physical Chemistry*, 100(13), pp.5541–5553. Available at: http://pubs.acs.org/doi/abs/10.1021/jp951507c.

Sengupta, P.K. & Kasha, M., 1979. Excited state proton-transfer spectroscopy of 3-hytdroxyflavone and quercetin. *Chemical Physics Letters*, 68(2-3), pp.382–385.

Shana O. Kelley, J.K.B., 1999. Electron Transfer Between Bases in Double Helical DNA. , 283(January), pp.375–381.

Shim, J. et al., 2013. Detection and Quantification of Methylation in DNA using Solid-State Nanopores. *Scientific Reports*, 3, pp.1–8. Available at: http://www.nature.com/doifinder/10.1038/srep01389.

Shiota, K., 2004. DNA methylation profiles of CpG islands for cellular differentiation and development in mammals. *Cytogenetic and Genome Research*, 105(2-4), pp.325–334. Available at: http://www.karger.com/DOI/10.1159/000078205.

Shvadchak, V. V et al., 2009. Sensing peptide-oligonucleotide interactions by a two-color fluorescence label: application to the HIV-1 nucleocapsid protein. *Nucleic acids research*, 37(3), p.e25. Available at: http://www.pubmedcentral.nih.gov/articlerender.fcgi?artid=2647317&tool=pmcentrez&rendertype=abstract.

Shynkar, V. V et al., 2007. Fluorescent biomembrane probe for ratiometric detection of apoptosis. *J. Am. Chem. Soc.*, 129(7), pp.2187–2193. Available at: http://www.ncbi.nlm.nih.gov/pubmed/17256940.

Shynkar, V. V et al., 2003. Picosecond time-resolved fluorescence studies are consistent with reversible excited-state intramolecular proton transfer in 4 ’-(dialkylaminoe)-3-hydroxyflavones. *J. of Physical Chemistry A*, 107(45), pp.9522–9529. Available at: <Go to ISI>://WOS:000186425000004.

Singleton, S.F. et al., 2001. Facile synthesis of a fluorescent deoxycytidine analogue suitable for probing the RecA nucleoprotein filament. *Organic Letters*, 3, pp.3919–3922.

Sinkeldam, R.W., Greco, N.J. & Tor, Y., 2010. Fluorescent analogs of biomolecular building blocks: Design, properties, and applications. *Chemical Reviews*, 110(5), pp.2579–2619. Available at: http://pubs.acs.org/doi/full/10.1021/cr900301e?source=chemport.

Spadafora, M. et al., 2009. Efficient Synthesis of Ratiometric Fluorescent Nucleosides Featuring 3-Hydroxychromone Nucleobases. *Tetrahedron*, 65, pp.7809–7816. Available

at: http://www.sciencedirect.com/science/article/pii/S0040402009010473 [Accessed July 15, 2015].

Steinhauer, C., Itano, M. & Tinnefeld, P., 2013. Super-Resolution Fluorescence Imaging with Blink Microscopy. In A. A. Sousa & M. J. Kruhlak, eds. *Nanoimaging SE - 8*. Methods in Molecular Biology. Humana Press, pp. 111–129.

Stoddart, D. et al., 2009. Single-nucleotide discrimination in immobilized DNA oligonucleotides with a biological nanopore. *Proceedings of the National Academy of Sciences of the United States of America*, 106(19), pp.7702–7707.

Strandjord, A.J.G. et al., 1983. Excited-state dynamics of 3-hydroxyflavone. *The Journal of Physical Chemistry*, 87(7), pp.1125–1133. Available at: http://dx.doi.org/10.1021/j100230a008.

Strandjord, A.J.G. & Barbara, P.F., 1985. The proton-transfer kinetics of 3-hydroxyflavone: solvent effects. *The Journal of Physical Chemistry*, 89(11), pp.2355–2361. Available at: http://dx.doi.org/10.1021/j100257a041.

Suzuki, M.M. & Bird, A., 2008. DNA methylation landscapes: provocative insights from epigenomics. *Nature reviews. Genetics*, 9(6), pp.465–476.

Tahiliani, M. et al., 2009. Conversion of 5-Methylcytosine to 5-Hydroxymethylcytosine in Mammalian DNA by MLL Partner TET1. *Science*, 324(5929), pp.930–935. Available at: http://www.sciencemag.org/cgi/doi/10.1126/science.1170116.

Tamulaitis, G. et al., 2007. Nucleotide flipping by restriction enzymes analyzed by 2-aminopurine steady-state fluorescence. *Nucleic Acids Research*, 35(14), pp.4792–4799. Available at: http://nar.oxfordjournals.org/lookup/doi/10.1093/nar/gkm513.

Tang, K.-C. et al., 2011. Fine tuning the energetics of excited-state intramolecular proton transfer (ESIPT): white light generation in a single ESIPT system. *Journal of the American Chemical Society*, 133(44), pp.17738–45. Available at: http://www.ncbi.nlm.nih.gov/pubmed/21957929.

Tomin, V.I. & Javorski, R., 2007. Temporal characteristics of the fluorescence of the anionic form of 3-hydroxyflavone. *Optics and Spectroscopy*, 103, pp.952–957.

Tomin, V.I. & Jaworski, R., 2014. Spectral properties of the anionic form of the molecular probe FET. , 81, pp.360–364.

Torimura, M. et al., 2001. Fluorescence-quenching phenomenon by photoinduced electron transfer between a fluorescent dye and a nucleotide base. *Analytical sciences : the international journal of the Japan Society for Analytical Chemistry*, 17(1), pp.155–160.

Unoki, M., Nishidate, T. & Nakamura, Y., 2004a. ICBP90, an E2F-1 target, recruits HDAC1 and binds to methyl-CpG through its SRA domain. *Oncogene*, 23(46), pp.7601–7610.

Unoki, M., Nishidate, T. & Nakamura, Y., 2004b. ICBP90, an E2F-1 target, recruits HDAC1 and binds to methyl-CpG through its SRA domain. *Oncogene*, 23(46), pp.7601–7610.

Vicarelli, L. et al., 2015. Controlling Defects in Graphene for Optimizing the Electrical Properties of Graphene Nanodevices. *ACS Nano*, 9(4), pp.3428–3435. Available at: http://dx.doi.org/10.1021/acsnano.5b01762.

Villar-Garea, A. & Esteller, M., 2003. DNA demethylating agents and chromatin-remodelling drugs: which, how and why? *Current drug metabolism*, 4(1), pp.11–31.

Wade, P. a, 2001. Methyl CpG binding proteins: coupling chromatin architecture to gene regulation. *Oncogene*, 20, pp.3166–3173.

Wang, P. et al., 2000. Use of Oligodeoxyribonucleotides with Conformationally Constrained Abasic Sugar Targets To Probe the Mechanism of Base Flipping by HhaI DNA (Cytosine C5)-methyltransferase. *Journal of the American Chemical Society*, 122(50), pp.12422–12434. Available at: http://dx.doi.org/10.1021/ja001989s.

Ward, D.C., Reich, E. & Stryer, L., 1969. Fluorescence studies of nucleotides and polynucleotides. I. Formycin, 2-aminopurine riboside, 2,6-diaminopurine riboside, and their derivatives. *The Journal of biological chemistry*, 244(5), pp.1228–1237.

Waterland, R.A. & Jirtle, R.L., 2003. Transposable elements: targets for early nutritional effects on epigenetic gene regulation. *Molecular and cellular biology*, 23(15), pp.5293–300. Available at: http://www.pubmedcentral.nih.gov/articlerender.fcgi?artid=165709&tool=pmcentrez&rendertype=abstract.

Weller, A., 1956. Innermolekularer Protonenübergang im angeregten Zustand. *Zeitschrift für Elektrochemie, Berichte der Bunsengesellschaft für physikalische Chemie*, 60(9-10), pp.1144–1147. Available at: http://dx.doi.org/10.1002/bbpc.19560600938.

Wilson, J.N. & Kool, E.T., 2006. Fluorescent DNA base replacements: reporters and sensors for biological systems. *Organic & Biomolecular Chemistry*, 4(23), pp.4265–4274. Available at: http://dx.doi.org/10.1039/B612284C.

Woolfe, G.J. & Thistlethwaite, P.J., 1981. Direct Observation of Excited State Intramolecular Proton Transfer Kinetics in 3-Hydroxyflavone. , 5(1977), pp.6916–6923.

Wu, P. & Nordlund, T.M., 1990. Base stacking and unstacking as determined from a DNA decamer containing a fluorescent base. *Biochemistry*, (1988), pp.2222–2228.

Yoshikawa, H. et al., 2001. SOCS-1, a negative regulator of the JAK/STAT pathway, is silenced by methylation in human hepatocellular carcinoma and shows growth-suppression activity. *Nature genetics*, 28(may), pp.29–35.

Yushchenko, D. a et al., 2006. Modulation of dual fluorescence in a 3-hydroxyquinolone dye by perturbation of its intramolecular proton transfer with solvent polarity and basicity. *Photochemical & photobiological sciences : Official journal of the European Photochemistry Association and the European Society for Photobiology*, 5(11), pp.1038–44. Available at: http://www.ncbi.nlm.nih.gov/pubmed/17077900.

Zhao, G.-J. & Han, K.-L., 2012. Hydrogen Bonding in the Electronic Excited State. *Accounts of Chemical Research*, 45(3), pp.404–413. Available at: http://dx.doi.org/10.1021/ar200135h.

Zhu, R. et al., 2010. Nanomechanical recognition measurements of individual DNA molecules reveal epigenetic methylation patterns. *Nature nanotechnology*, 5(11), pp.788–791.

Vasyl KILIN

Analyse par de nouveaux outils de fluorescence du mécanisme de la protéine UHRF1 dans la méthylation de l'ADN

Résumé

Les profils de méthylation de l'ADN sont des marques épigénétiques essentielles contrôlant l'expression génétique spécifique des tissus. Ces profils sont fidèlement reproduits par l'enzyme DNMT1 qui est dirigée par la protéine UHRF1 vers les sites CpG hémiméthylés (HM). La spécificité élevée d'UHRF1 vis-à-vis de ces sites CpG HM est liée à la capacité de son domaine SRA de basculer sélectivement les résidus méthylcytosine (mC). Par conséquent, la compréhension de la capacité d'UHRF1 à lire les séquences d'ADN et de basculer leurs résidus mC est une question importante en épigénétique moléculaire. Dans le présent travail, nous avons utilisé des analogues de nucléobases sensibles à l'environnement pour étudier le basculement de base induit par SRA. Nous avons découvert qu'un étiquetage par la 2-thiényl-3-hydroxychromone (3HCnt) à proximité de la cible CpG méthylée, permet le suivi de ce basculement SRA-induit de mC et de sa dynamique. Les spectroscopies de fluorescence à l'état stationnaire et de "*stopped flow*" ont montré des différences significatives entre les ADNs HM et non méthylé (NM) vis-à-vis de la reconnaissance et la cinétique de liaison du SRA. Effet, nous avons montré que SRA est capable de se lier et de glisser avec une cinétique rapide sur le duplex NM, en accord avec le rôle de lecteur d'UHRF1. Par contre, la cinétique de basculement de mC s'avère beaucoup plus lente, ce qui augmente sensiblement la durée de vie d'UHRF1 lié à un site CpG hémi-méthylé et donc la probabilité de recruter DNMT1 afin de dupliquer fidèlement le profil de méthylation de l'ADN. Nous avons ainsi obtenu pour la première fois un test capable de suivre le basculement de la base induit par UHRF1, ce qui nous a permis de proposer un mécanisme pour le recrutement de DNMT1 par UHRF1 sur les sites HM.

Résumé en anglais

DNA methylation patterns are key epigenetic marks which control tissue specific gene expression. These patterns are faithfully replicated by the DNMT1 enzyme which is directed by the UHRF1 protein to hemi-methylated (HM) CpG sites. The high specificity of UHRF1 to HM CpG sites is related to the ability of its SRA domain to selectively flip methylcytosine (mC) residues. Therefore, the understanding of how UHRF1 reads DNA sequences and flips mC residues is an important question in molecular epigenetics. In the present work, we apply environment-sensitive nucleobase analogues to study the SRA-induced base flipping. We found that only labelling by 2-thienyl-3-hydroxychromone (3HCnt) outside but close to the target methylated CpG allows monitoring the SRA-induced mC-flipping and its dynamics. Fluorescence steady-state spectroscopy and stopped flow measurements showed significant differences in the recognition and binding kinetics of SRA for HM and non-methylated (NM) DNA. Indeed, SRA was found to bind and slide with fast kinetics on NM duplexes, in line with the reader role of UHRF1. In contrast, the kinetics of mC flipping was found to be much slower, substantially increasing the lifetime of UHRF1 bound to a CpG site in HM duplexes and thus, the probability of recruiting DNMT1 in order to faithfully duplicate the DNA methylation profile. Therefore, we proposed for the first time an assay able to sensitively monitor the UHRF1-induced base flipping, which helped us to provide a possible mechanism for the UHRF1 directing function on DNMT1.